UNDERSTANDING THE COMPOSITION AND EVOLUTION OF THE LUNAR SURFACE THROUGH LABORATORY SPACE WEATHERING SIMULATIONS AND REMOTE SENSING

A DISSERTATION SUBMITTED TO THE GRADUATE DIVISON OF THE UNIVERSITY OF HAWAI‘I AT MĀNOA IN PARTIAL FULFILLMENT OF THE REQUIREMENTS FOR THE DEGREE OF

DOCTOR OF PHILOSOPHY
IN
GEOLOGY AND GEOPHYSICS

December 2019

By
Laura M. Corley

Dissertation committee:

Jeffrey J. Gillis-Davis, Chairperson
Paul G. Lucey
G. Jeffrey Taylor
Hope A. Ishii
Robert Jedicke

Keywords: Moon, Lunar Surface, Lunar Remote Sensing, Space Weathering, Spectroscopy

ACKNOWLEDGEMENTS

I would like to thank Jeff Gillis-Davis for being an outstanding advisor. He took a step back and let me figure things out on my own, but he was always available for help when I needed it. Most times that I required his help was when I was struggling with something I had to do or build in the lab. Thanks to Jeff, I became much more comfortable with building things, crushing rocks, using liquid nitrogen, and of course, shooting lasers, in addition to all of the academic things. I also want to thank Jeff for understanding how important family is. Four and a half years into my PhD, I had my daughter. Jeff never made me feel like he was concerned I wouldn't graduate or questioned my progress.

All of my professors from my undergraduate and graduate studies at the University of Hawai‘i at Mānoa have contributed to my success. Thank you to Chip Fletcher for hiring me as an undergraduate. I started off doing research in coastal geology with Chip, and when I was considering graduate school he advised me to look into planetary geology because of my interest in remote sensing. I would like to thank Ed Scott for getting me hooked on planetary geology in his class. Thank you to Paul Lucey for hiring me as an undergraduate and for the advice on all of my projects since then. Who better to turn me into a "lunatic" than Paul? Thank you to Jeff Taylor for teaching me about things other than the Moon, like Mars, for the advice on my first paper, and for inviting me to give a talk at the GRAIL meeting. Thank you to Gary Huss for the cosmochemistry knowledge and for the occasional use of a few things in his lab. I want to thank Hope Ishii for giving me my "driver's license" on the FIB and for advice in personal matters.

Thank you to my comprehensive exam and dissertation committee members, which included Paul Lucey, Jeff Taylor, Bridget Smith-Konter, Scott Rowland, Hope Ishii, and Robert Jedicke. I wouldn't have made it this far without all of you guiding me. I thank my summer internship advisors from the Lunar and Planetary Institute, Patrick McGovern and Georgiana Kramer. Thanks for picking an amazing project for me that I was able to continue after I left Houston and include in my dissertation, with the help of your guidance and expertise. I would also like to thank Jim Head and Francis Nimmo for

the comments on the manuscript. Thank you to everyone at the LPI for making the internship a great experience.

I would like to thank Peter Schultz for his guidance on our experimental approach and for his comments on my manuscript. Thank you to the crew at the Ames Vertical Gun Range for ensuring the impact experiments ran smoothly and that as many shots as possible were fired during our visit. I am also grateful that Paul Holick at the Stillwater Mining Co. provided the most pristine, lunar-like plagioclase that he could find.

Thank you to all of the collaborators who helped with different aspects of the research presented in this dissertation, including David Trang, Myriam Lemelin, Walter Kiefer, Mark Wieczorek, Maria Zuber, Kathryn Powell, Hope Ishii, John Bradley, Kenta Ohtaki, and Andrew Ichimura.

I thank Vi Nakahara, Lily Shao, Grace Furuya, Rena Lefevre, Susan Vangorder, and Leona Anthony for their very important administrative support. Thank you to Brooks Bays for helping me with my illustrations. Thanks to Ethan Kastner and Eric Pilger for all of the technical support.

I want to thank Caroline Caplan, Christie Jilly-Rehak, and Casey Honniball for being the best officemates. Thank you to David Trang, Myriam Lemelin, Sarah Crites, Elizabeth Shields, Melissa Adams, and Heather Kaluna for the friendship and the academic advice. Thank you to Kelsey Prissel and Andrea Bruck for the type of friendship that is not affected by distance or time.

Finally, I would like to thank my family. Thank you, Mom and Dad, for your advice and encouragement. Thank you, Natalie, for making sure I took a break from school and enjoyed the island once in a while. Thank you to my in-laws for the support and coming to help out with moving and watching Hazel while I was finishing my dissertation. Most importantly, thank you to Mike and Hazel. Mike, I wouldn't be where I am today without you. You believed in me more than anyone. Thank you, Hazel, for the bright light that shines within you. My biggest motivation was to make you proud.

This work was supported by the NASA Earth and Space Science Fellowship (grant NNX14AP20H) and NASA grant NNX13AG58G.

ABSTRACT

Without an atmosphere, the lunar surface is vulnerable to space weathering, a process by which solar wind, galactic rays, and micrometeoroids bombard a planetary body and alter the surface's physical, chemical, and spectral properties. The most well studied spectral changes are in the visible to near-infrared wavelengths, where increasing exposures to space weathering results in decreased reflectance, spectral reddening, and subdued absorption bands. Thus, mineralogical and compositional analyses of planetary bodies via spectral reflectance measurements are complicated by the space weathering process. The first part of this dissertation investigates sites on the lunar surface that contain olivine, a mineral that is relatively sparse in the crust and is critical to understanding the magmatic history of the Moon. We examine both known and previously unidentified olivine exposures using hyperspectral visible to near-infrared data from the Moon Mineralogy Mapper. In an effort to determine the origins and transport mechanisms that led to these individual exposures, we estimate crustal thicknesses using the Gravity Recovery and Interior Laboratory, investigate geologic settings using images from the Lunar Reconnaissance Orbiter Camera, and estimate mineral abundances using radiative transfer modeling. Our combined geophysical and spectral investigation allows for the identification of both volcanic and mantle-derived olivine.

The second part of this dissertation characterizes space weathering effects in order to improve compositional and mineralogical analyses of spectral data in the future. We simulate space weathering (i.e., micrometeoroid bombardment) in the laboratory via kinetic impact, laser irradiation, and a combination of the two methods on lunar analog material to understand the various physical and spectral changes produced by each method and determine which method produces the most accurate lunar space weathering effects. We conclude that a combination of the two methods best replicates lunar-like space weathering, in part because subsequent laser irradiation of the analog that was first weathered by kinetic impacts enhances darkening of the material and produces more submicroscopic iron. This effect is likely due to the lower melting/vaporization temperature of the glass relative to minerals, which allows iron to be extracted from the glass more easily than from a crystalline structure. We also examine how space

weathering affects regoliths in cold environments. We perform laser irradiation when minerals are held at two different temperatures, 85 K and 295 K. With equal amounts of irradiation, we find that the olivine and pyroxene irradiated at 85 K have higher reflectance than those irradiated at 295 K. Analyses of our samples using Scanning Transmission Electron Microscopy suggest that space weathering of low-temperature regolith produces less melting and less submicroscopic iron. Our results help to quantify the effects of space weathering on low-temperature regolith, which needs to be considered when interpreting spectral measurements at different latitudes, geologic settings, and distance from the Sun.

TABLE OF CONTENTS

ACKNOWLEDGEMENTS iii

ABSTRACT v

LIST OF TABLES xi

LIST OF FIGURES xiii

LIST OF ABBREVIATIONS xvii

CHAPTER 1: INTRODUCTION xvii

1.1 The ancient, but ever-changing, lunar surface 1

1.2 Formation of the primary mantle and crust 1

1.3 Evolution of the surface through impact cratering 2

1.4 Evolution of the surface through space weathering 3

1.4.1 Space weathering processes and their physical and chemical effects 3

1.4.2 Spectral changes 6

CHAPTER 2: OLIVINE-BEARING LITHOLOGIES ON THE MOON: CONSTRAINTS ON ORIGINS AND TRANSPORT MECHANISMS FROM M^3 SPECTROSCOPY, RADIATIVE TRANSFER MODELING, AND GRAIL CRUSTAL THICKNESS 8

2.1 Introduction 9

2.2 Hypotheses for the Origin of Observed Olivine and Mechanisms of Transport to Surface 12

2.2.1 Transport by Basin-forming Impacts 15

2.2.2 Magmatic Transport 19

2.3 Methods 21

2.3.1 M^3 Data 21

2.3.2 Olivine Algorithms for Spectral Identification 22

2.3.3 Quantifying Olivine in Identified Spectra 24

2.3.4 FeO Content as a Constraint 26
2.3.5 Spectral Library 26
2.3.6 Geophysical and Geological Contextual Data 28
2.4 Results 30
2.4.1 Crisium 33
2.4.2 Nectaris 35
2.4.3 Humorum 36
2.4.4 Roche/Tsiolkovsky 36
2.5 Discussion 37
2.5.1 Crisium 38
2.5.2 Nectaris 41
2.5.3 Humorum 42
2.5.4 Roche/Tsiolkovsky 43
2.5.5 Implications for sample return 44
2.6 Conclusions 45
CHAPTER 3: A COMPARISON OF THE EFFECTS OF KINETIC IMPACT AND LASER IRRADIATION FOR SPACE WEATHERING SIMULATIONS 47
3.1 Introduction 48
3.2 Methods 52
3.2.1 Target Material 52
3.2.2 Pulsed Laser Irradiation 53
3.2.3 AVGR Kinetic Impacts 54
3.2.4 Reflectance Measurements and Radiative Transfer Modeling 55
3.2.5 Scanning Transmission Electron Microscopy (S/TEM) Analyses 55
3.2.6 Ferromagnetic Resonance 57

3.3 Results 57
3.3.1 Effects of AVGR Kinetic Impacts 57
3.3.2 Effects of Pulsed Laser Irradiation 62
3.3.3 Effects of Combined AVGR Impact and Laser Irradiation 66
3.3.4 Ferromagnetic Resonance Spectroscopy 69
3.4 Discussion 71
3.4.1 AVGR Kinetic Impacts 71
3.4.2 Pulsed Laser Irradiation 72
3.4.3 Combined AVGR Kinetic Impact and Laser Irradiation 73
3.4.4 Ferromagnetic Resonance Spectroscopy 74
3.5 Conclusions 75
CHAPTER 4: TEMPERATURE-DEPENDENT EFFECTS OF SPACE WEATHERING OBSERVED USING LASER IRRADIATION SIMULATIONS 77
4.1 Introduction 78
4.2 Methods 80
4.2.1 Target Material 80
4.2.2 Laser irradiation 81
4.2.3 Reflectance Measurements and Radiative Transfer Modeling 83
4.2.4 Scanning Transmission Electron Microscopy (S/TEM) 83
4.3 Results 84
4.3.1 Spectral Changes and SMFe Abundance Estimates from Radiative Transfer Modeling 84
4.3.2 S/TEM Analyses 88
4.4 Discussion 105
4.5 Conclusion 108
CHAPTER 5: CONCLUSION AND FUTURE WORK 110

APPENDIX A: DETAILED INFORMATION ON OLIVINE DETECTIONS 114

APPENDIX B: SUPPORTING DATA FOR CHAPTER 3 119

APPENDIX C: ELEMENTAL COMPOSITIONS OF MATERIALS WEATHERED AT 85 K AND 295 K OBTAINED FROM EDS 125

REFERENCES 128

LIST OF TABLES

Table 3.1 Elemental compositions (atomic %) of the plagioclase shown Figure 3.2a and glass-welded aggregate shown in Figure 3.2b, obtained from S/TEM EDS analyses..... 61

Table 4.1 The abundances (wt. %) of nanophase Fe and microphase Fe in the laser-irradiated olivine and pyroxene, estimated using radiative transfer modeling..... 87
Table 4.2 Measurements of the maximum and minimum thicknesses of amorphous rims and the maximum diameters of vesicles and SMFe obtained from S/TEM images..... 88
Table 4.3 Elemental compositions (atomic %) of the pyroxene sample irradiated at 85 K (Figure 4.15) obtained from the TEM EDS spectra shown in Figure 4.21.. 101
Table 4.4 Elemental compositions (atomic %) of the plagioclase sample irradiated at 295 K (Figure 4.23) obtained from TEM EDS..... 104
Table A.1 Information on each olivine detection, including the region, latitude, longitude, mineralogical composition estimated using radiative transfer modeling, the Mg# used for the model, the FeO content, a description of the location, and our interpreted origin and transport mechanism…….134

Table B.1 Elemental compositions (atomic %) of the laser-irradiated pyroxene and plagioclase grains, obtained from S/TEM EDS analyses..... 123
Table B.2 Elemental compositions (atomic %) of the plagioclase grain exposed to AVGR kinetic impacts and laser irradiation, obtained from S/TEM EDS analyses. 123
Table B.3 Reflectance changes of the lunar highlands analog exposed to AVGR kinetic impacts, laser irradiation, and combined AVGR kinetic impacts and laser irradiation, expressed as a percent change relative to the fresh material. 124

Table C.1 Elemental compositions (atomic %) of the olivine grain laser irradiated at 295 K (Figure 4.6), obtained from S/TEM EDS analyses. 125
Table C.2 Elemental compositions (atomic %) of the olivine grain irradiated at 85 K (Figure 4.10), obtained from S/TEM EDS analyses. 125

Table C.3 Elemental compositions (atomic %) of the pyroxene grain laser irradiated at 295 K (Figure 4.15), obtained from S/TEM EDS analyses. 125
Table C.4 Elemental compositions (atomic %) of the pyroxene grain laser irradiated at 85 K (Figures 4.18 & 4.19), obtained from S/TEM EDS analyses..... 126
Table C.5 Elemental compositions (atomic %) of the plagioclase grain laser irradiated at 295 K (Figure 4.23), obtained from S/TEM EDS analyses. 126
Table C.6 Elemental compositions (atomic %) of the plagioclase grain laser irradiated at 85 K (Figure 4.6), obtained from S/TEM EDS analyses..... 127

LIST OF FIGURES

Figure 2.1 A "matrix" showing endogenic categories of origin and transport for olivine on the lunar surface.. 13
Figure 2.2 Basin and complex crater transport of olivine. 14
Figure 2.3 Magmatic transport of olivine. 18
Figure 2.4 M^3 mosaics of (a) Crisium, (b) Nectaris, (c) Humorum basins and (d) Roche and Tsiolkovsky craters, from which olivine-bearing spectra were identified. 21
Figure 2.5 M^3 spectra (reflectance as a function of wavelength) showing Fe-dominated olivine (Crisium), Mg-dominated olivine (Humorum), and an olivine-pyroxene mixture (Crisium) 23
Figure 2.6 True-color M^3 mosaic of Crisium basin (left) showing an area of interest, a small patch of mare called Lacus Perseverantiae (top right). 24
Figure 2.7 Locations of Mg# 65 olivine and Mg# 90 olivine at (a) Crisium, (b) Nectaris, (c) Humorum basins, and (d) near Roche and Tsiolkovsky craters. Base maps are crustal thickness (color scale) maps created from GRAIL and LOLA with shading from LOLA topography 29
Figure 2.8 Locations of Mg# 65 olivine and Mg# 90 olivine at (a) Crisium, (b) Nectaris, (c) Humorum basins, and (d) near Roche crater. Base maps are WAC mosaics. 30
Figure 2.9 Examples of the best spectral fit between the modeled library spectra and the M3 spectra, along with the residuals between the observed and the modeled spectra. 31
Figure 2.10 Mineral abundances (wt.%), which were estimated with radiative transfer modeling for M^3 olivine spectra from (a) Crisium, (b) Nectaris, (c) Humorum basins, and (d) near Roche crater analyzed on rock classification diagrams 32
Figure 2.11 The abundance (wt.%) of olivine versus plagioclase for which the modeled library spectra are calculated. 33
Figure 2.12 LRO WAC mosaic of Crisium basin showing locations of Mg# 65 olivine and Mg# 90 olivine. LRO images of areas of interest include: a) Picard crater (WAC), b) the mare and southern rim of Crisium (WAC), c) Eimmart A crater (NAC), d) a mechanically stable outcrop on the rim of Eimmart A (NAC). 34
Figure 2.13 LRO NAC mosaic showing the approximate locations of olivine detections at Beaumont L crater on mare Nectaris, inset from the WAC mosaic map. 35

Figure 2.14 LRO WAC images showing the location of Mg# 65 olivine detections on a graben on the rim of Humorum basin, inset from the WAC mosaic. 36
Figure 2.15 LRO WAC images, inset from the WAC mosaic, showing the location of Mg# 65 olivine detections at a) Tsiolkovsky crater, b) mare inside Bolyai crater, and c) Pauli crater. 37

Figure 3.1 Glass-welded aggregates created in AVGR impact experiments, shown at the cm-scale using optical imaging and the μm-scale using SE imaging. 58
Figure 3.2 S/TEM (Left) HAADF and (Right) brightfield images of (a) adjacent plagioclase grains and (b) glass-welded aggregate from AVGR impact experiments 60
Figure 3.3 (Top) Absolute reflectance spectra and (Bottom) reflectance, normalized to 700 nm, of the lunar highlands analog weathered by 60 min pulsed laser irradiation, by kinetic impact shots at the AVGR, and by a combination of both methods 62
Figure 3.4 a) SE image of a pyroxene grain laser irradiated for 60 min. b) S/TEM HAADF image of the FIB section. 64
Figure 3.5 Electron nanodiffraction pattern of a SMFe particle contained in the rim of the laser irradiated pyroxene grain. 65
Figure 3.6 a) SE image of a plagioclase grain exposed to 60 min of laser irradiation. b) S/TEM brightfield image of the plagioclase grain..... 65
Figure 3.7 a) SE image of a plagioclase grain exposed to 60 min of laser irradiation. b) S/TEM brightfield image of the FIB section, which contains a plagioclase crystal encased in glass ("plag-glass") 66
Figure 3.8 S/TEM HAADF image showing the entire FIB section of the plagioclase grain from AVGR kinetic impacts that was subsequently irradiated for 60 min with pulsed laser irradiation 67
Figure 3.9 S/TEM HAADF image of a plagioclase grain from AVGR kinetic impacts that was subsequently irradiated for 60 min with pulsed laser irradiation. 68
Figure 3.10 S/TEM HAADF image and EDS spectra of a plagioclase grain from AVGR kinetic impacts that was subsequently irradiated for 60 min with pulsed laser irradiation. 69

Figure 3.11 a) Normalized FMR spectra of highland soils and laboratory weathered highland soil analogs. b) Soil maturity index I_s/FeO vs wt% FeO for the lunar soils and weathered soil analogs..... 70

Figure 4.1 Experimental setup for laser irradiation 82
Figure 4.2 Absolute reflectance (a) and reflectance normalized to 650 nm (b) of fresh and laser-irradiated San Carlos olivine 85
Figure 4.3 Absolute reflectance (a) and reflectance normalized to 750 nm (b) of fresh and laser-irradiated orthopyroxene 85
Figure 4.4 Scaled reflectance showing the fits (dashed lines) of the radiative transfer model to olivine (a) and orthopyroxene (b) samples laser irradiated at 85 K and 295 K for 60 minutes..... 86
Figure 4.5 Absolute reflectance (a) and reflectance normalized to 700 nm (b) of fresh and laser-irradiated lunar highlands analog..... 87
Figure 4.6 Secondary electron images of an olivine grain irradiated 60 minutes by laser irradiation at 295 K 89
Figure 4.7 Brightfield image of the olivine grain irradiated at 295 K from Figure 4.5.. . 89
Figure 4.8 S/TEM brightfield images showing the SMFe contained in the rim of the olivine irradiated at 295 K..... 90
Figure 4.9 Electron diffraction of SMFe particles contained in the rim of the olivine grain irradiated at 295 K confirms that the SMFe is metallic Fe..... 91
Figure 4.10 Secondary electron images of an olivine grain irradiated 60 minutes by laser irradiation at 85 K 92
Figure 4.11 HAADF image of the FIB section from the olivine grain irradiated at 85 K from Figure 4.9 92
Figure 4.12 S/TEM brightfield images of the olivine grain irradiated at 85 K 93
Figure 4.13 Electron diffraction of SMFe particles contained in the rim of the olivine grain irradiated at 85 K confirms that the SMFe is metallic Fe..... 94
Figure 4.14 Secondary electron images of a pyroxene grain irradiated 60 minutes by laser irradiation at 295 K..... 95
Figure 4.15 S/TEM brightfield image of the pyroxene grain irradiated at 295 K 95

Figure 4.16 Brightfield images of the pyroxene grain irradiated at 295 K 96
Figure 4.17 Electron diffraction of SMFe particles contained in the rim of the pyroxene grain irradiated at 295 K confirms that the SMFe is metallic Fe..... 97
Figure 4.18 Secondary electron images of a pyroxene grain irradiated 60 minutes by laser irradiation at 85 K..... 98
Figure 4.19 Brightfield image of the pyroxene grain irradiated at 85 K..... 99
Figure 4.20 TEM images of the pyroxene grain irradiated at 85 K..... 100
Figure 4.21 a) Electron diffraction pattern of SMFe particles contained in the rim of the pyroxene grain irradiated at 85 K confirms that the SMFe is metallic Fe. 100
Figure 4.22 EDS spectra from the pyroxene irradiated at 85 K..... 101
Figure 4.23 Secondary electron images of a plagioclase grain irradiated 60 minutes by laser irradiation at 295 K..... 102
Figure 4.24 TEM HAADF image of the plagioclase irradiated at 295 K 103
Figure 4.25 Secondary electron images of a plagioclase grain irradiated 60 minutes by laser irradiation at 85 K..... 105
Figure 4.26 S/TEM HAADF image of the plagioclase irradiated at 85 K..... 105

Figure B.1 Top: brightfield image of the host plagioclase (with twinning) from the AVGR kinetic impact experiments (Figure 3.2a). Bottom: the diffraction pattern matches that of bytownite in the [010] zone axis.. 119
Figure B.2 Top: brightfield image showing the inclusions in the shocked plagioclase from the AVGR kinetic impact experiments (Figure 3.2a). Bottom: the diffuse halo in the corresponding electron diffraction pattern indicates that the inclusions are amorphous. 120
Figure B.3 Top: brightfield image of the shocked surface of the plagioclase from the AVGR kinetic impact experiments (Figure 3.2a). Bottom: the electron diffraction pattern confirms that the surface had been broken and shocked..... 121
Figure B.4 The polycrystalline texture of the shocked plagioclase surface of the plagioclase grain from the AVGR kinetic impact experiments indicates that it was broken up by the impact shock. 122
Figure B.5 Electron paramagnetic resonance (EPR) spectra for the fresh lunar highlands analog and the analog weathered by kinetic impacts at the AVGR..... 122

LIST OF ABBREVIATIONS

Abbreviation/Symbol	Definition
A	FMR signal amplitude
Å	angstrom
amu	atomic mass unit
An	anorthite
at.%	atomic percent
AVGR	Ames Vertical Gun Range
cm	centimeter
CPX	clinopyroxene
CRISM	Compact Reconnaissance Imaging Spectrometer
EDS	Energy Dispersive x-ray Spectroscopy
En	enstatite
EPR	electron paramagnetic resonance
ESR	electron spin resonance
FIB	Focused Ion Beam
FMR	ferromagnetic resonance
Fo	forsterite
Fs	ferrosilite
g	gram
Ga	billion years ago
GHz	gigahertz
GRAIL	Gravity Recovery and Interior Laboratory
ΔH_{pp}	peak-to-peak linewidth squared
HAADF	high-angle annular darkfield
Hz	hertz
IR	infrared
I_s	FMR intensity
I_s/FeO	intensity of FMR normalized to total iron content
J	joule

k	imaginary index of refraction
K	Kelvin
keV	kiloelectronvolt
kV	kilovolt
kg	kilogram
kJ	kilojoule
km	kilometer
LOLA	Lunar Orbiter Laser Altimeter
LRO	Lunar Reconnaissance Orbiter
LROC	Lunar Reconnaissance Orbiter Camera
m	meter
M^3	Moon Mineralogy Mapper
mbar	millibar
MeV	Megaelectronvolt
Mg#	molar MgO/(MgO+FeO)
MGM	Modified Gaussian Model
mil	0.0254 millimeters
min	minute
mJ	millijoule
mm	millimeter
MI	Multiband Imager
mrad	milliradian
NAC	Narrow Angle Camera
Nd:YAG	neodymium-doped yttrium aluminum garnet
NIR	near-infrared
nm	nanometer
ns	nanosecond
Ol’	olivine index
OL	olivine
OPX	orthopyroxene
PLG	plagioclase

PSR	Permanently Shadowed Region
R	reflectance
RMS	root-mean-square
SE	Secondary Electron
sec	second
SMFe	submicroscopic iron
SPA	South Pole-Aitken
sr	steradian
S/TEM	Scanning Transmission Electron Microscopy
TC	Terrain Camera
TEM	Transmission Electron Microscopy
μm	micrometer
UV	ultraviolet
VNIR	visible to near-infrared
VIS	visible
vol.%	volume percent
W	watt
WAC	Wide Angle Camera
Wo	wollastonite
wt.%	weight percent
yr	year

CHAPTER 1

INTRODUCTION

1.1 The ancient, but ever-changing, lunar surface

The Moon allows the study of a variety of Solar System processes, including how a celestial body forms, evolves, and is modified by exposure to the space environment. The lunar highlands represent the primary anorthositic crust, while the maria are a secondary crust generated by mare volcanism. The maria were emplaced ~4 Ga to 1.2 Ga (Head and Wilson, 1992, Hiesinger et al., 2011) and although they are younger, they are nearly as ancient as the highlands when compared with average ages of Earth's surface. Without an atmosphere and magnetic field like Earth's, the lunar surface is vulnerable to the space environment. The physical, chemical, and spectral properties of the ancient terrains are ever-changing, because solar wind, galactic rays, and micrometeoroids constantly alter the surface in a process known as space weathering. In this dissertation, we use remote sensing to investigate olivine surface exposures as products of either the primary mantle or subsequent volcanism. The spectral features used to determine compositions are complicated by the space weathering process. Part of this dissertation is an attempt to understand space weathering effects so that they may be removed more accurately from spectral data in the future. We use laboratory space weathering simulations to determine the best technique and conditions to replicate lunar space weathering. First, we present some concepts necessary to understand the three research Chapters, including the crystallization of the magma ocean, formation of impact basins and maria, and an overview of space weathering.

1.2 Formation of the primary mantle and crust

The prevailing hypothesis for the Moon's formation is that Theia, a body approximately the size of Mars, collided with Earth. The impact debris formed a disk of material in Earth's orbit, which accreted into a satellite orbiting Earth (Hartmann and Davis, 1975). The rapid accretion would have generated a fully molten Moon, referred to as a lunar magma ocean (Wood, 1970), which subsequently cooled and solidified. The primary mantle and crust fractionally crystallized from this magma ocean of ultramafic (<

48 wt.% SiO_2) to basaltic (48-52 wt% SiO_2) major-element composition (Elkins-Tanton et al., 2011). Olivine was the first major phase to crystallize, beginning with magnesium-rich olivine (forsterite, Mg_2SiO_4) that sank due to its higher density than the magma. As this Mg-rich olivine continued to crystallize, the magma became increasingly iron-rich and iron-rich minerals eventually crystallized. The next major phase to crystallize was orthopyroxene, which also sank, causing the remaining magma ocean to become increasingly aluminum-rich. After ~80% of the magma ocean had crystallized, plagioclase began to crystallize, which was less dense and floated, forming the primary anorthositic crust. Ilmenite was the last and densest major phase to crystallize. It has been hypothesized that this correlation between density and percentage of magma ocean crystallization (i.e., the gradation from Mg-rich silicates to denser Fe-rich silicates and ilmenite) produced an unstable density gradient, which drove overturn of the cumulate pile via subsolidus convection (Ringwood and Kesson, 1976; Herbert, 1980; Ryder, 1991; Spera 1992). In the post-overturn model of the lunar interior, there are locations where the least dense, early-phase Mg-rich cumulates, which would have initially been at the bottom of the cumulate pile, could now be much closer to the surface, potentially accessible by excavation via a very large impact (Hess and Parmentier, 1995).

1.3 Evolution of the surface through impact cratering

The Moon has been subjected to impact cratering throughout its history. The surface may have experienced a short period of intense cratering, known as the Late Heavy Bombardment, which concluded ~3.8 billion years ago (Tera et al., 1974). The bombardment reworked the primary crust via cratering events of various sizes, including large impacts that created impact basins hundreds to thousands of kilometers in diameter and often subsequently filled with basaltic lava (i.e., the maria). These large impacts formed a 10-20 km thick zone of fractured and brecciated highlands rock called the megaregolith (Hartmann, 1973). Hence, the primary crust, as it first crystallized from the magma ocean, no longer remains intact. However, cumulates of both the primary crust and mantle have likely been observed. For example, millimeter fragments of pure anorthosite were identified in samples returned by the Apollo missions and sparked the lunar magma ocean hypothesis (e.g., Wood, 1970). Furthermore, it is hypothesized that the impacts that created some of the basins excavated the lower crust and/or upper mantle

(Miljković et al., 2015). Olivine has been detected remotely at several large impact basins, with compositions consistent with mantle lithologies (Yamamoto et al., 2010; Arnold et al., 2016; Corley et al., 2018). Hence, by bringing rocks from depth to the surface, impacts serve as a crude bore hole. We can study these excavated cumulates of the original crust and mantle remotely or with returned samples.

In Chapter 2, we use remote sensing to investigate olivine surface exposures as products of either the primary mantle or subsequent volcanism. Hyperspectral visible to near-infrared (VNIR) data from Chandrayaan-1's Moon Mineralogy Mapper (M^3) allow detection of both known and previously unidentified olivine exposures. In an effort to determine the origins and transport mechanisms that led to these individual exposures, we estimate mineral abundances using radiative transfer modeling and examine crustal thickness estimates, topography and slope maps, and images from the Lunar Reconnaissance Orbiter Camera (LROC). Our combined geophysical, spectral, and radiative transfer modeling investigation allows for the identification of both volcanic and mantle-derived olivine.

1.4 Evolution of the surface through space weathering

The Moon lacks an atmosphere and a strong magnetic field to protect it from the space environment. As a result, it experiences a process known as space weathering, in which micrometeorite impacts, high-energy particles from solar flares and cosmic rays, and low-energy particles from solar wind cause physical and chemical changes in surface materials. The effects of space weathering are superimposed on the impact processes that mechanically churn the regolith. The lunar regolith was formed early by both large and small impacts that excavated fresh bedrock and caused rock to be pulverized, melted, and brecciated. Frequent small impacts continue to comminute (break down) and garden (mix) the regolith, building it up to a thickness of ~4-15 meters (McKay et al. 1991). The space-weathered soil is the result of maturation, the combined effects of all of these mechanisms.

1.4.1 Space weathering processes and their physical and chemical effects

The solar wind, which are the lowest energy particles streaming from the Sun at ~1 keV/amu, directly implants ions (mostly H^+ and He^+, along with other noble gases) into lunar materials with a penetration depth of ~50 nm (Bibring et al., 1972; Walker,

1980). These particles partially vaporize the target material and cause radiation damage, creating an amorphous outer layer on crystalline grains (Walker, 1980; McKay et al., 1991). Solar wind ions eject cations with the lowest binding energy from the target material, a process called sputtering that results in chemical fractionation (Hapke, 1966). When the ions are not incident vertically to the surface, high mass atoms (Y and heavier elements) are preferentially sputtered forward and low mass atoms (Ca and lighter elements) are preferentially sputtered backward (Paruso et al., 1978; Hapke, 2001). With atoms lighter than Ca being more efficiently backscattered out of the target, initially a sputtered surface that is enriched in heavy atoms, such as Ti and Fe, is produced (Bradley, 1994). Light elements are also more efficiently recoil-implanted into deeper regions of the target by incoming ions. Bradley (1994) hypothesized that after prolonged ion fluence, sputter-erosion exposes the light-element enriched region. Based on these mechanisms, sputter-deposited films on the surfaces of lunar regolith grains could be either enriched or depleted in heavier atoms, depending on the location relative to the surfaces being directly sputtered by the solar wind (Hapke, 2001) and the amount of sputter-erosion present (Bradley, 1994). However, Hapke (2001) argues that the backscattered, lighter atoms are more likely to escape from the regolith, so lunar sputter deposits should be enriched in heavier atoms.

Keller and McKay (1997) showed that sputter-deposited amorphous rims on lunar soil grains are enriched in Si and O and depleted in Ca and Al, for plagioclase, and Fe, for pyroxene. Some interfaces have a rough texture, suggesting radiation damage in the form of sputter-erosion occurred. Depletions in Ca and Fe are consistent with the model of Bradley (1994). Si and O appear to sputter at nearly equivalent rates, resulting in enrichment in both Si and O (Keller and McKay, 1997). In addition, rims that Keller and McKay (1997) classified as vesicular, with radiation damage indicating that they are also formed by the solar wind, have a slight enrichment in O and depletion in Mg, Ca, and Fe. The loss of cations in the rims manifests as an enrichment in O, because there are insufficient cations to balance the oxygen (Keller and McKay, 1997).

The solar wind and micrometeorite impacts act together to alter the regolith, but the effects of micrometeorite bombardment can also be separate from the solar wind. The effects of micrometeorite impacts include the comminution of soil particles, gardening of

the regolith, melting, and vaporization of material (Pieters and Noble, 2016). The vaporization that occurs from a micrometeorite impact causes higher volatility elements contained in the target material, such as O, to escape and elements with higher vapor pressures (e.g. Fe, Si, and Ti) to condense into glass coatings and onto surrounding grains (Hapke, 1975). Keller and McKay (1997) observed Fe-inclusion rich rims that were depleted in O and Al and enriched in Fe, Si, Ti, Mg, S, and Ca, indicating that the rims were formed due to vapor deposition from micrometeorite impacts. In addition, the inclusion-rich rims have smooth interfaces that suggest they are the result of vapor deposition from micrometeorite bombardment, not from the solar wind. Although rims solely formed by solar wind tend to have an enrichment in O, Hapke (2001) notes that the fractionation processes from solar wind and micrometeoroid bombardment acting together leave lunar rims with a depletion in O and enrichment in Fe.

In addition to the chemical fractionation that occurs due to sputtering and micrometeorite impact, inclusions of pure iron metal, called submicroscopic iron (SMFe), form in space-weathered rims. The depletion of oxygen is compensated by the reduction of the major oxide with the lowest binding energy, which is FeO in most mafic silicates (Hapke, 2001). This reduction of Fe is the source of SMFe in rims on both sputtered and micrometeorite-impacted grains (Hapke et al., 1975). Although solar wind H^+ was previously considered necessary to enable the reduction of Fe^{2+} in minerals to Fe^0, observations have shown that Fe is reduced during the deposition of vapors generated by both solar wind sputtering and impact vaporization (Keller & McKay, 1993; Hapke, 2001). The process of condensation of Fe-bearing silicate vapors is intrinsically reducing; H^+ is a sputtering agent but is not necessary for reduction (Hapke, 2001). This is demonstrated by laser irradiation space weathering simulations that produce SMFe, indicating that micrometeorite bombardment alone is capable of the reduction of Fe and formation of SMFe (e.g., Sasaki, et al., 2001). SMFe is also found in agglutinates, which are individual particles (<1 mm) that are aggregates of smaller lunar soil particles including mineral grains, glasses, and even older agglutinates, bonded together by vesicular glass (Hapke et al., 1975; McKay et al., 1991; Hapke, 2001). Agglutinates are formed predominantly by micrometeorite impacts into the uppermost, solar wind-saturated layer of the regolith (Housley et al., 1973).

Although the solar wind sputtering and micrometeorite bombardment are the dominant processes, high-energy particles also contribute to space weathering. Cosmic rays are high-energy protons and neutrons (≥100 MeV/amu) that penetrate into lunar materials to depths of up to 1 meter (Walker, 1980). These particles produce nuclear reactions that give a variety of both stable and radioactive spallation products (e.g. ^{21}Ne, ^{15}N, and secondary electrons). The cosmogenic isotopic compositions can be used to calculate surface exposure ages. Cosmic rays, as well as solar flares, produce particle tracks in lunar soil grains, because the passage of heavily ionizing particles through the insulating solid creates a path of atomic damage. Particle-track densities can also be used to measure the exposure age of a sample (McKay et al., 1991). The percentage of soil grains with track densities greater than 10^9/cm^2 is called the track maturity index, which increases with increasing soil maturity.

Solar flare particles have energies of < 1 MeV/amu to ≥100 MeV/amu (with more low-energy particles than high-energy particles) and penetrate to depths of a few millimeters to several centimeters (Walker, 1980). The flux of solar flare particles is much lower than the flux of solar wind particles (~10^{-2} versus ~10^{10} nuclei/cm^2/sr/sec; Scherer et al., 2006). Solar flare particles also result in implanted ions, but the most significant results are the secondary effects including radionuclide production (e.g. ^{26}Al, ^{53}Mn). In addition, solar flare protons produce free electrons that can be trapped at lattice defects (Walker, 1980). Furthermore, like cosmic rays, the heavy components of solar flares (with atomic numbers ≥20, mostly Fe ions) produce particle tracks in grains.

1.4.2 Spectral changes

Along with the physical and chemical changes caused by space weathering, there are three optical effects in the VNIR that are attributed to the presence of SMFe: decreased reflectance, spectral reddening (increase of the spectral slope), and weakened absorption bands (Hapke et al, 1975; Pieters et al., 1993; Fischer and Pieters, 1994; Fischer and Pieters, 1996; Pieters et al., 2000; Hapke, 2001; Noble et al., 2001). At UV wavelengths, increased reflectance and spectral bluing (decreased spectral slope at longer wavelengths) occur as a function of space weathering (Hendrix and Vilas, 2006; Hendrix et al., 2012; Denevi et al., 2014). The spectral effects have been established by studies comparing lunar samples and spectra. Mature lunar samples contain SMFe in amorphous

rims on silicate minerals (Keller and McKay, 1993; Keller and McKay, 1997; Noble et al., 2005) and in agglutinates (Duke et al, 1970). Ultraviolet to near-infrared remote sensing is one of the most powerful and widely used techniques for mineralogical identification (Adams and McCord, 1970; Burns, 1970; Bell and Hawke, 1995; Burbine and Binzel, 2002; Blewett et al., 2009; Cloutis et al., 2012), and spectral changes due to space weathering hinder the ability to determine the original composition of space-weathered bodies using remote sensing data. In order to accurately estimate surface composition with remote optical measurements from the UV (Hendrix and Vilas, 2006) through the thermal-IR (Lucey et al., 2017), a thorough understanding of the complex processes of space weathering is critical.

Various laboratory experiments are used to simulate the space weathering process and to understand the spectral effects so that they can be accounted for in compositional models. Chapters 3 and 4 describe laboratory experiments intended to simulate the process of micrometeorite bombardment. Chapter 3 investigates the effects of kinetic impact, laser irradiation, and a combination of the two methods on a lunar highlands analog. The purpose of these experiments is to evaluate the various physical and spectral changes produced by each method in order to determine which method produces the most accurate lunar space weathering effects. Chapter 4 examines the effects of cold temperatures on space weathering. Low surface temperatures of the polar regions and the extremely low temperatures of permanently shadowed regions (PSRs) (as low as 25 K) may affect the volume of melt and vapor produced and the subsequent development of SMFe. To test for temperature-dependent effects of space weathering, we compare materials weathered by laser irradiation at low temperature (85 K) with the same materials laser irradiated at room temperature (295 K).

CHAPTER 2

OLIVINE-BEARING LITHOLOGIES ON THE MOON: CONSTRAINTS ON ORIGINS AND TRANSPORT MECHANISMS FROM M^3 SPECTROSCOPY, RADIATIVE TRANSFER MODELING, AND GRAIL CRUSTAL THICKNESS

Published as: Corley, L. M., McGovern, P. J., Kramer, G. Y., Lemelin, M., Trang, D., Gillis-Davis, J. J., Taylor., G. J., Powell, K. E., Kiefer, W. S., Wieczorek, M., and Zuber, M. T. (2018), Olivine-bearing lithologies on the Moon: Constraints on origins and transport mechanisms from M^3 spectroscopy, radiative transfer modeling, and GRAIL crustal thickness, Icarus, 300C, 287-394. DOI: 10.1016/j.icarus.2017.09.012.

Abstract – High-resolution hyperspectral data from Chandrayaan-1's Moon Mineralogy Mapper (M^3) allow detection of olivine on the lunar surface. Olivine exposed at the surface may originate as mantle material or igneous products (intrusive or extrusive). Potential transport mechanisms include excavation of the mantle or lower crustal material by impacts that form basins and complex craters, differentiation of impact melt sheets, or magmatic emplacement of lavas, cumulates, or xenoliths. A sample of the lunar mantle, which has not been conclusively identified in the lunar sample collection, would yield fundamental new insights into the composition, structure, and evolution of the lunar interior. Olivine identified in remote spectral data is generally accepted to originate from the primary mantle, because abundant olivine is expected to exist in the mantle and lower crust, yet have sparse occurrences in the upper crust. In this study, we identified 111 M^3 single-pixel spectra with characteristic absorption features consistent with olivine at Crisium, Nectaris, and Humorum basins and near the crater Roche. In an effort to determine the origins and transport mechanisms that led to these individual exposures, we estimated mineral abundances using radiative transfer modeling and examined crustal thickness estimates, topography and slope maps, and images from the Lunar Reconnaissance Orbiter Camera (LROC). At Crisium basin, where crustal thickness is near 0 km (Wieczorek et al., 2013), mantle olivine may have been exposed by basin-forming impact and deposited on the rim. Picard crater, which is superposed on the floor

of Crisium, also exhibits potential mantle olivine in its ejecta. Within Nectaris basin, olivine exposures are confined to the rims of small craters on the mare, which are inferred to excavate a layer of olivine-rich mare basalt. Olivine occurrences on the rim of Humorum basin, including those located on a graben, are likely to be cumulates of a shallow intrusion that were transported magmatically to the surface. Near Roche crater, olivine may have originated in shallow intrusions (dikes) that reached the subsurface and were exposed by impacts. In addition to verifying both known and previously unidentified olivine exposures, our combined geophysical, spectral, and radiative transfer modeling investigation has allowed identification of both igneous and mantle-derived olivine.

2.1 Introduction

Olivine is an abundant constituent of the lunar mantle that constrains models of lunar origin and evolution (e.g., Snyder et al., 1992; Elkins-Tanton et al., 2011). Remote detection of surface olivine is a challenge, in part because of its rarity, as evidenced by the almost complete absence of large-scale samples (e.g., dunite clasts) in the lunar sample collection, and also because, in the visible to near-infrared spectra, the signature of olivine can easily be obscured by relatively small amounts of the more common mineral, pyroxene (e.g., Pieters, 1983; Crown and Pieters, 1987). Nonetheless, olivine has been detected on the surface using high-spatial resolution hyperspectral data. Yamamoto et al. (2010) used data from the Kaguya Spectral Profiler (SP) to identify olivine exposures located on the rims and central peaks of several large impact basins, where the crust was previously thinned as a result of basin excavation. They conclude that the spectra with the indicative olivine signature are consistent with the presence of dunite, with a likely origin from the upper mantle.

Several other studies have estimated olivine composition and investigated the geologic context for the purpose of determining origin and emplacement mechanisms of olivine. Arnold et al. (2016) confirm the presence of olivine at many of the Yamamoto et al. (2010) detection sites with Chandrayaan-1's Moon Mineralogy Mapper (M^3) spectra and estimated olivine abundance using mid-infrared data from the Lunar Reconnaissance Orbiter (LRO) Diviner Lunar Radiometer Experiment. They found that olivine-bearing locations have a wide range of olivine/plagioclase ratios, with most being troctolitic in

composition. Powell et al. (2012) also examined Crisium basin using M^3 spectra. They detected olivine within mare flows, intrusive landforms, and in areas of thick crust, and conclude that both magmatic and mantle olivine is present. Isaacson et al. (2011) used the Modified Gaussian Model (MGM) to examine the spectral diversity in olivine-rich M^3 spectra from Mare Moscoviense, the Copernicus central peak, Aristarchus, and Marius crater. Their MGM-derived absorption-band positions enabled the comparison of the relative Mg (i.e. forsterite) contents of the olivine. Olivine spectra at Moscoviense are Mg-rich but exhibit diversity that suggests varied Fe/Mg contents. The most Mg-rich spectra are similar in composition to olivine found in Mg-suite rocks that are ~Fo_{90}. Copernicus has spectrally and compositionally homogeneous olivine that is also relatively Mg-rich, which indicates a single magmatic or mantle source, rather than a source that evolved over time. They conclude that the relatively Mg-rich composition suggests a plutonic origin, because olivine in mare basalt is usually more Fe-rich (e.g., Papike et al., 1976). However, the diversity in composition at Moscoviense requires a different process than that responsible for olivine at Copernicus. Olivine spectra from Marius and Aristarchus had contamination from pyroxene and an unknown phase, respectively, preventing the estimation of Mg#. The spectral differences indicate different lithologies than olivine exposures at Copernicus and Moscoviense. Mustard et al. (2011) also identified olivine-rich M^3 spectra in impact melt and ejecta deposits on the southeastern wall and rim of Aristarchus and conclude that they originate from a shallow pluton, an olivine-rich region of Imbrium ejecta, or olivine-rich Procellarum basalts that were either excavated or melted by the impact and subsequently crystallized.

Studies have also identified olivine with evidence for types of origin other than mantle and plutonic. Staid et al. (2011) used M^3 spectra to confirm the presence of Fe-rich olivine in fresh material in high-Ti maria on the western nearside. The stratigraphic evolution and Fe-rich compositions of these basalts indicate that the magma sources were evolved residual melts, rather than assimilation of primitive (Mg-rich) mantle olivine. Spectrally similar mare basalts are scarce outside the Procellarum-Imbrium region but do occur as small flows or ponds in areas of late-stage regional volcanism, supporting their interpretation that the olivine in high-Ti maria originated from evolved residual melts.

Using the LRO Narrow Angle Camera (NAC) and Kaguya Terrain Camera (TC), Dhingra et al. (2015) investigated the geologic context and albedo differences of olivine occurrences identified at Copernicus Crater with M^3 and found evidence for multiple styles of origin. The northern wall has smooth deposits that contain olivine. The spectra are lower in albedo than other olivine exposures, suggesting that abundant or coarse-grained olivine resides in a dark matrix. They propose that these exposures originated from olivine-bearing clasts in the target material that were entrained into a mafic impact melt, which cooled rapidly. Mare basalt was part of the pre-impact lithology, which might have been a source for the mafic material that is necessary in order to explain the opaque, mafic glass. They also found olivine in the central peak and crater floor, which they evoke a different origin in order to explain. Olivine on the central peak is mixed with plagioclase and likely to have been uplifted crustal material from a depth of ~15 km. Olivine exposed at high-standing mounds on the crater floor represent large broken, unmelted fragments that were embedded in the impact melt and might be from the same source material as the central peak. As these studies demonstrate, it is important to establish the geologic context and the composition in order to interpret the origins and transport mechanisms, as well as any genetic relationships, of olivine exposures within a region.

In this study, we use M^3 data to search for olivine at Crisium, Nectaris, and Humorum basins, three areas where Yamamoto et al. (2010) detected olivine. We also search for olivine near Roche crater, where Andrews-Hanna et al. (2013) identified a possible massive dike, similar to one found at Crisium that is associated with olivine (Yamamoto et al., 2010; Powell et al., 2012). Unlike Spectral Profiler, which Yamamoto et al. (2010) used for detecting olivine, M^3 is an imaging spectrometer, so each spectrum and its geologic context is evident in the same data. An olivine index algorithm based on the weighted depth and breadth of the 1-μm olivine absorption helped us identify locations with relatively high abundances of olivine. Topography and slope maps, created using Lunar Orbiter Laser Altimeter (LOLA) data (Smith et al., 2010a), crustal thickness models (Wieczorek et al., 2013) from the Gravity Recovery and Interior Laboratory (GRAIL) (Zuber et al., 2013) and LOLA (Smith et al., 2016) data sets, and images from the LRO Wide Angle Camera (WAC) and Narrow Angle Camera (NAC) (Robinson et

al., 2010) allow us to put olivine detections into precise geologic and geophysical contexts through identification of features not spatially resolvable by M^3. Furthermore, this is the first study to estimate the olivine abundance of each location using radiative transfer modeling with M^3 data. Here, we use radiative transfer modeling to estimate both Mg# (MgO/(MgO+FeO)) and mineral abundances (i.e., olivine, orthopyroxene, clinopyroxene, and plagioclase) for each M^3 olivine-bearing spectrum. In addition to identifying the locations of olivine exposures, we seek to establish both the origin of exposed olivine and the means by which it was transported to the surface or near-surface.

2.2 Hypotheses for the Origin of Observed Olivine and Mechanisms of Transport to Surface

We identify five different explanations for exposures of lunar olivine, based on where they originated and how they were transported to the surface. We consider that these olivine exposures either (1) originated from the primary mantle or mafic lower crust, (2) are igneous in origin, or (3) crystallized from differentiated impact melt; and that these olivine-bearing materials were transported to the surface either (A) by basin or complex crater impact excavation or (B) magmatically. We focus on endogenic possibilities. Meteoritic (i.e., exogenic) olivine deposited by an impactor (Yue et al., 2013) is difficult to test, because olivine and spinel, which are excavated from depth by large impacts, are also abundant in many asteroids and meteorites (Burbine and Binzel, 2002; Sunshine et al., 2008; Yamamoto et al., 2010; Gross and Treiman, 2011; Pieters et al., 2011). The matrix shown in Figure 2.1 summarizes the endogenic possibilities in terms of origin (columns) and transport (rows). In this classification, a piece of mantle rock that is transported to the surface is considered to be primary in origin, i.e., a relict of primary lunar differentiation (e.g., Dymek et al., 1975). Olivine that crystallized out of a magmatic system within the crust (as an intrusion) or on the surface is considered to be igneous in origin. Impact melt is somewhat ambiguous in terms of origin, as an impact melt sea incorporates mafic material from the upper mantle along with crustal material (e.g. Vaughan et al., 2013), making it partly mantle in origin. Furthermore, the material melts, differentiates, and crystallizes, which is also technically an igneous origin. Thus, we consider olivine that crystallized from an impact melt sea to have an impact melt origin in order to distinguish this near-surface process from a more traditional igneous

origin via melting primarily induced by the Moon's internal heat under relatively high pressure in the mantle. Olivine excavated from depth by basin and complex crater impacts (e.g., Miljković et al., 2015; Lemelin et al., 2015) is considered to have an impact transport mechanism. This transport mechanism can be applied to all styles of origin: the impact could have excavated materials derived from the mantle or lower crust that contain olivine, originally deep-seated crustal plutons that crystallized olivine, or olivine cumulates from a differentiated impact melt sea (Figure 2.2). We make the important distinction that "impact" transport is implicitly basins and complex craters, as impact craters typically excavate materials from about one-tenth of their diameter (Melosh et al., 1989; Potter et al., 2015); km-scale or smaller craters may expose the lower parts of extrusive flows containing crystallized olivine, but such olivine would still fall under the category of magmatic transport in our classification. Olivine that is transported to the (near-) surface via magmatism is considered to fall under the category of magmatic transport (Figure 2.3). This class of transport can include mantle xenoliths entrained in the volcanic eruption and olivine crystallized from the magma and transported by volcanism. This includes olivine in plutons and magma chamber cumulates.

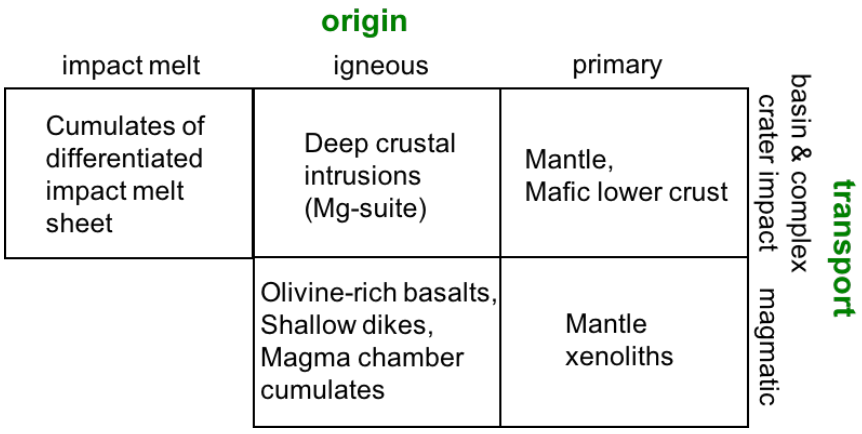

Figure 2.1 A "matrix" showing endogenic categories of origin and transport for olivine on the lunar surface. Top left: olivine that crystallized from a differentiated impact melt sheet as a result of basin impact. Top center: igneous olivine that originated from deep crustal intrusions, such as Mg-suite plutons or magma chamber cumulates, and were subsequently exposed by basin impact. Top right: primary olivine that crystallized from the lunar magma ocean and was exposed by basin impact. Bottom left: igneous olivine that was transported magmatically to the surface, including either the eruption of olivine-

rich basalts or eruptions that carried magma chamber cumulates as xenoliths. Bottom right: primary olivine from the mantle that was brought to the surface by a magma conduit that ripped out primary olivines as mantle xenoliths.

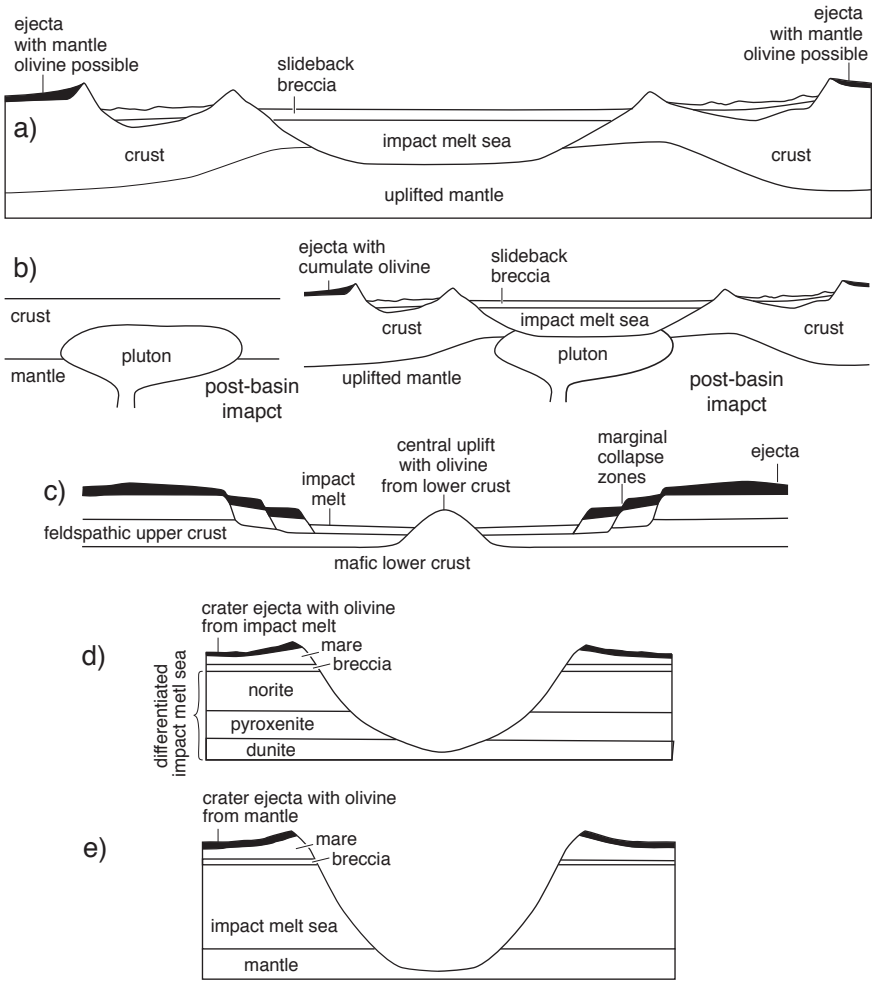

Figure 2.2 Basin and complex crater transport of olivine. a) basin impact excavates mantle, resulting in mantle uplift, melting of both crust and mantle to produce an impact melt sea, and ejecta on the basin rim with possible mantle olivine; b) a pluton (such as Mg-suite) intrudes into the deep crust and then is excavated by basin-forming impact, with olivine from the pluton exposed in ejecta on the basin rim; c) formation of a complex crater results in central uplift, with olivine from more mafic material of the primary lower crust exposed on the central peak (after Melosh, 1989 and French, 1998). d) impact melt sea differentiates (via equilibrium crystallization of a homogeneous melt sea; e.g. Vaughan et al., 2013), producing norite, pyroxenite, and dunite layers, and a

subsequent impact (simple crater that is tens of km in diameter) penetrates through the mare to the bottom of the impact melt, exposing olivine from the dunite layer in the crater walls and ejecta; e) a larger simple crater inside the basin penetrates through the mare and impact melt to the uplifted mantle, exposing olivine from the mantle in the crater walls and ejecta.

2.2.1 Transport by Basin-forming Impacts

One possible origin for distributions of olivine on the surface is that basin-forming impacts may have excavated mantle olivine that formed as primary magma ocean cumulates (Figure 2.2a). The Moon's primary mantle and crust crystallized from a magma ocean of ultramafic to basaltic major-element composition. Olivine would have been the first major phase to crystallize, beginning with a high Mg# (forsteritic) that decreased with increasing crystallization of the mantle (e.g., Shearer and Papike, 1999). Estimates of Mg# are >92 for the first magma ocean cumulates and ~40 for the last cumulates (Shearer and Papike, 1999; Elkins-Tanton et al., 2011). On this basis, the compositions of exposed olivine would provide important clues to their origin. For example, as the magma ocean crystallized, early, high Mg# mafic cumulates were covered by cumulates of increasingly lower Mg#. Ilmenite was the last and densest major phase to crystallize. It has been hypothesized that this correlation between density and percentage of magma ocean crystallization produced an unstable density gradient, which drove overturn of the cumulate pile via subsolidus convection (Ringwood and Kesson, 1976, Herbert, 1980; Ryder, 1991; Spera, 1992). Inferences about the deep mantle density structure from GRAIL and laser ranging data are consistent with such a magma ocean overturn (Matsuyama et al., 2016). In the post-overturn model, there would be locations where the least dense early-phase Mg-rich cumulates, which would have been initially at the bottom of the cumulate pile, could now be at a more accessible location for transport to the surface by impact (Hess and Parmentier 1995, Elkins-Tanton et al., 2011). Hence, where gravity measurements indicate that the crust is thin and the mantle is close to the surface, mantle olivine may be present at impact basins (Muller and Sjogren, 1968; Wise and Yates, 1970; Wieczorek and Phillips, 1998; Yamamoto et al., 2010; Elkins-Tanton et al., 2011; Melosh et al., 2013; Miljković et al., 2015). In this way, large

impact basins that penetrated the crust over one of these overturned mantle cumulate locations could expose Mg-rich olivine in the rim or ejecta.

Another possible origin of exposed olivine is that basin-forming impacts resulted in impact melt seas that subsequently differentiated, producing olivine-rich layers (Figure 2.2a and 2.2d). Impacts that form basins >300 km in diameter produce >10^5 km^3 of impact melt (Cintala and Grieve, 1998; Abramov et al., 2012.) Some of the generated impact melt is excavated forming the transient cavity, and more melt is subsequently ejected during modification (Hawke and Head, 1977; Cintala and Grieve, 1998; Osinski et al., 2011). Hydrocode modeling showed that the Orientale impact produced ~10^6 km^3 of impact melt (Potter et al., 2013a). Vaughan et al. (2013) suggests that this melt formed an impact melt sea that is ~15 km thick and ~350 km in diameter, and GRAIL gravity data indicates a likely melt sheet thickness of ~10 km (Zuber et al., 2016). Large-scale igneous differentiation of a homogeneous melt sea with equilibrium crystallization would have produced layers of norite, pyroxenite, and dunite (Vaughan et al., 2013, e.g. Figure 2.2d). Similarly, the South Pole-Aitken (SPA) impact is predicted to have formed a 50-km thick melt sea that differentiated, forming layers of dunite, pyroxenite, gabbro, and norite (Potter et al., 2012; Hurwitz and Kring, 2014). Stratigraphies of impact melt seas vary depending on equilibrium versus fractional crystallization, slow versus rapid cooling, pre- versus post-overturn, homogeneous versus density-stratified melt, dominant crystal size, and depth of melt sea (e.g. Vaughan et al., 2013; Hurwitz and Kring, 2014; Cassanelli and Head, 2016). Large craters inside basins could excavate through the mare and impact melt, to expose dunite cumulates from the base of the impact melt sea (Figure 2.2b). By the same mechanism, larger craters in basins could excavate the uplifted mantle that underlies the impact melt (Figure 2.2e).

An alternative possibility is that large basin-forming impacts could have excavated igneous olivine located in older plutons (Figure 2.2b). Plutons with high olivine contents might be representative of Mg-suite rocks that are thought to have formed when mantle overturn brought deep, Mg-rich cumulates to the base of the crust where they hybridized with crustal anorthosite and in some places a residual KREEP (potassium, rare earth element, and phosphorus) layer (Shearer and Papike, 1999; Elardo et al., 2011; Shearer et al., 2015a). Decompression melting and radiogenic heating

facilitated incorporation of the anorthositic crust into the ultramafic melt and intrusion into the shallow crust (Shearer and Papike, 1999; Elardo et al., 2011; Shearer et al., 2015a). Thus, Mg-suite plutons exposed by impact basins would contain secondary, igneous olivine.

Likewise, basin impacts could have penetrated into basaltic magma chambers residing in the deep crust that might contain high concentrations of olivine cumulates generated during crystallization (Figure 2.2b). The creation of such intrusive bodies may have been facilitated by lithospheric stresses and deformation related to the largest impact events, such as the event that created the South Pole-Aitken (SPA) Basin. Scenarios of this sort include fracturing focused antipodally-offset to the SPA impact (Schultz and Crawford, 2011) or the more widespread effects of pressure pulses coursing through the entire Moon, creating lithospheric stress states that facilitate magma ascent and intrusion (Kring et al., 2015; McGovern et al., 2015). The composition of these olivine cumulates vary depending on the composition of the starting magma. Although exposure of high-Mg olivine magma chamber cumulates may be indistinguishable from Mg-suite olivine in M^3 data, exposure of high concentrations of mid- to low-Mg olivine could be more telling of a secondary, igneous origin.

Excavation of basins and complex craters could also expose the mafic lower crust (Figure 2.2c). Assuming that a significant percentage of impact melts is derived from the deepest region of the target material, Ryder and Wood (1997) hypothesized that the lunar crust becomes more mafic with depth based on the mafic (e.g. noritic) composition of impact melts associated with Imbrium Basin (Apollo 15) and Serenitatis Basin (Apollo 17). Remote sensing of central peaks (e.g., Pieters, 1982) has been used to examine the composition of the crust with depth, as central peaks sample a range of depths. Several studies have found evidence that the crust becomes more mafic with depth (e.g., Pieters, 1982; Pieters, 1986; Tompkins and Pieters, 1999; Ohtake et al., 2009, Donaldson Hanna et al., 2014), whereas other studies have not (e.g., Cahill et al., 2009; Song et al., 2013; Lemelin et al., 2015). Central peaks analyzed by Lemelin et al. (2015) revealed no statistically significant increase in mafic mineral abundances with proximity to the crust/mantle boundary or with depth from the current lunar surface. However, the 34 central peaks studied have olivine contents ranging from 1 wt.% to 11 wt.%. Although

the central peaks could be sampling mafic intrusions into the lower crust or mafic material incorporated into impact melts, we also consider the possibility that complex craters excavated mafic material from the primary crust.

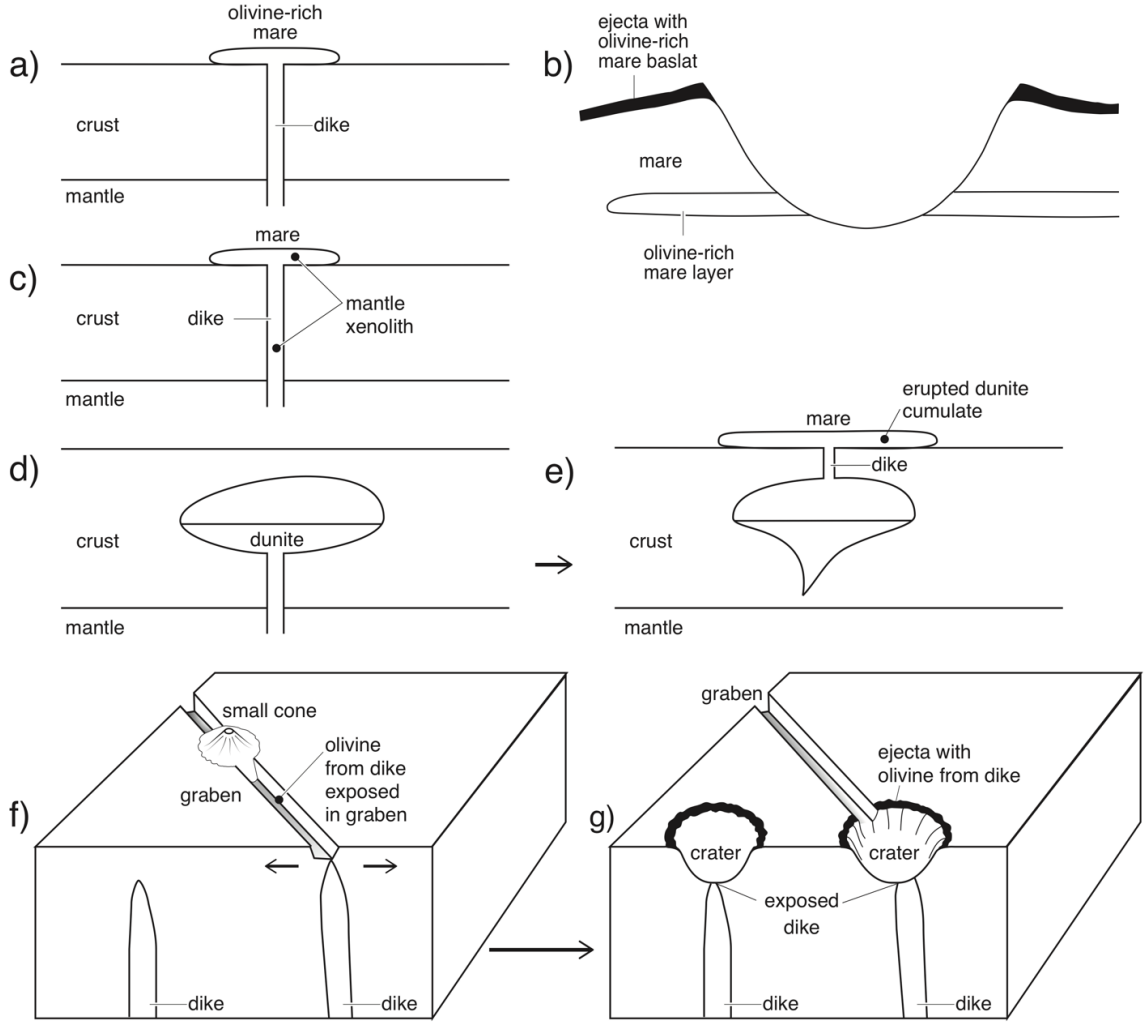

Figure 2.3 Magmatic transport of olivine. a) olivine-rich mare basalt is erupted onto the surface; b) buried olivine-rich basalt layer is excavated by impact with olivine exposed in crater walls and ejecta; c) mantle xenoliths are transported to the surface by a dike and erupted in mare basalts; d) crustal magma chamber differentiates and crystallizes dunite, and then e) dunite cumulates are erupted with mare basalt; f) dikes stall, cool, and solidify, with shallower dikes producing a near-surface stress field that can yield small cones and graben with a potential for exposed olivine from dike (after Head and Wilson, 2017), and g) craters excavate dikes and expose olivine in crater walls and ejecta.

2.2.2 Magmatic Transport

Another possibility is that the observed olivine could have been magmatically transported to the surface. For this transport scenario, the most common origin is olivine-rich basalts erupted onto the surface as flows (Figure 2.3a). Late-stage, high-Ti mare basalts on the western nearside have abundant olivine (Staid and Pieters, 2001; Staid et al., 2011). Spectrally similar mare basalts are scarce outside the Procellarum-Imbrium region (Staid et al., 2011), indicating that other extensive olivine-rich mare flows are uncommon. However, it is possible that there are smaller flows or buried mare basalt layers that are olivine-rich (Figure 2.3b). For example, Kaur et al. (2015) identified olivine-bearing spectra in the dark-haloed crater Beaumont L, which they conclude is an excavated layer of olivine-rich basalt. Olivine-rich basalts have also been identified in the lunar sample collection. Apollo 12 olivine basalts have an average olivine content of ~20 vol. %, while Apollo 15 olivine basalts contain ~7 vol.% olivine (Papike et al., 1976).

An alternative, although rare, possibility is that a dike carried mantle xenoliths to the surface (Figure 2.3c). Analysis of stress states from lithospheric loading by the maria suggests that the areas around large impact basins are particularly favorable for magma ascent via dikes (Solomon and Head, 1979; Solomon and Head, 1980; McGovern et al., 2014). Furthermore, Andrews-Hanna et al. (2013) identified positive-density linear gravity anomalies that they interpret to be ancient (pre-Nectarian) dikes. One of the largest proposed dikes is located at Crisium in the vicinity of previous olivine detections. Magmatically transported olivine could represent samples of the primitive lunar mantle, if a volcanic conduit carried primary mantle olivine xenoliths towards the surface. The Mg# of magmatically transported mantle xenoliths could be informative of the spatial scale (i.e., global, regional, or local) of mantle overturn. It is unlikely that mantle xenoliths could be identified using remote sensing, as mantle xenoliths would probably be too small to be detected with the spatial resolution of hyperspectral instruments.

Similarly, exposed olivine could be representative of magma chamber cumulates transported to the surface by the eruption of mare basalts (Figure 2.3d and 2.3e). While the presence of intra-crustal magma chambers has been established via gravity-topography analysis in regions such as the Marius Hills volcanic complex (Kiefer, 2013), prevailing scenarios for mare basalt eruption invoke rapid magma ascent through dike

systems that directly traverse the crust-mantle boundary driven by overpressure from positive buoyancy in the mantle (Head and Wilson, 2017; Wilson and Head, 2017), leaving scant opportunity for long-term stalling and ponding of magma in shallow reservoirs (to allow cumulate formation). Further, the very high correlation of lunar topography and gravity at moderate to short wavelengths (Zuber et al., 2013) suggests a sparse distribution of intra-crustal magma chambers, although the attenuation of gravity signals with depth at those wavelengths might render difficult detection of chambers deep in the crust or at the buoyancy trap at the base of the crust. Nonetheless, the greater thickness of farside crust makes stalling of ascending magmas (and therefore cumulate generation in chambers) more likely and in early lunar history conditions may have been more favorable for creation of relatively long-lived magma bodies at the crust-mantle boundary (Head and Wilson, 2017). The composition of magma chamber olivine cumulates will vary depending on the composition of the original melt. Therefore, the origin of observed olivine (mantle or igneous) may remain ambiguous in the absence of sample analyses.

In addition, dikes could have reached the shallow subsurface and been exposed by impacts (Figure 2.3f and 2.3g). Such intrusions are likely more common on the farside, as it is predicted that ascending magma stalled and cooled in dikes before reaching the surface as a result of the thicker crust (Head and Wilson, 2017; Wilson and Head, 2017). Although some stalled dikes are deep and have no surface manifestation, emplacement of a dike at shallow depth could create a near-surface stress field that yields graben and small cones (Head and Wilson, 2017; Figure 2.3f). For example, Rima Sirsalis, a linear graben near Mare Humorum, is interpreted to be associated with an underlying dike that has a magnetic signature (Srnka et al., 1979; Head and Wilson, 1993; Hood et al., 2001). In contrast, the location of linear rilles relative to impact basins suggest they are graben produced by large-scale tectonic stresses, such as loading due to the filling of basins with mare basalts (Solomon and Head, 1979; Solomon and Head, 1980). Thus, olivine exposures could originate from subsurface dikes, which may or may not be associated with impact basins and do not always have surface manifestations.

2.3 Methods

2.3.1 M^3 Data

The M^3 imaging spectrometer has a spatial resolution of 140 m and its imaging capability allowed us to associate olivine-bearing spectra with geologic features (Figure 2.4). The M^3 spectra have high spectral resolution (83 bands from 540 to 2980 nm) that can be used to distinguish mineral signatures. We used level 2 M^3 reflectance data, which is thermally, geometrically, and photometrically corrected (Green et al., 2011; Lundeen et al., 2012; Besse et al., 2013). Some of the M^3 data have a low signal to noise ratio due to instrument temperatures that were outside the nominal thermal range (Green et al., 2011; Lundeen et al., 2012). Hence, we were unable to confirm some previous olivine detections due to noise.

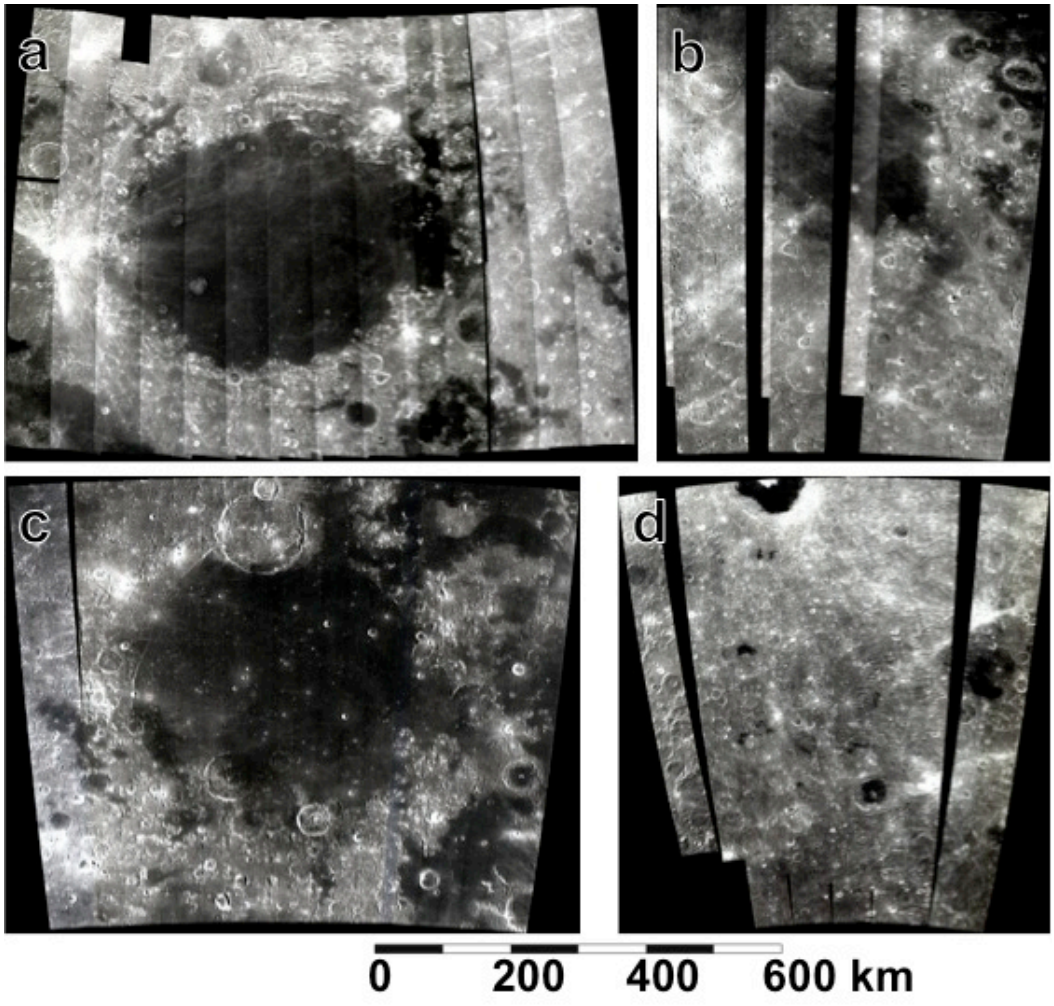

Figure 2.4 M^3 mosaics of (a) Crisium, (b) Nectaris, (c) Humorum basins and (d) Roche and Tsiolkovsky craters, from which olivine-bearing spectra were identified. Mosaics are

displayed in true-color with band 5 (700 nm) in red, band 3 (620 nm) in green, and band 1 (540 nm) in blue.

2.3.2 Olivine Algorithms for Spectral Identification

To aid in the search for olivine-bearing locations we used two olivine indices: one developed for M^3 (referred to here as "M^3 olivine index") and another based on an algorithm developed for the Compact Reconnaissance Imaging Spectrometer for Mars (CRISM) onboard the Mars Reconnaissance Orbiter (Pelkey et al., 2007) (referred to here as "CRISM olivine index"). The CRISM olivine index algorithm is modified for specific M^3 band centers. Visual inspection of the spectra identified with the M^3 olivine index revealed that the index was highlighting the locations of pyroxene-dominated spectra as well as olivine and olivine-pyroxene mixtures. Since we are looking for spectra with strong olivine signatures, we relied more on the CRISM olivine index, which was better at discerning between olivine and pyroxene. The spectrum of pure olivine has three overlapping absorption features at approximately 0.85, 1.05, and 1.25 μm, (e.g., Burns, 1970; Sunshine and Pieters 1998; Trang et al., 2013), which yield a composite absorption band centered near 1 μm (Figure 2.5). The CRISM olivine index assigns a relative value to an M^3 pixel based on the weighted depth and breadth of the 1-μm absorption as given by the equation:

$$Ol' = \left(\frac{R_{1699}}{0.1 * R_{1050} + 0.1 * R_{1210} + 0.4 * R_{1329} + 0.4 * R_{1469}}\right) - 1$$

where R is the reflectance measured at each M^3 wavelength given as a subscript in nanometers.

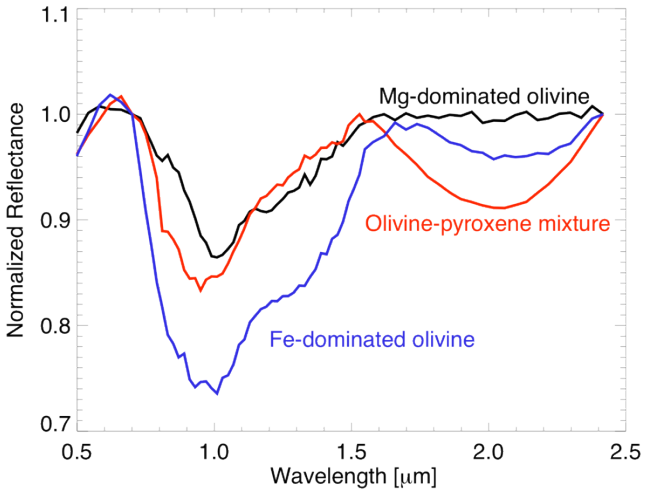

Figure 2.5 M^3 spectra (reflectance as a function of wavelength) showing Fe-dominated olivine (Crisium), Mg-dominated olivine (Humorum), and an olivine-pyroxene mixture (Crisium). A two-step continuum removal consisted of a straight-line tangential to the spectrum at 750 and 2500 nm and a subsequent two-degree polynomial fit.

The algorithm is formulated to scale with olivine abundance, such that greater values indicate higher olivine concentrations. However, a number of factors beyond olivine abundance (e.g. additional minerals, grain size, space weathering) influence the 1-μm absorption feature, and in turn influence the olivine index value. Thus, the olivine index is not a parameter from which an absolute quantitative abundance can be derived. Instead, we used it only as a reconnaissance tool to help identify locations where relatively high abundances of olivine are exposed. Applying the algorithm to the M^3 images reveals spatial variations of olivine abundance that can be matched to morphologic features (Figure 2.6).

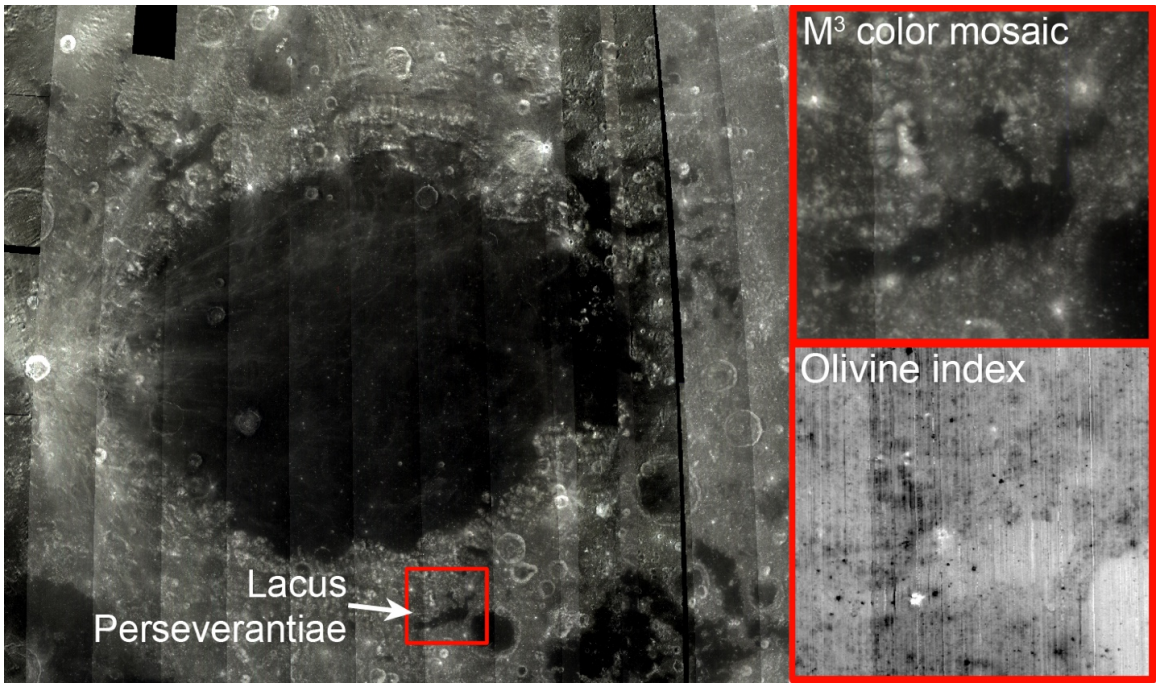

Figure 2.6 True-color M^3 mosaic of Crisium basin (left) showing an area of interest, a small patch of mare called Lacus Perseverantiae (top right). True color is displayed with band 5 (700 nm) in red, band 3 (620 nm) in green, and band 1 (540 nm) in blue. The CRISM olivine index reveals spatial variations in olivine abundance (Lacus Perseverantiae, bottom right). Bright pixels, in this case a small crater on the mare, have higher olivine abundance.

2.3.3 Quantifying Olivine in Identified Spectra

To ensure that the algorithm identified olivine correctly, the full M^3 spectra of pixels with high olivine index values were visually examined. The absorption features of Fe-bearing plagioclase and pyroxene superimposed on olivine spectra can confound an unambiguous detection. Olivine has one broad composite absorption band centered near 1 μm (e.g., Sunshine and Pieters, 1998), Fe-bearing plagioclase exhibits a weak absorption band centered near 1.25 μm (e.g. Adams and Goulland, 1978; Serventi et al., 2013), and pyroxene has an absorption band centered near 1 μm, which is more narrow and symmetric than the 1-μm band of olivine, and an additional absorption band centered near 2 μm (e.g. Singer, 1981). Thus, the presence of plagioclase and/or pyroxene with olivine makes it difficult to quantitatively estimate the abundance of olivine by visual inspection. Our investigation is aimed at identifying olivine-bearing lithologies. Hence,

we included spectra of olivine-pyroxene mixtures with a weak 2-μm band (Singer, 1981), in addition to purer olivine-plagioclase mixtures lacking a 2-μm band. To estimate the abundances of olivine, orthopyroxene, clinopyroxene, and plagioclase in our visually confirmed olivine-bearing spectra, we used radiative transfer modeling. Radiative transfer equations describe the scattering of light during interaction with grains, and can be used to model the reflectance spectra of mineral mixtures varying in grain size, chemistry, and space weathering effects (e.g. Hapke, 1981; 1993; 2001). In addition to estimating olivine abundances, radiative transfer modeling also allowed us to distinguish between Mg-dominated and Fe-dominated olivine lithologies based on M^3 spectra. Fe-dominated olivine spectra have a deeper and more asymmetric 1-μm absorption band than Mg-dominated spectra (Figure 2.5; Hazen et al., 1977; Burns, 1993; Trang et al., 2013; Isaacson et al., 2014). Based on work by Sunshine and Pieters (1998) that measured the reflectance spectra of olivines with a range of compositions between Fo_1 and Fo_{97}, we estimate that the Mg-dominated olivine spectra are approximately Fo_{90} and the Fe-dominated olivine spectra are approximately Fo_{65}. The same type of qualitative comparison was used by Staid et al. (2011) to estimate the composition of M^3 olivine spectra. Isaacson and Pieters (2010) successfully predicted the forsterite compositions of chromite-bearing lunar olivines using a modified approach to MGM deconvolutions of laboratory spectra. However, Isaacson et al. (2011) demonstrated that by standardizing the continuum slope used to deconvolve remotely sensed olivine spectra with MGM, only relative forsterite compositions can be estimated.

To quantify mineral abundances for M^3 pixels identified as having olivine by the CRISM olivine index, we compared radiative transfer modeled spectra with these M^3 spectra. Before comparing modeled and remote spectra, we removed a continuum that consisted of a straight-line tangential to the spectrum at 750 and 2500 nm. If the resulting continuum-removed spectra had reflectance greater than 1.0, we removed a subsequent two-degree polynomial fit. The continuum is removed in order to remove the spectral slope, which is the change in reflectance with respect to wavelength in the absence of spectral absorptions. Continuum points were chosen at 750 and 2500 nm, because they are located at opposite ends of the spectrum away from spectral absorptions. To derive compositions from our M^3 olivine exposures, we found the closest spectral match by

using an evenly weighted average of the correlation and the median absolute difference in reflectance between the modeled spectra and the given M^3 spectrum, as given by the equation:

$$Weighted\ criteria = \big(0.5 * (1 - correlation)\big) + (0.5 * median\ absolute\ difference)$$

2.3.4 FeO Content as a Constraint

The weak absorption band of plagioclase is masked by the presence of mafic minerals. Therefore, we used FeO as a constraint to allow us to determine plagioclase abundance (e.g. Lemelin et al., 2015). We calculated the FeO abundance of each library spectrum based on the stoichiometric abundance of each mineral (e.g., olivine, orthopyroxene, clinopyroxene, and plagioclase). We computed the FeO abundances corresponding to each M^3 pixel with an FeO algorithm from Lemelin et al. (2015) that is a refinement of the work by Otake et al. (2012) and uses absolute reflectance from Multiband Imager (MI) data:

$$\theta_{Fe1} = \tan^{-1}(((R_{950}/R_{750}) - y_{0Fe})/(R_{750} - x_{0Fe}))$$

$$\theta_{Fe2} = 0.0656e^{(3.6681*\theta Fe1)}$$

$$FeO\ (wt.\%) = (1.0708 * \theta_{Fe2}) - 0.3986$$

where $x_{0Fe} = 0.04$, $y_{0Fe} = 1.39$, and R is absolute reflectance from MI at the wavelength given as a subscript in nanometers. The FeO data obtained from the algorithm were downsampled from 62 m/pixel to 140 m/pixel to match the spatial resolution of M^3. We searched for the best spectral match by comparing each M^3 spectrum with a subset of library spectra that are within ± 2 wt.% FeO of the given pixel determined using the FeO algorithm.

2.3.5 Spectral Library

The modeled spectra are part of a spectral library that is identical to those used by Lemelin et al. (2015), except calculated for M^3 specific wavelengths. Lemelin et al. (2015) compared modeled spectra to spectra from central peaks acquired by MI, which includes nine bands in the ultraviolet-visible and near infrared. The library uses optical constants from Lucey (1998) and has been refined by Lucey et al. (2014a) in order to better correspond to the quantified mineral abundances of the spectra acquired by the Lunar Soil Characterization Consortium (LSCC). To estimate uncertainty in our mineral

abundances, we added a level of noise typical of M^3 spectra to modeled spectra of various compositions, found the closest spectral matches between the noisy modeled spectra and the entire library of modeled spectra, and then calculated the differences between the mineral abundances of the best spectral matches and the known compositions of the noisy modeled spectra. The errors in mineral abundances are 4 wt.% for olivine, orthopyroxene, and clinopyroxene, and 8 wt.% for plagioclase.

We assumed a grain size of 17 μm, because the 10- to 20-μm size fraction of lunar soil is shown to dominate the optical properties of the bulk soil (Pieters et al., 1993; Lucey, 2006a). To investigate the effect of grain size on modeled mineral abundances, we also tested the model using a grain size of 100 μm. The error between the modeled mineral abundances for 17 μm and 100 μm is 7 wt.% for olivine, 5 wt.% for orthopyroxene, and 8 wt.% for clinopyroxene and plagioclase. Thus, changing the grain size did not lead to large changes in the estimated mineral abundances. The endmembers of the spectral libraries are all crystalline. If shocked plagioclase were present in the remote spectra, the plagioclase abundance would be underestimated when comparing remote spectra with the library because shocked plagioclase has a diminished 1.25-μm absorption compared to crystalline plagioclase (Johnson and Hörz, 2003). The spectral library does not include ilmenite, but abundances of less than 15 wt.% ilmenite do not affect the relative mineral abundance estimations (Lucey, 2004).

Mafic mineral abundances were calculated in 10 wt.% abundance intervals from 0 wt.% to 100 wt.%, and plagioclase abundances were calculated at 1 wt.% abundance intervals. The library of modeled spectra consists of spectral mixing of each of the four minerals at different abundances for a total of 6,601 compositions. Spectra were also computed for these mineral mixtures at seven different amounts of submicroscopic iron (SMFe), which includes the optical effects of two sizes of SMFe: nanophase iron and microphase iron (i.e. Britt-Pieters particles that are 1-μm in size.) Nanophase iron darkens and reddens spectra, whereas microphase iron neutrally darkens spectra and decreases the depth of absorption bands (Lucey and Riner, 2011). When including space weathering, this gives a total of 46,207 modeled spectra. In addition, modeled spectra were computed at two different values of Mg#, 65 and 90. In total, we had 92,414 modeled spectra to compare to our remote spectra.

2.3.6 Geophysical and Geological Contextual Data

In an effort to constrain structural and magmatic evolution, we examined the geophysical settings of the four study regions using products from measurements of gravity by the GRAIL mission (Zuber et al., 2013) and topography by LOLA. We make use of an updated version of the crustal thickness map presented by Wieczorek et al. (2013) that uses the GRAIL extended mission gravity model JGGRAIL_900C11A. The locations of our olivine detections were plotted on the crustal thickness models (Figure 2.7) and were also compared with LOLA topography and LOLA-derived surface slopes (Smith et al., 2010b; 2016). WAC and NAC images from LRO of the regions with olivine exposures allowed for further observation of geologic settings and morphology (Robinson et al., 2010). For geologic context, locations of the olivine detections are displayed on WAC base maps (e.g., Figure 2.8).

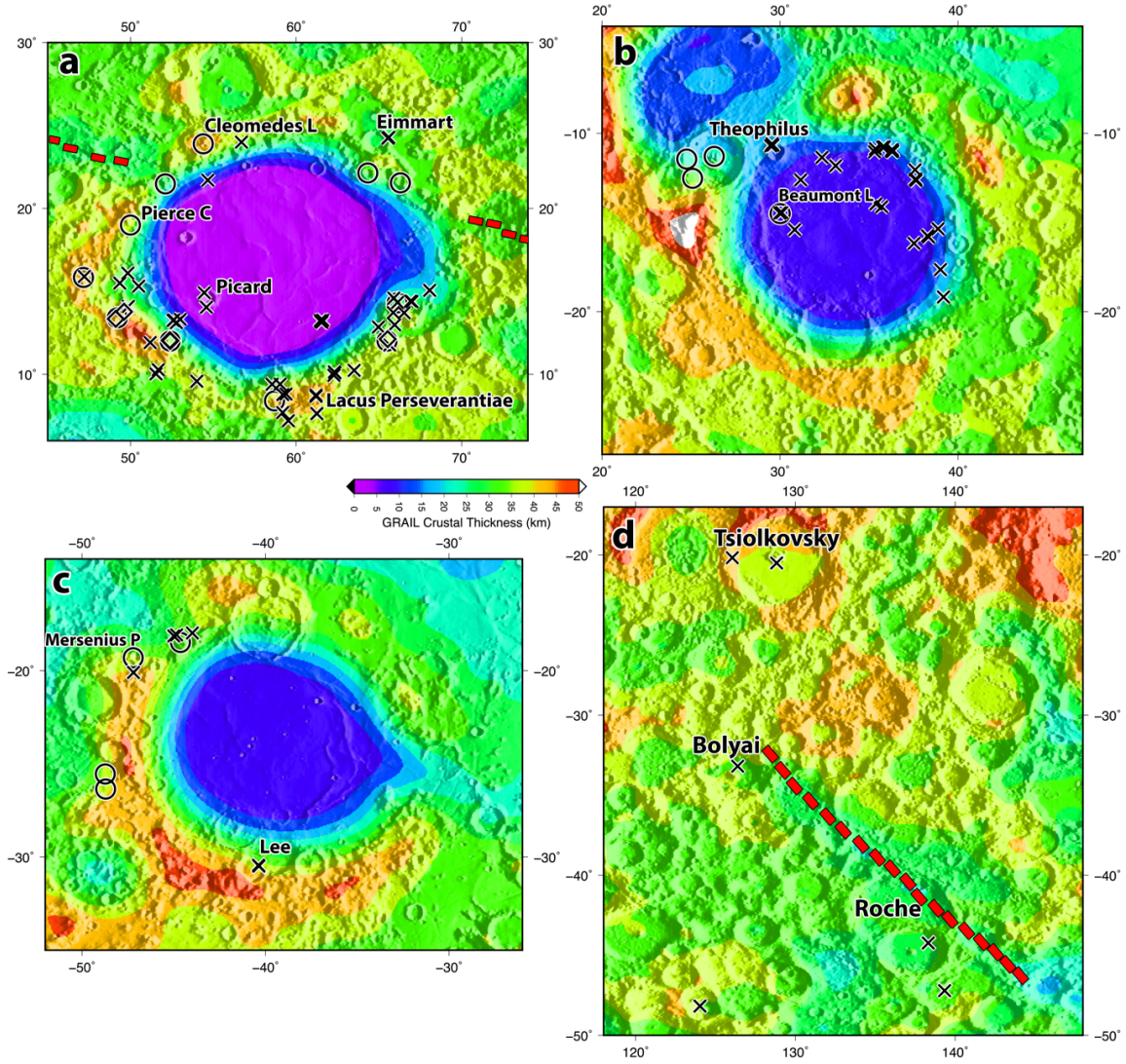

Figure 2.7 Locations of Mg# 65 olivine (×) and Mg# 90 olivine (◊) at (a) Crisium, (b) Nectaris, (c) Humorum basins, and (d) near Roche and Tsiolkovsky craters. Detections from Yamamoto et al. (2010) are shown as circles. Base maps are crustal thickness (color scale) maps created from GRAIL and LOLA (Wieczorek et al., 2013) with shading from LOLA topography (Smith et al., 2010b; 2016). The approximate locations of the linear gravity anomalies at Crisium (a) and Roche (d) are shown in red dashed lines (Andrews-Hanna et al. 2013).

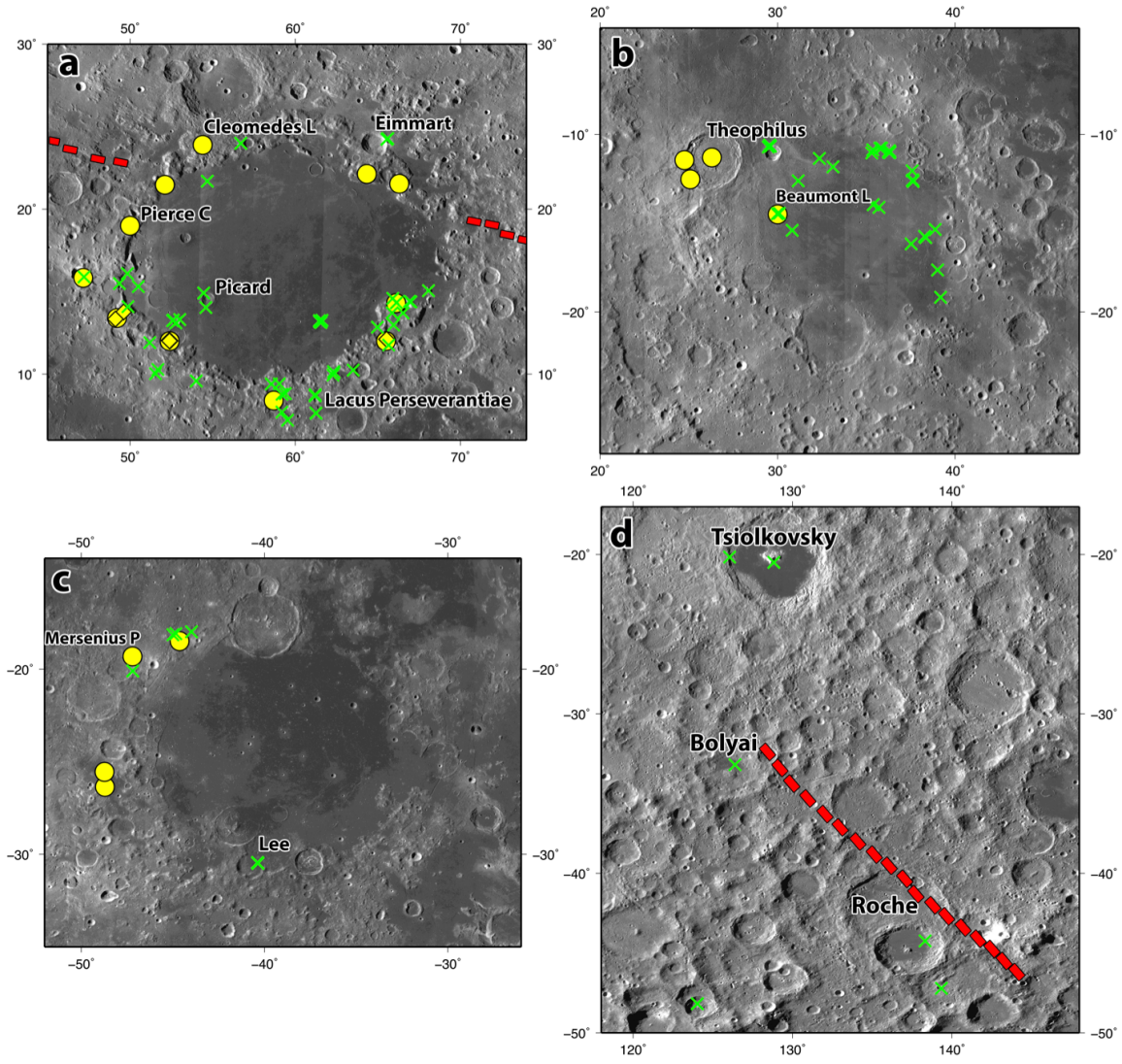

Figure 2.8 Locations of Mg# 65 olivine (×) and Mg# 90 olivine (◊) at (a) Crisium, (b) Nectaris, (c) Humorum basins, and (d) near Roche crater. Detections from Yamamoto et al. (2010) are shown as circles. The approximate locations of the linear gravity anomalies at Crisium (a) and Roche (d) are shown in red (Andrews-Hanna et al. 2013). Base maps are WAC mosaics.

2.4 Results

We produced M^3 mosaics of our four study areas, Crisium, Nectaris, and Humorum basins and Roche crater. The olivine index algorithm was applied to each M^3 mosaic from which we confirmed a total of 111 M^3 pixels (140 m per pixel) with olivine-bearing spectra throughout the four study areas. By comparing the M^3 olivine spectra

with the library of radiative transfer modeled spectra with an Mg# of 65 and 90 (Figure 2.9), we found that only six olivine-bearing spectra had best spectral matches with Mg# 90 spectra, all of which occur on the basin rim of Crisium. Olivine abundances vary from 3 wt.% to 36 wt.% throughout all of the study areas (see Appendix A for details of composition). Figure 2.10 shows ternary diagrams with estimated mineral abundances for each of the four study areas. For each 1 wt.% interval of plagioclase in the modeled spectra, the mafic minerals are calculated at 10 wt.% intervals (e.g. Figure 2.11), causing mineral abundances on the ternary diagrams to plot along lines that trend towards the plagioclase apex.

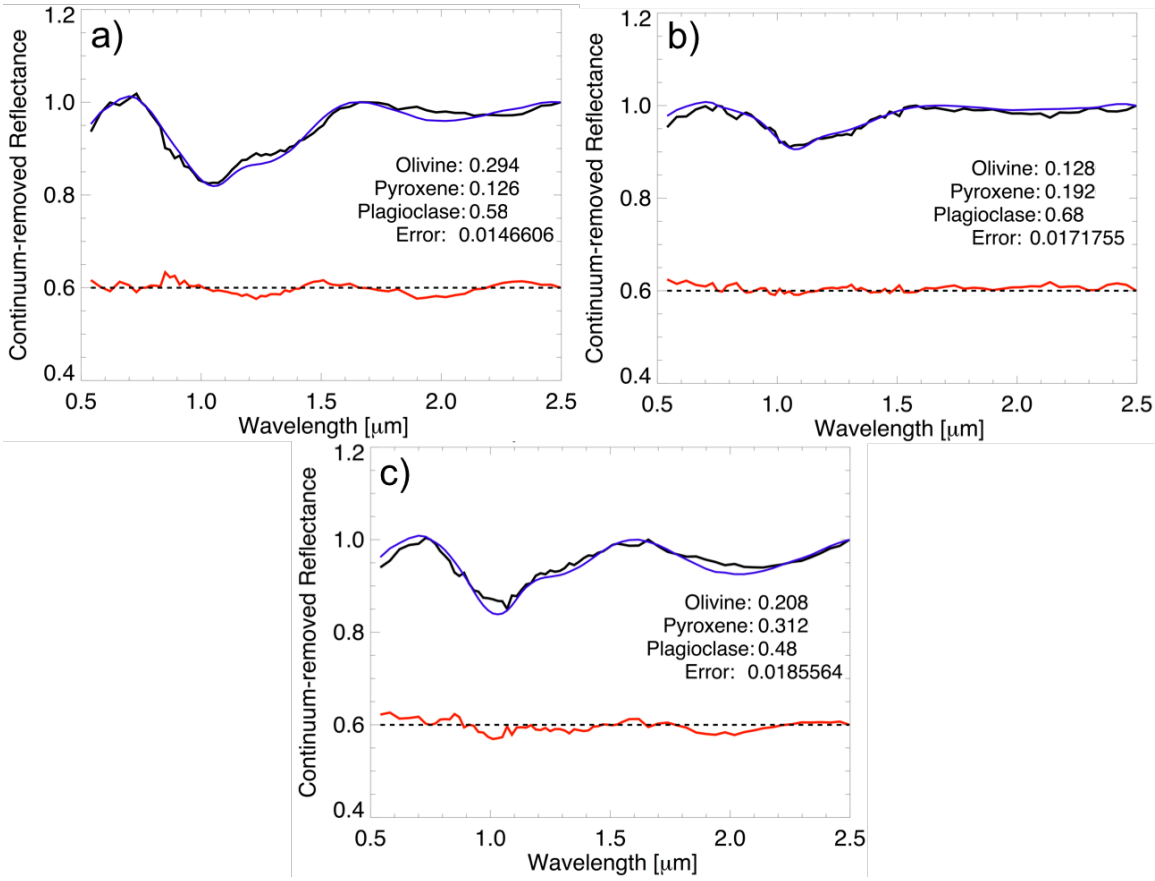

Figure 2.9 Plots show the best spectral fit between the modeled library spectra (blue) and the M3 spectra (black), along with the residuals between the observed and the modeled spectra (red) offset 0.6 from a reflectance of 0, for (a) an Fe-dominated olivine from Mare Nectaris, (b) a Mg-dominated olivine from the rim of Crisium, and (c) an olivine-dominated pyroxene mixture from the rim of Greaves crater inside Mare Crisium. The

abundances of olivine, pyroxene, and plagioclase are shown for each spectral match as weight fractions, along with the error.

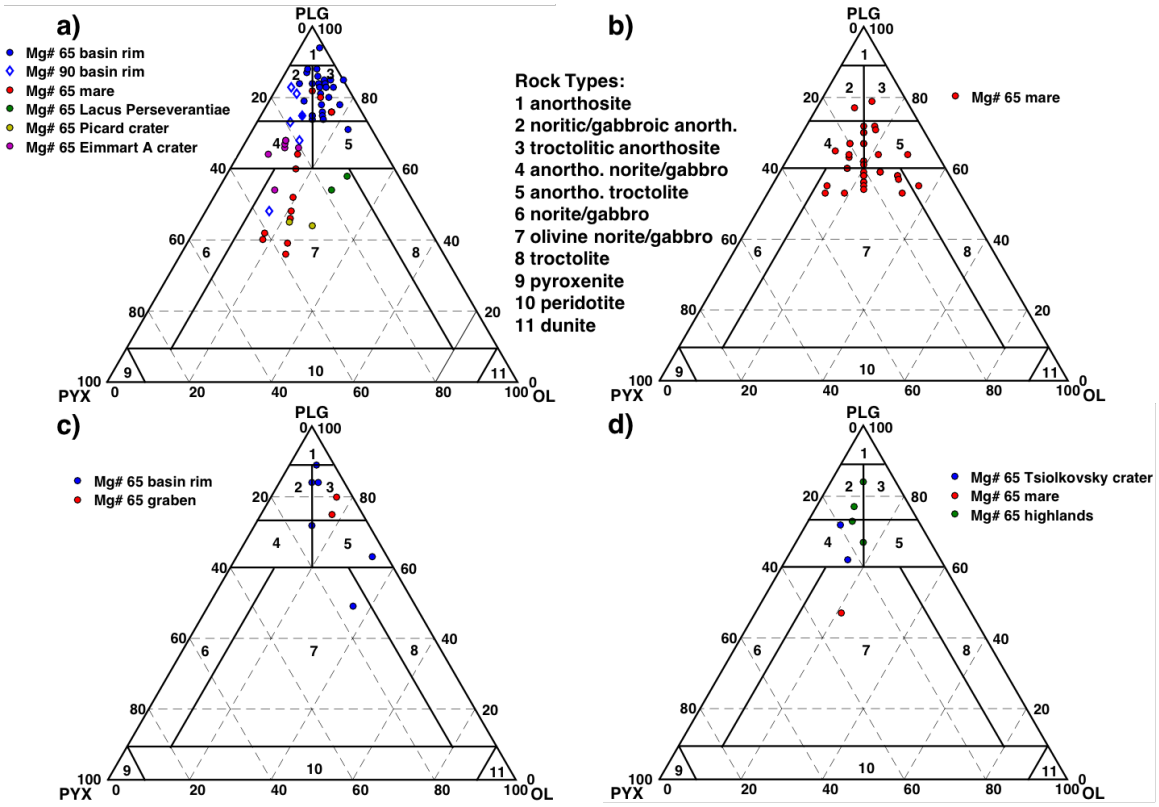

Figure 2.10 Mineral abundances (wt.%), which were estimated with radiative transfer modeling for M^3 olivine spectra from (a) Crisium, (b) Nectaris, (c) Humorum basins, and (d) near Roche crater analyzed on rock classification diagrams of Stöffler et al. (1980). Circles indicate Mg# 65 spectra and diamonds indicate Mg# 90 spectra. Points are color-coded based on geologic setting. Spectra from the maria are shown in red. For Crisium and Humorum basins, spectra from the basin rims are shown in blue. Spectra from Lacus Perseverantiae at Crisium are shown in green, and spectra from Picard crater are shown in yellow. For Humorum, spectra from the graben are shown in red. Spectra from Roche crater are classified as Tsiolkovsky crater (blue), mare (red), and highlands (green).

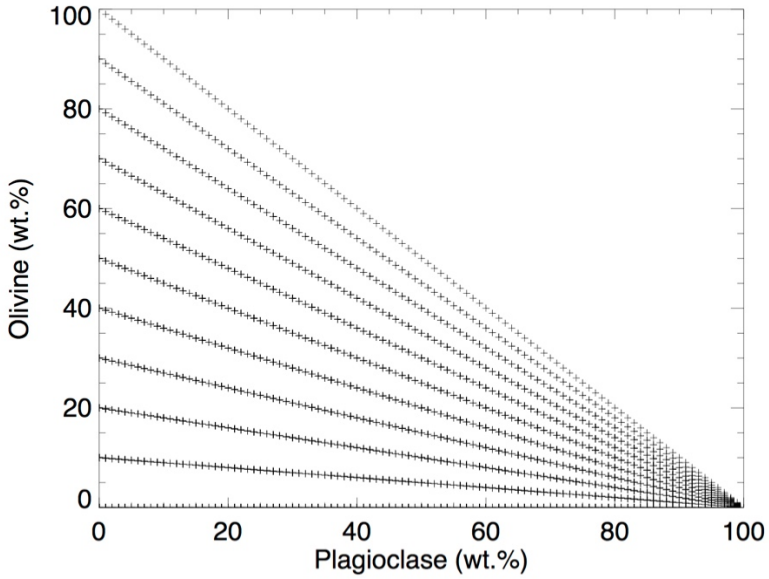

Figure 2.11 The abundance (wt.%) of olivine versus plagioclase for which the modeled library spectra are calculated. For each 1 wt.% interval of plagioclase in the modeled spectra, the mafic minerals (olivine in this figure) are calculated at 10 wt.% intervals, which cause mineral abundances on the ternary diagrams to plot along lines that trend towards the plagioclase apex. (e.g. Figure 2.8).

2.4.1 Crisium

At Crisium basin we identified 60 spectra with signatures that represent olivine or olivine-dominated mixtures, with an average olivine content of 14 wt.% for all olivine-bearing spectra. These spectra are located on the rims of small craters, on massifs at the rim of Crisium, and on mare both inside and outside of Crisium basin (Figure 2.8a). The six spectra that were estimated to be Mg# 90 are all located on the southern rim of Crisium (Figure 2.12). Olivine-bearing spectra from the rim of Crisium are on the irregular massifs and platform massifs members that were mapped by Sliz and Spudis (2016). We were able to confirm many olivine locations that were detected by Yamamoto et al. (2010). However, we were unable to confirm the olivine detections at Cleomedes L crater (23.8° N, 54.4° E) and Pierce C crater (18.8° N, 49.9° E), both on the basin rim, because the M^3 spectra at these locations exhibited too much noise. The maximum olivine content estimated in this study is 29 wt.% and is located at Lacus Perseverantiae, a narrow inlier of mare embedded in the rim of Crisium basin (Figure 2.6). We report

many olivine detections where olivine was previously undiscovered by Yamamoto et al. (2010), including on the main basin-filling mare of Crisium. One such discovery is located on the rim and in the ejecta of Picard crater, (Figure 2.12a), where two spectra have olivine contents of 24 wt.% and 28 wt.%. Crustal thickness models based on joint analysis of GRAIL data (Wieczorek et al., 2013) and LOLA topography (Smith et al., 2010b; 2016) indicate that the crustal thickness in the center of the Crisium impact basin is close to zero. In contrast, the majority of our olivine detections correlate with crustal thickness maxima on the rim of Crisium between 2 km and 90 km from the mare border. Olivine was also found on the wall of Eimmart A, which is a small crater located on the rim of Eimmart (Figure 2.12c).

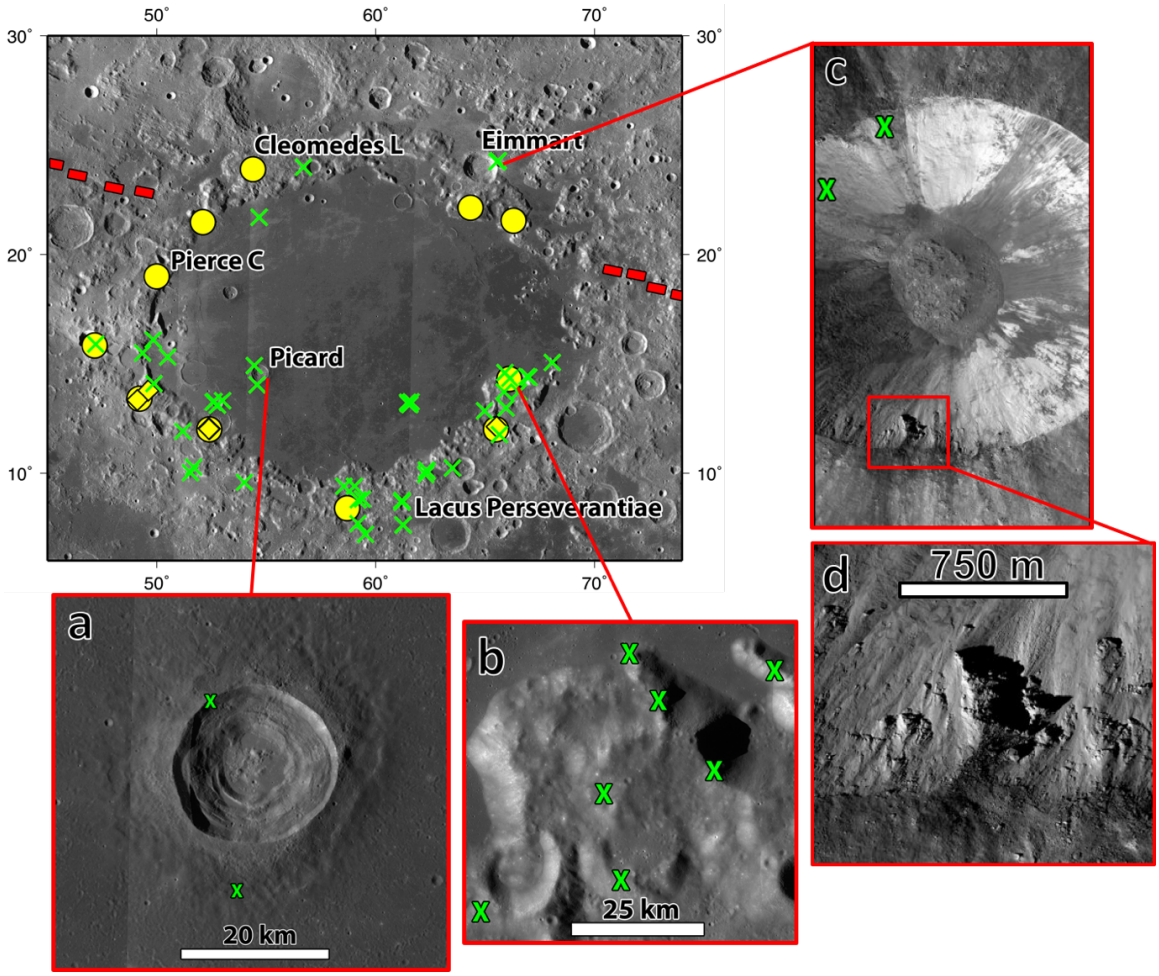

Figure 2.12 LRO WAC mosaic of Crisium basin showing locations of Mg# 65 olivine (X) and Mg# 90 olivine (◊). Detections from Yamamoto et al. (2010) are shown as circles. LRO images of areas of interest include: a) Picard crater (WAC), b) the mare and

southern rim of Crisium (WAC), c) Eimmart A crater (NAC), d) a mechanically stable outcrop on the rim of Eimmart A (NAC).

2.4.2 Nectaris

All of the olivine detections at Nectaris are confined to the mare (Figure 2.8b). Crustal thickness inside Nectaris basin is as low as 5 km in some areas (Figure 2.7b). We were unable to confirm the Yamamoto et al. (2010) olivine locations at Theophilus crater. The CRISM olivine index did identify locations on the rim and central peak of Theophilus. After thorough inspection of the data, these locations were ultimately not included in our study, because they have a low signal to noise ratio that makes mineral abundance estimations unreliable. Many more olivine locations were found in the mare, for a total of 36 olivine spectra. At Nectaris, the average olivine abundance is 20 wt.% and the maximum is 36 wt.%, which is located on the rim of Beaumont L crater (14.4° S, 30.0° E, Figure 2.13).

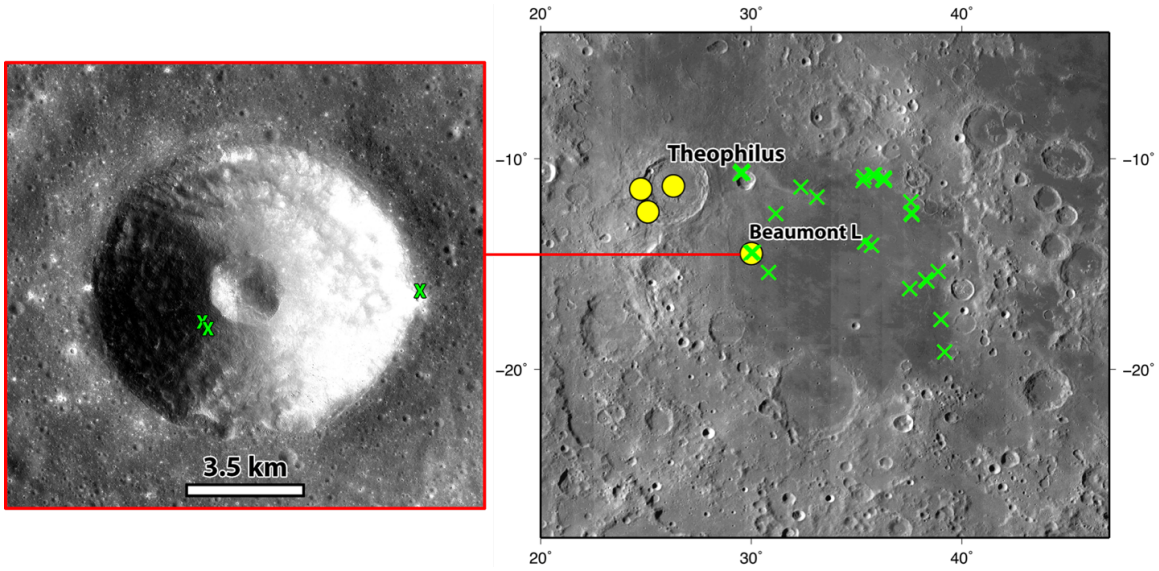

Figure 2.13 LRO NAC mosaic showing the approximate locations of olivine detections at Beaumont L crater on mare Nectaris, inset from the WAC mosaic map. Mg# 65 olivine detections from this study are shown as x's and detections from Yamamoto et al. (2010) are shown as circles.

2.4.3 Humorum

A total of 8 olivine spectra were detected at Humorum basin (Figure 2.8c). In this investigation, we confirmed an olivine location at Mersenius P crater (19.9° S, 47.8° W) from Yamamoto et al. (2010), but we were unable to confirm two locations west of Mare Humorum due to low signal to noise ratios. A new olivine discovery was made at the mare-flooded Lee crater (30.7° S, 40.7° W). In addition, two olivine-bearing spectra with 17 wt.% olivine were found on a graben in northwest Humorum (Figure 2.14), near an olivine detection from Yamamoto et al. (2010). All of the olivine detections at Humorum are located on its rim, where crustal thickness is ~40 km. The average olivine abundance at Humorum is 18 wt.%, with the maximum of 36 wt.% olivine at Lee crater.

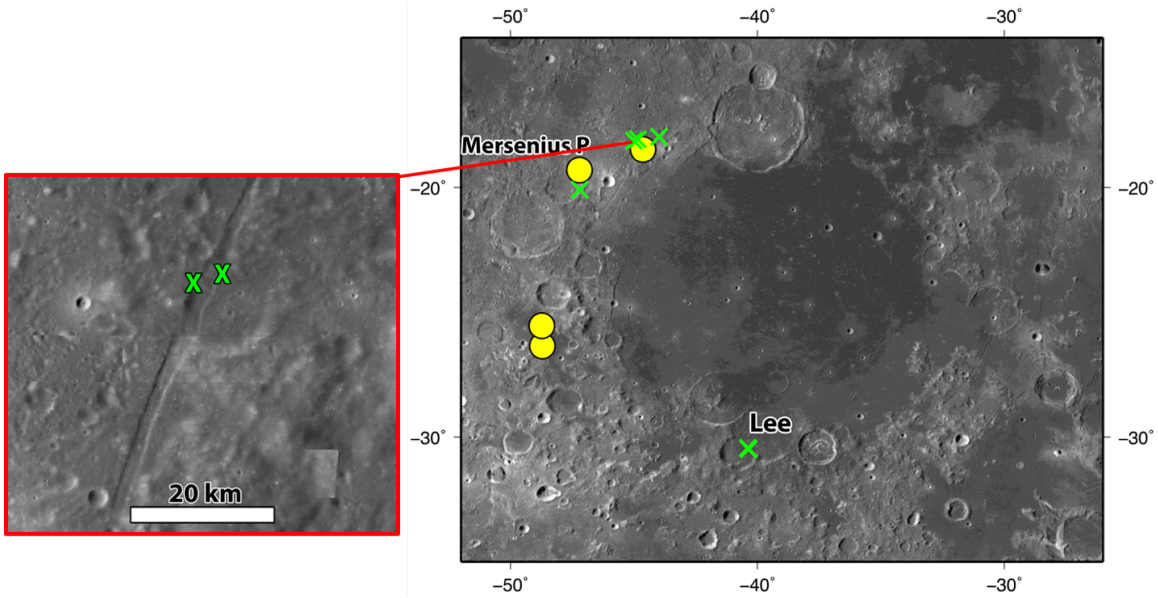

Figure 2.14 LRO WAC images showing the location of Mg# 65 olivine detections (x's) on a graben on the rim of Humorum basin, inset from the WAC mosaic. The detections from Yamamoto et al. (2010) is shown as circles.

2.4.4 Roche/Tsiolkovsky

Roche, a 153-km diameter Nectarian-aged crater located on the lunar farside (42.2° S, 136.3° E) at the edge of South Pole-Aitken (SPA) Basin (Wilhems and El-Baz, 1977), had not been previously investigated for olivine using high spectral resolution data. Andrews-Hanna et al. (2013) identified a linear gravity gradient anomaly at Roche using GRAIL data, which they interpret to be an ancient (pre-Nectarian) dike. We

identified 7 olivine-bearing spectra near Roche (Figure 2.8d). Some of our detections were in close proximity to the proposed dike, and two were within the nearby central peak crater, Tsiolkovsky (Figure 2.15a). Olivine spectra at Roche/Tsiolkovsky have an average olivine abundance of 13 wt.%, with the maximum of 21 wt.% olivine on a small patch of mare that partially infilled Bolyai crater (Figure 2.15b). Two olivine spectra are also located on the floor of the 47-km diameter Pikel'ner crater, south of Bolyai. Olivine-bearing spectra were also identified near Pauli crater, which is an 84-km diameter Imbrium-aged crater (Wilhems and El-Baz, 1977) superposed on Roche (Figure 12.5c). One detection, with 9 wt.% olivine, is located at the contact of the mare and material from the crater wall. Another olivine-bearing spectrum, which is very similar in composition, is located on the rim of a 9-km diameter crater southeast of Pauli.

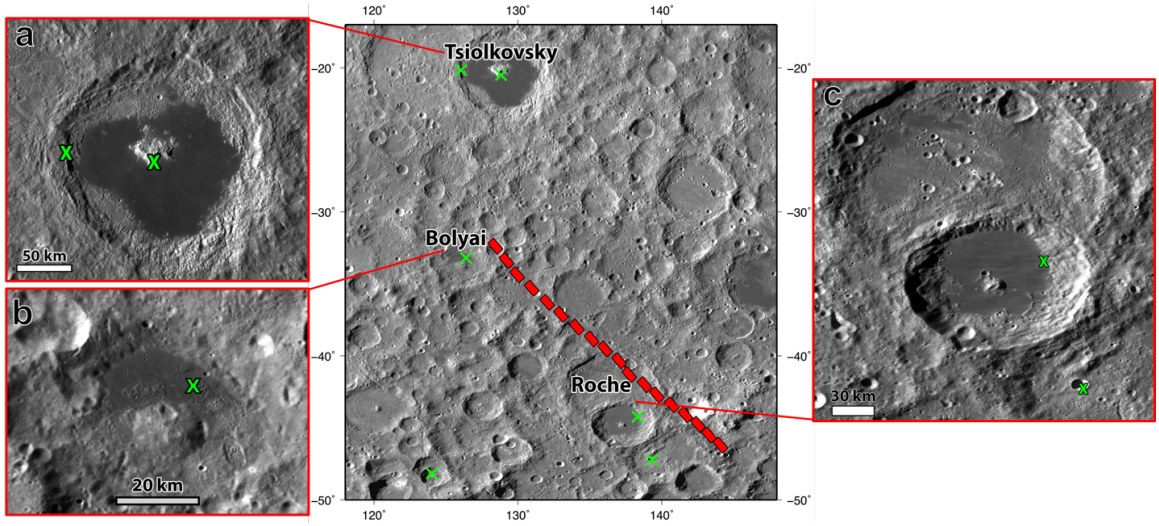

Figure 2.15 LRO WAC images, inset from the WAC mosaic, showing the location of Mg# 65 olivine detections (x's) at a) Tsiolkovsky crater, b) mare inside Bolyai crater, and c) Pauli crater.

2.5 Discussion

The integration of the geophysical settings and estimated mineral abundances allow for the interpretation of the origins and the transport mechanisms of the olivine exposures examined in this study. Possible transport mechanisms include excavation of the mantle, lower crust, or impact melt by basin-forming impact, or magmatic emplacement of olivine-rich basalts, cumulates, or xenoliths. Furthermore, mineral abundances also provide insight into the lunar mantle overturn and the origin of olivine

exposures. Although Arnold et al. (2016) provide an upper limit of detections for olivine-plagioclase mixtures with less than ~10% pyroxene, we analyzed spectra that contain a significant amount of pyroxene in addition to olivine and plagioclase. These mafic-rich lithologies are certainly relevant to interpretations of the specific origins and transport mechanisms of olivine-bearing material. The olivine-bearing spectra identified by both our study and Arnold et al. (2016) have a wide range of olivine abundances, likely indicating contamination with more feldspathic crustal material and/or different origins between olivine-bearing sites. We first discuss each location separately, and then summarize our results concerning the origin of olivine and the manner by which it was transported to the surface. The implications of our results concerning future sample return missions are then discussed.

2.5.1 Crisium

There is a diversity of possible origins for olivine located on the mare basalts within and around Crisium basin. Examination of the crustal thickness model (Figure 2.7a) suggests that olivine exposed on the main mare at Picard crater could be mantle olivine (e.g., Figure 2.2e; Wieczorek and Phillips, 1998; Miljković et al., 2015). Wieczorek and Phillips (1998) postulated that mantle deposits might also be associated with the smaller 18-km diameter crater Pierce located within the mare, but we find no olivine exposures with this crater. Instead, Pierce crater has widespread pyroxene exposures. The crustal thickness in the center of the Crisium impact basin is predicted to be close to zero. Given the 23-km diameter of the crater Picard, as well as the approximately 1.4 km thickness of the basalts in this basin as measured by the Apollo Radar Sounder (Maxwell and Phillips 1978, Peeples et al. 1978), this crater is large enough to have penetrated through the thin basalt cover and into underlying impact melt, crust, or mantle. Thus, Picard crater could contain material from deep layers of mare basalt (e.g., Head et al., 1978), cumulates of differentiated impact melt (Figure 2.2d), primary crust, and mantle material (Figure 2.2e). Hydrocode simulations by Miljković et al. (2015) indicate that the Crisium impact melt sheet was composed of less than 1.5% crustal material mixed with mantle material. Perfect segregation during crystallization would have resulted in an anorthositic layer at the surface. The impact melt exposures mapped by Spudis and Sliz (2017) have a feldspathic highlands composition with

moderately low FeO content (8-10 wt.%). One of our olivine exposures (located 15.3°, 50.5°E, with 7 wt.% FeO) is located at an impact melt deposit mapped by Spudis and Sliz (2017). The feldspathic composition (9 wt.% olivine, 4 wt.% orthopyroxene, 5 wt.% clinopyroxene, 82 wt.% plagioclase), could represent cumulates of a crustal impact melt layer with contamination from mare basalt. This crustal impact melt layer, along with mare basalts, would likely obscure olivine that crystallized from deep in the impact melt sea. Picard crater is large enough that it may have excavated deep impact melt cumulates or mantle material (Figure 2.2d and 2.2e). The estimated mineral abundances for the olivine spectra on the rim and in the ejecta of Picard crater indicate that these rocks are olivine-rich norites (22 wt.% olivine, 11 wt.% orthopyroxene, 22 wt.% clinopyroxene, 45 wt.% plagioclase and 28 wt.% olivine, 17 wt.% orthopyroxene, 11 wt.% clinopyroxene, 44 wt.% plagioclase).

Other olivine-rich areas are located almost exclusively on the rim of Crisium near local crustal thickness maxima, just exterior to the mare on the Irregular Massif and Platform Massif units (e.g., Sliz and Spudis, 2016). The locations of these exposures are consistent with representing mantle material that was uplifted during the initial stages of formation of the Crisium basin, as modeled by Miljković et al. (2015). Thus, olivine exposures on the basin rim are the best candidate sites for mantle olivine (Figure 2.2a). Any olivine excavated from the basin-forming impact and deposited north of the second basin ring could have been buried by later Imbrium ejecta. Imbrium ejecta (Sliz and Spudis, 2016) and grooves related to Imbrium ejecta (Schultz and Crawford, 2016) are present outside the second basin ring. However, Imbrium ejecta does not occur inside the second ring. Thus, burial by ejecta is not the reason for the paucity of olivine detections on the northern rim massifs bordering the mare.

The olivine-bearing spectra from the rim of Crisium have shallow, symmetric 1-μm absorptions, indicating they are magnesian with an Mg# of approximately 90 (Burns, 1993; Sunshine and Pieters, 1998; Isaacson et al., 2014). Although all except six of the olivine detections on the rim of Crisium were estimated to be Mg# 65 using our model, the individual spectra appear more magnesian than spectra from the mare that were also estimated as Mg# 65. The spectral libraries use only two Mg#s for all minerals (either Mg# 65 or 90). Therefore, two possibilities exist that explain this observation. First,

olivine on the rim of Crisium might be closer in composition to Mg#65 than Mg#90 and therefore gets classified at the lower Mg#. Secondly, it is possible that the detections from the basin rim contain high-Mg olivine from the mantle along with crustal contamination that is lower in Mg. Our model does not account for this scenario, because all minerals have the same Mg# (e.g., we do not model olivine of Mg#90 with the other three minerals of Mg#65).

If olivine on the rim of Crisium is indeed mantle olivine, Mg-rich composition supports the idea that mantle overturn occurred in this location (e.g., Elkins-Tanton et al., 2011). Estimated bulk mineral abundances reveal that most of these rocks from the basin rim are troctolitic and noritic/gabbroic anorthosites, with fewer anorthositic troctolites, anorthositic norites/gabbros, olivine-rich norites, and anorthosites (Figure 2.10a). Such compositions are consistent with an upper mantle disrupted by overturn, perhaps with some amount of highland contamination. However, troctolites and norites are also consistent with Mg-suite rocks in the sample suite, which could have been exposed by the basin forming impact (e.g., Figure 2.2b). Mg# alone cannot distinguish between the mantle and Mg-suite origins. Overturned olivine at the crust-mantle boundary is expected to have an Mg# of 90, whereas Mg-suite rocks exhibit a range in Mg# of about 70 to 90, with troctolites having higher Mg# than norites (Taylor, 2009; Elkins-Tanton et al., 2013). Although Zhu et al. (2013) propose that a lower potassium concentration at the rim compared to the mare is the result of the redistribution of material from an exposed pluton, low thorium concentrations (Jolliff et al., 2000) indicate that neither a KREEP layer nor Mg-suite pluton was excavated.

Magmatic processes, including dikes, could have transported olivine to the rim of Crisium (e.g., Figure 2.3f and 2.3g). We identified olivine on the wall of the crater Eimmart A. NAC imagery (Figure 2.12c and 2.12d) of the southern wall of Eimmart A shows an outcrop that appears mechanically stronger, which Powell et al. (2012) suggested could be a dike. Öhman et al., 2016 mapped this outcrop and others like it that could be composed of more competent rock than the surroundings or simply reflect preservation due to the young age of the crater. It is possible that olivine at Eimmart A is excavated material that was uplifted from depth during basin formation. In contrast, olivine located at the mare pond Lacus Perseverantiae was likely transported

magmatically because here the crust is too thick (greater than 10% of the crater diameter) for the craters where the olivine is detected to have penetrated to the mantle. These olivine exposures are unique compared to others at Crisium, because they are olivine-rich norites with the highest olivine abundances of 28 and 29 wt.% (Figure 2.10a). They may be cumulates from a magma chamber, possibly brought to the surface during mare eruption (e.g., Figure 2.3d).

2.5.2 Nectaris

Olivine exposures in Nectaris basin are confined to the rims of small craters (<5 km diameter) on the mare. Although the crustal thickness within Nectaris basin is as low as 5 km in some areas (Figure 2.7b), none of the craters where olivine is found are large enough to have penetrated through the mare and into the underlying impact melt, crust, and mantle. Olivine-rich material here was likely magmatically transported to the surface by dikes to produce mare lava flows. Estimated mineral abundances reveal that the compositions are predominantly olivine-rich norites and anorthosite-rich troctolites and norites, as well as a few troctolites, troctolitic anorthosites, and noritic anorthosites (Figure 2.10b). Our detections have comparable olivine contents to olivine-rich basalt Apollo samples, such as sample 12002 that contains 20 vol.% olivine (Taylor et al., 1991). However, these detections are much higher in plagioclase than any known Apollo or lunar meteorite basalt (Li et al., 2016) and may contain ejecta from the craters Theophilus and Madler.

Small craters on Mare Nectaris probably exposed layers of olivine-rich mare basalt (Figure 2.3b). We confirmed detections by Kaur et al. (2015) of olivine-bearing spectra in the 4-km, dark-haloed crater Beaumont L, which they conclude is an excavated olivine-rich Copernicus-type (Hawke and Bell, 1982; Giguere et al., 2003) cryptomare deposit. The number and distribution of olivine detections at Nectaris suggests that a significant volume of Nectaris is filled with olivine-rich mare basalt. The confinement of detections to crater rims suggests that the uppermost (youngest) mare units contain less olivine, although space-weathering processes could remove olivine spectral signatures in surface units. Kaur et al. (2015) found that two other dark-haloed craters on mare Nectaris are not rich in olivine, like Beaumont L, but are dominated by high-Ca pyroxene. Due to the smaller size (~ 2 km) and shallower excavation depth of these dark-

haloed craters, they conclude that these craters penetrated Theophilus and Madler ejecta deposits, exposing underlying mare and forming dark haloes, but did not excavate deep enough to reach the stratigraphically lower olivine-rich mare that Beaumont L exposed. Although we did not detect olivine in either of the smaller dark-haloed craters, we did confirm the presence of olivine in craters of smaller size. Thus, the mare could contain multiple layers of olivine-rich basalt. Our observations are consistent with olivine-rich layers of variable thickness intercalated with pyroxene-rich layers (e.g., Kaur et al., 2015) with highlands contamination.

2.5.3 Humorum

At Humorum basin, graben (Figure 2.14) with detections of olivine were likely created by extensional stresses caused by the loading of mare basalt (e.g., Solomon and Head, 1979; Solomon and Head, 1980). Extensional stresses would also have been favorable to the formation of dikes. The rock type associated with the olivine-bearing material on the graben is troctolitic anorthosite with 17 wt.% olivine (Figure 2.10c). Olivine-rich rock types on the basin rim of Humorum are olivine-rich norites, anorthositic norites, anorthositic troctolites, and troctolitic anorthosites (Figure 2.10c). We conclude that olivine on the basin rim, including olivine on the graben in northwest Humorum, are likely cumulates of shallow intrusions that were transported magmatically to the surface (e.g., Figure 2.3f and 2.3g). The graben could be a surface manifestation of a stalled dike, as emplacement of a dike at shallow depth can create a near-surface stress field that causes the formation of graben (Head and Wilson, 2017; Figure 2.3f). Rima Sirsalis, a linear graben near Humorum, is interpreted to be associated with an underlying dike that has a magnetic signature (Srnka et al., 1979; Head and Wilson, 1993; Hood et al., 2001).

The scarcity of olivine at Humorum indicates that the source of olivine is not simply Humorum ejecta excavated from subsequent impacts on massifs. If the impact that formed Humorum had excavated olivine-rich material from depth, we would expect to find widespread olivine around the basin. The presence of a wide range of lithologies could reflect the fact that such cumulates would vary depending on the melt composition of the intrusions. An alternative explanation for the presence of mafic material at Humorum is the excavation of preexisting ancient maria during basin impact (Bussey and

Spudis, 2000). The region south of Humorum is known for ancient mare volcanism (i.e., cryptomare) >3.9 Ga (e.g., Whitten and Head, 2015) that predates that basin, which was recognized in dark-haloed craters on the floors of old impact basins, inter-crater plains, and ejecta of large craters (Schultz and Spudis, 1979). Bussey and Spudis (2000) suggested that energetic local mixing and secondary cratering, during the deposition of Humorum ejecta, incorporated the ancient mare material into the continuous ejecta. This process may have been so disruptive to an ancient mare underneath Humorum that dark-haloed craters farther south of Humorum are the only obvious evidence remaining today. Although the incorporation of ancient mare basalts into basin ejecta would result in more mafic material on the basin rim, the paucity of olivine detections suggests that this mechanism is not responsible for the presence of our olivine detections.

2.5.4 Roche/Tsiolkovsky

We detected olivine at several sites around Roche (Figure 2.6d) and on the central peak and wall of nearby Tsiolkovsky crater (Figure 2.13a), where Pieters and Tompkins (1999) and Lemelin et al. (2015) identified olivine-bearing material with Clementine data and MI data, respectively. Estimated mineral abundances from the spectra are indicative of anorthositic norites and noritic anorthosites (Figure 2.10d). An olivine-rich norite, located on a small mare pond in Bolyai crater, is likely magmatic olivine (Figure 2.3a, Figure 2.10d, Figure 2.15b). Due to the thicker crust on the lunar farside, material exposed near Roche crater is not likely to be impact-exposed mantle. Although olivine detections are not present at the exact location of the dike proposed by Andrews-Hanna et al. (2013), other magmatic intrusions could have reached the shallow subsurface and been exposed by small impacts (Figure 2.3f and 2.3g). Such intrusions are likely common on the farside, as it is predicted that ascending magma stalled and cooled in dikes before reaching the surface as a result of the thicker crust (Head and Wilson, 2017; Wilson and Head, 2017). The widths of such dikes that stalled on the farside at a few-km depth would be ~50 m. Dikes of this size would not have been identified in the gravity data, because isolated dikes with widths of up to tens of meters have gravity anomalies below the detections limits of GRAIL (Andrews-Hanna et al., 2013).

For the olivine detections at Tsiolkovsky (Figure 2.15a), comparisons may be drawn with detections of olivine-rich material in other complex craters near the outer

regions of the South Pole-Aitken Basin, such as the central peak of Schrödinger basin (Kramer et al., 2013). Current understanding of impact cratering mechanics (e.g., Baker et al., 2011; Baker et al., 2012; Potter et al., 2013b; Baker and Head, 2015) indicates that material in the central peaks or peak rings of complex craters like Tsiolkovsky and Schrödinger derive material from deep in the crust, possibly as deep as the crust-mantle boundary, depending on the crater/basins diameter and crustal thickness at a given site. However, the crustal thickness derived from GRAIL in the center of Tsiolkovsky is ~36 km, and the crater diameter suggests that the central peak excavated and exposed material from ~19 km below the actual surface (Lemelin et al., 2015). Therefore, in this case, olivine exposures from the mantle are unlikely. Our estimated olivine abundances at Tsiolkovsky are 8 and 15 wt.% (Figure 2.10d), whereas Lemelin et al. (2015) estimated a maximum of 46 wt.% and average of 5 wt.% olivine using Multiband Imager data. Although it is unlikely that Tsiolkovsky penetrated the crust-mantle boundary, it is possible that Tsiolkovsky excavated mafic material in the crust (Figure 2.2c).

2.5.5 Implications for sample return

Dunites are rare in the lunar sample collection. Samples 72415 through 72418 are fragments of the only hand sample-sized predominantly olivine (dunite) collected from the Moon (Ryder, 1992). Fragments from this dunite were initially labeled as primary (i.e., mantle) in origin (Dymek et al., 1975), although subsequent analysis revealed zoning in the olivine that suggests a shallow intrusive origin (Ryder, 1992). Sample 76535 is a troctolite (~37% Fo_{88} olivine and 58% plagioclase, Gooley et al., 1974). Symplectites of Cr-spinel, Ca-clinopyroxene, and Mg-orthopyroxene in samples 72415 and 76535 are indicative of mantle origin (Schmitt, 2016). Olivine-dominated clasts are also present in some lunar breccias (Snyder et al., 1995). Sample 67955 is a poikilitic, noritic anorthosite (~6 vol% olivine) that is distinct from pristine lunar highlands rocks and is likely a monomictly brecciated impact melt rock (Norman et al., 2014). Dunite xenoliths in basalt sample 74275 likely represent olivine cumulates that crystallized from a low-Ti mare basalt at intermediate to shallow crustal levels, were subsequently sampled by the 74275 magma, and transported over a period of ~30-70 days to the surface (Shearer et al., 2015b). Although mantle material has not been identified in regolith samples returned from the Crisium region by Luna 20 and 24, high-Mg (Fo_{77}) olivine

fragments from Luna 24 could originate from a coarse-grained cumulate rock that was not observed as a discrete rock fragment (Basu et al., 1977).

In any event, to date no samples of the lunar mantle have been unambiguously identified in the lunar sample collection. Obtaining such a sample would be a major accomplishment, with the potential to yield fundamental new insights into the composition, structure, and evolution of the lunar interior. The olivine sites associated with the southern rim of Crisium basin and Picard crater are appealing targets for future sample return missions, because they may contain pieces of mantle rock. However, olivine may also arise from magmatic processes within the lunar crust (Ryder, 1992; Yamamoto et al., 2010), but obtaining such samples would also be valuable as they would provide constraints on magma chamber and dike dynamics, as well as magma and source rock compositions. Olivine exposures on mare units that are not associated with craters large enough to completely penetrate the crust are likely to originate from layers of olivine-rich mare flows (e.g. Staid et al., 2011; Kaur et al., 2015). Magmatic processes can transport olivine via dikes through the crust, either as entrained xenoliths of mantle rock or as products of magmatic evolution (cumulates). Examples of the latter may include the Lacus Perseverantiae and Humorum basin olivine sites.

2.6 Conclusions

The application of a radiative transfer model to high-resolution M^3 data have allowed for estimation of mineral abundances of olivine-rich material at Crisium, Humorum, and Nectaris basins and near Roche crater. Modeled crustal thickness estimates from GRAIL and LOLA (Wieczorek et al., 2013), LOLA topography maps, and WAC and NAC images were used to examine the geophysical and morphologic settings and put our olivine locations into geologic context. Detailed investigations of each study area using these data sets allowed for the interpretation of origin and transport mechanisms for olivine exposures. Crustal thickness estimates at Nectaris and Humorum basins and Roche crater indicate that olivine was transported by magmatic processes. At Humorum basin, olivine sites on graben indicate magmatic transport (e.g., Figure 2.3f and 3g), likely the result of loading of basin-filling mare basalt creating extensional stresses favorable to the formation of dikes. In addition, detections of olivine near Roche crater might originate from magmatic intrusions in the subsurface (Figure 2.3f and 2.3g),

possibly related to the ancient dike proposed by Andrews-Hanna et al. (2013), which were later exposed by small impacts. The central peak of nearby Tsiolkovsky crater contains olivine-bearing material that likely originates from mafic material deep in the crust (Figure 2.2c). Olivine exposures in Nectaris basin are confined to the rims of small craters that punctured the mare, probably exposing a layer of olivine-rich mare basalt (Figure 2.3b). Crisium contains a diversity of olivine-bearing lithologies. Olivine-rich norites with up to 29 wt.% olivine at Lacus Perseverantiae are possible exposed magma chamber cumulates (Figure 2.3d and 2.3e). Mantle olivine may have been exposed by the basin-forming impact and deposited on the rim of Crisium and by Picard crater (Figure 2.2a and 2.2e), where crustal thickness is near 0 km. Picard crater could also contain olivine that crystallized from a differentiated impact melt sea (Figure 2.2d), which would be a desired sample return site that would allow for accurate dating of the Crisium impact event and the determination of the target composition. Olivine exposures on the basin rim are the best candidate sites for mantle olivine, as this is where simulations by Miljković et al. (2015) predict uplifted mantle material to occur. Under the assumption that Mg-rich olivine is indicative of a mantle derivation, identification of Mg-rich olivine on the southern rim of Crisium suggests that mantle overturn occurred in this region.

CHAPTER 3

A COMPARISON OF THE EFFECTS OF KINETIC IMPACT AND LASER IRRADIATION FOR SPACE WEATHERING SIMULATIONS

Submitted for publication as: Corley, L. M., Gillis-Davis, J. J., Ichimura, A. S., Ishii, H. A., Bradley, J. P., Trang, D., and Ohtaki, K. (2019) A comparison of the effects of kinetic impact and laser irradiation for space weathering simulations, Icarus.

Abstract – We compare and contrast the effects of kinetic impact, laser irradiation, and a combination of the two methods on a lunar highlands analog. The purpose of these experiments is to evaluate the various physical and spectral changes produced by each method in order to determine which method produces the most accurate lunar space weathering effects. Kinetic impact experiments, in which quartz projectiles were fired into a powdered highlands analog, were performed with a light-gas gun at the NASA Ames Vertical Gun Range. A Nd:YAG, nanosecond laser was also used to irradiate the analog. Our analyses of the weathered materials include Scanning Transmission Electron Microscopy (S/TEM), visible to near-infrared spectral measurements, radiative transfer modeling of the spectra, and electron paramagnetic resonance (EPR) and ferromagnetic resonance (FMR) measurements, with this being the first study to report FMR spectra resulting from laser irradiation and irradiation plus kinetic impacts and place the results on the I_s/FeO maturity index. These analyses show that, although our impact experiments created agglutinate-like aggregates, the material does not exhibit spectral changes consistent with space weathering and no submicroscopic metallic iron (SMFe) was detected. While our laser experiments are not capable of producing agglutinates, an amorphous rim containing nanophase iron (<40 nm) was observed on a laser-irradiated grain. In addition, laser irradiation resulted in typical space weathering spectral trends (e.g., darker, redder, and reduced spectral contrast). The material that was subjected to both weathering methods exhibited a lower albedo and has a slightly higher I_s/FeO maturity index than that of the material that was only laser irradiated. Modeling indicates that the twice-weathered material contains slightly more SMFe than the material that only

underwent laser irradiation, and S/TEM analyses detected SMFe on a plagioclase grain. Thus, laser irradiation of material weathered at the AVGR, which contains glass-welded aggregates, enhances the darkening produced by laser weathering. Based on our analyses, a combination of the two methods best simulates lunar-like space weathering.

3.1 Introduction

Ultraviolet to near-infrared remote sensing is one of the most powerful and widely used techniques for mineralogical identification in planetary science (Adams and McCord, 1970; Burns, 1970; Bell and Hawke, 1995; Burbine and Binzel, 2002; Lucey, 2004; Blewett et al., 2009; Cloutis et al., 2012; Crites and Lucey, 2015). Spectral changes due to a process known as space weathering, however, hinder the ability to use remote sensing data to determine the original surface composition. The space weathering process is a complex combination of processes (e.g., bombardment by micrometeoroids and solar-wind ions) that acts on surfaces of airless bodies and causes physical, chemical, and optical changes. These effects have been established by studies comparing lunar samples and ultraviolet (UV) to near-infrared spectra (e.g., Pieters et al., 2000; Hapke, 2001; Noble et al., 2001; Pieters and Noble, 2016; Hendrix and Vilas, 2006; Denevi et al., 2014).

The optical effects of space weathering in the visible and near-infrared (VNIR) include decreased albedo, spectral reddening, and subdued absorption bands (e.g., Hapke, 2001). At UV wavelengths, increased albedo and spectral bluing occur as a function of space weathering (Hendrix and Vilas, 2006; Hendrix et al., 2012; Denevi et al., 2014). These spectral changes in the UV and VNIR with maturity (i.e., degree of space weathering) are attributed to the presence of submicroscopic iron (SMFe) (Hapke et al, 1975; Pieters et al., 1993; Fischer and Pieters, 1996; Pieters et al., 2000; Lucey et al., 2000; Noble et al., 2001; Hendrix and Vilas, 2006; Lucey and Noble, 2008). Mature lunar samples contain SMFe in amorphous rims on silicate minerals (Keller and McKay, 1993; Keller and McKay, 1997; Noble et al., 2005) and in agglutinates (Duke et al, 1970). The SMFe found in agglutinates is at least twice as large, averaging ~7 nm in diameter, as those in amorphous rims (~3 nm) (Keller and Clemett, 2001) and may even be thirty times larger (Basu, 2005). In order to accurately estimate surface composition with remote optical measurements from the UV (Hendrix and Vilas, 2006) through the

thermal-IR (Lucey et al., 2017), a thorough understanding of the complex processes of space weathering is critical.

Various laboratory experiments aim to simulate the space weathering process in order to provide an understanding of the physical, chemical, and spectral effects so that changes in the optical properties can be accounted for in compositional models, such as radiative transfer models. While impact experiments are physically equivalent to the micrometeoroid bombardment process, it is difficult to achieve lunar impact velocities (~16 km/sec). Laser irradiation provides an analog to micrometeoroid bombardment. The energy deposition of nanosecond pulsed laser replicates the ion formation by micrometeoroid impacts (Kissel and Krueger, 1987). Laboratory simulations of the solar wind component of space weathering are carried out with light ions (e.g., H^+, D_2^+, He^+; Burke et al., 2011; Dukes et al., 1999; Hapke 1973; Pillinger, 1979; Schaible and Baragiola, 2014)) and heavy ions (e.g., Ar^+, Xe^+; Yin et al., 1972; Bringa et al., 2007) at energies from keV to MeV.

In this work, we focus on the micrometeorite component of space weathering and exclude contributions from the solar wind. The premise of this research is to establish similarities and differences in the space weathering effects that pulsed-laser irradiation and kinetic impact experiments produce by comparing results from these two types of simulations at similar energies. Nanosecond-pulsed laser irradiation is an accepted proxy for simulating effects of micrometeoroid impacts (Yamada et al., 1999; Sasaki et al., 2001; Sasaki et al., 2003; Brunetto et al., 2006; Loeffler et al., 2008; Bentley et al., 2011; Kaluna and Gillis-Davis, 2017). A nanosecond-pulsed laser is capable of melting and vaporizing target material as a result of rapid and localized intense deposition of energy, which is similar to an impact (Bibring et al., 1974; Pirri, 1977). Laser irradiation of mafic silicates approximates the spectral effects of the micrometeoroid component of space weathering and produces SMFe. For instance, Yamada et al. (1999) first showed that the spectrum of olivine matches spectra from a subset of olivine-rich S-type asteroids after pulsed laser irradiation. Scanning transmission electron microscopy (S/TEM) and electron spin resonance (ESR) of laser-irradiated olivine grains confirmed that amorphous rims contain vapor-deposited SMFe, similar to rims observed on lunar grains (Sasaki et al., 2001, 2003).

Laser weathering does have limitations to how faithfully it can reproduce important physical components of micrometeoroid impacts (e.g., agglutinates, shock, and mineral-dependent effects), because the laser energy deposition only approximates the transformation of kinetic to thermal energy of a hypervelocity projectile. The lack of agglutinates is important because they comprise up to 60%, by volume, of a mature lunar regolith (McKay and Basu, 1983) and are the major carrier of much of the SMFe in a lunar soil (Taylor et al., 2001). These regolith particles are a major constituent causing spectral darkening and the component of the magnetic intensity value used to estimate cumulative surface exposure age (i.e., I_s/FeO, Morris, 1978). The relative abundance of agglutinates in a soil provides a bulk measure of the exposure history of a given soil, because agglutinate abundance increases with time until a steady state is reached (McKay et al. 1991). Agglutinates also contain larger microphase iron, which is deficient in amorphous rims and tends to darken more than redden spectra (Noble et al., 2007; Lucey and Riner, 2011).

Impact shock effects are important because reflectance variations of shocked plagioclase, for example, have implications for analyses and modeling of VNIR remote sensing of impact-cratered planetary and asteroidal surfaces (e.g., Lucey, 2002; Johnson and Hörz, 2003). The lack of impact shock effects may be less of a problem as the rapid temperature rise caused by infrared lasers induces stresses and surface damage due to uncontrolled melting and ablation of the target, which can affect the optical properties of the material (Brunetto et al., 2006). Laser irradiation experiments also produce strong optical-dependent effects that are related to mineralogy. Differences in the extinction coefficient (i.e., *k*, which characterizes wavelength dependent absorption) between two minerals (e.g., olivine vs. pyroxene) may influence the mineral's susceptibility to ablate in response to laser irradiation (1064 nm wavelength). For example, pyroxene, a relatively dark mineral, shows signs of significant melting under laser irradiation while plagioclase does not (Noble et al., 2011). Such mineral-dependent effects are not observed in lunar materials (Hörz and Cintala, 1997) – i.e., plagioclase becomes maskelynite (through shock) or melts before pyroxene, which has a higher liquidus temperature. Laser irradiation cannot be considered an exact simulation, because the efficiency of photon-transfer of energy and momentum-transfer of energy into heat is

different. Models of momentum transfer efficiency are done using crater-scaling law relations (Cheng et al., 2016); however, there is a general lack of knowledge concerning how impact-generated thermal energy itself is converted into a given amount of shock melt and $npFe^0$, especially when mechanical shock adds to the process (Loeffler et al. 2016). Hence, mineral chemistry may influence space weathering effects for kinetic impact experiments due to shock effects, while photon wavelength relative to a mineral's spectral absorption features may influence a mineral's response to laser energy.

Results from previous kinetic impact experiments indicate that kinetic impactors can replicate some space weathering effects. Such impact experiments replicate regolith comminution (Hörz et al., 1984; Cintala and Hörz, 1988), produce glass-welded aggregates morphologically similar to lunar agglutinates (Hörz et al., 1984; See et al., 1987), and generate vapor phases (Schultz and Eberhardy, 2015; Bruck Syal and Schultz, 2014), including Fe vapor (Adams et al., 1997). Furthermore, comminution-induced chemical fractionation was observed in both the bulk target material and melt from the glass-welded aggregates, which were enriched in Al_2O_3, CaO, and Na_2O and depleted in FeO and MgO (Hörz et al., 1984). While lunar agglutinates contain ubiquitous SMFe, Christoffersen et al. (2013) found that the glass-welded aggregates do not contain SMFe. To date, it has been unclear if SMFe forms in rims on individual grains that have experienced kinetic impact simulations. If kinetic impacts do not produce SMFe in rims or agglutinates, then kinetic impacts should not be used to study spectral changes of lunar soils. Nonetheless, prior results indicate that impact experiments can potentially replicate other vital effects of space weathering, including agglutinate formation, non-optical-dependent effects, and shock. However, a fundamental limitation of light-gas guns is that they cannot impart energy equivalent to that of lunar impacts. Shock heating by lower impact energies produces melt with little to no vapor component (Gault et al., 1972). The condensation of Fe-metal from a vapor phase is necessary for the production of SMFe from impact (Hapke 2001).

The maximum velocity of light-gas guns like the Ames Vertical Gun Range (AVGR) is ~6 km/sec (i.e., equivalent to 1.8 mJ for a 0.1 μg particle), which is comparable to impacts for asteroidal surfaces (Hörz and Cintala, 1997). Although experiments at the electrostatic Dust Accelerator Laboratory at the Colorado Center

for Lunar Dust and Atmospheric Studies can produce dust velocities that range from 1-110 km/sec (Shu et al., 2012), we chose not to use this facility for our experiments; the particle flux rate is around ~30 per minute, which is equivalent to only 5 years of the lunar meteoroid flux (Love and Brownlee, 1993), and the particle mass at 15 km/sec is 10^{-16}–10^{-18} kg, which is 6-10 orders of magnitude lower than the peak micrometeoroid mass hitting the Moon (10^{-10}–10^{-8} kg). Also the experimental setup does not allow accommodation for loose granular material. Impacts into compressed powders or individual minerals would not simulate space weathering effects compatible with a mature regolith. While hypervelocity dust experiments can reproduce features of individual microcraters (Christoffersen et al., 2017), it cannot produce bulk properties of a mature lunar regolith at short time scales.

The light-gas guns, magnetically levitated dust, and short-pulse lasers each have their advantages and limitations. Laser irradiations are best at delivering energy equivalent to lunar and higher impact energies, with a flux that can simulate regolith maturation at an abbreviated timescale. However, kinetic impact experiments should not be overlooked as they can reproduce some important aspects of space weathering that lasers cannot. The degree to which either type of experiment, kinetic impact or laser irradiation, reproduces both the physical and spectral changes resulting from space weathering in the lunar environment has yet to be fully examined. Hence, our experimental setup and analytical methods are designed to determine if lunar-like space weathering effects can be best reproduced by pulsed laser or kinetic experiments. We compare and contrast the results from laser irradiation and kinetic impact experiments to determine if the two types of experiments produce similar physical and spectral effects, and if either technique or a combination of the two produces space weathering effects similar to those observed in lunar regolith.

3.2 Methods

3.2.1 Target Material

The target sample that we used in both experiments was selected based on lunar highlands-like composition and grain size. We created a lunar highlands regolith analog, which is a mixture of 85% plagioclase (An_{80}) provided by the Stillwater Mining Company, 10% orthopyroxene ($Wo_1En_{69}Fs_{30}$), and 5% San Carlos olivine (Fo_{90}). This

mineral ratio was modeled after Apollo sample 68415, which is representative of the bulk composition of the Ferroan Highlands Terrain based on orbital and lunar sample data (meteorite and Apollo 16 sample: Korotev et al., 2003; Gillis et al., 2004). The mineral components were analyzed quantitatively with Electron Probe Microanalysis (EPMA) using the JEOL Hyperprobe JXA-8500F and with InXitu Inc. X-ray diffraction / X-ray fluorescence (XRD/XRF) at the University of Hawai‘i at Mānoa. The rocks were pulverized and dry-sieved to a grain size of <75 μm by Activation Laboratories Ltd. This grain size was selected, because the mean grain size of analyzed lunar soils averages between 60 and 80 μm (McKay et al., 1991). This maximum grain size is larger than the optically active size fraction of the Moon, which is 10–20 μm (Pieters et al., 1993); however, our simulant does contain grains in the 10–20 μm size region. The total amount of analog produced for these experiments was 53.5 kg.

3.2.2 Pulsed Laser Irradiation

High-velocity micrometeoroid impacts were simulated with a pulsed 1064-nm Continuum Surelite Nd:YAG laser, under vacuum at ~10^{-6} mbar, at the University of Hawai‘i at Mānoa. The laser pulse frequency is 20 Hz, and the pulse length is 5–7 nsec. The laser imparts 10^{10} W/cm^2 of energy into the sample using a pulse energy of 30 mJ. This pulse duration is comparable to the timescale of real micrometeoroid impacts on the Moon, and this energy regime is where evaporation and ion formation is expected (Kissel and Krueger, 1987; Yamada et al., 1999). The laser spot size on the sample is ~0.25 mm. The beam was rastered across 0.5 g of the sample, which was held in a silica glass vial, at 1-min intervals for a total of 60 min. Thus, the samples were irradiated with a total energy of 2.2 kJ. The energy deposition per mass is 4.4 kJ/g. In comparison, the lunar surface receives ~5–10 J/m^2/yr from micrometeoroids (Lucey et al., 2006b). Therefore, the energy used to irradiate our samples is equivalent to approximately 800 million years of space weathering on the lunar surface (e.g., Grün et al., 1991). In addition to fresh lunar highlands regolith analog, a sample that had been exposed to the AVGR kinetic impacts was also irradiated with the laser using the same conditions.

The experimental setup at the University of Hawai‘i is similar to that of Yamada et al. (1999) and Moroz et al. (2014). One major difference is that we irradiate uncompressed powders, whereas they use compressed pellets. In experiments that use

compressed pellets, only the uppermost surface layer is subject to heating and alteration (Moroz et al., 2014). Thus, laser irradiation of compressed pellets is probably not capable of simulating space weathering effects consistent with a mature regolith. Uncompressed powders are a better analog to regoliths on the surfaces of planetary bodies in which frequent small impacts comminute and garden the lunar regolith into fine particles (McKay et al. 1991). Similarly, when the pulsed laser irradiates our uncompressed powders, it also stirs and gardens the material, effectively space weathering the entire volume.

Forty minutes of laser irradiation using our setup is equivalent to the 5-shot laser experiments with olivine of Yamada et al. (1999) and Sasaki et al. (2001) (Gillis-Davis et al., 2017); however, we found that our highlands regolith analog requires significantly longer irradiation time to darken, redden, and reduce spectral contrast compared to mafic silicates due to its lower production of SMFe. The lower SMFe production is due to the lower susceptibility of plagioclase to laser ablation at 1064 nm and lower iron composition. This mineral-dependent weathering was previously observed in our laser weathering experiments (Corley et al., 2017). Furthermore, principal component analysis of the VNIR spectra indicates that samples with 40 min total irradiation only begin to transition from immature to submature (Kaluna and Gillis-Davis, 2017). Thus, we irradiate felsic plagioclase mixtures for a total of 60 min.

3.2.3 AVGR Kinetic Impacts

Kinetic impact experiments were performed with the 0.30 caliber light-gas gun at the NASA Ames Vertical Gun Range (AVGR). A series of 16 individual shots at an angle of 90° were fired into the same target material, 42 kg of the highlands regolith analog, over a 5-day period. The projectiles were ¼-inch quartz spheres that were fragmented into random small shards by striking a thin, 1.5-mil Mylar film as it entered the target chamber, which had pressures of $\sim 10^{-1}$ mbar. Three grams of material were collected after each shot, and the crater was reset after every third shot so that projectiles would not penetrate to the bottom of the target basin. The target material was not contained during the impacts; thus, high-speed fractions that were ejected were not sampled. The average crater size produced by all projectiles in a single shot was 18 cm in diameter and 4 cm deep. The average velocity of the shots was 5.52 km/s, and the

average energy per shot was 4.54 kJ (for a total of 72.7 kJ). As a whole, the 42-kg target received ~0.00173 kJ/g. Only the middle third of the target was impacted with projectiles; therefore, the energy distribution relative to mass is ~0.0052 kJ/g. For comparison, the energy distribution relative to mass for the laser irradiation is 4.4 kJ/g, which is nearly 10^3 times that of the kinetic impacts.

3.2.4 Reflectance Measurements and Radiative Transfer Modeling

Spectral reflectance measurements of all samples were obtained at the University of Hawai‘i at Mānoa with a FieldSpec 4 Spectrometer (Analytical Spectral Devices Inc.), which measures reflectance from the ultraviolet to near-infrared (0.35–2.5 μm) with a full-width-half-max spectral resolution of 3 nm for the 0.35–1.0μm portion and 10 nm for the 1.0–2.5μm portion of the spectrum. Spectra were acquired with a 30° incidence angle and 0° emission angle outside of the vacuum chamber. Reflectance was measured relative to a 99% reflectance Spectralon standard (LabSphere). In order to determine the error in spectral measurements, 40% and 60% reflectance standards were also measured. Our errors in reflectance measurements are typically ~0.5%. Past spectral data comparisons have shown good agreement between measurements obtained at NASA's Reflectance Experiment Laboratory (RELAB) and at the University of Hawai‘i at Mānoa (Gillis-Davis et al., 2008). Using radiative transfer modeling (e.g., Hapke, 1993; 2001) with modifications for the larger SMFe by Lucey and Riner (2011), we estimated the abundance of microphase iron (>40 nm in diameter) and nanophase iron (<40 nm). We compared our measured reflectance spectra with model spectra from material with the same composition as our initial target analog material plus varying abundances of microphase and nanophase iron. The best spectral match was chosen using the criterion of the lowest root-mean-square (RMS) difference between a given model spectrum and a sample's measured spectrum. Radiative transfer modeling, along with ferromagnetic resonance measurements (Section 2.6), allowed us to estimate the SMFe abundances of the bulk material, whereas we can only analyze a few grains with STEM.

3.2.5 Scanning Transmission Electron Microscopy (S/TEM) Analyses

Microanalyses were carried out at the Advanced Electron Microscopy Center (AEMC) at the Hawai‘i Institute of Geophysics and Planetology. Six electron transparent sections were prepared using the Helios 660 dual-beam Focused Ion Beam (FIB)

instrument and analyzed using S/TEM. Dual-beam FIB is used to rapidly and reliably prepare electron-transparent thin sections (70–100 nm thick) for S/TEM analysis of a specific location (accurate to < 50 nm) (Ishii et al., 2009; Ishii et al., 2010a; Ishii et al., 2010b). Samples were carbon-coated prior to secondary electron (SE) imaging in conjunction with FIB preparation. Specimens were extracted by Ga-ion milling with protective Pt layers over the region of interest to prevent ion damage. SE imaging in the FIB was used to examine grain surfaces and morphology prior to harvesting (FIB) sections. In addition, energy dispersive x-ray spectroscopy (EDS, AZtec Energy Xmax N80 silicon drift detector, Oxford Instruments) allowed us to determine the composition of the grains before FIB preparation. Some preliminary SE imaging was also done using the S-4800 Field Emission Scanning Electron Microscope (Hitachi) at the Pacific Biosciences Research Center's Biological Electron Microscope Facility.

S/TEM microanalyses were performed using the 60–300 kV, dual Cs-corrected and monochromated high-base Titan (Thermo Fisher, formerly FEI). The Titan is ideal for low-electron dose, high signal/noise analyses of amorphous silicates (Bradley and Dai, 2009; Bradley et al., 2014). Analyses included conventional brightfield, darkfield, high-angle annular darkfield (HAADF) images (0.8 Å resolution, with magnifications of 10,000X–100,000X) that allowed the microstructures, including amorphous material and SMFe, to be examined. We used electron (nano)-diffraction to distinguish amorphous and crystalline material, which was especially useful when analyzing agglutinate-like material. Chemical analyses were obtained using EDS (Genesis 4000 Si(Li) detector, EDAX) in conjunction with a Cliff-Lorimer thin-film correction procedure calibrated against thin-film mineral standards. EDS enabled us to determine if amorphous material differed in composition from the host grains and determine nanoparticle composition (e.g., SMFe), as well as reveal any compositional stratigraphy within amorphous material. Electron nanodiffraction at 300 kV in the S/TEM microprobe mode with 0.3 mrad semi-angle was used to identify the Fe-rich particles at the rim. The electron beam was focused on a single particle whose relative orientation to the beam was close to a zone axis. The nano-crystalline Pt protection layer in the FIB section was used to obtain an electron diffraction pattern under identical conditions, which was used as an *in-situ* calibration.

3.2.6 Ferromagnetic Resonance

Due to the excess of metallic iron (e.g., SMFe) in mature lunar soils relative to the rocks from which they are derived (Fuller et al., 1975), the intensity of the ferromagnetic resonance signal (FMR) normalized to the total iron content (I_s/FeO) can be used as an index for soil maturity that correlates with other maturity indices (Morris, 1976). Thus, we used FMR spectra as another proxy to compare laser irradiation and kinetic impact experiments. In order to place the space weathered simulations on the I_s/FeO maturity index, three highland lunar soils were measured to properly calibrate the spectrometer response. FMR and electron paramagnetic resonance (EPR) of all samples were measured at San Francisco State University on a Varian E-12 spectrometer operating at 9.1 GHz with modulation amplitude of 5 Gauss and 50 μW of power. The microwave power level was below saturation. Approximately 2 mg of each specimen was placed in 2 mm o.d. fused silica tubes. The microwave frequency was measured with a EIS 545A frequency counter and the magnetic field was calibrated with two g-value standards, 2,2-diphenyl-1-picrylhydrazyl (DPPH) and a National Bureau of Standards single crystal ruby. The g-value approximated on the basis of these standards is ~2.1, which is similar to the g-value estimated by Morris (1976). The I_s/FeO maturity index values were calculated following the method of Morris (1976) in which the FMR intensity (I_s) is divided by the weight percent FeO in the specimen. The intensity, $I_s=(\Delta H_{pp})2A/m$, equals the product of the peak-to-peak linewidth (ΔH_{pp}) squared and signal amplitude (A) of the FMR resonance at a g-value of ~2.1. To compare I_s/FeO values of different samples, I_s is weighted by the mass of the specimen to account for different amounts of lunar soil or soil analog in each 2 mm o.d. fused silica tubes.

3.3 Results

3.3.1 Effects of AVGR Kinetic Impacts

Each of our AVGR impact experiments created glass-welded aggregates that are similar to agglutinates in size and morphology (Figure 3.1). Their sizes range from ~1 mm up to 5 cm, with the majority being less than 1 cm. These aggregates are composed of melt that cements numerous crystalline grains together. They have delicate textures with spindle-like structures and abundant vesicles, much like lunar agglutinates. However, the aggregates do not appear darker than the fresh material by visual

inspection. A direct comparison of reflectance measurements of aggregates and the powdered, bulk material is not possible. The size of the aggregates collected from the experiments is too small relative to the spot size of the spectrometer, and to crush up multiple aggregates would change the fundamental nature of their surface (Hapke et al., 1970). There is also a conspicuous absence of SMFe in the aggregates based on S/TEM analyses.

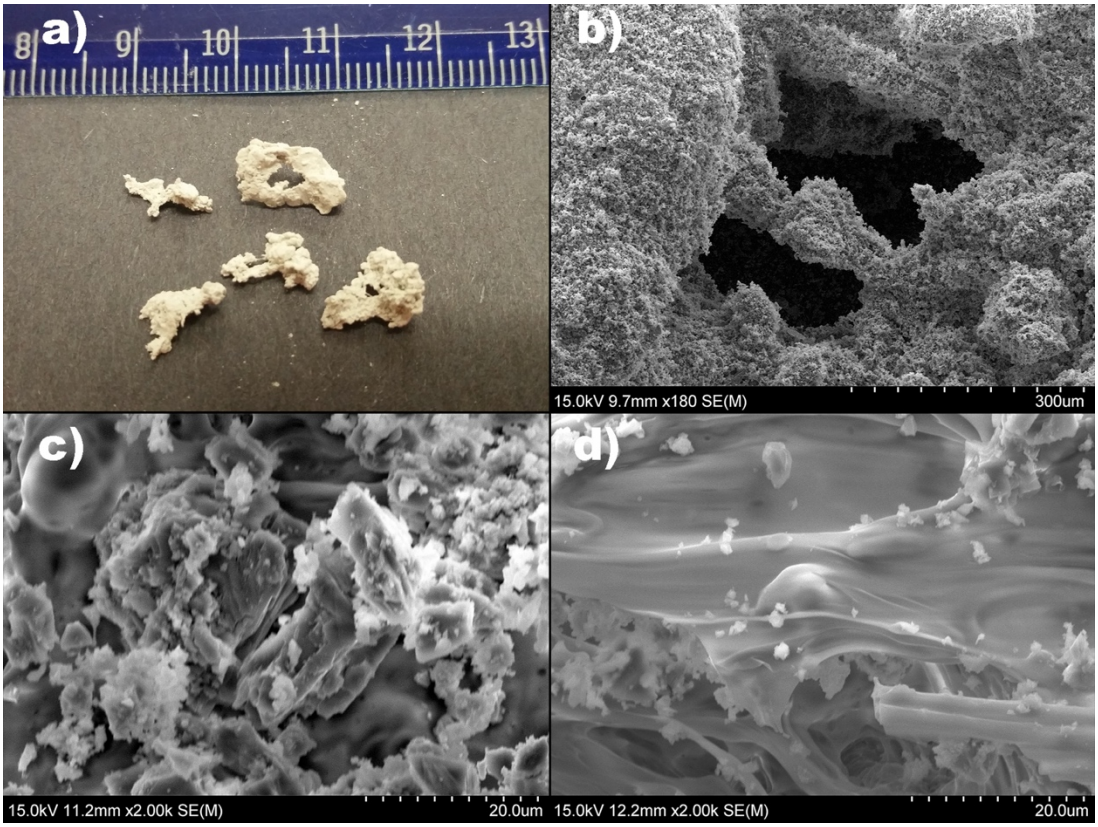

Figure 3.1 Glass-welded aggregates created in AVGR impact experiments, shown at the cm-scale using optical imaging and the μm-scale using SE imaging. (a) In optical imaging, they have delicate textures with abundant vesicles and spindle-like structures. (b) SEM imaging shows large vesicles (>100 μm across) and small grains adhered to the surface of the aggregate. The greater detail at higher magnification in (c) and (d) shows that the aggregates are cemented by melt with clasts intermixed in varying proportions. The abundance of clasts indicates how much flow and homogenization the aggregate experienced. For instance, the image in (d) with the fewest number of clasts shows flow textures similar to schlieren textures found in lunar impact glass.

S/TEM analyses of two adjacent plagioclase grains and an aggregate from the AVGR kinetic impact experiments revealed complex compositions, textures, and mineral relationships. The coupled plagioclase grains (Figure 3.2a) consist of an original, undamaged plagioclase grain with a shocked plagioclase surface that appears to have broken off from the host grain. No amorphous rim was observed on the outer surface of the shocked area. The shocked area contains inclusions that are high in Fe and Mg, likely relict crystalline mafic inclusions like those that have been observed in Stillwater plagioclase (e.g., Loferski and Arculus, 1993). The aggregate (Figure 3.2b) consists of amorphous material with elemental chemistry consistent with plagioclase stoichiometry with slightly elevated Fe, large vesicles, small rounded crystalline plagioclase that may have devitrified, larger more angular plagioclase crystals (one with lamellae), and an area of amorphous silica (SiO_2). The amorphous silica likely originated from the quartz projectile. Fragmented shards of the projectiles were small and would have melted and quenched rapidly, failing to mix with the other phases in the highlands analog. The relatively low velocity of the projectile results in less of the projectile being vaporized and more of its volume being only melted. Amorphous silica from the projectiles likely makes up a significant portion of the melt fraction in the aggregates. Both the individual plagioclase grain and the aggregate from the kinetic impact experiments lack SMFe (Figure 3.2). Elemental compositions obtained using S/TEM EDS are reported in Table 3.1. Diffraction images are available in Appendix B.

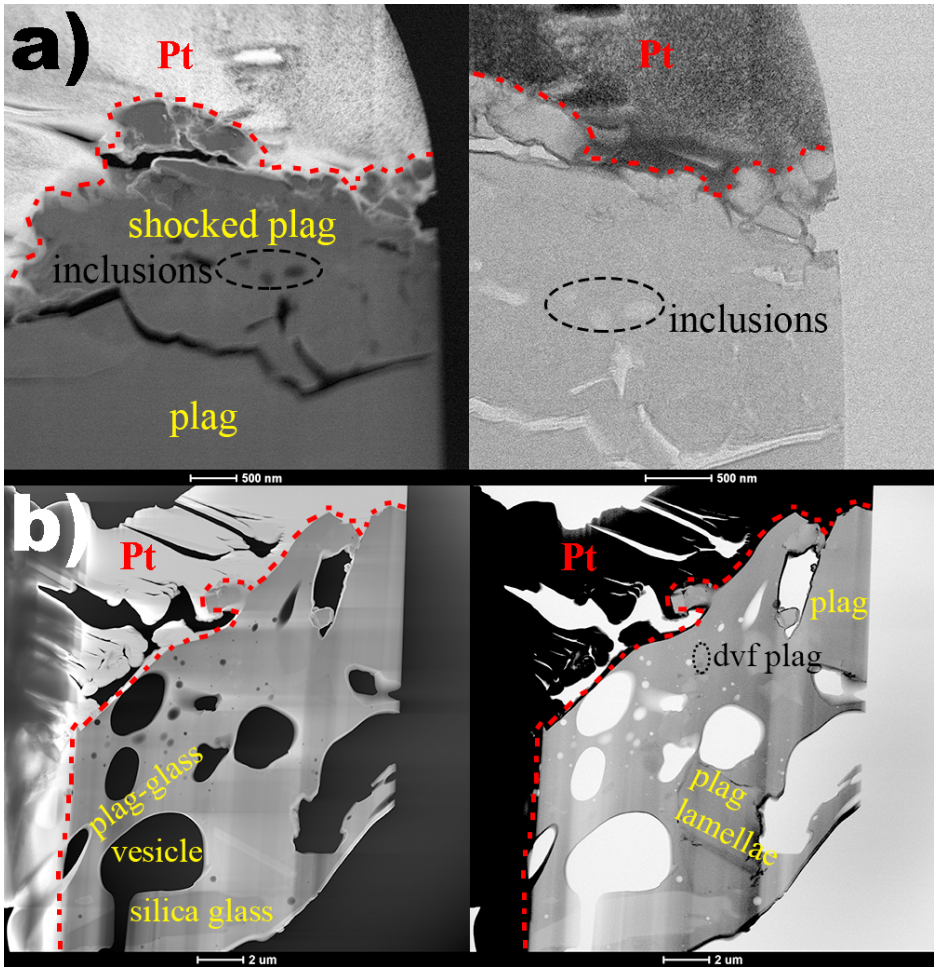

Figure 3.2 S/TEM (Left) HAADF and (Right) brightfield images of (a) adjacent plagioclase grains and (b) glass-welded aggregate from AVGR impact experiments. The adjacent plagioclase grains (a) consists of an undamaged plagioclase grain ("plag") and a shocked plagioclase surface ("shocked plag"). The shocked area contains inclusions that are high in Fe and Mg ("inclusions"). The aggregate (b) consists of amorphous plagioclase ("plag-glass") with large vesicles, small rounded crystalline plagioclase that may have devitrified ("dvf plag"), larger, more angular plagioclase crystals (one with lamellae, "plag lamellae"), and an area of amorphous silica ("silica glass"). The approximate boundary between the platinum strap (Pt) and the sample is delineated with a red dashed line. To achieve sufficient thinning at the surface, the bottom portion of the aggregate sample was overthinned in the FIB, opening vesicles in the lower left and lower right corners of the section. Scale bars equal 500 nm in (a) and 2 μm in (b).

Table 3.1 Elemental compositions (atomic %) of the plagioclase shown Figure 3.2a and glass-welded aggregate shown in Figure 3.2b, obtained from S/TEM EDS analyses. The shocked plagioclase in the grain from Figure 3.2a is elevated in Fe, due to the inclusions that are presumed to be original to the Stillwater plagioclase (e.g., Loferski and Arculus, 1993). The "plagioclase-glass" from Figure 3.2b is slightly elevated in Fe compared to the crystalline plagioclase. The "devitrified plagioclase" lacks Fe, which could be because it is the source of the additional Fe present in the glass.

atomic %	plagioclase (Fig. 3.2a)		plagioclase aggregate (Fig 3.2b)		
	plag.	shocked plag.	plag. glass	devitrified plag.	silica glass
O	62.7 ± 0.4	62.5 ± 0.4	60.7 ± 0.2	57.6 ± 0.3	67.9 ± 0.4
Si	16.1 ± 0.1	16.3 ± 0.1	17.5 ± 0.1	19.2 ± 0.1	29.2 ± 0.1
Al	14.5 ± 0.1	14.4 ± 0.1	13.8 ± 0.1	17.0 ± 0.1	0.89 ± 0.01
Ca	5.44 ± 0.01	5.08 ± 0.01	5.46 ± 0.01	6.18 ± 0.01	0.07 ± 0.01
Na	1.12 ± 0.01	1.36 ± 0.01	2.06 ± 0.01		1.98 ± 0.01
Fe	0.12 ± 0.01	0.37 ± 0.01	0.49 ± 0.01		

Reflectance spectra of the bulk target material also indicate that no detectable SMFe was produced from AVGR experiments. The material collected from the center of the target, which was impacted repeatedly by 16 shots, exhibited little-to-no lunar-like spectral changes (Figure 3.3). A slight darkening and reduction of the strength of absorption bands occurred (see Appendix B), but there was no significant spectral reddening, i.e., the reduction in albedo was similar across all wavelengths, which is a spectral signature similar to carbon and not nanophase iron. Radiative transfer modeling also supports that the material contains a negligible amount of SMFe. Furthermore, this material does not have an FMR signal and has instead an EPR signal consistent with that of the fresh lunar highlands analog, indicating that it lacks superparamagnetic material (i.e., an absence of SMFe, see Appendix B).

It is likely that there is no SMFe and that carbon is the spectrally-neutral darkening agent. The surface of the target material beyond the impact zone and the white tarp covering the floor of the chamber darkened gradually over the series of experiments.

There are two likely sources that caused the surface darkening: (1) deposition of carbon from vaporized sabot material and/or black powder used in the primary stage of the light-gas gun – This carbon component was reduced, although possibly not eliminated, by a blast suppression system. and/or (2) entrainment of carbon deposited in the chamber by previous experiments.

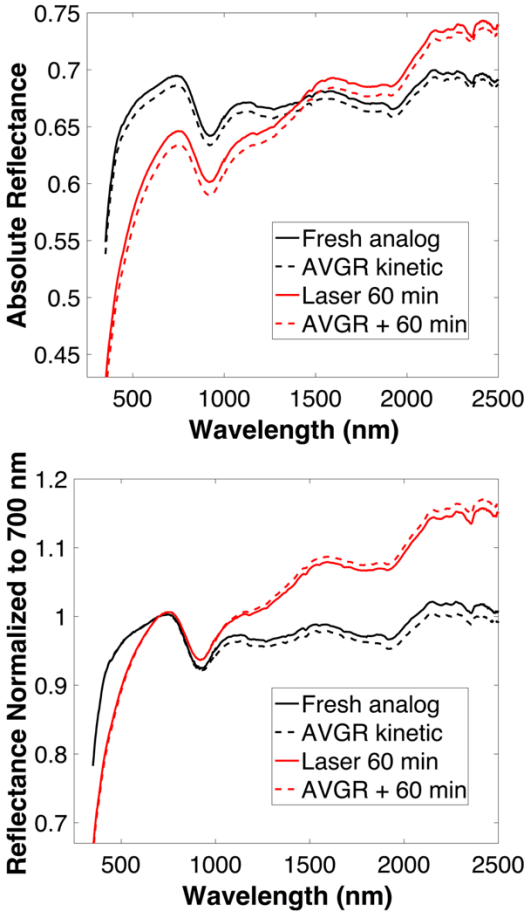

Figure 3.3 (Top) Absolute reflectance spectra and (Bottom) reflectance, normalized to 700 nm, of the lunar highlands analog weathered by 60 min pulsed laser irradiation, by kinetic impact shots at the AVGR, and by a combination of both methods (reflectance data in Appendix B).

3.3.2 Effects of Pulsed Laser Irradiation

Reflectance measurements of the laser irradiated material show darkening, reddening, and a reduction of absorption bands consistent with typical space weathering trends (Figure 3.3 & Appendix B). In the NIR, >1500 nm, these samples exhibit an

increased reflectance compared to spectra of fresh highlands simulant. A pyroxene grain from this irradiated material (Figure 3.4) has a ~225-nm thick rim that contains larger SMFe (~10 nm in diameter) concentrated in a ~60-nm thick band at the base of the rim, and smaller SMFe particles (a few nm in diameter) distributed in the upper ~125 nm of the rim. There is a narrow 40-nm layer between these two SMFe-bearing layers that is sparse in SMFe. Without examining other mafic grains, it is unknown whether this distribution of SMFe in amorphous rims is present on just this one grain or if it occurs on other grains. However, we have not observed stratigraphy like this in any of our other laser irradiated rims thus far (e.g., Gillis-Davis et al., 2017). S/TEM nanodiffraction confirmed that the SMFe is metallic Fe. The nanodiffraction pattern matches that of α-Fe (bcc) (Z=100) (Figure 3.5). The reported value for d_{011} is 2.0 Å (Jette and Foote, 1935), and the measured value for d_{011} is 2.1 Å.

The SMFe particles are the result of melt/vapor condensation from FeO-bearing silicates exposed to the laser. From the 15 or so plagioclase grains that we observed with melted surface textures, we selected two for S/TEM analyses and did not observe SMFe (Figures 3.6 and 3.7). SMFe may be present on other plagioclase grains that were not selected for S/TEM analysis. It is likely that at least some plagioclase grains have SMFe bearing rims. Based on radiative transfer modeling, the bulk material is estimated to contain 0.007 ± 0.001 wt.% nanophase iron and no microphase iron. The estimated lack of microphase iron is consistent with what we observed on the pyroxene grain, which had SMFe only up to ~10 nm in diameter – microphase iron is > 50 nm. In comparison with experimental results from Noble et al. (2007), the lunar highlands regolith has about 0.19 wt.% SMFe with an average grain size of ~15 nm. With such a low estimated nanophase iron abundance, it is not surprising that SMFe was not detected on the few plagioclase grains analyzed using TEM. Although the abundance of SMFe in the surface layer encasing the mineral grain is low based on modeling of the laser irradiated sample, an intense FMR signal indicates the presence of SMFe (see Section 3.4).

Despite the lack of observed SMFe on the laser irradiated plagioclase grains, these grains showed obvious alteration due to laser irradiation. Secondary electron (SE) image of an irradiated plagioclase grain (Figure 3.6a) revealed melt splashes on the surface. S/TEM analysis of the grain shows it possesses an amorphous rim that varies in

thickness from ~40 to 120 nm. (Figure 3.6b). A separate laser irradiated plagioclase grain is morphologically different (Figure 3.7). The entire particle appears to be composed of small mineral grains embedded in a thick layer of melt and is rather agglutinate-looking, based on the ratio of glass to mineral phases (Figure 3.7a). S/TEM analysis (Figure 3.7b) shows a plagioclase crystal encased in glass. Near the top of Figure 3.7b, a portion of the glass directly surrounds the crystal and varies in thickness from ~100—1000 nm. The bottom two-thirds of Figure 3.7b exhibits only glass. Glass comprises 76% of the cross section and plagioclase constitutes the rest. The glass contains vesicles, and MgO and FeO, while the plagioclase crystal does not (Appendix B).

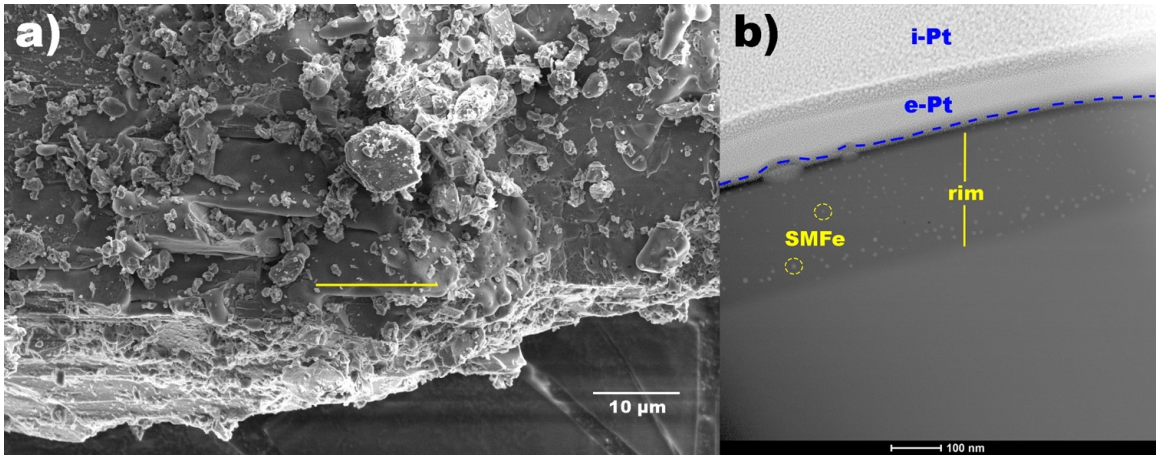

Figure 3.4 a) SE image of a pyroxene grain laser irradiated for 60 min. The yellow line indicates the approximate location of the FIB section. b) S/TEM HAADF image of the FIB section. The approximate boundary between the sample and the platinum strap (electron-beam deposited Pt (e-Pt) and ion-beam deposited Pt (i-Pt)) is delineated in a blue dashed line. The rim contains abundant SMFe (bright spots), with larger SMFe particles (~10 nm in diameter) concentrated in a narrow band at ~165 nm depth.

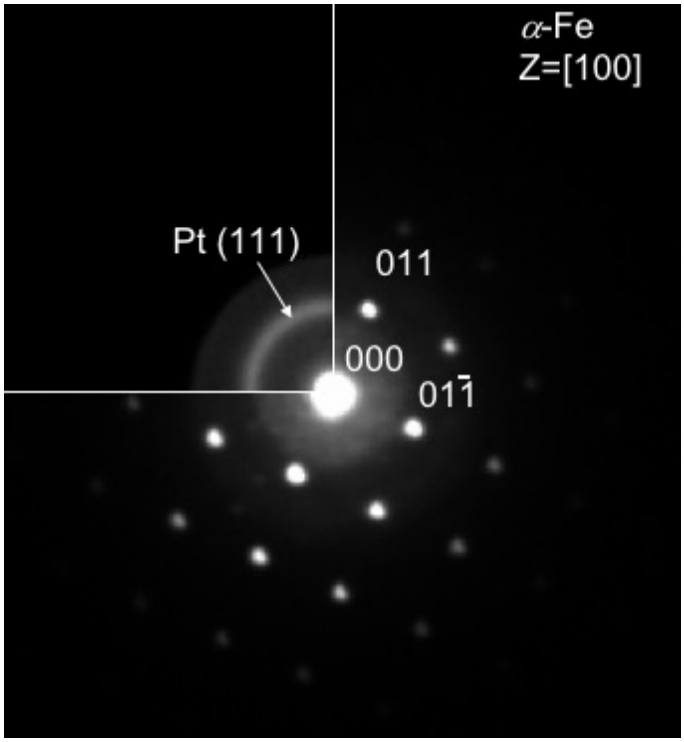

Figure 3.5 Electron nanodiffraction pattern of a SMFe particle contained in the rim of the laser irradiated pyroxene grain (Figure 3.4). The nanodiffraction pattern matches that of α-Fe (bcc) in the [100] zone axis orientation. The Pt (111) diffraction ring (upper left quadrant) from the protection layer was used for in situ diffraction camera length calibration.

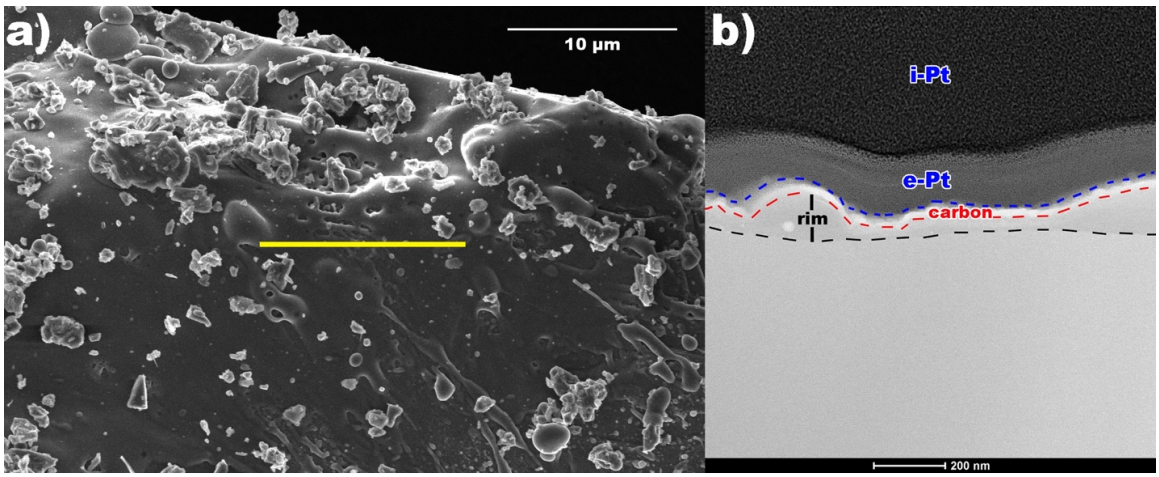

Figure 3.6 a) SE image of a plagioclase grain exposed to 60 min of laser irradiation. The yellow line indicates the approximate location of the FIB section. b) S/TEM brightfield image of the plagioclase grain. Contrast is inverted from that of the HAADF image in

Figure 3.4b. The approximate boundary between the sample and the platinum strap (electron-beam deposited Pt (e-Pt) and ion-beam deposited Pt (i-Pt)) is delineated in a blue dashed line. The boundary between the carbon-coat and the rim is delineated in red, and the boundary of the rim with the host grain is delineated in black. Unlike the irradiated pyroxene (Figure 3.4), this irradiated plagioclase lacks SMFe. The bright spot near the word "rim" (b) is a vesicle.

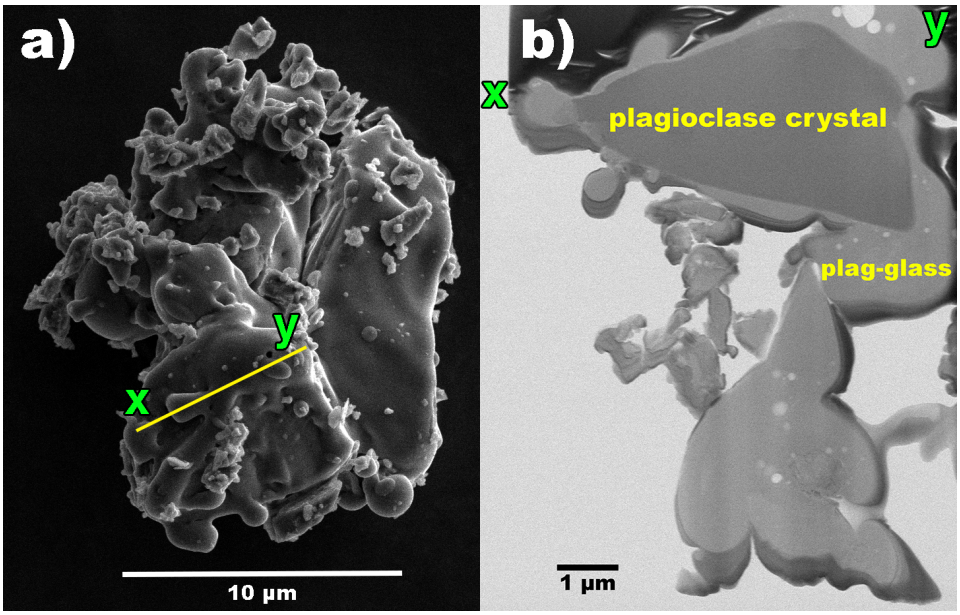

Figure 3.7 a) SE image of a plagioclase grain exposed to 60 min of laser irradiation. The yellow line indicates the approximate location of the FIB section, with x and y indicating the orientation of the section in b. b) S/TEM brightfield image of the FIB section, which contains a plagioclase crystal encased in glass ("plag-glass"). Unlike the plagioclase crystal, the glass contains Mg and Fe. However, no SMFe was detected. The dark border surrounding the entire glass particle is Pt redeposited during preparation of the FIB section.

3.3.3 Effects of Combined AVGR Impact and Laser Irradiation

In addition to irradiating the fresh regolith analog material with the laser, we irradiated some of our material that was first exposed to kinetic impact weathering using the AVGR. S/TEM imaging of a plagioclase grain (Figure 3.8) from this material showed SMFe within a rim (Figure 3.9), which was confirmed with EDS (Figure 3.10). The rim is discontinuous along the surface of the grain but contains SMFe in multiple locations.

This result is significant, because rims with SMFe were not observed on plagioclase grains that were weathered by only one method (i.e., by either laser irradiation or kinetic impacts). In comparing SMFe size and distribution between this grain and the pyroxene grain from the laser irradiated material (Figure 3.4), SMFe in this grain is more evenly distributed throughout the rim and of similar size distribution. In addition, the reflectance spectrum of this material weathered by both methods is darker than the spectrum of the material that was only laser irradiated (Figure 3.3 & Appendix B). Based on radiative transfer modeling, the bulk material contains no microphase iron and 0.008 wt.% nanophase iron (0.001 wt.% or 1.14 times more than the sample exposed to only laser irradiation, which is less than the RMS). Furthermore, like the laser irradiated sample, the bulk material that was subjected to both laser irradiation and kinetic impacts exhibits an FMR signal that indicates the presence of SMFe (see section 3.4).

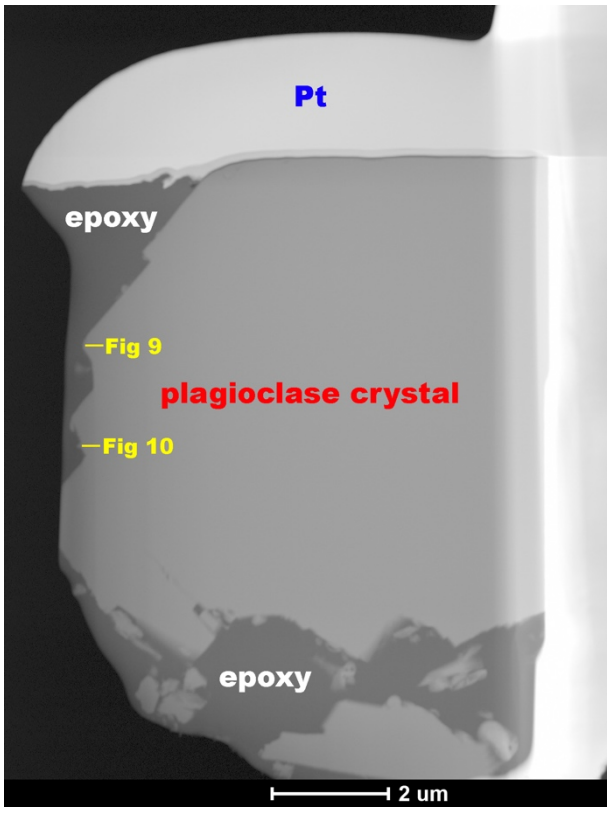

Figure 3.8 S/TEM HAADF image showing the entire FIB section of the plagioclase grain from AVGR kinetic impacts that was subsequently irradiated for 60 min with pulsed laser irradiation. This sample was mounted in epoxy (dark gray) prior to FIB

preparation. The approximate locations for the images of the rim shown in Figures 3.9 & 3.10 are indicated.

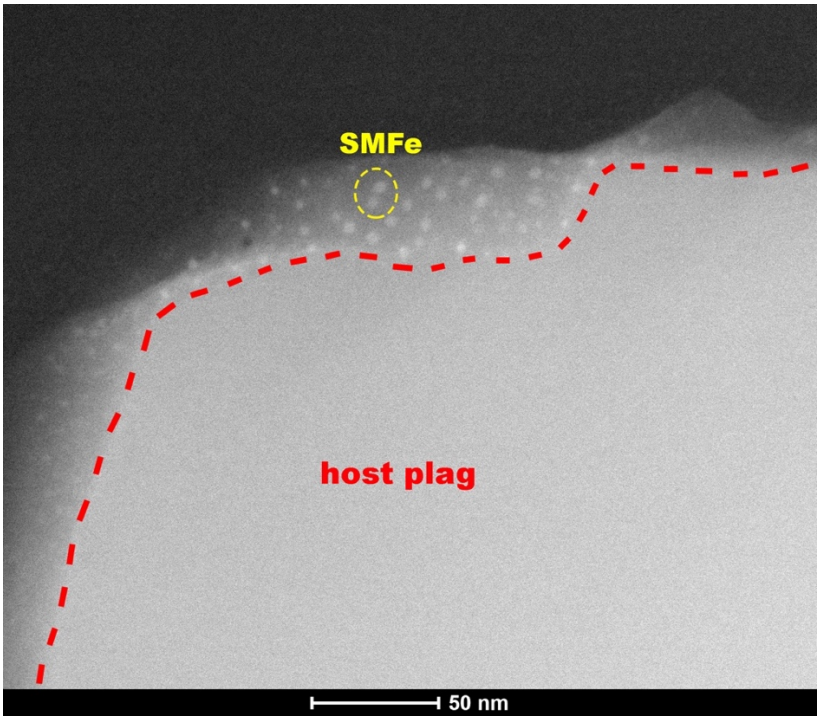

Figure 3.9 S/TEM HAADF image of a plagioclase grain from AVGR kinetic impacts that was subsequently irradiated for 60 min with pulsed laser irradiation. The approximate boundary between the host plagioclase and the rim is delineated in a red dashed line. Bright spots in the rim are SMFe, confirmed with EDS (see Figure 3.10).

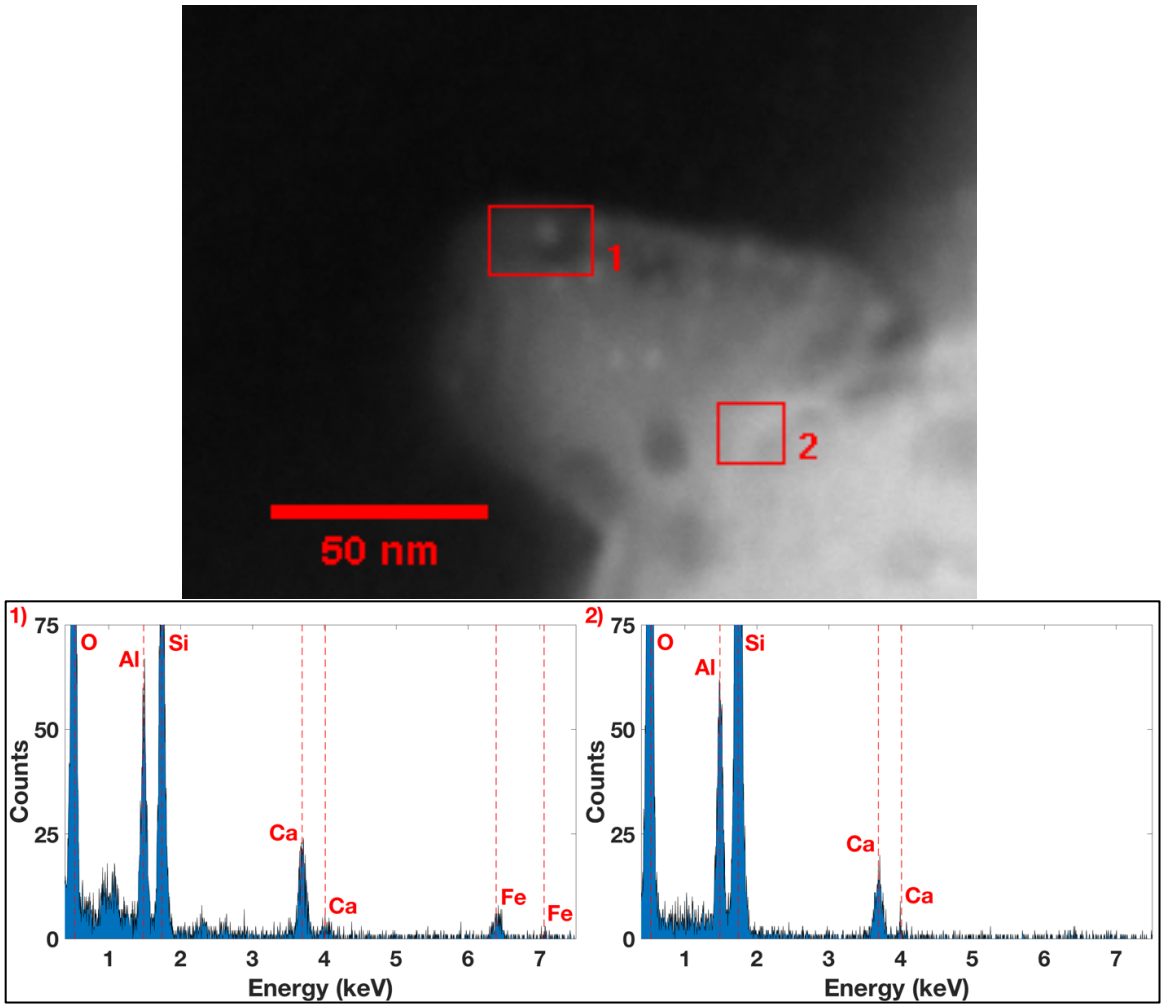

Figure 3.10 S/TEM HAADF image and EDS spectra of a plagioclase grain from AVGR kinetic impacts that was subsequently irradiated for 60 min with pulsed laser irradiation. (1) EDS confirms that bright spots in the discontinuous rim are SMFe. (2) For comparison, an EDS spectrum from an area near the rim without SMFe shows no Fe X-ray signal. Dark spots are electron radiation damage to the sample from prolonged electron imaging.

3.3.4 Ferromagnetic Resonance Spectroscopy

Figure 3.11 compares the FMR spectra acquired from three highland lunar soils to the space weathered lunar soil analogs. The FMR spectra from the mature (64421), submature (61501), and immature (67511) soils are similar in lineshape but vary in amplitude and linewidth. Consequently, the intensity varies due to the different abundance of SMFe in the highland soils. The calculated I_s/FeO values are close to those

published by Morris (1976) when plotted against the weight % FeO, Figure 3.11b. As shown in Figures 3.4b, 3.5, and 3.9, nanophase Fe particles were observed by S/TEM after the highland analog material was weathered by laser irradiation and laser irradiation plus kinetic impacts at AVGR. The FMR spectra of these laboratory weathered analogs are also shown in Figure 3.11a and are similar in lineshape to the spectra of the highland lunar soils. The FMR peak-to-peak linewidths (ΔH_{pp}) of the analogs are 51.9 mT and 54.1 mT for the laser irradiated and irradiated plus AVGR impacted samples, respectively, which are slightly less than the ΔH_{pp} of the lunar soils (55.4, 56.4, 55.2 mT for highland soils 67511, 61501, and 64421, respectively). A reasonable estimate of the FeO wt% is 5.0 for the highland analog material. The mass-weighted intensity I_s of the laser irradiated and irradiated plus AVGR impacted samples are less than the highlands soils by factors of 28, 20, and 2.4 for the mature, submature, and immature soils, respectively. Consequently, we determine that the I_s/FeO exposure index equals 2.9 and 3.1 for the laser irradiated and irradiated plus AVGR impacted samples, respectively (Figure 3.11b). The material weathered only by AVGR kinetic impacts does not have an FMR signal and instead has an EPR signal consistent with that of the fresh lunar highlands analog (Appendix B), indicating that it lacks superparamagnetic material (i.e., there is an absence of SMFe).

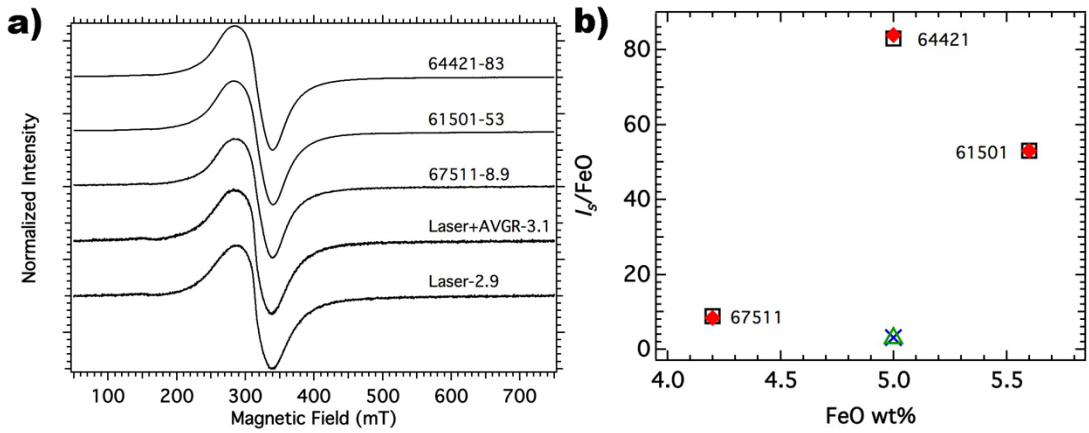

Figure 3.11 a) Normalized FMR spectra of highland soils and laboratory weathered highland soil analogs. The I_s/FeO values are indicated after the sample name. b) Soil maturity index I_s/FeO vs wt% FeO for the lunar soils and weathered soil analogs; black open squares and red diamonds are the I_s/FeO values determined by Morris and in this

study, respectively. The green triangle and black 'X' are the I_s/FeO values for the laser irradiated and irradiated plus AVGR, respectively.

3.4 Discussion

3.4.1 AVGR Kinetic Impacts

The AVGR kinetic impact experiments are capable of producing agglutinate-like particles that are unlike anything produced with pulsed laser irradiation and much like lunar agglutinates. These aggregates (Figures 3.1 & 3.2) are composed of melt that cements numerous crystalline grains together. They have delicate textures with spindle-like structures and abundant vesicles. Samples from the kinetic impact experiments also show evidence of shock effects, both as the mechanical breaking of the surface of grains (Figure 3.2a) and as shock defects in individual crystals.

Unlike lunar agglutinates, however, the aggregates do not appear darker than the fresh material, and they lack SMFe, which is an important effect of space weathering. While AVGR impact experiments have demonstrated the creation of melt/vapor deposits (Schultz and Eberhardy, 2015) and vaporization of iron (Adams et al., 1997), no SMFe was observed with S/TEM analysis, no typical space weathering spectral trend was observed in the reflectance measurements (Figure 3.3), no SMFe is expected based on radiative transfer modeling, and no superparamagnetic material was detected using FMR. The AVGR sample has an EPR signal similar to that of the fresh lunar highlands analog, indicating that it lacks superparamagnetic material (i.e., there is an absence of SMFe).

The absence of SMFe in the AVGR produced aggregates should not be interpreted to support or preclude the need for solar-wind implanted H, as the laser irradiated samples contain SMFe. An alternate explanation may be that either too little of the vapor phase is produced, which is necessary for SMFe formation, or too little of the vapor phase is captured. Due to the rapid melting and quenching of the quartz projectiles, as demonstrated by the amorphous silica in the aggregate, the iron-bearing phases in the highlands analog may not have readily vaporized. Making dark aggregates with a different target composition has been demonstrated. Bruck Syal et al. (2015) produced darkened aggregates using organic materials, with a lower vaporization temperature than iron, and proposed that this process is responsible for the low reflectance of Mercury. However, the darkening agent in these aggregates is carbon and not SMFe.

Vaporization of target material is necessary to separate iron-bearing silicate (e.g., Fe^{2+} in Fe_2SiO_4 and $FeSiO_3$) into Fe metal in impacts (Hapke, 2001). The impact velocity at AVGR (~6 km/s) is considerably lower than micrometeoroid impact velocities into the lunar surface (~16 km/s). Hence, much less energy is partitioned into vaporization at lower velocities (Hörz and Cintala, 1997; Cintala and Grieve, 1998), which translates to minor amounts of vapor produced. The impact speeds that the AVGR is capable of are not sufficient to produce large amounts of vapor from impacts that use silicates. Although vapor has been observed in previous work (Adams et al., 1997; Bruck Syal and Schultz, 2014; Schultz and Eberhardy, 2015), it expands at high speeds and is not trapped within the craters (for vertical impacts) where our samples were collected. Any vapor that is produced gets distributed over a large volume in the vacuum tank, which translates to low retention of vapor deposits. Together, the minor amount of vapor produced, coupled with low vapor preservation probability, likely results in negligible formation and retention of SMFe-containing vapor deposits on the target material.

3.4.2 Pulsed Laser Irradiation

Reflectance measurements of the laser irradiated material show darkening, reddening, and a reduction of the strength of absorption bands consistent with typical space weathering trends (e.g., Figure 3.3). Preferential light absorption at shorter wavelengths due to the presence of SMFe is a reasonable explanation for the decreased reflectance and reddening between 350 and 1500 nm that we observe in the reflectance spectrum. These results are consistent with spectral changes of previous experiments that laser irradiated olivine and pyroxene (e.g., Yamada et al., 1999). Modeling of the spectrum indicates that the bulk material contains 0.007 wt.% nanophase iron. Although we did not confirm the presence of SMFe on our plagioclase grains, SMFe was detected on pyroxene (Figure 3.4) and the bulk material has an FMR signal that indicates the presence of superparamagnetic material (Figure 3.11). Moroz et al. (2014) found that spectral changes of laser irradiated plagioclase in the visible portion of the spectrum were likely caused by SMFe, even though they did not detect SMFe in their samples with TEM. Their samples have an increase in NIR reflectance that they attribute to laser-induced textural changes. Our laser and laser+AVGR samples also have increased NIR reflectance at wavelengths greater than ~1500 nm, which may also be due to textural

changes. Although we cannot directly compare our measurements with Moroz et al. (2014) due to the fact that they used pure plagioclase powder in pressed pellets, the outcomes of the reflectance measurements in the NIR region are nevertheless similar. Furthermore, the grain in Figure 3.7 is composed of original plagioclase crystals encased in quenched melt, which is different from an individual plagioclase grain with an amorphous rim (e.g., Figure 3.6) and indicates that textural changes do occur with laser irradiation of this material. Using SEM, we saw that these glass-encrusted grains, which have a melted, agglutinate-looking surface, were not uncommon in the bulk material. All of the glass-encrusted grains that we examined had a plagioclase composition (i.e., we did not find any pyroxene or olivine grains with these melted, agglutinate-looking surfaces). This is notably different from the finding of Noble et al. (2011) that pyroxene showed signs of significant melting while plagioclase did not. Nonetheless, these extremely melted grains differ from the glass-welded aggregates created in the AVGR kinetic impact experiments. They are much smaller, do not contain abundant vesicles, and do not have the same delicate spindle-like textures of the aggregates.

3.4.3 Combined AVGR Kinetic Impact and Laser Irradiation

SMFe in a rim on a plagioclase grain was found in material weathered using the combined methods of AVGR kinetic impacts and laser irradiation. This finding is significant, because rims with SMFe were not observed on plagioclase grains that were weathered by only one method (i.e., by either laser irradiation or kinetic impacts). It might be reasoned that detection of SMFe in this sample or the non-identification of SMFe in the kinetic impact and laser only sample is the result of limited sampling; however, modeling and analytical measurements offer independent evidence to support the conclusion that the impact and laser samples contain more SMFe. First, the reflectance spectrum of the material weathered by both methods is darker and redder than the spectrum of the material that was only laser irradiated (Figure 3.3). Radiative transfer modeling indicates the material contains slightly more nanophase iron than the sample that had only been exposed to laser irradiation. Second, the FMR peak-to-peak linewidth (ΔH_{pp}) of the laser irradiated plus AVGR impacted sample is most similar to highlands soils, and the I_s/FeO exposure index is slightly higher for the laser irradiated plus AVGR

impacted sample relative to the laser only (Figure 3.11). In contrast, the material that was weathered only with the AVGR impacts lacks an FMR signal.

A hypothesis that is consistent with the observations, the modeling, and the measurements is that easier melting of the glassy agglutinate-like aggregates in relation to minerals contained in the AVGR sample allowed faster spectral changes and SMFe production by subsequent laser irradiation. This effect would be due to the lower melting/vaporization temperature of the glass relative to minerals, which allowed Fe to be extracted from the glass more easily than from a crystal structure. Furthermore, the glass in the aggregates is elevated in Fe relative to plagioclase (Table 3.1), accelerating the creation of SMFe-bearing rims. This is consistent with the hypothesis of Moroz et al. (2014) that the differences in responses of different materials to laser irradiation, which has been shown by previous work (Yamada et al., 1999), are likely caused by their differences in electrical conductivities, wavelength of mineral absorption, and melting points.

3.4.4 Ferromagnetic Resonance Spectroscopy

Although previous work by Kurahashi et al. (2002), Sasaki et al. (2003), and Bentley et al. 2009 confirmed the presence of nanophase iron by FMR spectroscopy, the present study is the first to report FMR spectra resulting from laser irradiation and irradiation plus kinetic impacts and place the results on the maturity index (Figure 3.11b). The ability to place experimentally weathered samples on the I_s/FeO maturity index was attained by measuring the FMR spectra of three highland soils (Figure 3.11a) that span nearly the full range of magnetic intensity (i.e., maturity). The calculated I_s/FeO values are almost identical to those published by Morris (1976) when plotted against the weight % FeO (Figure 3.11b). The soil maturity index I_s/FeO is the ratio of the FMR intensity to the weight percent FeO. Using an average I_s/FeO value of 3.0 for the laser irradiated and irradiated plus AVGR impacted analogs, the mass-weighted intensity I_s of the analogs are less than the highland soils by factors of 28, 20, and 2.4 for the mature, submature, and immature soils, respectively. Since the FMR intensity is calculated from I_s=(ΔH_{pp})2A and the linewidths of the soil analogs are similar to those of the highland lunar soils, the low amplitude of the analogs is responsible for the low I_s/FeO values. The amplitude of the FMR signal is related to the amount of SMFe in the specimen, which is clearly less for

the soil analogs. We conclude that nanosecond pulsed laser irradiation of soil analog materials does not fully capture the effects of space weathering. It is clear from TEM observations that nanophase iron particles are present in amorphous rims and yield FMR signals similar in lineshape to those of lunar soils. However, the abundance of SMFe measured by I_s is less than would be expected based solely on the loss of spectral contrast in reflectance spectra. Taylor et al. (2010) found a correlation between lunar soil size fraction, agglutinate abundance, and I_s/FeO value. The smallest size fraction, < 10 μm, had more agglutinates and larger I_s/FeO values than the < 250 μm fraction used in FMR measurements (Morris, 1978). Our laser weathering experiments as currently implemented do not produce agglutinates that contain proportionally greater amounts of SMFe as are found in lunar soils. Thus, alternative methods of producing impact melt glass using laser irradiation need to be investigated with respect to their ability to produce agglutinate-like materials that contain SMFe.

3.5 Conclusions

Although the AVGR is useful for studying crater formation and morphology, and for creating agglutinate-like aggregates, the kinetic impact experiments with our experimental setup are not suitable simulations to study lunar-like space weathering spectral changes and FMR signal. Due to its relatively low impact velocity, the AVGR likely produces a relatively small volume of vapor, which is necessary for SMFe formation, and any vapor that is produced is not retained on the sample surface. However, the AVGR is a better proxy for space weathering on asteroids, where the impact speeds are comparable. Our results suggest that lower impact velocities cause less efficient space weathering on asteroids.

In contrast, laser irradiation is best suited for studying a broad range of space weathering effects. In our experiments, the highlands analog became darker, redder, and lost spectral contrast due to laser irradiation but did not get as dark or as red as mature lunar highlands. In addition, the amorphous rims, SMFe, and melt deposits encasing grains (Figures 3.4, 3.6 & 3.7) are similar to those found on lunar soil grains. As a consequence of the higher vapor to melt ratio, however, no agglutinates are produced. The absence of agglutinates is a current weakness in the ability of laser irradiation to simulate lunar space weathering, as agglutinates comprise ~60% of mature lunar regolith

(McKay and Basu, 1983) and are the major carrier of much of the SMFe in a lunar soil (Taylor et al., 2001). In addition, once the transition from mineral to iron-bearing glass is made, additional exposure to the space weathering environment may help expedite SMFe formation. Experiments are needed to investigate whether different compositions, grain sizes, laser powers, etc. are capable of producing lunar-like agglutinates that yield more lunar-like spectral and magnetic properties.

The method's current inability to produce agglutinates and shock effects, however, has possibilities for asteroidal applications. For instance, while agglutinitic glasses dominate lunar soils, they are virtually absent in gas-rich brecciated meteorites (Hörz and Schaal, 1981; McKay et al., 1989) and the Itokawa return samples (Tsuchiyama et al., 2011; Tuschiyama, 2014). This result is thought to be a function of the lower average impact velocities in the asteroid belt and possible poor retention during the impact process because of the object's low escape velocity (Housen et al., 1983). In addition, owing to the lower impact speed, all asteroidal ejecta will be substantially less shocked (Hörz and Cintala 1997), and therefore shock effects would be less critical to reproduce. Hence, laser space weathering using current parameters would possibly be more directly comparable to asteroidal space weathering and studying weathering effects related to amorphous rims on airless bodies.

Laser irradiation of our material impact-weathered at the AVGR, enhances the darkening produced by solely laser weathering. We infer that because the material that had been weathered at the AVGR contains the agglutinate-like aggregates, the spectrum was altered more rapidly with the subsequent laser irradiation due to the lower melting/vaporization temperature of glass relative to minerals, which allowed Fe to be extracted from the glass more readily than from crystal, and to the higher Fe content in the glass compared to the plagioclase. This hypothesis suggests agglutinates are a critical component for replicating lunar space weathering in the laboratory. Furthermore, a rim containing SMFe was observed on a plagioclase grain weathered using the combined methods, but not on plagioclase weathered by only one method, further indicating that a combination of the two methods best simulates lunar-like space weathering.

CHAPTER 4

TEMPERATURE-DEPENDENT EFFECTS OF SPACE WEATHERING OBSERVED USING LASER IRRADIATION SIMULATIONS

In preparation for publication as: Corley, L. M., Gillis-Davis, J. J., Trang. D., Lucey, P. G., Ohtaki, K., Ishii, H. A. (2019), Temperature-dependent effects of space weathering observed using laser irradiation simulations.

Abstract – Space weathering significantly changes the visible to near-infrared optical properties of airless planetary bodies, resulting in decreased reflectance, spectral reddening, and subdued absorption bands. These optical changes are caused by the presence of submicroscopic iron (SMFe) in agglutinates and amorphous rims, which is observed in lunar soils returned by the Apollo and Luna missions. Micrometeoroid impacts and solar wind irradiation are key processes that produce SMFe. The Lunar Orbiter Laser Altimeter (LOLA) onboard the Lunar Reconnaissance Orbiter may detect relative amounts of space weather through its albedo measurements. LOLA measured a trend of increased albedo at 1064 nm with decreasing surface temperature and a spike in 1064-nm albedo in permanently shadowed regions (PSRs). Although the LOLA albedo increase could be due to the presence of ice, the increased reflectance is also consistent with diminished space weathering. It is currently unknown how surface temperature influences the production of SMFe and the resulting spectral effects. The low surface temperatures of polar regions and PSRs (as low as 50K) may affect the volume of impact melt/vaporization produced and the subsequent development of SMFe. To test this hypothesis, we compare visible to near-infrared (VNIR) reflectance spectra of materials irradiated with a pulsed laser at low temperature and at room temperature. Scanning Transmission Electron Microscopy (S/TEM) analyses of our samples suggest that the space weathering at low temperatures produces thinner amorphous rims and less SMFe. We found that olivine and pyroxene irradiated at 85 K has a higher reflectance and exhibits less reddening than the samples irradiated at 295 K. Irradiation of a lunar highlands analog at 85 K results in slightly reduced reddening but does not yield a

statistically significant increased reflectance with lower temperature. Based on radiative transfer modeling estimates, the olivine and pyroxene irradiated at 85 K contains 64–85% the abundance of SMFe of the samples irradiated at 295 K. The 5% and 6% greater measured reflectance at 1064 nm for the 85 K samples of olivine and pyroxene, respectively, compared to their room-temperature counterparts is consistent with the observed anticorrelation trend between surface temperature and LOLA albedo. Thus, reduced space weathering caused by low temperatures may contribute to the trend of increased albedo with decreasing temperature measured by LOLA, as well as latitudinal trends in ultraviolet to near-infrared data that have previously been attributed to lower solar wind flux at higher latitudes. Our results help to quantify the effects of surface temperature on space weathering, which may need to be considered when interpreting spectral measurements at different latitudes and different planetary bodies.

4.1 Introduction

Craters in the lunar polar regions have areas that are permanently shaded from the Sun due to the small tilt of the lunar rotation axis with respect to the ecliptic, allowing them to reach very low temperatures (Urey, 1952; Watson et al., 1961; Vasavada, 1999). The Diviner Lunar Radiometer Experiment measured temperatures as low as ~20 K in some of the shadowed regions (Paige et al., 2010). These extremely cold, permanently shadowed regions (PSRs) could act as cold traps for volatiles in the lunar environment (Watson et al., 1961). The PSRs may be reservoirs for water ice that originated from comets or wet asteroids, or was produced by chemical interaction with hydrogen from solar wind (Arnold, 1979; Housley et al., 1973). Volatiles have been detected using radar and orbital neutron spectroscopy (Nozette et al., 1996; Fledman et al., 2000; Mitrofanov et al., 2010). In addition, volatiles were detected when the Centaur rocket struck the shadowed Cabeus crater, with spectroscopic measurements by the Lunar Crater Observation and Sensing Satellite (LCROSS) and the Lyman Alpha Mapping Project (LAMP) (Colaprete et al., 2010; Gladstone et al., 2010). Diagnostic near-infrared (NIR) absorption features of water ice in spectra acquired from the Moon Mineralogy Mapper (M^3) indicate that ~3.5% of cold traps exhibit ice exposures and some ice-bearing pixels may contain ~30 wt.% water ice intimately mixed with dry regolith (Li et al., 2018). In addition, water ice is hypothesized to contribute to the higher normal albedo at 1,064 nm

measured by the Lunar Orbiter Laser Altimeter (LOLA) onboard the Lunar Reconnaissance Orbiter (LRO) in PSRs. However, diminished space weathering could also contribute to higher LOLA albedo, because a lack of space weathering causes regolith to be more reflective compared to more mature regolith.

Zuber et al. (2012) found that permanently shadowed Shackleton crater has a higher LOLA albedo than the surrounding terrain and the interiors of nearby craters. They suggested that the albedo anomaly is caused either by less intense space weathering due to shadowing or due to a layer of ~20% surficial ice that is about one micrometer-thick. Lucey et al. (2014b) analyzed the global normal albedo from LOLA and found that regions within permanent shadow in the polar regions are more reflective than polar surfaces that are sometimes illuminated ("non-PSRs"). They also suggest that this is due to water frost or a reduction in the effectiveness of space weathering. Lucey et al. (2014b) showed that PSRs are consistently brighter than non-PSRs when sky view is held constant, which suggests that differences in the intensity of space weathering sources (solar wind or micrometeoroids) imposed by sky access are not responsible for the albedo difference between PSRs and non-PSRs. Fisher et al. (2017) found a general trend of increasing LOLA reflectance with decreasing maximum temperature present throughout both the north and south polar regions, which they attribute to a temperature or illumination-dependent space weathering effect.

Trends have also been recognized in the UV-NIR that are consistent with a temperature-dependence on space weathering, yet they have been attributed to diminished flux of the solar wind. High latitudes (>75°) have lower continuum slopes than lower latitudes, consistent with diminished space weathering (Yokota et al., 2011). In addition, large-scale latitudinal variations in the far-UV slope imply a gradient in space weathering, presumed to occur because low latitudes experience more weathering by the solar wind (Hendrix et al., 2012). Hemingway et al. (2015) identified a latitudinal variation in the spectral properties of the maria using Clementine mosaics that are similar to those of lunar swirls, where magnetic fields locally affect the solar wind flux but not micrometeoroid bombardment. Based on the assumption that solar wind flux is reduced at higher latitudes, like it is at lunar swirls, Hemingway et al. (2015) conclude that reduced solar wind flux is responsible for the latitudinal variation in spectral properties.

However, the LOLA measurements discussed above are also consistent with a temperature-dependent space weathering effect, making this an area of research that can benefit from space weathering simulations such as ours.

Low surface temperatures of the lunar polar regions and the extremely low temperatures of permanently shadowed regions (PSRs) (as low as 25 K; Paige et al., 2010) may affect the space weathering process. The volume of melt and vapor produced and the subsequent development of SMFe may be diminished at low temperatures (Cintala, 1992). To test for temperature-dependent effects of space weathering, we compare materials weathered by pulsed laser irradiation at low temperature (85 K) with the same materials laser irradiated at room temperature (295 K). Several bases for comparison were used in this study, including: VNIR spectral reflectance measurements, radiative transfer modeling, and S/TEM analyses. We investigate if laser irradiation at low temperature results in different spectral changes compared to irradiation at higher temperature and if low temperature affects the production and/or character of amorphous rims and SMFe. If surface temperatures do influence space weathering processes, reduced space weathering would be expected to occur even at equatorial regions during the nighttime, where temperatures fall below 100 K (Vasavada et al., 2012). In addition, reduced space weathering would affect the poles of Mercury, where PSRs are as cold as 50 K (Paige et al., 2013).

4.2 Methods

4.2.1 Target Material

To simulate the lunar regolith, we selected material to be irradiated based on lunar-like composition and grain size. We created a lunar highlands regolith analog, which is a mixture of 85% plagioclase (An_{80}) provided by the Stillwater Mining Company, 10% orthopyroxene ($Wo_1En_{69}Fs_{30}$), and 5% San Carlos olivine (Fo_{90}). This mixture was modeled after Apollo sample 68415, which is representative of the bulk composition of the Ferroan Highlands Terrain based on orbital and lunar sample data (meteorite and Apollo 16 sample: Korotev et al., 2003; Gillis et al., 2004). We also irradiated olivine and orthopyroxene individually, because it allows us to observe how the individual minerals respond to space weathering. In addition, the olivine and pyroxene compositions are consistent with those found in the maria and are typically

used in space weathering simulations, which allows for comparison of our results with other studies. Mafic minerals are used in space weathering experiments, because their higher iron content causes them to weather readily, producing SMFe and spectral changes quickly. Before irradiation, the fresh minerals were analyzed quantitatively with Electron Probe Microanalysis (EPMA) using the JEOL Hyperprobe JXA-8500F and with InXitu Inc. X-ray diffraction / X-ray fluorescence (XRD/XRF) at the University of Hawai‘i at Mānoa. The rocks were pulverized and dry-sieved to a grain size of <75 μm by Activation Laboratories Ltd. This grain size was selected, because the mean grain size of returned and analyzed lunar soils averages between 60 and 80 μm (McKay et al., 1991). Our maximum grain size (75 μm) is larger than the optically active size fraction of the Moon, which is 10–20 μm (Pieters et al., 1993); however, our samples do contain grains in the 10–20 μm size region.

4.2.2 Laser irradiation

Samples were placed in a thermally controlled vacuum chamber that can be cooled to liquid nitrogen temperatures at the University of Hawai‘i at Mānoa. The chamber is the same used by Hinrichs and Lucey (2002) but we modified the lid, such that it has a window allowing for the laser to irradiate the sample with an incidence angle of 0°. Samples were held by a Teflon funnel in an aluminum cup and placed on the brass cold-plate. Aluminum was selected as the sample holder to avoid the possibility of extra SMFe being produced if an iron-bearing cup were to be hit by the laser. The Teflon funnel helps to keep the material inside the sample cup as the laser stirs the material, which allows the sample to be homogeneously space weathered. Experiments were performed at 295 K and 85 K, all under vacuum pressure of ~10^{-6} mbar. To achieve temperatures of 85 K, liquid nitrogen, which has a minimum temperature of 77 K, was used. The radiation environment inside the chamber, including an inner radiation shield that acts as a black body and a liquid nitrogen radiator that faces the surface of the sample, helps to keep the sample cold. A thermocouple on the cold-plate measured the temperature during the experiments. High-velocity micrometeoroid impacts were simulated with a pulsed 1064-nm Continuum Surelite Nd:YAG laser. The laser pulse frequency is 20 Hz, and the pulse length is 5–7 nsec. The laser imparts 10^{10} W/cm^2 of energy into the sample using a pulse energy of 30 mJ. This pulse duration is comparable

to the timescale of real micrometeoroid impacts on the Moon, and this energy regime is where evaporation and ion formation is expected (Kissel and Krueger, 1987; Yamada et al., 1999). The laser spot size on the sample is ~0.25 mm. The beam was rastered across 0.5 g of the sample. The olivine and pyroxene were irradiated for a total of 60 minutes. During irradiation of the lunar highlands analog, too much material was dispersed outside of the sample holder and funnel, which restricted the total irradiation time of this sample to 40 minutes.

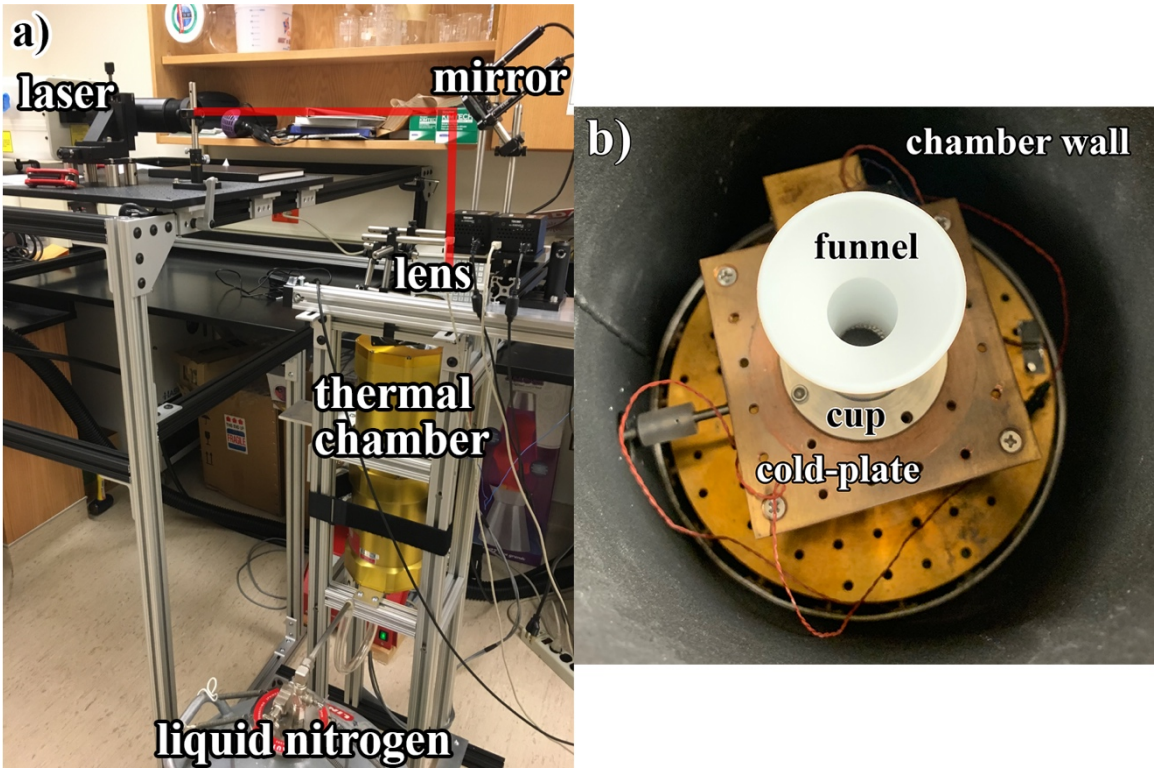

Figure 4.1 Experimental setup for laser irradiation. a) Samples were placed in a thermally controlled vacuum chamber that can be cooled to liquid nitrogen temperatures. The laser was reflected off of a mirror and down to a lens that focuses it to a spot size of ~0.25 mm on the sample. The chamber has a window that allows for the laser to irradiate the sample with an incidence angle of 0°. b) Samples were held by a Teflon funnel in an aluminum cup and placed on the brass cold-plate. There is an additional radiation shield (not pictured) that sits over the sample cup and funnel.

4.2.3 Reflectance Measurements and Radiative Transfer Modeling

Reflectance measurements were obtained with a FieldSpec 4 Spectrometer (Analytical Spectral Devices Inc.), which measures reflectance from ultraviolet to near-infrared wavelengths (0.35–2.5 μm). The full-width-half-max spectral resolution is 3 nm for the 0.35–1.0μm portion of the spectrum and 10 nm for the 1.0–2.5μm portion. Spectra were acquired outside of the vacuum chamber at 295 K, with a 30° incidence angle and 0° emission angle. Reflectance was measured relative to a 99% reflectance Spectralon standard (LabSphere). In order to determine the error in spectral measurements, reflectance standards that encapsulate the minimum and maximum reflectance of our samples were measured. Depending on the sample, 20%, 40%, 60%, and 80% reflectance standards were measured immediately before and after the reflectance measurements of our samples were acquired. The standard deviation of our reflectance measurements is typically ~0.5%.

Using a radiative transfer model (e.g., Hapke, 1993) modified to model spectral effects due to space weathering (Hapke, 2001; Lucey and Riner, 2011; Trang et al., 2017; Trang and Lucey, 2019), we estimated the abundance of microphase iron (>40 nm in diameter) and nanophase iron (<40 nm). We compared our measured reflectance spectra with model spectra from material with the same composition as the fresh material plus varying abundances of microphase and nanophase iron. The best spectral match was chosen using the criterion of the lowest root-mean-square (RMS) difference between a given model spectrum and a sample's measured spectrum. Radiative transfer modeling allows us to estimate the SMFe abundances of the bulk material, whereas we can only analyze a few grains with S/TEM. Hence, we compare SMFe abundances from the two techniques, as they provide independent measurements of the sample quantity but at different scales.

4.2.4 Scanning Transmission Electron Microscopy (S/TEM)

Microanalyses of all samples were done at the Advanced Electron Microscopy Center (AEMC) at the Hawai'i Institute of Geophysics and Planetology. Electron transparent sections, between 70 and 100 nm thickness, were prepared using the Helios 660 dual-beam Focused Ion Beam (FIB) instrument, which allows for S/TEM analyses and is accurate for a specific location to < 50 nm (Ishii et al., 2009; Ishii et al., 2010a;

Ishii et al., 2010b). The samples were carbon-coated prior to secondary electron (SE) imaging and FIB preparation. SE imaging in the FIB allowed us to survey the bulk material and examine grain surfaces in detail before selection of a grain for FIB preparation. The regions of interest were protected using layers of nano-crystalline Pt (~ 4 μm in total thickness) to prevent ion damage and then extracted using Ga-ion milling. Energy dispersive x-ray spectroscopy (EDS, AZtec Energy Xmax N80 silicon drift detector, Oxford Instruments) allowed us to determine the compositions of the grains when selecting grains for FIB preparation.

S/TEM microanalyses were performed using the 60–300 kV, dual Cs-corrected and monochromated high-base Titan (Thermo Fisher, formerly FEI), which is ideal for low-electron dose, high signal/noise analyses of amorphous silicates (Bradley and Dai, 2009; Bradley et al., 2014). We collected conventional brightfield, darkfield, and high-angle annular darkfield (HAADF) images (0.8 Å resolution, with magnifications of 10,000X–100,000X) in order to examine the silicate grains, amorphous rims, and SMFe. Elemental compositions were obtained using EDS (Genesis 4000 Si(Li) detector, EDAX) in conjunction with a Cliff-Lorimer thin-film correction procedure calibrated against thin-film mineral standards. EDS enabled us to determine if amorphous material differed in composition from the silicate grains, ascertain nanoparticle composition (e.g., SMFe), and observe any stratigraphy within amorphous rims. Electron diffraction at 300 kV in the S/TEM microprobe mode with 0.3 mrad semi-angle was used to identify the Fe inclusions in the rims. An electron diffraction pattern of the Pt protection-layer on each FIB section was obtained under identical and used as an *in-situ* calibration.

4.3 Results

4.3.1 Spectral Changes and SMFe Abundance Estimates from Radiative Transfer Modeling

The irradiated olivine and pyroxene exhibit darkening, reddening, and subdued absorption bands characteristic of space weathering (Figures 4.1 & 4.2). The olivine (Figure 4.1a) and pyroxene (Figure 4.2a) irradiated at 85 K exhibit higher reflectance overall than the samples irradiated at 295 K. At 1,064 nm (the wavelength that is of special interest because it is the wavelength of the LOLA albedo measurements), the olivine irradiated at 85 K is 5% brighter than the olivine irradiated at 295 K (Figure 4.1a).

The pyroxene irradiated at 85 K is 6% brighter at 1,064 nm than the pyroxene irradiated at 295 K (Figure 4.2a). The NIR continuum was calculated as a straight-line from the reflectance at 650 and 1700 nm for the olivine and 750 and 2450 nm for the pyroxene. The continuum for both the pyroxene and olivine irradiated at 295 K is ~1% greater than the 85 K spectra (Figures 4.1b & 4.2b).

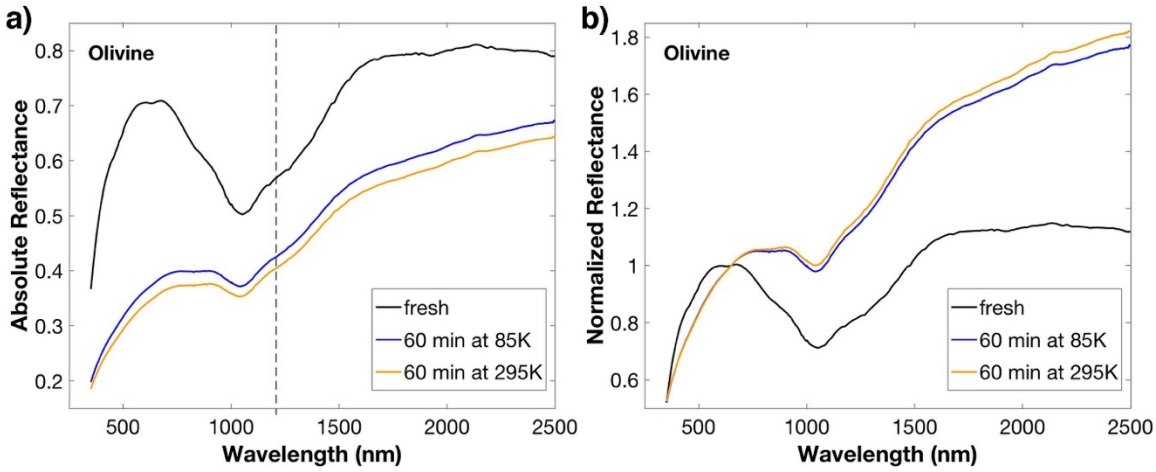

Figure 4.2 Absolute reflectance (a) and reflectance normalized to 650 nm (b) of fresh and laser-irradiated San Carlos olivine. The dashed line in (a) is located at 1,064 nm, the wavelength at which LOLA operates.

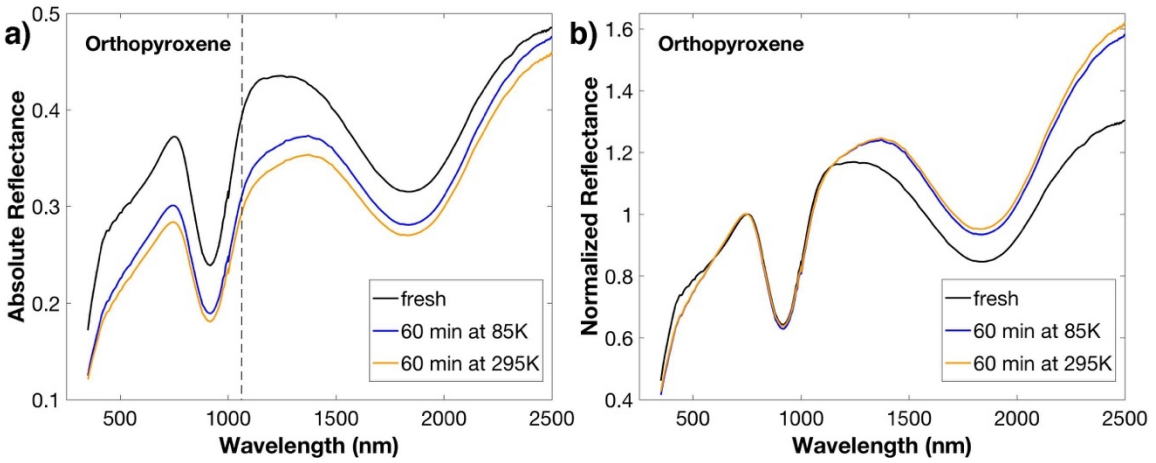

Figure 4.3 Absolute reflectance (a) and reflectance normalized to 750 nm (b) of fresh and laser-irradiated orthopyroxene. The dashed line in (a) is located at 1,064 nm, the wavelength at which LOLA operates.

The best-fitting spectra obtained from radiative transfer modeling of the laser-irradiated olivine and pyroxene are shown in Figure 4.3. The estimated nanophase Fe and microphase Fe abundances obtained from the model spectra are listed in Table 4.1. Based on these estimates, the olivine irradiated at 85 K contains 84% the abundance of nanophase Fe and 74% the abundance of microphase Fe of the olivine irradiated at 295 K. The pyroxene irradiated at 85 K contains 85% the abundance of nanophase Fe and 64% the abundance of microphase Fe as the pyroxene irradiated at 295 K.

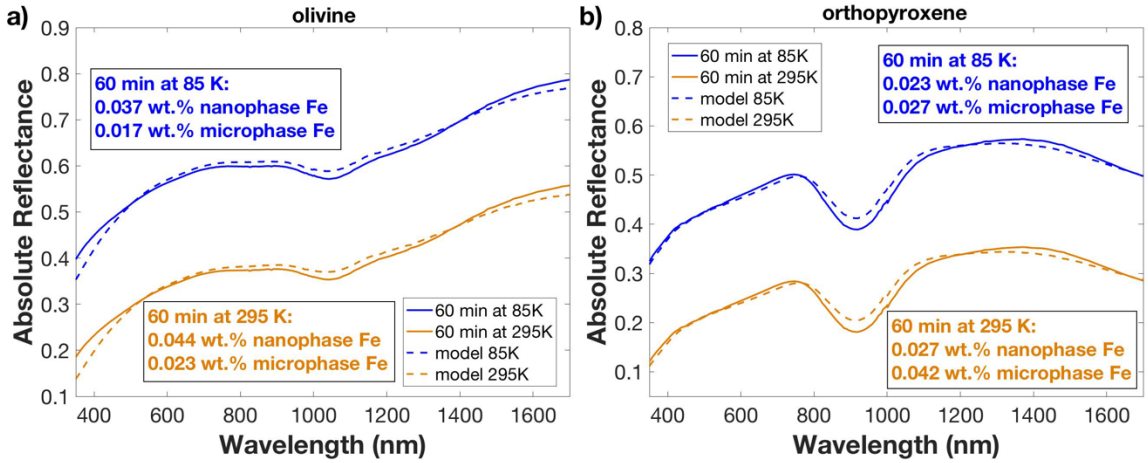

Figure 4.4 Scaled reflectance showing the fits (dashed lines) of the radiative transfer model to olivine (a) and orthopyroxene (b) samples laser irradiated at 85 K and 295 K for 60 minutes. The 85 K spectra are offset by 0.2 relative to the 295 K spectra. The abundance (wt.%) of nanophase Fe and microphase Fe of the modeled spectra are given.

Table 4.1 The abundances (wt. %) of nanophase Fe and microphase Fe in the laser-irradiated olivine and pyroxene, estimated using radiative transfer modeling. The root-mean-square of the SMFe abundances is 0.011 wt.%. Modeled spectra are shown in Figure 4.3.

	SMFe abundance (wt. %)	
	nanophase Fe	**microphase Fe**
olivine 85 K	0.037	0.017
olivine 295 K	0.044	0.023
pyroxene 85 K	0.023	0.027
pyroxene 295 K	0.027	0.042

Reflectance measurements of the laser irradiated lunar highlands analog show a slight darkening at wavelengths less than 1000 nm, as well as slight reddening of the spectral slope (Figure 4.4). In the NIR, >1100 nm, these samples exhibit an increased reflectance compared to spectra of fresh analog. Laser irradiation of the highlands analog at 85 K yielded only a 0.2% increase in brightness at 1064 nm compared to irradiation at 295 K (Figure 4.4a). We consider this to be insignificant because the standard deviation of our measurements from reflectance standards is ~0.5%. However, the sample irradiated at 85 K did exhibit slightly reduced reddening (7% less) in the NIR compared to the 295 K sample (Figure 4.4b).

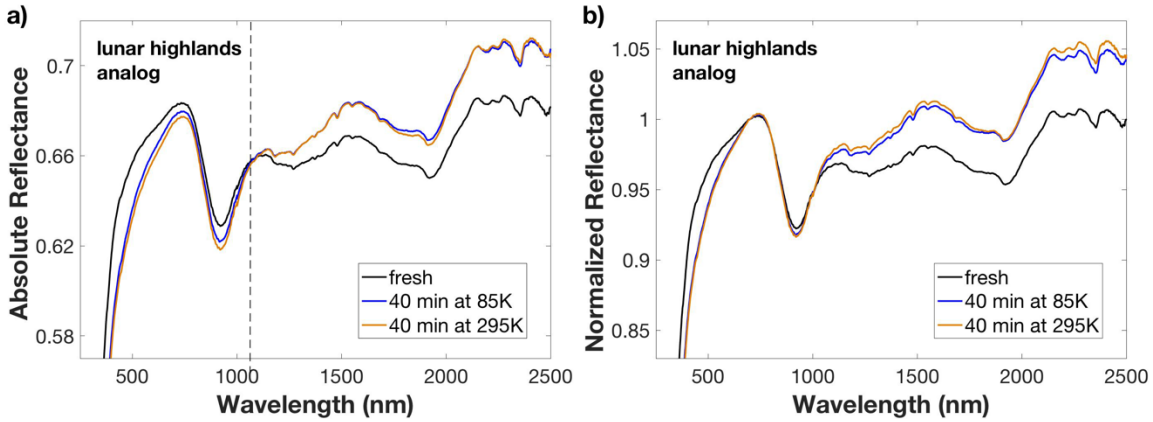

Figure 4.5 Absolute reflectance (a) and reflectance normalized to 700 nm (b) of fresh and laser-irradiated lunar highlands analog. The dashed line in (a) is located at 1,064 nm, the wavelength at which LOLA operates.

4.3.2 S/TEM Analyses

Secondary electron imaging prior to FIB sample preparation for S/TEM analyses revealed amorphous rims on the olivine and pyroxene samples irradiated at both temperatures. These samples had amorphous rims, melt splashed onto surfaces, grains cemented together by melt, small grains adhering to the top of melt, and vesicles in amorphous surfaces. Compared to the mafic samples, the irradiated lunar highlands analog had grains with discontinuous amorphous rims and much less melt altogether. Table 4.2 summarizes the measurements of amorphous rims, vesicles, and SMFe for each sample. An olivine grain and a pyroxene grain from each of the 85 K and 295 K irradiated mafic samples and a plagioclase grain, from the irradiated lunar highlands analog samples, were selected for FIB preparation and S/TEM analyses.

Table 4.2 Measurements of the maximum and minimum thicknesses of amorphous rims and the maximum diameters of vesicles and SMFe obtained from S/TEM images.

	maximum rim thickness (nm)	**minimum rim thickness (nm)**	**maximum diameter of vesicles (nm)**	**maximum diameter of SMFe (nm)**
olivine 85 K	230	100	200	10
olivine 295 K	1400	230	none	10
pyroxene 85 K	1900	150	1500	10
pyroxene 295 K	1120	320	390	10
analog 85 K	130	200	100	none
analog 295 K	1000	200	290	none

The olivine grain from the 295 K sample selected for FIB preparation is approximately 55 μm x 20 μm in size with a continuous amorphous rim (Figure 4.5a). The area chosen for FIB extraction contained the rim (a thicker portion and a thinner portion), adhered grains, and vesicles (Figure 4.5b). Brightfield imaging confirmed that the section of the grain extracted using FIB has an amorphous rim of varying thickness, between 230 and 1,400 nm thick (Figure 4.6). SMFe is present throughout the rim, with more SMFe concentrated at the base (Figure 4.7). The SMFe is small and is classified as nanophase Fe, with particles < ~10 nm in diameter. S/TEM diffraction confirms that the

SMFe is metallic Fe (Figure 4.8). The diffraction pattern has a first ring of 0.41 nm that corresponds to the reported $2d_{011}$ of 0.40 nm for α-Fe and a second ring of 0.29 nm that corresponds to the reported $2d_{002}$ of 0.28 nm (Jette and Foote, 1935).

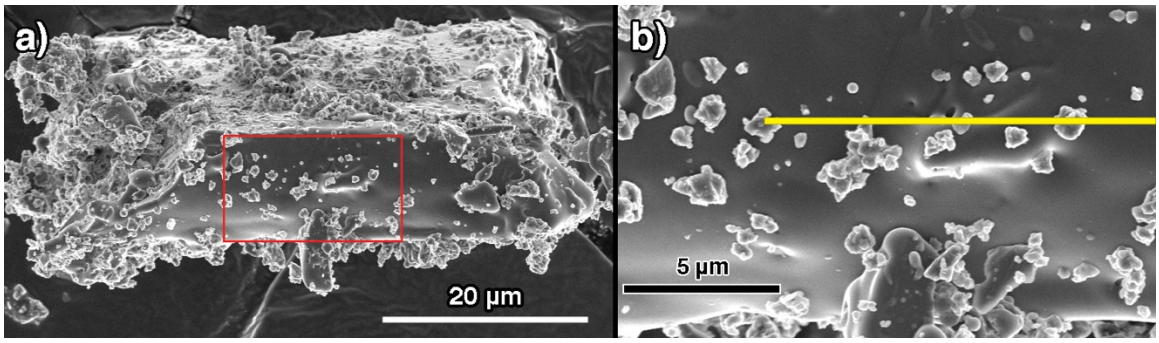

Figure 4.6 Secondary electron images of an olivine grain irradiated 60 minutes by laser irradiation at 295 K. a) the red box corresponds to the area of interest shown in (b). b) the yellow line indicates the approximate location of the FIB section that was extracted for TEM analysis.

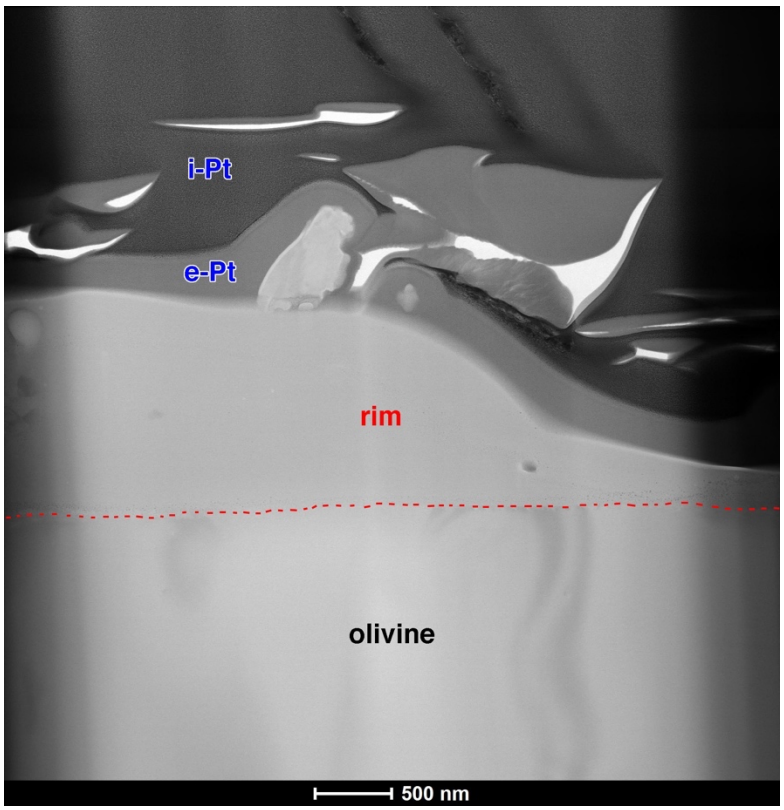

Figure 4.7 Brightfield image of the olivine grain irradiated at 295 K from Figure 4.5. The grain has an amorphous rim of varying thickness and a small crystalline grain adhered to

the surface. The approximate boundary between the olivine host grain and the amorphous rim is shown in the red dashed line. The platinum strap is labeled with electron-beam deposited Pt as “e-Pt” and ion-beam deposited Pt as “i-Pt”.

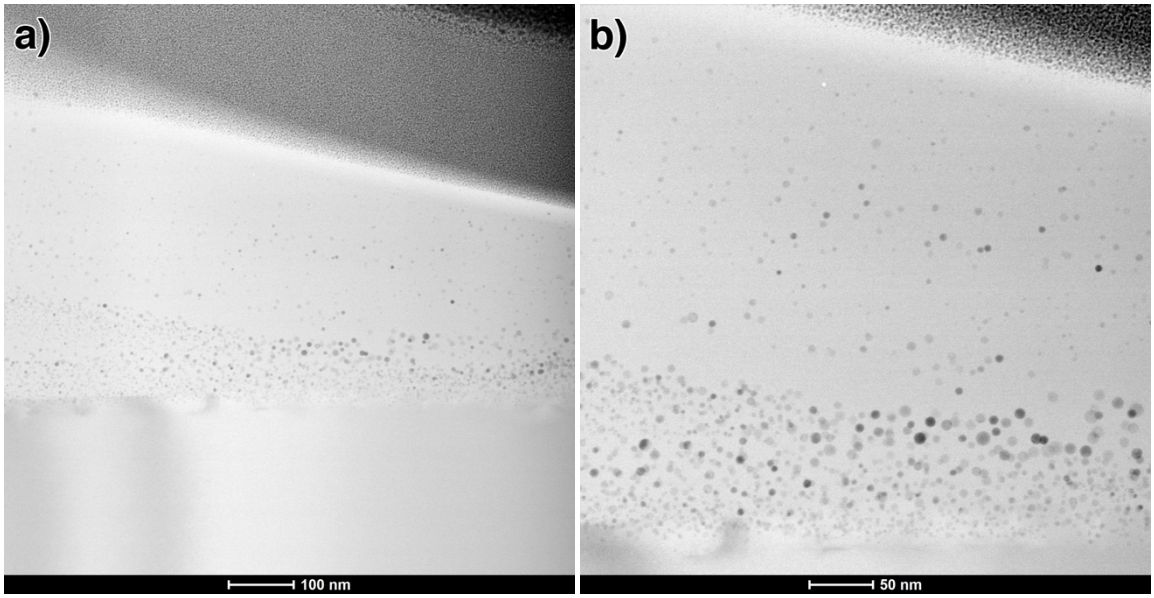

Figure 4.8 S/TEM brightfield images showing the SMFe contained in the rim of the olivine irradiated at 295 K from Figure 4.6. Both images are from a thinner portion of the amorphous rim, but were selected because they show the distribution and size of SMFe very well. The SMFe particles vary in size (< ~10 nm in diameter) and are more concentrated in the bottom one-third of the rim.

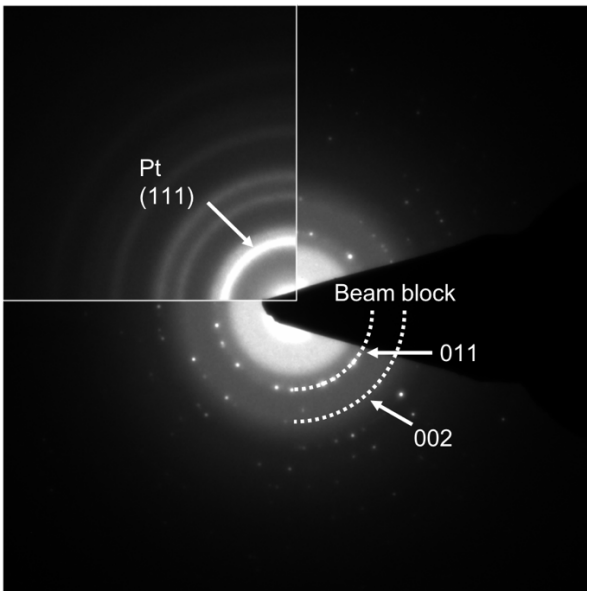

Figure 4.9 Electron diffraction of SMFe particles contained in the rim of the olivine grain irradiated at 295 K confirms that the SMFe is metallic Fe. The diffraction pattern has a first ring of 0.41 nm that corresponds to the reported $2d_{011}$ of 0.40 nm for α-Fe and a second ring of 0.29 nm that corresponds to the reported $2d_{002}$ of 0.28 nm (Jette and Foote, 1935). The Pt (111) diffraction ring (upper left quadrant) from the protection layer was used for in-situ diffraction camera length calibration.

The olivine grain irradiated at 85 K chosen for FIB preparation is approximately 60 x 70 μm in size and has an amorphous rim (Figure 4.9). S/TEM imaging showed that the amorphous rim is discontinuous, varying in thickness from ~100–230 nm, and contains vesicles and SMFe (Figures 4.10 & 4.11). The vesicles are up to 200 nm in diameter, with the majority < 100 nm in diameter. The rim has rounded melt blebs, some of which look like lobes indicating the direction the melt flowed (Figure 4.10). There is an elongated bubble in the rim (Figure 4.11b) that is a gap where the underside of a lobe of melt came to rest on the surface. It is lined with Pt, an artifact of FIB preparation, and is surrounded by smaller, irregular/stretched vesicles. SMFe is more concentrated at the base of the rim but is present throughout (Figure 4.11). Like the 295 K sample, the nanophase Fe particles are < ~10 nm in diameter. A grain adhered to the surface of the rim also has a rim with vesicles and SMFe (Figure 4.11b). The electron diffraction pattern confirms that the SMFe is metallic Fe (Figure 4.12), with the same indexing and ring spacing as the pattern from the 295 K sample.

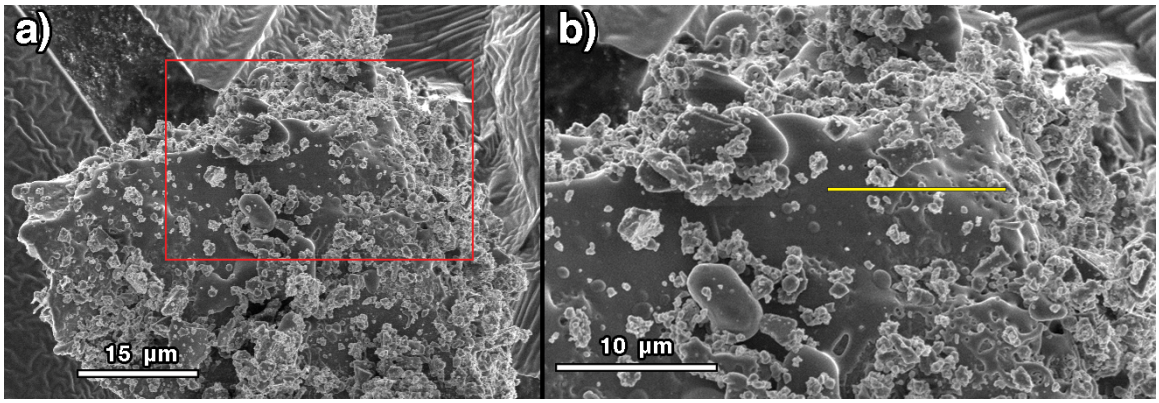

Figure 4.10 Secondary electron images of an olivine grain irradiated 60 minutes by laser irradiation at 85 K. a) the red box corresponds to the area of interest shown in (b). b) the yellow line indicates the approximate location of the FIB section that was extracted for TEM analysis.

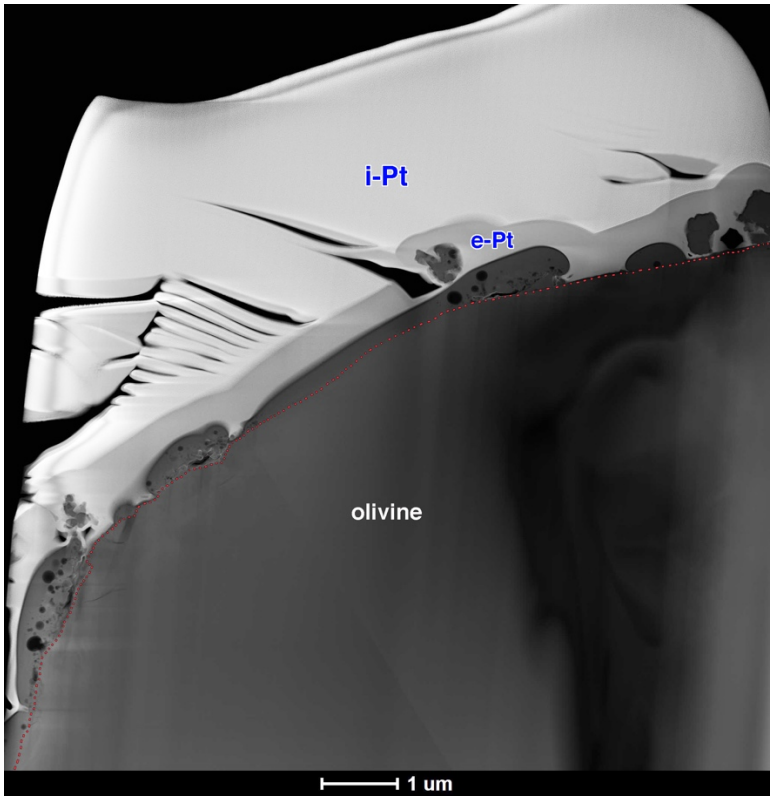

Figure 4.11 HAADF image of the FIB section from the olivine grain irradiated at 85 K from Figure 4.9. The grain has a thin, discontinuous amorphous rim that contains vesicles (black circles). The approximate boundary between the olivine host grain and the

amorphous rim is shown in the red dashed line. The platinum strap is labeled with electron-beam deposited Pt as “e-Pt” and ion-beam deposited Pt as “i-Pt”.

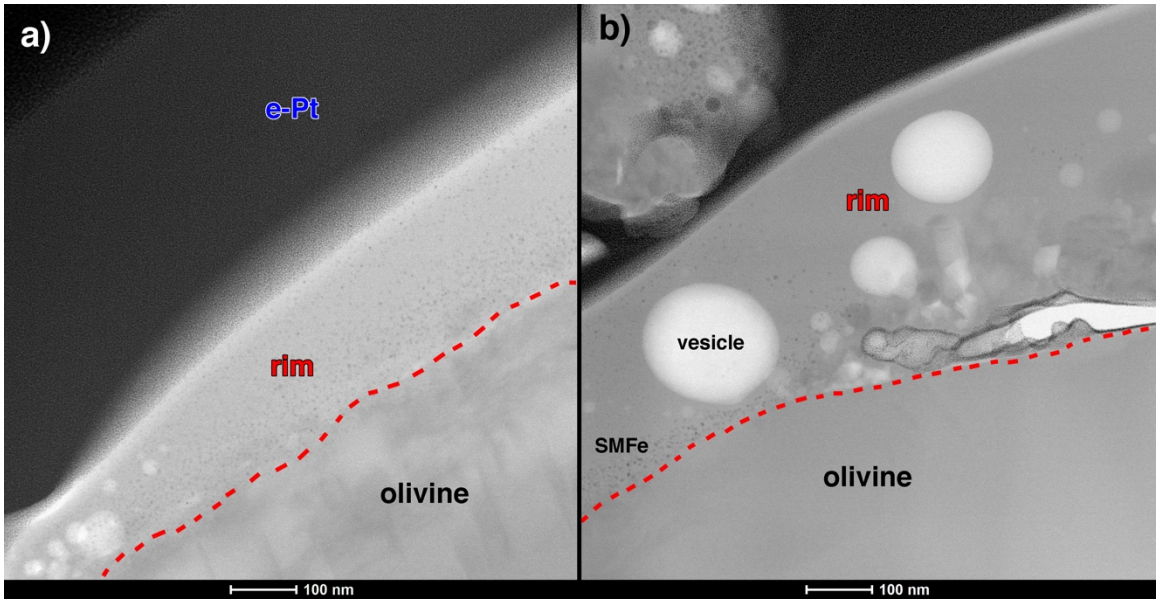

Figure 4.12 S/TEM brightfield images of the olivine grain irradiated at 85 K from Figure 4.10. The approximate boundary between the olivine host grain and the amorphous rim is shown in the red dashed line. The platinum strap is labeled with electron-beam deposited Pt as “e-Pt”. a) The amorphous rim varies in thickness, with SMFe (small, dark circles) that is present throughout but more concentrated at the base of the rim. Vesicles (bright circles) are present in the rim on the bottom-left of the image. b) The amorphous rim contains large vesicles that are up to 200 nm in diameter and SMFe more concentrated at the base of the rim. The elongated bubble in the rim (middle-left of the image) is a gap where a lobe of melt came to rest on the surface. It is lined with Pt, an artifact of FIB preparation, and is surrounded by smaller, irregular/stretched vesicles. In the upper-right of the image, a small grain touches the rim of the host grain. This adhered grain also has a rim with vesicles and SMFe.

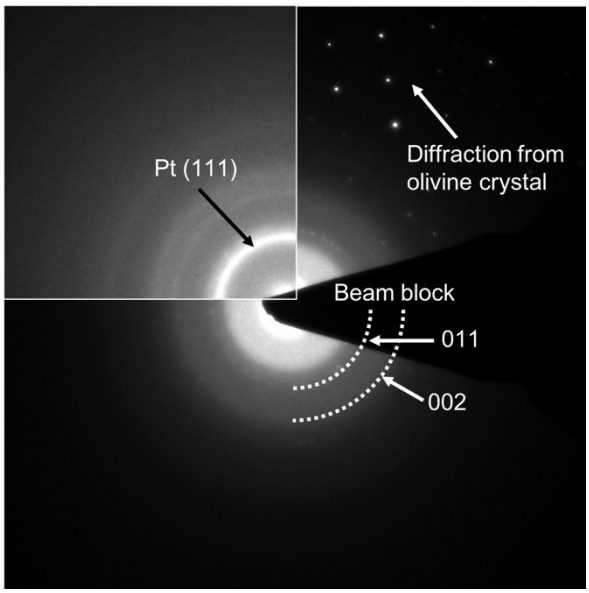

Figure 4.13 Electron diffraction of SMFe particles contained in the rim of the olivine grain irradiated at 85 K confirms that the SMFe is metallic Fe. The diffraction pattern has a first ring of 0.41 nm that corresponds to the reported $2d_{011}$ of 0.40 nm for α-Fe and a second ring of 0.29 nm that corresponds to the reported $2d_{002}$ of 0.28 nm (Jette and Foote, 1935). The Pt (111) diffraction ring (upper left quadrant) from the protection layer was used for in situ diffraction camera length calibration.

The pyroxene grain irradiated at 295 K is approximately 28 x 32 μm in size with a continuous amorphous rim with vesicles and adhered grains (Figure 4.13). Brightfield images reveal that the rim varies in thickness from ~320–1120 nm thick (Figure 4.14) and contains vesicles inside and on the surface of the rim as well as SMFe. The burst vesicles on the surface suggest the melt was fluid enough to relax and create divots before quenching. SMFe particles occur in a band ~75–100-nm thick near the base of the rim and are sparser near the surface (Figure 4.15). SMFe particles are also concentrated around the vesicles. The vesicles that appear darker gray in Figure 4.15 are contained entirely within the plane of the FIB section, and SMFe particles are visible near the surfaces of these vesicles. The bright vesicle that is labeled is partially cut open (i.e., this vesicle was "sliced"); thus, SMFe does not occur in the center (open vesicle) but only near the edges. SMFe particles near the base of the rim are up to 10 nm in diameter, while the particles near the surface of the rim are < ~5 nm in diameter. Electron diffraction

confirms that the SMFe is metallic Fe (Figure 4.16), with the same indexing and ring spacing as the pattern from the previous samples.

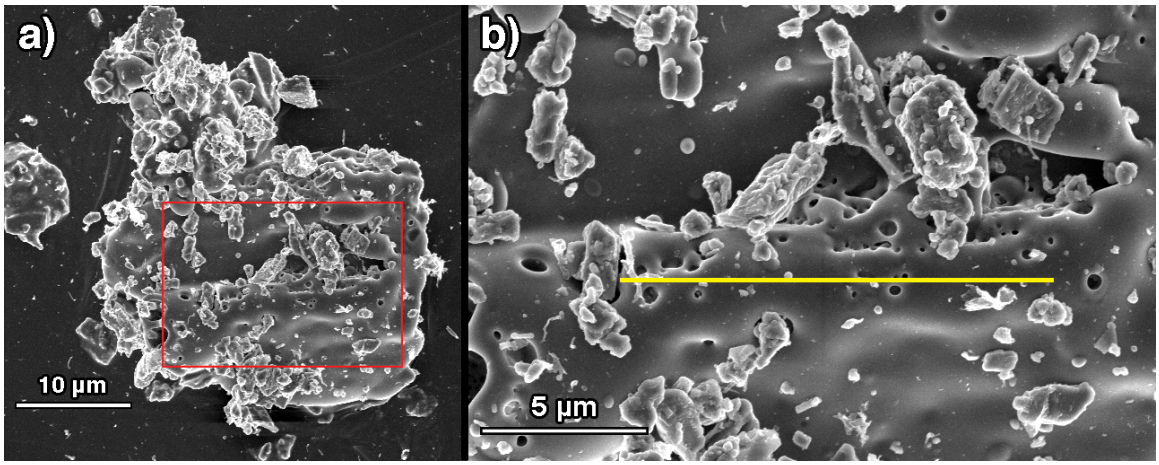

Figure 4.14 Secondary electron images of the pyroxene grain irradiated 60 minutes by laser irradiation at 295 K. a) the red box corresponds to the area of interest shown in (b). b) the yellow line indicates the approximate location of the FIB section that was extracted for TEM analysis.

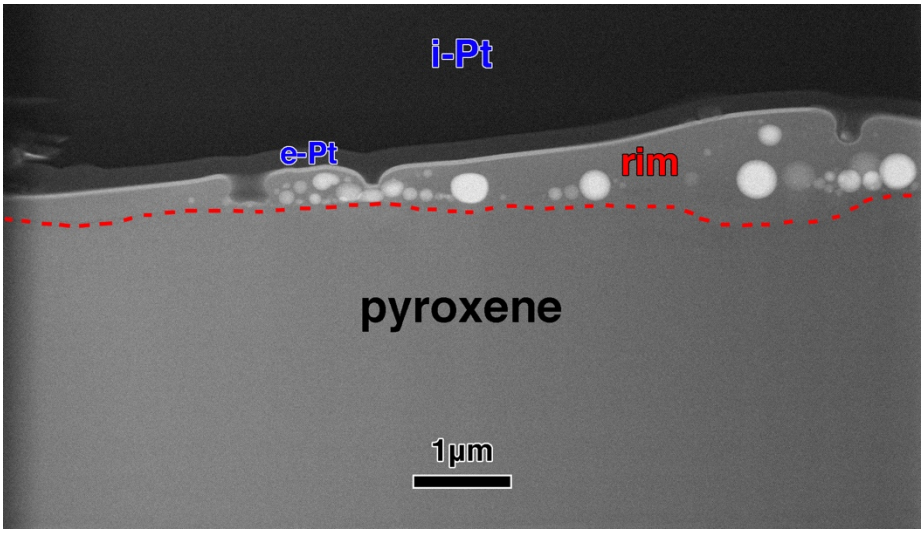

Figure 4.15 S/TEM brightfield image of the pyroxene grain irradiated at 295 K from Figure 4.13. The grain has an amorphous rim of varying thickness with vesicles (bright circles). "Popped" vesicles are also present on the surface of the rim (i.e., the three divots). The approximate boundary between the pyroxene host grain and the amorphous rim is shown in the red dashed line. The platinum strap is labeled with electron-beam deposited Pt as "e-Pt" and ion-beam deposited Pt as "i-Pt".

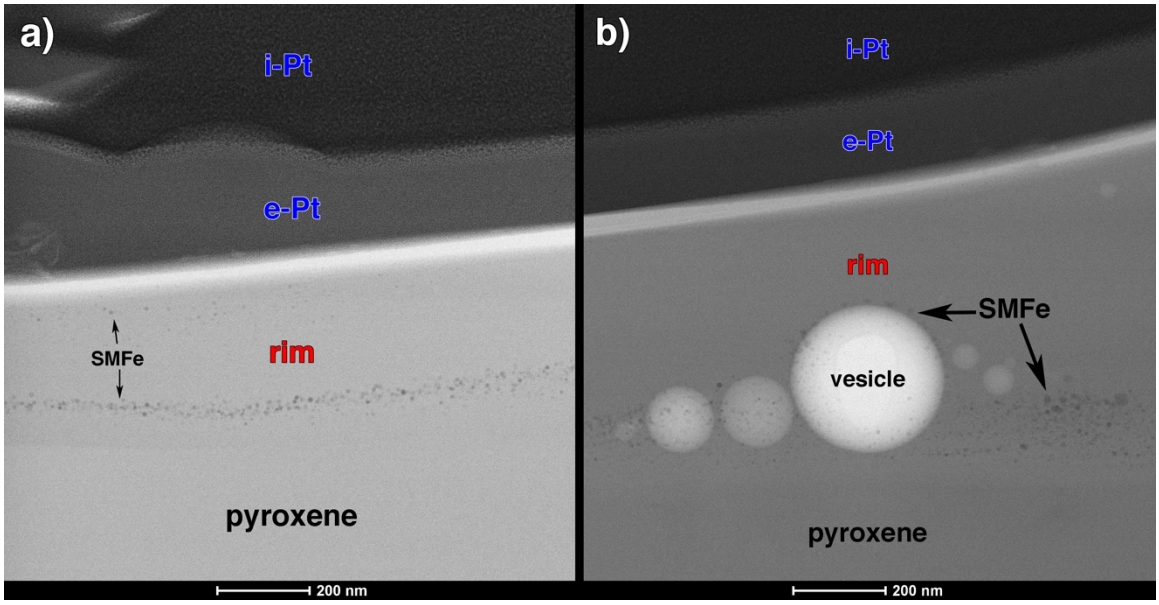

Figure 4.16 Brightfield images of the pyroxene grain irradiated at 295 K from Figure 4.14. The platinum strap is labeled with electron-beam deposited Pt as "e-Pt" and ion-beam deposited Pt as "i-Pt". a) SMFe particles (small, dark circles) occur in a band ~75–100-nm thick near the base of the rim and are sparser in a band near the surface. b) The amorphous rim also contains vesicles (large, bright circles) with SMFe concentrated around them. The vesicles that appear darker gray are contained entirely within the plane of the FIB section, and SMFe particles are visible near the surfaces of these vesicles. The bright vesicle that is labeled is partially cut open (i.e., this vesicle was "sliced"); thus, SMFe does not occur in the center but only near the edges.

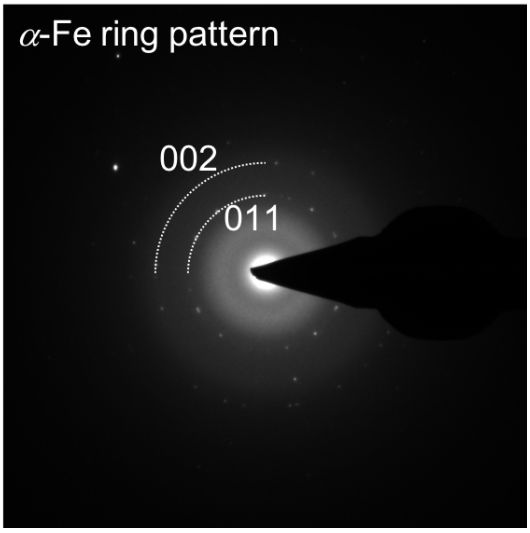

Figure 4.17 Electron diffraction of SMFe particles contained in the rim of the pyroxene grain irradiated at 295 K confirms that the SMFe is metallic Fe. The diffraction pattern has a first ring that corresponds to the reported $2d_{011}$ of 0.40 nm for α-Fe and a second ring that corresponds to the reported $2d_{002}$ of 0.28 nm (Jette and Foote, 1935).

The pyroxene grain from the sample irradiated at 85 K that we selected for FIB extraction has a continuous amorphous coating of varying thickness with vesicles and adhered grains on the surface (Figure 4.17). TEM imaging (Figures 4.18 & 4.19) shows that the amorphous rim varies in thickness from ~150 nm to ~1900 nm. There are many vesicles between ~20 nm and ~1500 nm in diameter, which are unusually large compared to the other samples. Most of the vesicles are irregularly shaped, as if they buoyantly rose and stretched. Like the pyroxene sample irradiated at 295 K (Figure 4.15), some of the vesicles have SMFe (<10 nm in diameter) concentrated around them. The electron diffraction pattern of the SMFe indicates it consists of metallic iron as it matches that of α-Fe (bcc) in the [100] zone axis orientation (Figure 4.20a). The pattern has a first ring that corresponds to the reported $2d_{011}$ of 0.40 nm for α-Fe (Jette and Foote, 1935). Within the amorphous rim at the right edge of the section, there is a single pyroxene crystal. This pyroxene crystal has a different electron diffraction pattern than the host pyroxene grain, indicating it has a different crystal orientation. There is a ~3800-nm-long and 400-nm-wide layer of polycrystalline spinel between the pyroxene host grain and the amorphous rim with the large vesicles directly on top of the spinel (Figure 4.19a). The electron

diffraction from this spinel layer matches that of magnesioferrite spinel ($MgFe_2O_4$) in the [351] zone axis orientation (Figure 4.20b).

TEM EDS spectra of the pyroxene host grain, the spinel layer, and an area of the amorphous rim without SMFe are shown in Figure 4.21, along with the elemental compositions in Table 4.3. Compared to pyroxene, the Mg-Fe oxide spinel has a large enrichment in O and depletion in Si. The spinel is also slightly enriched in Mg, Fe, and Ca and depleted in Al compared to the pyroxene. The spectrum from the amorphous rim, which does not contain SMFe in this area, is slightly depleted in Si and Fe compared to the pyroxene host grain. The rim is also slightly enriched in Mg, Al, and Ca compared to the pyroxene.

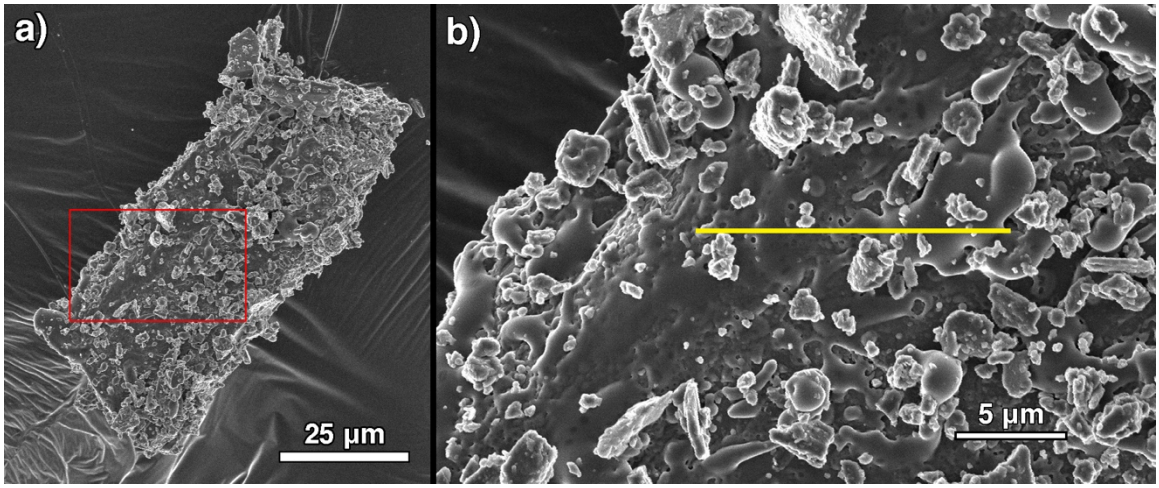

Figure 4.18 Secondary electron images of a pyroxene grain irradiated 60 minutes by laser irradiation at 85 K. a) The red box corresponds to the area of interest shown in (b). b) The yellow line indicates the approximate location of the FIB section that was extracted for TEM analysis.

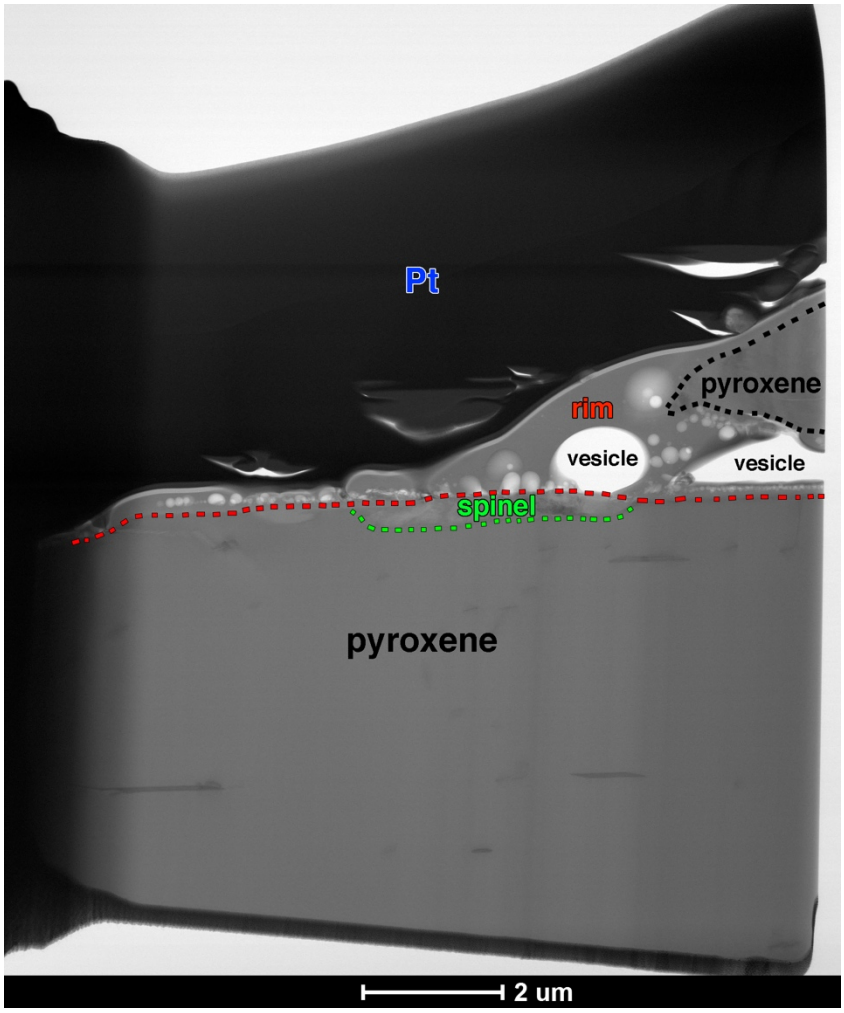

Figure 4.19 Brightfield image of the pyroxene grain irradiated at 85 K from Figure 4.17. The grain has an amorphous rim of varying thickness and many irregularly shaped vesicles. In one section, there is a layer of polycrystalline spinel between the pyroxene host grain and the amorphous rim, with vesicles directly on top of the spinel. Within the amorphous rim at the right edge of the section, there is a single pyroxene crystal. The approximate boundary between the pyroxene host grain and the spinel is shown in the green dashed line. The approximate boundary of the pyroxene crystal in the rim is shown in the black dashed line. The approximate boundary of the amorphous rim is shown in the red dashed line. The platinum strap is labeled as "Pt".

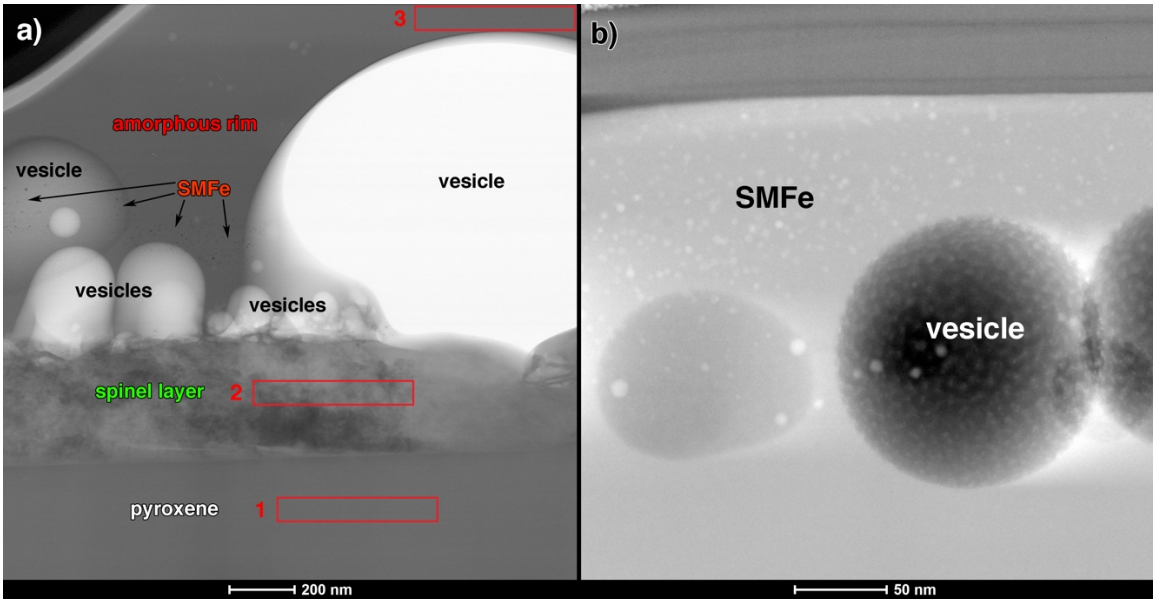

Figure 4.20 TEM images of the pyroxene grain irradiated at 85 K from Figure 4.18. a) This brightfield image shows the spinel layer in more detail, as well as SMFe particles (small, dark circles) that are not visible at the low magnification of Figure 4.18. In this two-dimensional view, there is SMFe in front of the vesicles. Areas that were measured with EDS are shown as red boxes (labeled 1–3). b) High magnification HAADF image showing vesicles (large, dark circles) and SMFe (small, bright circles). The large vesicle has a speckled pattern suggestive of vapor condensation on the wall of the vesicle.

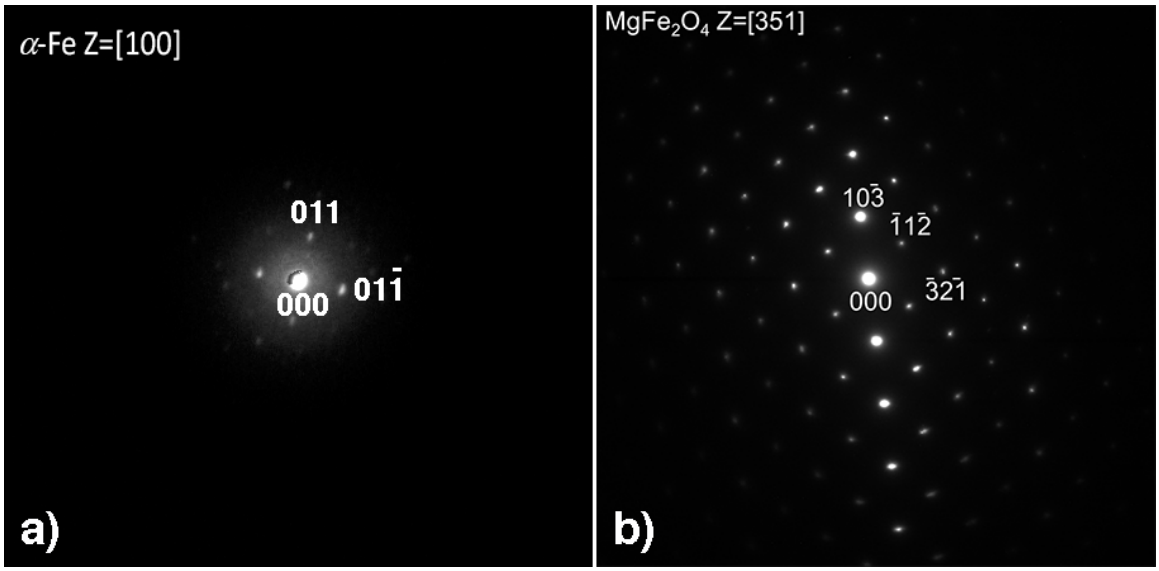

Figure 4.21 a) Electron diffraction pattern of SMFe particles contained in the rim of the pyroxene grain irradiated at 85 K confirms that the SMFe is metallic Fe. The diffraction

pattern matches that of α-Fe (bcc) in the [100] zone axis orientation. The pattern has a first ring that corresponds to the reported $2d_{011}$ of 0.40 nm for α-Fe (Jette and Foote, 1935). b) Electron diffraction pattern from the spinel layer shown in Figure 4.19a confirms it is a magnesioferrite spinel ($MgFe_2O_4$) in the [351] zone axis orientation.

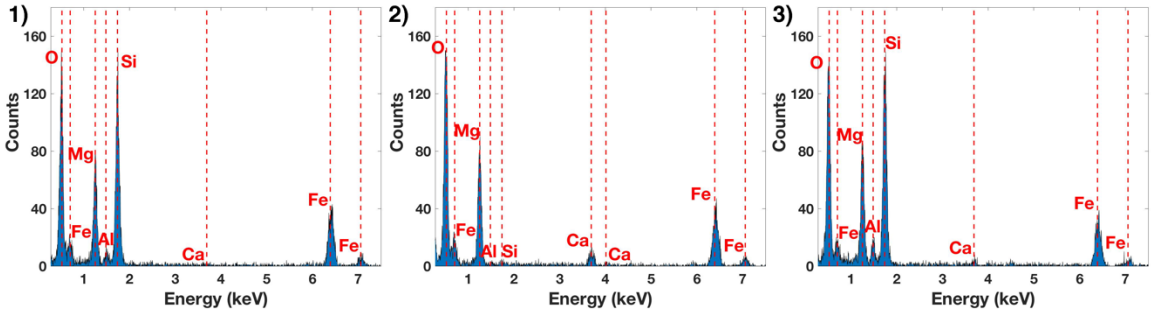

Figure 4.22 EDS spectra from the pyroxene irradiated at 85 K. The locations where the spectra were collected are shown in Figure 4.19. Spectrum 1 is from the pyroxene host grain, directly below the spinel layer. Spectrum 2 is from the spinel layer, and spectrum 3 is from an area in the amorphous rim without SMFe. Table 4.3 lists the elemental compositions obtained from the spectra.

Table 4.3 Elemental compositions (atomic %) of the pyroxene sample irradiated at 85 K (Figure 4.15) obtained from the TEM EDS spectra shown in Figure 4.21. Compared to pyroxene, the Mg-Fe oxide spinel is enriched in O and depleted in Si.

atomic %	pyroxene (1)	spinel (2)	amorphous rim (3)
O	60.3 ± 0.6	77.7 ± 0.9	60.3 ± 0.6
Si	20.3 ± 0.1	0.20 ± 0.01	19.8 ± 0.1
Mg	12.8 ± 0.1	14.8 ± 0.1	13.2 ± 0.1
Fe	5.62 ± 0.02	6.1 ± 0.03	4.37 ± 0.02
Al	0.94 ± 0.01	0.03 ± 0.01	2.07 ± 0.01
Ca	0.06 ± 0.01	1.14 ± 0.01	0.24 ± 0.01

Unlike the mafic samples, the irradiated lunar highlands analog material that we observed with SEM did not have any grains with continuous amorphous coatings. The plagioclase grain selected from the analog material irradiated at 295 K for FIB preparation has small areas of amorphous material on its surface with vesicles, as well as

many small, adhered grains (Figure 4.22). TEM imaging (Figure 4.23) and electron diffraction show that the host plagioclase grain has a layer of polycrystalline plagioclase, followed by a tear-drop shaped glass on the surface with a single plagioclase crystal inside. The glass contains vesicles but lacks SMFe. There is also an adhered grain that consists of polycrystalline plagioclase and glass with vesicles. The amorphous layer on the sample is between ~200 nm and ~1,000 nm thick. The elemental compositions of each area are listed in Table 4.4. Compared to the polycrystalline plagioclase layer directly below the glass, the glass is enriched in Ca and Al and depleted in Na. However, the glass is very similar in composition to the host plagioclase. Unlike the host plagioclase and the glass, the polycrystalline plagioclase and the single crystal of plagioclase within the glass both lack Fe and Mg. The polycrystalline plagioclase is depleted in Al and Ca and enriched in Na compared to the host plagioclase and glass. The pyroxene grain inside the rim has lamellae, in which the left side of the pyroxene is depleted in Al and Ca and enriched in Na (like the polycrystalline plagioclase) and the right side is closer in composition to the host plagioclase but has a slight enrichment in Al and Ca and depletion in Na.

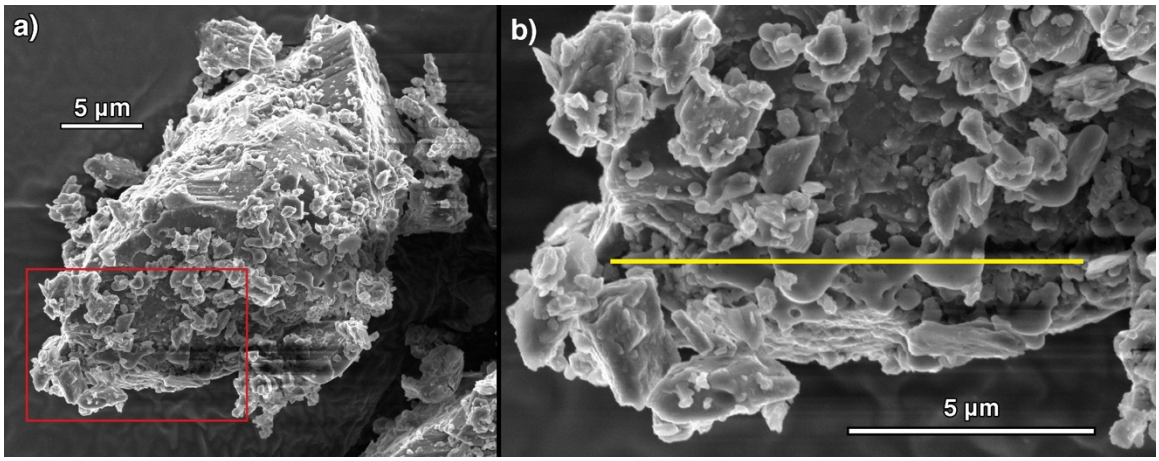

Figure 4.23 Secondary electron images of a plagioclase grain irradiated 60 minutes by laser irradiation at 295 K. a) the red box corresponds to the area of interest shown in (b). b) the yellow line indicates the approximate location of the FIB section that was extracted for TEM analysis.

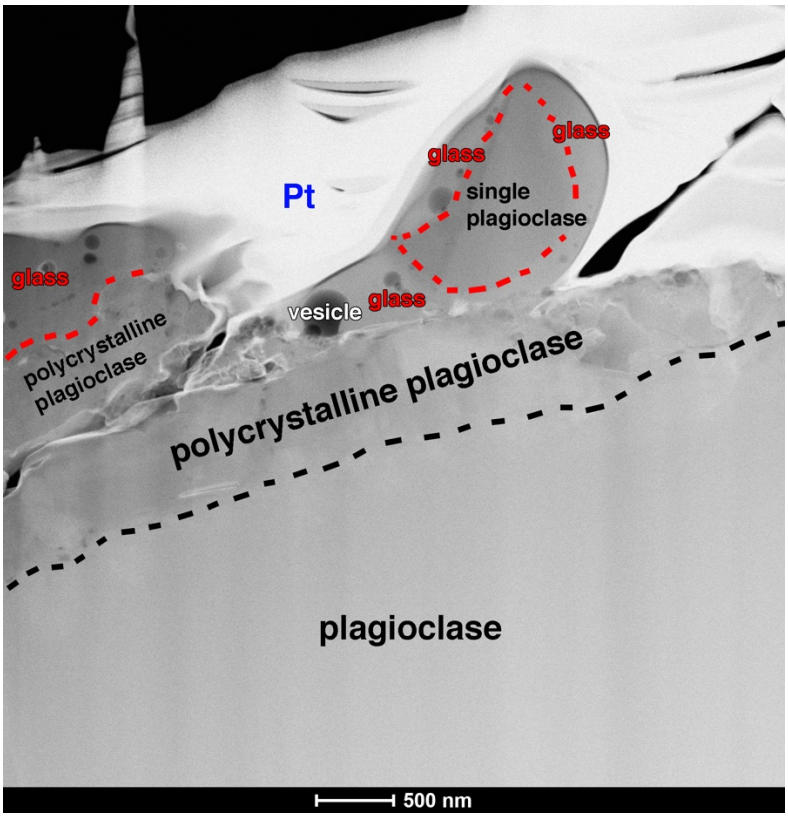

Figure 4.24 TEM HAADF image of the plagioclase irradiated at 295 K from Figure 4.22. The host plagioclase grain has a layer of polycrystalline plagioclase, followed by a tear-drop shaped glass on the surface with a single plagioclase crystal inside. The glass contains vesicles but lacks SMFe. The approximate boundary between the host plagioclase and polycrystalline plagioclase is shown by the black dashed line. There is also an adhered grain (top-left of sample) that consists of polycrystalline plagioclase and glass with vesicles. The approximate boundary of glass with plagioclase is shown by the red dashed line.

Table 4.4 Elemental compositions (atomic %) of the plagioclase sample irradiated at 295 K (Figure 4.23) obtained from TEM EDS.

atomic %	host plag.	poly-crystalline plag.	glass	plag. in glass (left)	plag. in glass (right)	poly-crystalline plag. (adhered grain)	glass (adhered grain)
O	58.2 ± 0.5	58.7 ± 0.6	55.2 ± 0.5	55.6 ± 0.6	58.5 ± 0.5	60.1 ± 0.7	62.9 ± 0.8
Si	17.8 ± 0.1	24.06 ± 0.1	18.37 ± 0.1	24.42 ± 0.1	17.0 ± 0.1	18.7 ± 0.1	16.6 ± 0.01
Al	15.7 ± 0.1	10.56 ± 0.1	16.76 ± 0.1	11.5 ± 0.1	16.5 ± 0.1	14.5 ± 0.1	13.3 ± 0.01
Ca	5.05 ± 0.01	1.25 ± 0.01	5.71 ± 0.02	2.10 ± 0.01	6.61 ± 0.02	6.66 ± 0.03	4.59 ± 0.02
Na	2.01 ± 0.01	5.40 ± 0.02	1.23 ± 0.01	6.38 ± 0.02	1.42 ± 0.01		1.33 ± 0.01
Mg	0.90 ± 0.01		2.19 ± 0.01				0.92 ± 0.01
Fe	0.29 ± 0.01		0.49 ± 0.01				0.35 ± 0.01

A plagioclase grain was also selected from the analog material irradiated at 85 K for FIB extraction. Out of the ~50 grains imaged using SEM, only 16 had areas that appeared melted. The grain that was selected was approximately 30 x 35 μm in size, but it may have been two or three grains cemented together by glass (Figure 4.24a). The area chosen for FIB preparation has an amorphous rim on at least one side (Figure 4.24b). S/TEM imaging shows that the rim has a uniform thickness, varying only from 130 nm to 200 nm (Figure 4.25a). The amorphous rim lacks SMFe and only has approximately 24 vesicles, all of which are concentrated in a section of the rim that is 600 nm in length (Figure 4.25b).

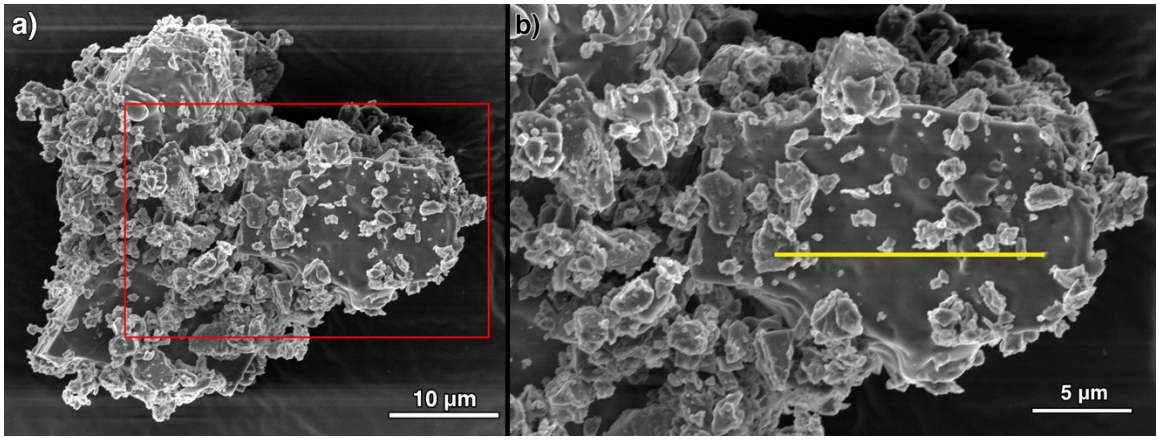

Figure 4.25 Secondary electron images of a plagioclase grain irradiated 60 minutes by laser irradiation at 85 K. a) The red box corresponds to the area of interest shown in (b). b) The yellow line indicates the approximate location of the FIB section that was extracted for TEM analysis.

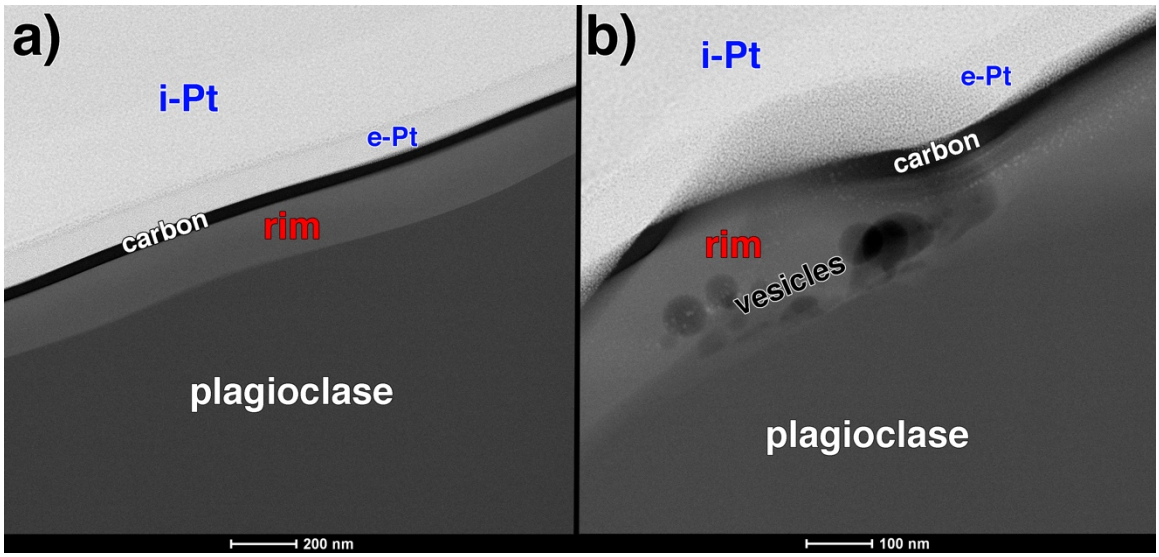

Figure 4.26 S/TEM HAADF image of the plagioclase irradiated at 85 K from Figure 4.24. a) The amorphous rim has a uniform thickness of ~150 nm. No SMFe was observed in the rim. b) The area shown in the image is the only section of the amorphous rim with vesicles. The platinum strap is labeled with electron-beam deposited Pt as "e-Pt" and ion-beam deposited Pt as "i-Pt". The carbon-coat is labeled as "carbon".

4.4 Discussion

Our measurements of the thicknesses of the amorphous rims suggest that space weathering at low temperature decreases the amount of melting and vaporization,

resulting in thinner amorphous rims. Based on the maximum rim thickness, the olivine and plagioclase irradiated at 85 K have amorphous rims that are 16% and 13% of the thickness of the rims on the 295 K samples, respectively. It was difficult to obtain a definitive estimate of the thickness of the amorphous rim on the pyroxene irradiated at 85 K, because the thicker portion of the rim (Figure 4.18) appears to be more like a large melt splash with unusually large vesicles and a large, recrystallized pyroxene grain. However, based on comparison of the minimum rim thicknesses, the pyroxene irradiated at 85 K has an amorphous rim that is 47% the thickness of the rim on the pyroxene irradiated at 295 K.

Temperature does not appear to have an effect on the size of the SMFe particles. Nanophase Fe particles are similar in size (< ~10 nm) in mafic samples irradiated at both temperatures. The radiative transfer modeling indicates that the differences in nanophase Fe and microphase Fe abundances between the 85 K and 295 K samples were similar for the olivine samples (0.007 wt.% difference in nanophase Fe and 0.006 wt.% difference in microphase Fe), but were greater for the pyroxene samples (0.004 wt.% difference in nanophase Fe and 0.015 wt.% difference in microphase Fe). Although microphase Fe (>40 nm in diameter) abundances estimated with the radiative transfer model vary between 0.017 wt.% (olivine irradiated at 85 K) and 0.042 wt.% (pyroxene irradiated at 295 K), no microphase Fe was observed with S/TEM. All of the SMFe particles we observed with S/TEM were <10 nm in diameter. This may be due to sampling bias, and it is possible the larger microphase Fe exists on amorphous rims in the bulk material. We intentionally chose grains that looked similar in appearance in order to analyze grains that were consistent across the set of experiments (e.g. with a uniform coating of melt), which may have caused us to inadvertently avoid grains containing microphase Fe.

The amorphous rims on the mafic grains from experiments at both temperatures have nanophase Fe that is more concentrated at the base of the rim (e.g., Figures 4.7, 4.11, & 4.15) and on the outer surfaces of vesicles near the base of the rims (e.g., Figure 4.15). These observations suggest that most of the nanophase Fe particles form when the vapor first begins to condense because of the high vapor pressure and melting temperature of Fe (e.g., Hapke, 2001). Due to the olivine irradiated at 85 K having a thinner rim, there is less SMFe compared to the olivine irradiated at 295 K, because

smaller volumes of melt and vapor result in less SMFe production. This observation is supported by the SMFe abundance estimates from radiative transfer modeling (Table 4.1) with the olivine irradiated at 85 K having 84% the abundance of nanophase of the olivine irradiated at 295 K. Similarly, modeling also indicates that the pyroxene irradiated at 85 K contains 85% the abundance of nanophase Fe of the pyroxene irradiated at 295 K. This reduction in nanophase Fe abundance is just outside the range predicted by Lucey et al. (2014b), which stated that if only difference in nanophase Fe abundances are responsible for the LOLA albedo anomaly of PSRs, then PSRs have between 50% and 80% the abundance of nanophase Fe in mature lunar regolith (their model did not estimate microphase Fe abundance). The difference in microphase Fe is greater for the two data sets, with the 85 K samples having 64% and 74% the abundance of microphase Fe of the 295 K samples. In order to see if these temperature effects become more pronounced as the samples mature, samples should be irradiated for a longer duration.

The magnesioferrite ($MgFe_2O_4$) layer between the host pyroxene and amorphous rim in the pyroxene irradiated at 85 K is interesting (Figure 4.18 and 4.19a). A phase change such as this has not been observed in any of the other irradiated samples we analyzed, for this chapter or Chapter 3, and no spinel was observed with EPMA analyses of the fresh material. The chemical fractionation that occurs due to vaporization may allow unusual minerals to form. For example, Anand et al. (2004) discovered Fe_2Si, which they named hapkeite, in lunar meteorite Dhofar 280. The authors attribute the formation of hapkeite to vaporization via micrometeorite impact, where thermal dissociation of FeO and SiO_2 and loss of O, Na, and K occurred. Another way that unusual phases could form is by partial vaporization, in which material has been heated to the vaporization temperature but with insufficient internal energy for complete vaporization, causing both liquid and vapor to be produced (Cintala, 1992). The cooler portions of this liquid+vapor volume behave as a gas-rich fluid and vapor could become trapped, preventing the vapor from escaping to free space, or be reabsorbed by the liquid component (Cintala, 1992). Furthermore, Nagahara et al. (1993) found that during vapor condensation, if condensed solids fail to react with vapor, the composition varies much more than that expected in equilibrium condensation. An incomplete reaction may be expected when condensed solids are removed from the coexisting vapor or if relatively

rapid cooling occurred (Nagahara et al., 1993). These different mechanisms during vapor condensation could lead to various enrichments and depletions in certain phases and may have caused the formation of magnesioferrite in our sample.

The irradiated lunar highlands analog showed minor evidence of space weathering. Due to experimental constraints, the lunar highlands analog was not irradiated for as long as the mafic samples. The lower irradiation time combined with factors including a lower iron content and a lower susceptibility to laser ablation at 1064 nm resulted in the irradiated analog samples having thinner amorphous rims than the mafic sample. Reflectance measurements showed some space weathering effects, including a slight darkening at wavelengths less than 1100 nm and a slight reddening of the spectral slope (Figure 4.4). In the NIR at >1100 nm these samples exhibit an increased reflectance compared to spectra of fresh analog, which may be attributed to laser-induced textural changes as Moroz et al. (2014) hypothesized. The sample irradiated at 85 K exhibited slightly reduced reddening (7% less) in the NIR compared to the 295 K sample. Although SMFe was not detected on either grain analyzed with S/TEM, the spectral reddening indicates some nanophase Fe is present in the bulk material, similar to the findings of Moroz et al. (2014), which may be due to the presence of mafic minerals. For example, in Chapter 3, we observed nanophase Fe on a pyroxene grain from the laser irradiated highlands analog.

4.5 Conclusion

Spectral measurements, radiative transfer modeling, and S/TEM analyses of our olivine and pyroxene laser irradiated at 85 K and 295 K suggest that surface temperature influences the space weathering process. Our measurements suggest that diminished space weathering due to low surface temperature could account for half of the ~10% increase in reflectance at 1064 nm for PSRs relative to surrounding areas measured by LOLA, with the other half being caused by the presence of ice. In addition, the 5–6% greater reflectance at 1064 nm for the 85 K olivine and pyroxene samples is consistent with the observed anticorrelation trend between surface temperature and LOLA albedo (Lucey, et al., 2014c; Fisher et al. 2017). Thus, diminished space weathering may contribute to the trend of increased albedo with decreasing surface temperature measured by LOLA. Furthermore, the decreased spectral reddening of the 85 K samples indicate

that the spectral shape is also a temperature-dependent space weathering effect. Our observations of the amorphous rims using S/TEM indicate that a decreased production of melt and SMFe are responsible for the differences in reflectance measurements. These temperature effects should be measurable both with latitude for a given body and as a function of solar distance. For example, higher maximum surface temperatures on Mercury compared to the Moon (Vasavada et al., 1999) likely contribute to the higher ratio of microphase Fe to nanophase Fe abundance that was reported by Riner & Lucey (2012). Our results help to quantify the effects of temperature on space weathering, which may need to be considered when interpreting spectral measurements at different latitudes and different planetary bodies.

In addition to a reduction in the amount of melt and SMFe produced from space weathering at low surface temperatures, the formation of unusual mineral phases should also be considered as a possible temperature-dependent space weathering effect. Our observation of a spinel layer that formed on the pyroxene sample irradiated at 85 K between the host pyroxene and amorphous rim indicates that oxide minerals can form in addition to the amorphous rim. Micrometeoroid impacts at temperatures of PSRs may cause oxygen to mobilize as a liquid and be available to form oxide minerals like spinel. This phenomenon would not be expected to occur during space weathering at locations above 90 K, the boiling point of oxygen. Additional mineral phases may need to be considered when interpreting spectral measurements of low surface-temperature planetary surfaces for composition and space weathering effects.

CHAPTER 5

CONCLUSION AND FUTURE WORK

In this dissertation, we used remote sensing to investigate olivine exposures on the lunar surface and performed space weathering simulations under different conditions to determine whether these experiments can accurately replicate the physical, chemical, and spectral effects of lunar space weathering. These works will be important to understanding the space weathering process and also improve mineralogical and compositional spectral models and measurements in estimating abundances. Here, we summarize the results from each chapter.

In Chapter 2, we used hyperspectral VNIR data to detect both known and previously unidentified olivine exposures on the Moon. Estimates of mineral abundances from radiative transfer modeling, crustal thickness estimates, topography, and high-resolution images allowed us to examine the geophysical and morphologic settings of the olivine exposures and interpret their origin as well as their emplacement onto the surface. We identified two types of olivine, volcanic and mantle-derived olivine. Crustal thickness estimates at Nectaris and Humorum basins and Roche crater indicate that olivine was transported by magmatic processes. Olivine occurrences on the rim of Humorum basin, including those located on a graben, likely originated from shallow intrusions, such as dikes, that were caused by extensional stresses from the loading of mare basalt. Detections of olivine near Roche crater might also originate from magmatic intrusions into the subsurface. The central peak of nearby Tsiolkovsky crater contains olivine-bearing material that likely originates from mafic material deep in the crust. Olivine exposures in Nectaris basin are confined to the rims of small craters that punctured the maria, exposing a layer of olivine-rich mare basalt. Crisium contains a diversity of olivine-bearing lithologies. Olivine-rich norites with up to 29 wt.% olivine at Lacus Perseverantiae are possible exposed magma chamber cumulates. Mantle olivine may have been exposed by the basin-forming impact and by Picard crater, which deposited the olivine on the rim of Crisium, where crustal thickness is near 0 km. Picard crater could also contain olivine that crystallized from a differentiated impact melt sea, which would

be a desired sample return site that would allow for accurate dating of the Crisium impact event and the determination of the target composition. Olivine exposures on the basin rim are the best candidate sites for mantle olivine. Under the assumption that Mg-rich olivine is indicative of a mantle origin, identification of Mg-rich olivine on the southern rim of Crisium suggests that mantle overturn occurred in this region. Our findings should be considered when selecting sites for future sample return missions, as sites such as the southern rim of Crisium basin and Picard crater may contain pieces of mantle rock.

In Chapter 3, we examined the effects of kinetic impact, laser irradiation, and a combination of the two methods on a lunar highlands analog to determine which method produces the most accurate lunar space weathering effects. Our analyses included S/TEM, VNIR spectral measurements, radiative transfer modeling of the spectra, and EPR and FMR measurements. Although our kinetic impact experiments at the AVGR created agglutinate-like aggregates, the material does not exhibit spectral changes consistent with space weathering, contain any detectable SMFe, or have an FMR signal, but instead has an EPR signal consistent with that of the fresh lunar highlands analog. While our laser experiments are not capable of producing agglutinates, an amorphous rim containing SMFe was observed on a laser-irradiated pyroxene grain but not on plagioclase. In addition, laser irradiation resulted in typical space weathering spectral trends (i.e., darker, redder, and reduced spectral contrast). However, the amplitude of the FMR signal, which is related to the amount of SMFe in the specimen, is less for the soil analogs compared to lunar soils. We conclude that nanosecond pulsed laser irradiation of soil analog materials does not fully capture the effects of space weathering, partly because our laser weathering experiments do not produce agglutinates, which contain proportionally greater amounts of SMFe in lunar soils. The material that was subjected to both weathering methods exhibited a lower albedo and has a slightly higher I_s/FeO maturity index than that of the material that was only laser irradiated. Modeling indicates that the twice-weathered material contains slightly more SMFe than the material that only underwent laser irradiation, and S/TEM analyses detected SMFe on a plagioclase grain. We infer that because the material that had been weathered at the AVGR contains the agglutinate-like aggregates, the spectrum was altered more rapidly with the subsequent laser irradiation due to the lower melting/vaporization temperature of glass relative to

minerals, which allowed Fe to be extracted from the glass more readily than from crystal, and to the higher Fe content in the glass compared to the plagioclase. Based on our analyses, a combination of the two methods best simulates lunar-like space weathering because kinetic impacts produce agglutinate-like aggregates that more readily produce SMFe through subsequent laser irradiation compared to crystalline material.

In Chapter 4, we tested the hypothesis that low temperature affects the space weathering process by comparing materials irradiated with a pulsed laser at 85 K and room temperature (295 K). Analyses of our samples suggest that space weathering at low temperatures produces thinner amorphous rims and less SMFe than space weathering at room temperature. Laser irradiation of the lunar highlands analog at 85 K results in slightly reduced reddening but does not yield a statistically significant increased reflectance compared to irradiation at 295 K. A lower irradiation time, combined with factors including a lower iron content and a lower susceptibility to laser ablation at 1064 nm, resulted in the irradiated analog samples having thinner amorphous rims than the mafic sample. Although SMFe was not detected on either of the plagioclase grains from the analog, spectral reddening indicates some nanophase Fe is present in the bulk material, similar to the findings of Moroz et al. (2014). We found that olivine and pyroxene irradiated at 85 K exhibit higher reflectance and less reddening than the samples irradiated at 295 K. Based on estimates from radiative transfer modeling, the olivine and pyroxene irradiated at 85 K contains 64–85% the abundance of SMFe of the samples irradiated at 295 K. The higher reflectance at 1064 nm of the 85 K olivine and pyroxene samples relative to room temperature samples is consistent with the observed anticorrelation trend between temperature and LOLA albedo. Thus, reduced space weathering may contribute to the trend of increased albedo with decreasing temperature measured by LOLA. These temperature effects should be measurable both with latitude for a given planetary body and as a function of solar distance. Our results help to quantify the effects of temperature on space weathering, which will be a factor in interpreting spectral data at different latitudes and on different airless bodies. Furthermore, our observation of a spinel layer that formed on the pyroxene sample irradiated at 85 K between the host pyroxene and the amorphous rim indicates that oxide minerals can form in addition to the amorphous rim at low temperatures. Therefore, additional mineral

phases may need to be considered when interpreting or modeling spectral data of planetary surfaces.

Our space weathering experiments have helped identify future areas of research that are critical to improving our understanding of the space weathering process. Although our AVGR kinetic impact experiments produced glass-welded aggregates that are morphologically similar to lunar agglutinates and are enriched in Fe relative to the host material, SMFe was not created. A technique for pulsed laser irradiation experiments to produce lunar-like agglutinates should be developed. Different compositions, grain sizes, laser powers, laser pulse durations, etc. may be capable of producing agglutinates that yield more lunar-like spectral and magnetic properties. It would also be beneficial to expand upon our investigation of the effects of temperature on space weathering. In the future, we plan to analyze FMR measurements of our samples weathered at 85 K and 295 K and place them on the I_s/FeO index, just as we did with our samples from Chapter 3. Experiments such as ours could be performed at a range of temperatures, to see whether there is a range in the effect of space weathering at decreased temperatures, similar to the observed trend of increased LOLA albedo with decreasing temperature. Furthermore, laser irradiation could be performed for a longer duration to see if differences in amorphous rim thickness, SMFe abundance, and spectral changes become more pronounced as the materials continue to mature and when these effects reach saturation so that differences are no longer observed depending on temperature. Ultimately, understanding how space weathering progresses at different temperatures could lead to the development of a temperature-dependent model of space weathering that can be applied based on solar distance, latitude, and illumination which will allow future models and measurements to accurately account for space weathering.

APPENDIX A

DETAILED INFORMATION ON OLIVINE DETECTIONS

Table A.1 The following table has information on each olivine detection, including the region, latitude, longitude, mineralogical composition estimated using radiative transfer modeling, the Mg# used for the model, the FeO content, a description of the location, and our interpreted origin and transport mechanism.

no.	Region	Latitude (deg)	Longitude (deg)	OL wt.%	OPX wt.%	CPX wt.%	PLG wt.%	Mg #	FeO wt.%	Location	Origin	Transport
1	Crisium	21.6989	54.6704	19.2	9.6	19.2	52	65	13.4	mare	volcanic	volcanic
2	Crisium	15.8966	47.2072	11.9	0	5.1	83	65	5.5	basin rim/ rim of Proclus	primary	impact
3	Crisium	13.7196	65.8679	16.8	0	7.2	76	65	7.6	mare	volcanic	volcanic
4	Crisium	9.4079	59.0341	17.6	0	4.4	78	65	7.3	basin rim	primary	impact
5	Crisium	7.6383	61.2497	29.4	8.4	4.2	58	65	13.3	Lacus Perseverant-iae	primary	volcanic
6	Crisium	7.6282	61.2547	27.6	4.6	13.8	54	65	13.9	Lacus Perseverant-iae	primary	volcanic
7	Crisium	14.9234	54.4541	22	11	22	45	65	15.3	mare/ rim of Picard	primary	impact
8	Crisium	14.4144	66.9138	9.6	0	6.4	84	65	5.0	basin rim	primary	impact
9	Crisium	14.3865	67.0003	14	0	6	80	65	6.4	basin rim	primary	impact
10	Crisium	14.3315	66.1249	15	0	10	75	65	7.6	basin rim	primary	impact
11	Crisium	13.7086	66.5283	10.2	0	6.8	83	65	5.3	basin rim	primary	impact
12	Crisium	13.7196	65.8679	16.8	0	7.2	76	65	7.6	basin rim	primary	impact
13	Crisium	12.9827	65.9520	10	0	15	75	65	7.0	basin rim	primary	impact
14	Crisium	12.8512	64.9754	14.4	0	9.6	76	65	7.3	basin rim	primary	impact
15	Crisium	12.1210	65.5304	3.4	1.7	11.9	83	90	1.6	basin rim	primary	impact
16	Crisium	11.9153	51.1856	12.5	0	12.5	75	65	7.3	basin rim	primary	impact
17	Crisium	11.7644	65.6551	15	0	0	85	65	5.4	basin rim	primary	impact
18	Crisium	10.2783	51.6775	7.2	1.2	3.6	88	65	3.8	basin rim	primary	impact
19	Crisium	10.2368	63.5077	8	0	8	84	65	4.8	basin rim/ rim of Auzout	primary	impact
20	Crisium	10.0227	51.5369	4.8	0	1.2	94	65	2.1	basin rim	primary	impact
21	Crisium	10.1452	62.3141	13.6	0	3.4	83	65	5.7	basin rim	primary	impact
22	Crisium	10.0899	62.3489	13	2.6	10.4	74	65	7.7	basin rim	primary	impact
23	Crisium	9.9410	62.2825	4.8	0	11.2	84	65	4.4	basin rim	primary	impact
24	Crisium	9.5811	54.0010	11.4	0	7.6	81	65	5.9	basin rim	primary	impact
25	Crisium	9.4048	58.5476	11.9	0	5.1	83	65	5.5	basin rim	primary	impact
26	Crisium	8.8143	59.3962	13.2	0	8.8	78	65	6.8	basin rim	primary	impact
27	Crisium	8.7786	59.1960	10.5	0	4.5	85	65	4.9	basin rim	primary	impact
28	Crisium	8.7515	61.2031	8.4	0	5.6	86	65	4.4	basin rim	primary	impact
29	Crisium	8.6764	61.2029	5.2	0	7.8	87	65	3.8	basin rim	primary	impact
30	Crisium	8.6764	61.1979	4.8	0	7.2	88	65	3.5	basin rim	primary	impact
31	Crisium	7.6959	59.1882	8.4	0	12.6	79	65	5.9	basin rim	primary	impact

no.	Region	Latitude (deg)	Longitude (deg)	OL wt.%	OPX wt.%	CPX wt.%	PLG wt.%	Mg #	FeO wt.%	Location	Origin	Transport
32	Crisium	7.2048	59.5332	11.2	0	4.8	84	65	5.2	basin rim	primary	impact
33	Crisium	23.9980	56.7026	12.5	0	12.5	75	65	7.3	basin rim/ rim of Cleomedes G	primary	impact
34	Crisium	14.0967	49.8711	12	0	3	85	65	5.0	basin rim	primary	impact
35	Crisium	13.7752	49.6058	8.1	0	18.9	73	90	2.5	basin rim	primary	impact
36	Crisium	13.3411	49.1077	15.6	5.2	31.2	48	90	4.5	basin rim/ rim of Glaisher	primary	impact
37	Crisium	12.0444	52.3568	5.7	3.8	9.5	81	90	1.9	basin rim	primary	impact
38	Crisium	12.0268	52.4134	10	0	15	75	90	2.4	basin rim	primary	impact
39	Crisium	12.0206	52.3830	12.8	0	19.2	68	90	3.0	basin rim	primary	impact
40	Crisium	14.5959	65.9061	23.2	5.8	0	71	65	9.6	basin rim	primary	impact
41	Crisium	15.0644	68.0661	15.6	0	10.4	74	65	7.9	basin rim	primary	impact
42	Crisium	15.3128	50.4958	9	3.6	5.4	82	65	5.4	mare	volcanic	volcanic
43	Crisium	15.4974	49.3507	16.8	4.8	2.4	76	65	7.7	basin	primary	impact
44	Crisium	16.0977	49.8370	12	0	8	80	65	6.2	mare	volcanic	volcanic
45	Crisium	13.2499	52.5716	20.8	5.2	26	48	65	14.4	mare/ rim of Greaves	volcanic	volcanic
46	Crisium	13.1771	61.4805	18	12	30	40	65	16.0	mare/ rim of Fahrenheit	volcanic	volcanic
47	Crisium	13.2467	61.4606	25.6	19.2	19.2	36	65	17.9	mare/ rim of Fahrenheit	volcanic	volcanic
48	Crisium	13.1368	61.5565	17.4	11.6	29	42	65	15.4	mare/ rim of Fahrenheit	volcanic	volcanic
49	Crisium	13.2653	61.6132	24.4	18.3	18.3	39	65	17.1	mare/ rim of Fahrenheit	volcanic	volcanic
50	Crisium	13.2764	52.6169	14.4	3.6	18	64	65	10.1	mare/ rim of Greaves	volcanic	volcanic
51	Crisium	13.1134	52.7704	16	8	16	60	65	11.3	mare/ rim of Greaves	volcanic	volcanic
52	Crisium	13.3155	53.0051	21.6	10.8	21.6	46	65	15.1	mare/ rim of Greaves	volcanic	volcanic
53	Crisium	14.0450	54.5837	28	16.8	11.2	44	65	16.4	mare/ rim of Picard	primary	impact
54	Crisium	24.2388	65.5550	9.9	9.9	13.2	67	65	9.0	Eimmart A	primary	impact
55	Crisium	24.2338	65.5548	9.6	12.8	9.6	68	65	8.8	Eimmart A	primary	impact
56	Crisium	24.2437	65.5552	7.2	14.4	14.4	64	65	9.4	Eimmart A	primary	impact
57	Crisium	24.2440	65.5443	13.6	10.2	10.2	66	65	9.7	Eimmart A	primary	impact
58	Crisium	24.2339	65.5493	9.6	12.8	9.6	68	65	8.8	Eimmart A	primary	impact

no.	Region	Latitude (deg)	Longitude (deg)	OL wt.%	OPX wt.%	CPX wt.%	PLG wt.%	Mg #	FeO wt.%	Location	Origin	Transport
59	Crisium	24.2389	65.5496	10.2	13.6	10.2	66	65	9.4	Eimmart A	primary	impact
60	Crisium	24.2824	65.6005	13.8	13.8	18.4	54	65	12.4	Eimmart A	primary	impact
61	Humorum	-30.4893	-40.3586	35.7	15.3	0	49	65	16.2	basin rim/ rim of Lee	volcanic	volcanic
62	Humorum	-30.4395	-40.3811	8	1.6	6.4	84	65	12.6	basin rim/ rim of Lee	volcanic	volcanic
63	Humorum	-20.0925	-47.1899	6.6	1.1	3.3	89	65	4.8	basin rim/ rim of	volcanic	volcanic
64	Humorum	-20.0974	-47.1901	6.6	1.1	3.3	89	65	3.5	Mersenius P basin rim/ rim of	volcanic	volcanic
65	Humorum	-20.0922	-47.1952	9.6	0	6.4	84	65	5.0	Mersenius P basin rim/ rim of	volcanic	volcanic
66	Humorum	-18.1328	-44.9976	17.5	0	7.5	75	65	7.9	Mersenius P graben	volcanic	volcanic
67	Humorum	-18.0740	-44.8390	16	0	4	80	65	6.6	graben	volcanic	volcanic
68	Humorum	-17.9740	-43.9851	14	2.8	11.2	72	65	8.2	basin rim	volcanic	volcanic
69	Nectaris	-12.0457	37.5826	14	5.6	8.4	72	65	8.3	mare	volcanic	volcanic
70	Nectaris	-12.6341	37.6236	29.4	4.2	8.4	58	65	13.2	mare	volcanic	volcanic
71	Nectaris	-12.5954	37.5919	22	8.8	13.2	56	65	12.9	mare	volcanic	volcanic
72	Nectaris	-12.5595	37.6165	21	8.4	12.6	58	65	12.3	mare	volcanic	volcanic
73	Nectaris	-12.6487	37.6342	24.6	4.1	12.3	59	65	12.4	mare	volcanic	volcanic
74	Nectaris	-15.4045	30.8238	32.9	9.4	4.7	53	65	14.9	mare	volcanic	volcanic
75	Nectaris	-14.4672	29.9969	30.1	4.3	8.6	57	65	13.5	mare/ rim of Beaumont L	volcanic	volcanic
76	Nectaris	-14.4720	29.9816	28.8	0	7.2	64	65	11.8	mare/ rim of Beaumont L	volcanic	volcanic
77	Nectaris	-14.4478	30.0992	36	0	9	55	65	14.6	mare/ rim of Beaumont L	volcanic	volcanic
78	Nectaris	-11.3502	32.3556	29.4	12.6	0	58	65	13.4	mare	volcanic	volcanic
79	Nectaris	-12.6098	31.1618	17.4	5.8	5.8	71	65	8.9	mare/ rim of Madler D	volcanic	volcanic
80	Nectaris	-15.3554	38.8768	21	8.4	12.6	58	65	12.3	mare	volcanic	volcanic
81	Nectaris	-15.8118	38.3394	24.6	4.1	12.3	59	65	12.4	mare	volcanic	volcanic
82	Nectaris	-15.7446	38.2851	22	13.2	8.8	56	65	13.0	mare	volcanic	volcanic
83	Nectaris	-16.1677	37.5276	22.5	9	13.5	55	65	13.2	mare	volcanic	volcanic
84	Nectaris	-17.6398	39.0112	18.8	4.7	23.5	53	65	13.1	mare	volcanic	volcanic
85	Nectaris	-19.1756	39.1804	16.5	9.9	6.6	67	65	9.8	mare	volcanic	volcanic
86	Nectaris	-10.9305	36.2705	21.6	7.2	7.2	64	65	11.0	mare	volcanic	volcanic
87	Nectaris	-10.9241	36.3109	19	11.4	7.6	62	65	11.3	mare	volcanic	volcanic

no.	Region	Latitude (deg)	Longitude (deg)	OL wt.%	OPX wt.%	CPX wt.%	PLG wt.%	Mg #	FeO wt.%	Location	Origin	Transport
88	Nectaris	-10.9761	36.2562	19.5	7.8	11.7	61	65	11.5	mare	volcanic	volcanic
89	Nectaris	-10.9961	36.2565	15	6	9	70	65	8.9	mare	volcanic	volcanic
90	Nectaris	-11.0196	36.3075	14.8	11.1	11.1	63	65	10.5	mare	volcanic	volcanic
91	Nectaris	-11.0087	36.3327	14.4	7.2	14.4	64	65	10.2	mare	volcanic	volcanic
92	Nectaris	-10.7675	35.8582	15	3	12	70	65	8.8	mare	volcanic	volcanic
93	Nectaris	-10.7702	35.7673	13.2	6.6	13.2	67	65	9.3	mare	volcanic	volcanic
94	Nectaris	-10.8668	35.3595	16.5	6.6	9.9	67	65	9.3	mare	volcanic	volcanic
95	Nectaris	-10.7803	35.7624	14.1	14.1	18.8	53	65	9.7	mare	volcanic	volcanic
96	Nectaris	-11.8212	33.1214	16	8	16	60	65	12.7	mare	volcanic	volcanic
97	Nectaris	-13.9551	35.3810	16	12	12	60	65	11.3	mare	volcanic	volcanic
98	Nectaris	-13.9598	35.3913	20.5	8.2	12.3	59	65	11.3	mare	volcanic	volcanic
99	Nectaris	-13.9599	35.3862	20.5	8.2	12.3	59	65	12.0	mare	volcanic	volcanic
100	Nectaris	-14.1154	35.7115	13.5	13.5	18	55	65	12.2	mare	volcanic	volcanic
101	Nectaris	-10.7068	29.4777	16.8	2.8	8.4	72	65	8.6	mare/ rim of Madler	volcanic	volcanic
102	Nectaris	-10.5920	29.5488	12.6	2.1	6.3	79	65	6.5	mare/ rim of Madler	volcanic	volcanic
103	Nectaris	-10.6627	29.5988	9.2	2.3	11.5	77	65	6.5	mare/ rim of Madler	volcanic	volcanic
104	Nectaris	-11.0438	35.3065	23	9.2	13.8	54	65	13.5	mare	volcanic	volcanic
105	Roche	-20.4963	128.8283	15.2	11.4	11.4	62	65	10.8	Tsiolkovskiy central peak	primary	impact
106	Roche	-33.1920	126.3901	21.2	10.6	21.2	47	65	14.8	Bolyai mare pond	volcanic	volcanic
107	Roche	-20.1662	126.0528	8.4	8.4	11.2	72	65	7.7	wall of Tsiolkovskiy	primary	impact
108	Roche	-47.2139	139.3417	8	6.4	1.6	84	65	4.9	highlands	volcanic	volcanic
109	Roche	-44.2379	138.3202	16.5	13.2	3.3	67	65	9.9	highlands	volcanic	volcanic
110	Roche	-48.1775	124.0329	9.2	9.2	4.6	77	65	6.7	rim of Pauli	volcanic	volcanic
111	Roche	-48.1770	124.0254	10.8	13.5	2.7	73	65	7.9	highlands	volcanic	volcanic

APPENDIX B
SUPPORTING DATA FOR CHAPTER 3

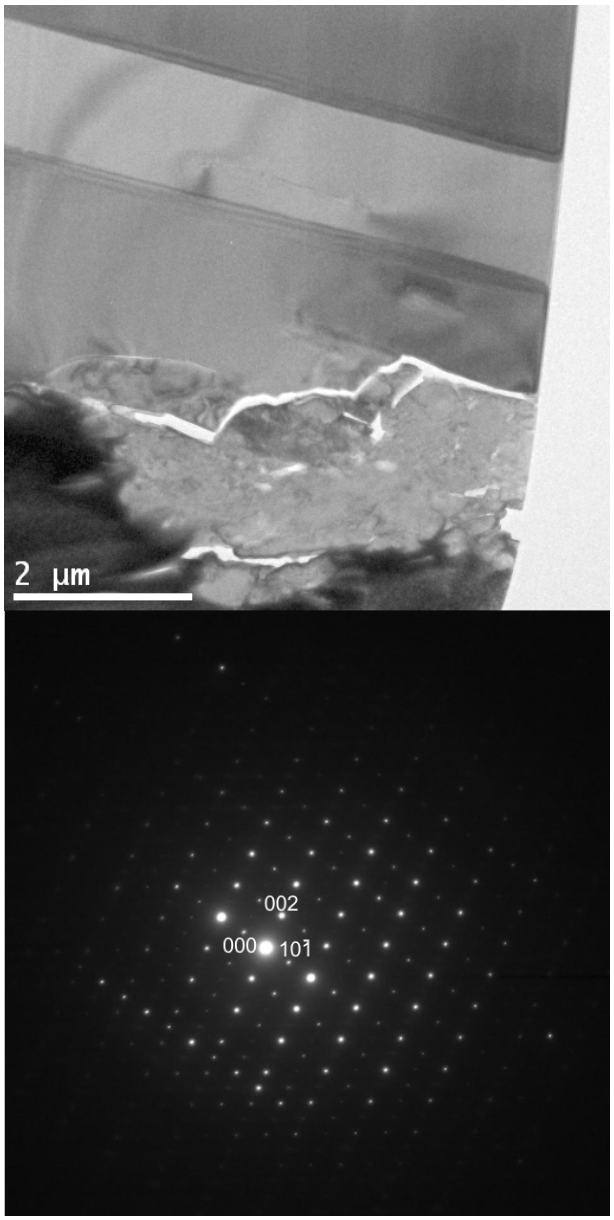

Figure B.1 Top: brightfield image of the host plagioclase (with twinning) from the AVGR kinetic impact experiments (Figure 3.2a). The image is flipped vertically relative to Figure 3.2a. Bottom: the diffraction pattern matches that of bytownite in the [010] zone axis. The reported value for d_{101} is 8.09 Å (Chiari et al., 1984), and the measured value is 8.19 Å. The reported value for d_{002} is 6.36 Å (Chiari et al., 1984), and the measured value is 6.37 Å.

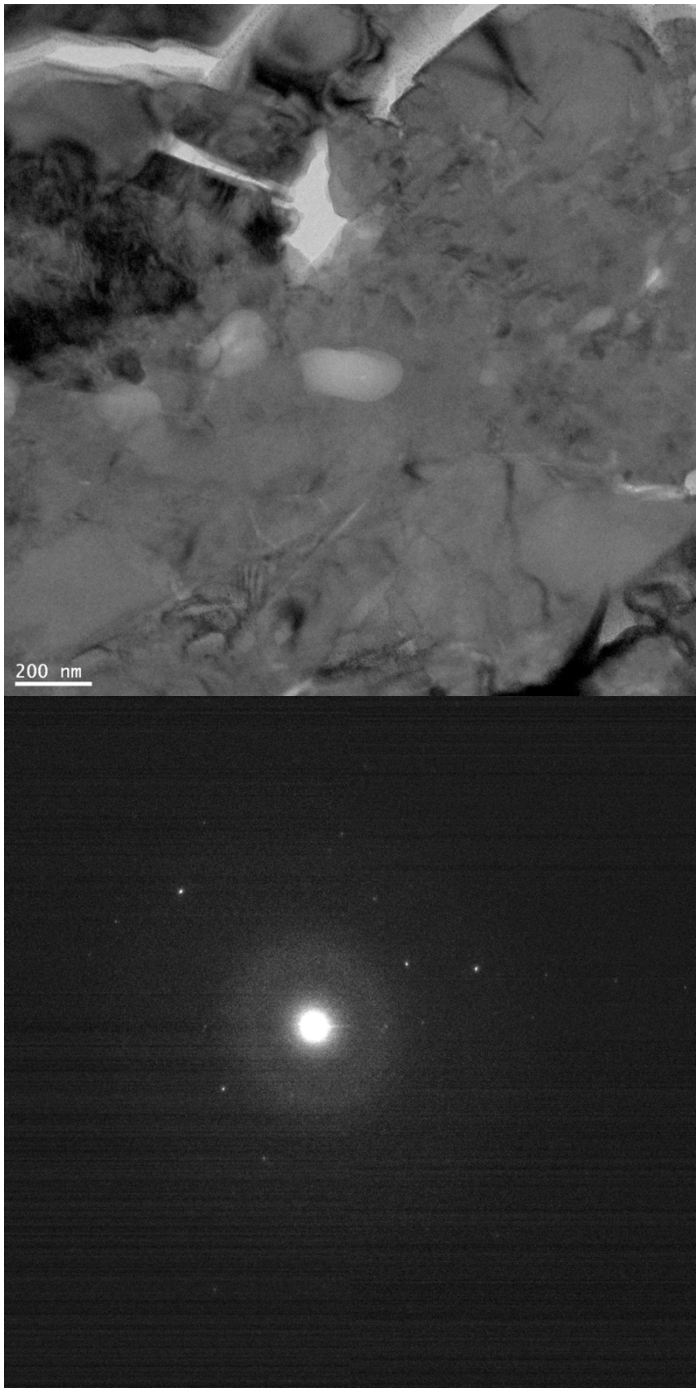

Figure B.2 Top: brightfield image showing the inclusions in the shocked plagioclase from the AVGR kinetic impact experiments (Figure 3.2a). The image is flipped vertically relative to Figure 3.2a. Bottom: the diffuse halo in the corresponding electron diffraction pattern indicates that the inclusions are amorphous. The diffraction spots are from the surrounding plagioclase crystal.

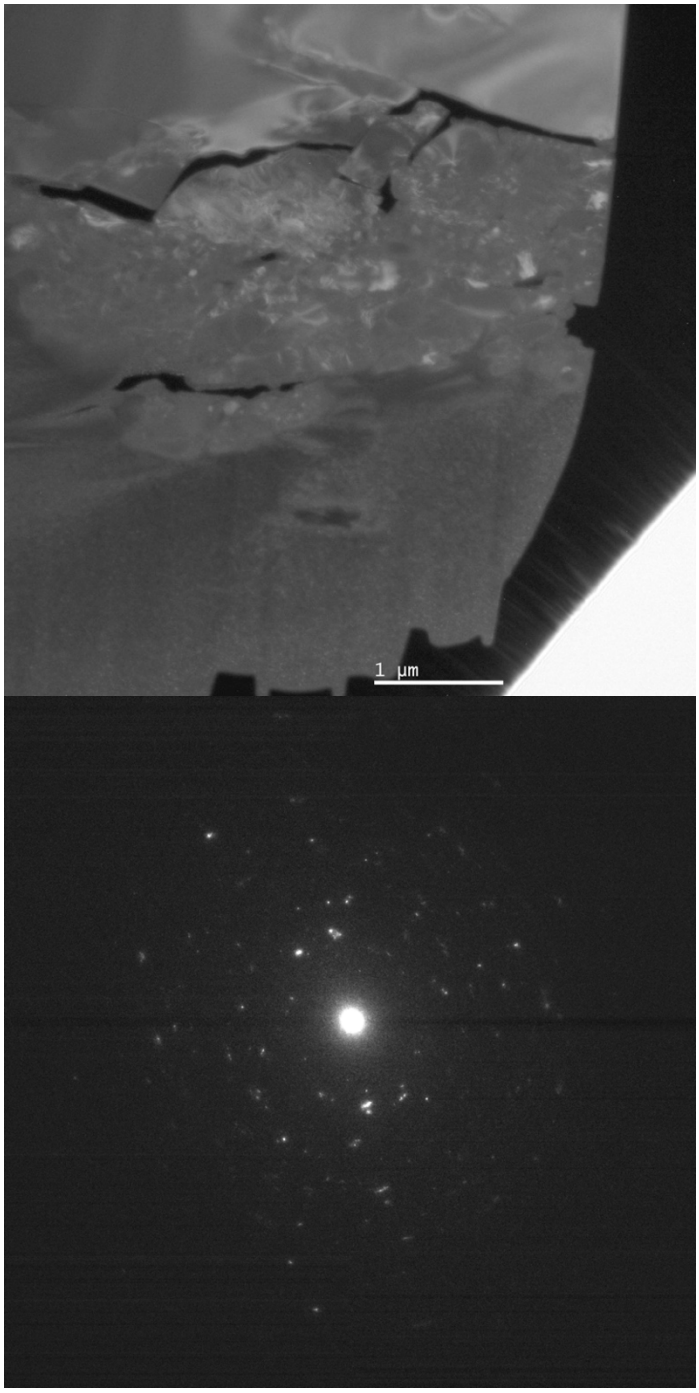

Figure B.3 Top: brightfield image of the shocked surface of the plagioclase from the AVGR kinetic impact experiments (Figure 3.2a). The image is vertically flipped relative to Figure 3.2a. Bottom: the electron diffraction pattern confirms that the surface had been broken and shocked, presumably by the AVGR impact. The polycrstyalline ring pattern is consistent with fragmentation resulting from shock to the single crystal plagioclase substrate.

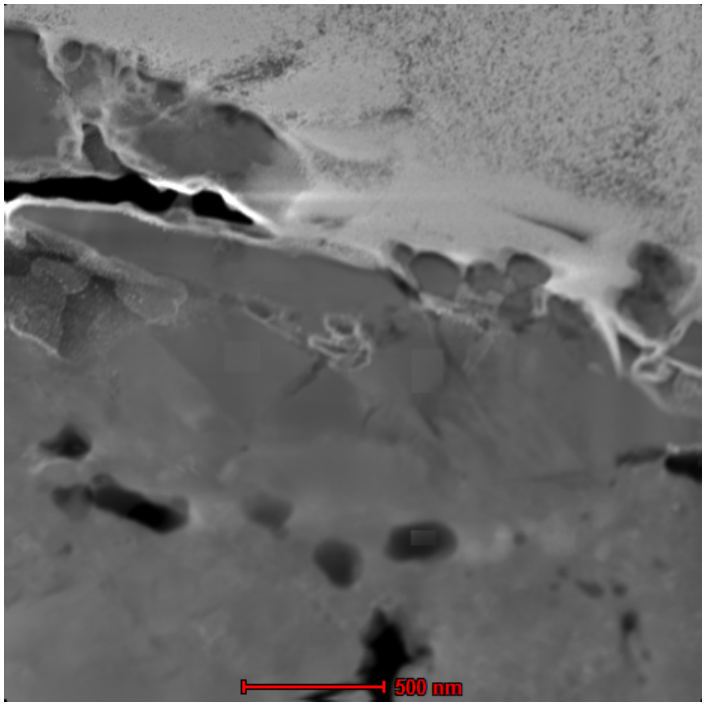

Figure B.4 The polycrystalline texture of the shocked plagioclase surface of the plagioclase grain from the AVGR kinetic impact experiments indicates that it was broken up by the impact shock. The electron diffraction pattern in Figure A.3, above, confirms this.

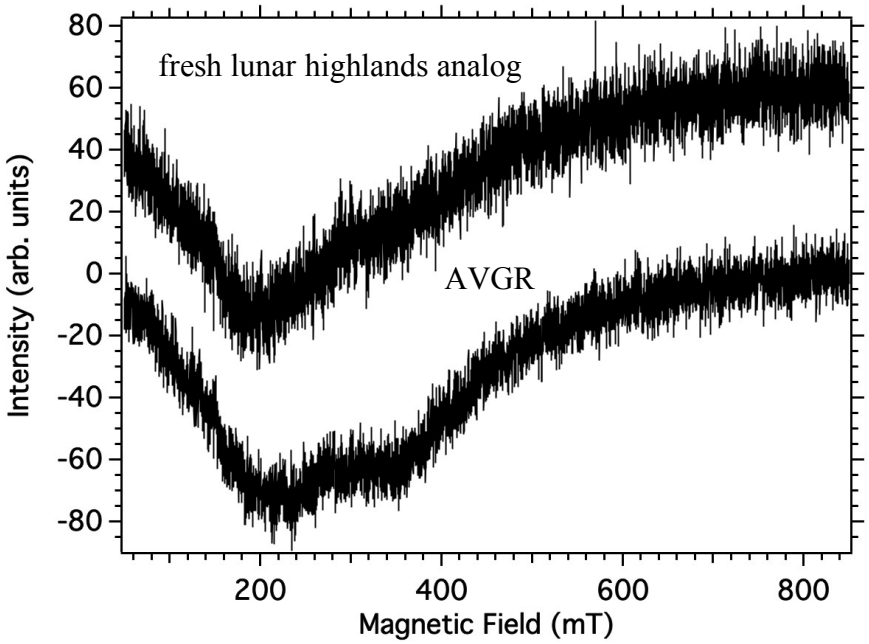

Figure B.5 Electron paramagnetic resonance (EPR) spectra for the fresh lunar highlands analog and the analog weathered by kinetic impacts at the AVGR.

Table B.1 Elemental compositions (atomic %) of the laser-irradiated pyroxene (Figure 3.4) and plagioclase (Figures 3.6 and 3.7) grains, obtained from S/TEM EDS analyses.

	pyroxene (Fig. 3.4)		**plagioclase (Fig. 3.6)**		**plagioclase (Fig. 3.7)**	
atomic %	**rim**	**pyroxene**	**rim**	**plagioclase**	**glass**	**plagioclase**
O	66.9 ± 0.3	68.1 ± 0.8	58.1 ± 0.4	64.1 ± 0.4	61.6 ± 0.8	58.2 ± 0.7
Si	15.8 ± 0.1	14.8 ± 0.1	21.3 ± 0.1	16.1 ± 0.1	16.2 ± 0.1	17.3 ± 0.1
Al	1.54 ± 0.01	1.45 ± 0.01	12.8 ± 0.1	13.34 ± 0.1	12.59 ± 0.1	18.3 ± 0.1
Ca			4.47 ± 0.01	5.11 ± 0.01	3.93 ± 0.01	6.15 ± 0.01
Na			1.86 ± 0.01	1.27 ± 0.01	1.10 ± 0.01	
Fe	4.57 ± 0.01	4.41 ± 0.01	0.15 ± 0.01	0.10 ± 0.01	0.37 ± 0.01	
Mg	11.2 ± 0.2	11.1 ± 0.1	1.32 ± 0.01		4.20 ± 0.01	

Table B.2 Elemental compositions (atomic %) of the plagioclase grain exposed to AVGR kinetic impacts and laser irradiation (Figure 3.10), obtained from S/TEM EDS analyses.

	plagioclase (Fig. 3.10)	
atomic %	**rim**	**plagioclase**
O	72.0 ± 0.9	64.6 ± 0.6
Si	16.5 ± 0.1	26.3 ± 0.1
Al	8.5 ± 0.1	7.6 ± 0.1
Ca	2.57 ± 0.01	1.52 ± 0.01
Fe	0.33 ± 0.01	

Table B.3 Reflectance changes of the lunar highlands analog exposed to AVGR kinetic impacts, laser irradiation, and combined AVGR kinetic impacts and laser irradiation, expressed as a percent change relative to the fresh material. The slope (i.e., continuum) was calculated at 700 and 2120 nm. The change in the 900-nm absorption was calculated based on the band depth at 918 nm (the reflectance at 918 nm subtracted from the continuum at 918 nm).

	AVGR kinetic	**laser 60 min**	**AVGR + laser**
change in reflectance at 750 nm	0.53%	-6.7%	-8.8%
change in slope	-70%	86%	87%
change in 900-nm absorption	-1.4%	-47%	-52%

APPENDIX C

ELEMENTAL COMPOSITIONS OF MATERIALS WEATHERED AT 85 K AND 295 K OBTAINED FROM ENERGY DISPERSIVE X-RAY SPECTROSCOPY (EDS)

Table C.1 Elemental compositions (atomic %) of the olivine grain laser irradiated at 295 K (Figure 4.6), obtained from S/TEM EDS analyses.

	olivine 295 K (Fig. 4.6)		
atomic %	**top of rim**	**bottom of rim**	**olivine**
O	61.5 ± 0.7	62.7 ± 0.7	63.4 ± 0.7
Si	10.9 ± 0.1	12.1 ± 0.1	11.6 ± 0.1
Mg	25.9 ± 0.2	23.3 ± 0.1	23.7 ± 0.1
Fe	1.80 ± 0.01	1.87 ± 0.01	1.33 ± 0.01

Table C.2 Elemental compositions (atomic %) of the olivine grain laser irradiated at 85 K (Figure 4.10), obtained from S/TEM EDS analyses.

	olivine 85 K (Fig. 4.10)			
atomic %	**top of rim**	**middle of rim**	**bottom of rim**	**olivine**
O	60.6 ± 0.8	63.5 ± 0.7	64.9 ± 0.8	65.0 ± 0.8
Si	13.6 ± 0.8	11.5 ± 0.5	11.9 ± 0.1	11.2 ± 0.1
Mg	24.3 ± 0.2	23.5 ± 0.1	21.4 ± 0.1	22.2 ± 0.2
Fe	1.53 ± 0.01	1.45 ± 0.01	1.92 ± 0.01	1.58 ± 0.01

Table C.3 Elemental compositions (atomic %) of the pyroxene grain laser irradiated at 295 K (Figure 4.15), obtained from S/TEM EDS analyses.

	pyroxene 295 K (Fig. 4.15)			
atomic %	**top of rim**	**middle of rim**	**bottom of rim**	**pyroxene**
O	52.0 ± 0.4	59.2 ± 0.5	61.3 ± 0.5	63.7 ± 0.6
Si	24.5 ± 0.1	21.6 ± 0.1	18.5 ± 0.1	17.9 ± 0.1
Mg	15.7 ± 0.1	11.8 ± 0.1	12.6 ± 0.1	11.6 ± 0.1
Fe	5.28 ± 0.02	5.72 ± 0.02	5.84 ± 0.02	5.51 ± 0.02
Al	2.11 ± 0.01	1.65 ± 0.01	1.59 ± 0.01	1.16 ± 0.01
Ca	0.35 ± 0.01		0.16 ± 0.01	0.13 ± 0.01

Table C.4 Elemental compositions (atomic %) of the pyroxene grain laser irradiated at 85 K (Figures 4.18 & 4.19), obtained from S/TEM EDS analyses.

atomic %	pyroxene 85 K (Figs. 4.18 & 4.19)			
	pyroxene	spinel	amorphous rim	pyroxene in rim
O	60.3 ± 0.6	77.7 ± 0.9	60.3 ± 0.6	59.9 ± 0.7
Si	20.3 ± 0.1	0.20 ± 0.01	19.8 ± 0.1	19.9 ± 0.1
Mg	12.8 ± 0.1	14.8 ± 0.1	13.2 ± 0.1	12.5 ± 0.1
Fe	5.62 ± 0.02	6.10 ± 0.03	4.37 ± 0.02	5.53 ± 0.02
Al	0.94 ± 0.01	0.03 ± 0.01	2.07 ± 0.01	2.13 ± 0.01
Ca	0.06 ± 0.01	1.14 ± 0.01	0.24 ± 0.01	

Table C.5 Elemental compositions (atomic %) of the plagioclase grain laser irradiated at 295 K (Figure 4.23), obtained from S/TEM EDS analyses.

atomic %	host plag.	poly-crystalline plag.	glass	plag. in glass (left)	plag. in glass (right)	poly-crystalline plag. (adhered grain)	glass (adhered grain)
O	58.2 ± 0.5	58.7 ± 0.6	55.2 ± 0.5	55.6 ± 0.6	58.5 ± 0.5	60.1 ± 0.7	62.9 ± 0.8
Si	17.8 ± 0.1	24.06 ± 0.1	18.37 ± 0.1	24.42 ± 0.1	17.0 ± 0.1	18.7 ± 0.1	16.6 ± 0.01
Al	15.7 ± 0.1	10.56 ± 0.1	16.76 ± 0.1	11.5 ± 0.1	16.5 ± 0.1	14.5 ± 0.1	13.3 ± 0.01
Ca	5.05 ± 0.01	1.25 ± 0.01	5.71 ± 0.02	2.10 ± 0.01	6.61 ± 0.02	6.66 ± 0.03	4.59 ± 0.02
Na	2.01 ± 0.01	5.40 ± 0.02	1.23 ± 0.01	6.38 ± 0.02	1.42 ± 0.01		1.33 ± 0.01
Mg	0.90 ± 0.01		2.19 ± 0.01				0.92 ± 0.01
Fe	0.29 ± 0.01		0.49 ± 0.01				0.35 ± 0.01

Table C.6 Elemental compositions (atomic %) of the plagioclase grain laser irradiated at 85 K (Figure 4.6), obtained from S/TEM EDS analyses.

	plagioclase 85 K (Fig. 4.25)	
atomic %	**amorphous rim**	**plagioclase**
O	46.5 ± 0.3	54.5 ± 0.3
Si	18.3 ± 0.1	20.7 ± 0.1
Al	24.2 ± 0.1	16.8 ± 0.1
Ca	9.1 ± 0.1	6.4 ± 0.1
Na	1.50 ± 0.01	1.58 ± 0.01
Fe	0.41 ± 0.01	

REFERENCES

Abramov, O., Wong, S. M., & Kring, D. A. (2012). Differential melt scaling for oblique impacts on terrestrial planets. *Icarus*, *218*(2), 906-916.

Adams, J. B., & McCord, T. B. (1970). Remote sensing of lunar surface mineralogy: Implications from visible and near-infrared reflectivity of Apollo 11 samples. *Geochimica et Cosmochimica Acta Supplement*, *1*, 1937.

Adams, J. B. & Goulland, L. H. (1978), Plagioclase feldspar: visible and near infrared diffuse reflectance spectra as applied to remote sensing. *Lunar and Planetary Science Conference Proceedings, 9,* 2901-2909.

Adams, M. A., Schultz, P. H., Sugita, S., & Goguen, J. D. (1997). Impact flash spectroscopy as a means to characterize asteroid surface compositions. In *Lunar and Planetary Science Conference*, *28,* 3.

Anand, M., Taylor, L. A., Nazarov, M. A., Shu, J., Mao, H. K., & Hemley, R. J. (2004). Space weathering on airless planetary bodies: Clues from the lunar mineral hapkeite. *Proceedings of the National Academy of Sciences*, *101*(18), 6847-6851.

Andrews-Hanna, J. C., Asmar, S. W., Head, J. W., Kiefer, W. S., Konopliv, A. S., Lemoine, F. G., Matsuyama, I., Mazarico, E., McGovern, P., Melosh, H. J., Neumann, G. A., Nimmo, F., Phillips, R. J., Smith, D. E., Solomon, S. C., Taylor, G. J., Wieczorek, M. A., Williams, J. G., & Zuber, M. T. (2013). Ancient igneous intrusions and early expansion of the Moon revealed by GRAIL gravity gradiometry. *Science*, *339*(6120), 675-678.

Arnold, J. R. (1979). Ice in the lunar polar regions. *Journal of Geophysical Research: Solid Earth*, *84*(B10), 5659-5668.

Arnold, J. A., Glotch, T. D., Lucey, P. G., Song, E., Thomas, I. R., Bowles, N. E., & Greenhagen, B. (2016). Constraints on olivine-rich rock types on the Moon as observed by Diviner and M^3: Implications for the formation of the lunar crust. *Journal of Geophysical Research: Planets*, *doi: 10.1002/2015JE004874.*

Baker, D. M., Head, J. W., Fassett, C. I., Kadish, S. J., Smith, D. E., Zuber, M. T., & Neumann, G. A. (2011). The transition from complex crater to peak-ring basin on

the Moon: New observations from the Lunar Orbiter Laser Altimeter (LOLA) instrument. *Icarus*, *214*(2), 377-393.

Baker, D. M., Head, J. W., Neumann, G. A., Smith, D. E., & Zuber, M. T. (2012). The transition from complex craters to multi-ring basins on the Moon: Quantitative geometric properties from Lunar Reconnaissance Orbiter Lunar Orbiter Laser Altimeter (LOLA) data. *Journal of Geophysical Research: Planets*, *117*(E12).

Baker, D. M. H. & Head, J. W. III (2015). Constraints on the depths of origin of peak rings on the Moon from Moon Mineralogy Mapper data, *Icarus, 258*, 164-180.

Basu, A., McKay, D. S., & Fruland, R. M. (1977). Petrography, mineralogy and source rocks of Luna 24 drill core soils. *LPI Contributions*, *304*, 18.

Basu, A. (2005). Nanophase Fe^0 in lunar soils. *Journal of earth system science*, *114*(3), 375-380.

Bell, J. F., & Hawke, B. R. (1995). Compositional variability of the Serenitatis/Tranquillitatis region of the Moon from telescopic multispectral imaging and spectroscopy. *Icarus*, *118*(1), 51-68.

Bentley, M. S., Ball, A. J., Potter, D. K., Wright, I. P., & Zarnecki, J. C. (2009). In situ multi-frequency measurements of magnetic susceptibility as an indicator of planetary regolith maturity. *Planetary and Space Science*, *57*(12), 1491-1499.

Bentley, M. S., Ball, A. J., Wright, I. P., & Zarnecki, J. C. (2011). On the application of magnetic methods for the characterisation of space weathering products. *Planetary and Space Science*, *59*(1), 79-91.

Besse, S., Sunshine, J., Staid, M., Boardman, J., Pieters, C., Guasqui, P., Malaret, E., McLaughlin, S., Yokota Y., Li, J.-Y. (2013) A visible and near-infrared photometric correction for Moon Mineralogy Mapper (M^3). *Icarus 222*, 229-242.

Bibring, J. P., Duraud, J. P., Durrieu, L., Jouret, C., Maurette, M., & Meunier, R. (1972). Ultrathin amorphous coatings on lunar dust grains. *Science*, *175*(4023), 753-755.

Bibring, J. P., Langevin, Y., Maurette, M., Meunier, R., Jouffrey, B., & Jouret, C. (1974). Ion implantation effects in “cosmic” dust grains. *Earth and Planetary Science Letters*, *22*(3), 205-214.

Blewett, D. T., Robinson, M. S., Denevi, B. W., Gillis-Davis, J. J., Head, J. W., Solomon, S. C., Holsclaw, G. M., & McClintock, W. E. (2009). Multispectral images of

Mercury from the first MESSENGER flyby: Analysis of global and regional color trends. *Earth and Planetary Science Letters*, *285*(3), 272-282.

Bradley, J. P. (1994). Irradiated Grains in Interplanetary Dust from Comets. *Science*, *265*, 12.

Bradley, J. P., & Dai, Z. R. (2009). Analytical SuperSTEM for extraterrestrial materials research. *Meteoritics & Planetary Science*, *44*(10), 1627-1642.

Bradley, J. P., Ishii, H. A., Gillis-Davis, J. J., Ciston, J., Nielsen, M. H., Bechtel, H. A., & Martin, M. C. (2014). Detection of solar wind-produced water in irradiated rims on silicate minerals. *Proceedings of the National Academy of Sciences*, *111*(5), 1732-1735.

Bringa, E. M., Kucheyev, S. O., Loeffler, M. J., Baragiola, R. A., Tielens, A. G. G. M., Dai, Z. R., ... & Felter, T. E. (2007). Energetic processing of interstellar silicate grains by cosmic rays. *The Astrophysical Journal*, *662*(1), 372.

Brunetto, R., Romano, F., Blanco, A., Fonti, S., Martino, M., Orofino, V., & Verrienti, C. (2006). Space weathering of silicates simulated by nanosecond pulse UV excimer laser. *Icarus*, *180*(2), 546-554.

Bruck Syal, M., & Schultz, P. H. (2014). Spatially-Resolved Spectroscopy of Impact-Generated Vapor Plumes. In *Lunar and Planetary Science Conference*, *45,* 2760.

Burbine, T. H., & Binzel, R. P. (2002). Small main-belt asteroid spectroscopic survey in the near-infrared. *Icarus*, *159*(2), 468-499.

Burke, D. J., Dukes, C. A., Kim, J. H., Shi, J., Famá, M., & Baragiola, R. A. (2011). Solar wind contribution to surficial lunar water: Laboratory investigations. *Icarus*, *211*(2), 1082-1088.

Burns, R. G. (1970), *Mineralogical Applications of Crystal Field Theory*, 1st ed., 224 pp., Cambridge University Press, New York.

Burns, R. G. (1993). *Mineralogical applications of crystal field theory*, Vol. 5, Cambridge University Press, New York.

Bussey, D. B. & Spudis, P. D. (2000). Compositional studies of the Orientale, Humorum, Nectaris, and Crisium lunar basins. *Journal of Geophysical Research: Planets*, *105*(E2), 4235-4243.

Cahill, J. T. S., Lucey, P. G., & Wieczorek, M. A. (2009). Compositional variations of the lunar crust: Results from radiative transfer modeling of central peak spectra. *Journal of Geophysical Research: Planets*, *114*(E9).

Cassanelli, J. P., & Head, J. W. (2016). Did the Orientale impact melt sheet undergo large-scale igneous differentiation by crystal settling? *Geophysical Research Letters*, *43*(21).

Chiari, G., Benna, P., & Bruno, E. (1984). The structure of bytownite (An_{85}). A new refinement. *Zeitschrift für Kristallographie-Crystalline Materials*, *169*(1-4), 35-50.

Christoffersen, R., Cintala, M. J., Keller, L. P., See, T. H., & Horz, F. (2013). Nanoscale mineralogy and composition of experimental regolith agglutinates produced under asteroidal impact conditions. In *Lunar and Planetary Science Conference*, *44,* 2605.

Christoffersen, R., Loeffler, M. J., Rahman, Z., Dukes, C., & IMPACT Team. (2017). Experimental Hypervelocity Dust Impact in Olivine: FIB/TEM Characterization of Micron-Scale Craters with Comparison to Natural and Laser-Simulated Small-Scale Impact Effects. In *Lunar and Planetary Science Conference*, *48*, 2578.

Cheng, A. F., Michel, P., Jutzi, M., Rivkin, A. S., Stickle, A., Barnouin, O., Ernst, C., Atchison, J., Pravec, P., Richardson, D. C., AIDA team, & AIM team (2016). Asteroid impact & deflection assessment mission: kinetic impactor. *Planetary and Space Science*, *121*, 27-35.

Cintala, M. J., & Horz, F. (1988). The effects of impact velocity on the evolution of experimental regoliths. In *Lunar and Planetary Science Conference Proceedings*, *18,* 409-422.

Cintala, M. J. (1992). Impact-induced thermal effects in the lunar and Mercurian regoliths. *Journal of Geophysical Research: Planets*, *97*(E1), 947-973.

Cintala, M. J., & Grieve, R. A. (1998). Scaling impact melting and crater dimensions: Implications for the lunar cratering record. *Meteoritics & Planetary Science*, *33*(4), 889-912.

Cloutis, E. A., Sanchez, J. A., Reddy, V., Gaffey, M. J., Binzel, R. P., Burbine, T. H., Hardersen, P. S., Hiroi, T., Lucey, P. G., Sunshine, J. M., & Tait, K. T. (2015).

Olivine–metal mixtures: Spectral reflectance properties and application to asteroid reflectance spectra. *Icarus*, *252*, 39-82.

Colaprete, A., Schultz, P., Heldmann, J., Wooden, D., Shirley, M., Ennico, K., Hermalyn, B., Marshall, W., Ricco, A., Elphic, R. C., Goldstein, D., Summy, D., Bart, G. D., Asphaug, E., Korycanksy, D., Landis, D., & Sollitt, L. (2010). Detection of water in the LCROSS ejecta plume. *Science*, *330*(6003), 463-468.

Corley, L. M., Gillis-Davis, J. J., Lucey, P. G., & Trang, D. (2017). The Effect of Temperature on the Reflectance Spectra of Pyroxene and a Highlands Analog Weathered by Laser Irradiation. In *Lunar and Planetary Science Conference, 48,* 1698.

Corley, L. M., McGovern, P. J., Kramer, G. Y., Lemelin, M., Trang, D., Gillis-Davis, J. J., Taylor, G. J., Powell, K. E., Kiefer, W. S., Wieczorek, M., & Zuber, M. T. (2018). Olivine-bearing lithologies on the Moon: Constraints on origins and transport mechanisms from M3 spectroscopy, radiative transfer modeling, and GRAIL crustal thickness. *Icarus*, *300*, 287-304.

Crites, S. T., & Lucey, P. G. (2015). Revised mineral and Mg# maps of the Moon from integrating results from the Lunar Prospector neutron and gamma-ray spectrometers with Clementine spectroscopy. *American Mineralogist*, *100*(4), 973-982.

Crown, D. & Pieters, C. M. (1987). Spectral properties of plagioclase and pyroxene mixtures and the interpretation of lunar soil spectra. *Icarus*, 72, 317-390.

Denevi, B. W., Robinson, M. S., Boyd, A. K., Sato, H., Hapke, B. W., & Hawke, B. (2014). Characterization of space weathering from Lunar Reconnaissance Orbiter Camera ultraviolet observations of the Moon. *Journal of Geophysical Research: Planets*, *119*(5), 976-997.

Dhingra, D., Pieters, C. M., & Head, J. W. (2015). Multiple origins for olivine at Copernicus crater. *Earth and Planetary Science Letters*, *420*, 95-101.

Donaldson Hanna, K. L., Cheek, L. C., Pieters, C. M., Mustard, J. F., Greenhagen, B. T., Thomas, I. R., & Bowles, N. E. (2014). Global assessment of pure crystalline plagioclase across the Moon and implications for the evolution of the primary crust. *Journal of Geophysical Research: Planets*, *119*(7), 1516-1545.

Duke, M. B., Woo, C. C., Bird, M. L., Sellers, G. A., & Finkelman, R. B. (1970). Lunar soil: Size distribution and mineralogical constituents. *Science*, *167*(3918), 648-650.

Dukes, C. A., Baragiola, R. A., & McFadden, L. A. (1999). Surface modification of olivine by H+ and He+ bombardment. *Journal of Geophysical Research: Planets*, *104*(E1), 1865-1872.

Dymek, R. F., A. L. Albee, and A. A. Chodos (1975), Comparative petrology of lunar cumulate rocks of possible primary origin: Dunite 72415, troctolite 76535, norite 78235, and anorthosite 62237. *Lunar and Planetary Science Conference Proceedings*, *6*, 301-341.

Elardo, S. M., Draper, D. S., & Shearer, C. K. (2011). Lunar Magma Ocean crystallization revisited: Bulk composition, early cumulate mineralogy, and the source regions of the highlands Mg-suite. *Geochimica et Cosmochimica Acta*, *75*(11), 3024-3045.

Elkins-Tanton, L. T., Burgess, S., & Yin, Q. Z. (2011). The lunar magma ocean: Reconciling the solidification process with lunar petrology and geochronology. *Earth and Planetary Science Letters*, *304*(3), 326-336.

Feldman, W. C., Lawrence, D. J., Elphic, R. C., Barraclough, B. L., Maurice, S., Genetay, I., & Binder, A. B. (2000). Polar hydrogen deposits on the Moon. *Journal of Geophysical Research: Planets*, *105*(E2), 4175-4195.

Fischer, E. M., & Pieters, C. M. (1994). Remote determination of exposure degree and iron concentration of lunar soils using VIS-NIR spectroscopic methods. *Icarus*, *111*(2), 475-488.

Fischer, E. M., & Pieters, C. M. (1996). Composition and exposure age of the Apollo 16 Cayley and Descartes regions from Clementine data: Normalizing the optical effects of space weathering. *Journal of Geophysical Research: Planets*, *101*(E1), 2225-2234.

French, B. M. (1998). Traces of catastrophe: A handbook of shock-metamorphic effects in terrestrial meteorite impact structures. *Technical Report, LPI-Contrib-954*.

Fuller, M., Wu, Y., & Wasilewski, P. J. (1975). The magnetic characteristics of returned lunar samples and their implications for regolith processes. S*ymposium on Origin and Evolution of the Lunar Regolith, The Moon*, *13*(1-3), 327-338.

Gault, D. E., Hörz, F., & Hartung, J. B. (1972). Effects of microcratering on the lunar surface. In *Lunar and Planetary Science Conference Proceedings*, *3,* 2713.

Gillis, J. J., Jolliff, B. J., Korotev, R. L. (2004). Lunar surface geochemistry: Global concentrations of Th, K, and FeO as derived from Lunar Prospector and Clementine data. *Geochim. Cosmochim. Acta 68,* 3791-3805.

Gillis-Davis, J. J., Lucey, P. G., Hammer, J. E., & Denevi, B. B. (2008). Syntheses and Reflectance Analyses of Lunar Green Glass Compositions: Information to Improve Understanding of Remotely Sensed Spectral Data. In *Lunar Planetary Science Conference, 39,* 1535.

Gillis-Davis, J. J., Lucey, P. G., Bradley, J. P., Ishii, H. A., Kaluna, H. M., Misra, A., & Connolly, H. C. (2017). Incremental laser space weathering of Allende reveals non-lunar like space weathering effects. *Icarus*, *286*, 1-14.

Gladstone, G. R., Hurley, D. M., Retherford, K. D., Feldman, P. D., Pryor, W. R., Chaufray, J. Y., Versteeg, M., Greathouse, T. K., Steffl, A. J., Throop, H., Parker, J. W., Kaufmann, D. E., Egan, A. F., Davis, M. W., Slater, D. C., Mukherjee, J., Miles, P. F., Hendrix, A. R., Colaprete, A., & Stern, S. A. (2010). LRO-LAMP observations of the LCROSS impact plume. *Science*, *330*(6003), 472-476.

Gooley, R., Brett, R., Warner, J., & Smyth, J. R. (1974). A lunar rock of deep crustal origin: Sample 76535, *Geochimica et Cosmochimica Acta*, *38,* 1329-1339.

Green, R. O., Pieters, C., Mouroulis, P., Eastwood, M., Boardman, J., Glavich, T., Isaacson, P., Annadurai, M., Besse, S., Barr, D., Buratti, B., Cate, D., Chatterjee, A., Green, R., Haemmerlee, V., Head, J., Hovland, L., Hyman, S., Klima, R., Koch, T., Kramer, G., Kumar, A. S. K., Lee, K., Lundeen, S., Malaret, E., McCord, T., McLaughlin, S., Mustard, J., Nettles, J., Petro, N., Plourde, K., Racho, C., Rodriguez, J., Runyon, C., Sellar, G., Smith, C., Sobel, H., Staid, M., Sunshine, J., Taylor, L., Thaisen, K., Tompkins, S., Tseng, H., Vane, G., Varanasi, P., White, M., & Wilson, D. (2011). The Moon Mineralogy Mapper (M^3) imaging spectrometer for lunar science: Instrument description, calibration,

on-orbit measurements, science data calibration and on-orbit validation. *Journal of Geophysical Research: Planets*, *116*(E10).

Griguere, T. A., Hawke, B., Blewett, D. T., Bussey, D. B. J., Lucey, P. G., Smith, G. A., Spudis, P. D., & Taylor, G. J. (2003). Remote sensing studies of the Lomonosov-Fleming region of the Moon. *Journal of Geophysical Research: Planets*, *108*(E11).

Gross, J., & Treiman, A. H. (2011). Unique spinel-rich lithology in lunar meteorite ALHA 81005: Origin and possible connection to M3 observations of the farside highlands. *Journal of Geophysical Research: Planets*, *116*(E10).

Grün, E., Fechtig, H., Hanner, M. S., Kissel, J., Lindblad, B. A., Linkert, D., Morfill, G., & Zook, H. A. (1991). In-situ exploration of dust in the solar system and initial results from the Galileo Dust Detector. In *Origin and Evolution of Interplanetary Dust*, 21-28.

Hapke, B. (1966). Optical properties of the moon's surface. *The Nature of the Lunar Surface,* W. Hess, D. Menzel, J. O'Keefe, 141–154.

Hapke, B. W., Cohen, A. J., Cassidy, W. A., & Wells, E. N. (1970). Solar radiation effects on the optical properties of Apollo 11 samples. *Geochimica et Cosmochimica Acta Supplement*, *1*, 2199.

Hapke, B. (1973). Darkening of silicate rock powders by solar wind sputtering. *The Moon*, *7*(3-4), 342-355.

Hapke, B., Cassidy, W., & Wells, E. (1975). Effects of vapor-phase deposition processes on the optical, chemical, and magnetic properties OE the lunar regolith. *Earth, Moon, and Planets*, *13*(1), 339-353.

Hapke, B. (1981). Bidirectional reflectance spectroscopy: 1. Theory. *Journal of Geophysical Research: Solid Earth (1978–2012)*, *86*(B4), 3039-3054.

Hapke, B. (1993). *Theory of Reflectance and Emittance Spectroscopy*, Topics in Remote Sensing (No. 3), Cambridge University Press, New York.

Hapke, B. (2001). Space weathering from Mercury to the asteroid belt. *Journal of Geophysical Research: Planets, 106*(E5), 10039-10073.

Hartmann, W. K. (1973). Ancient lunar mega-regolith and subsurface structure. *Icarus*, *18*(4), 634-636.

Hartmann, W. K., & Davis, D. R. (1975). Satellite-sized planetesimals and lunar origin. *Icarus*, *24*(4), 504-515.

Hawke, B.R., Head, J.W. (1977). Impact melt on lunar crater rims. In: Roddy, D.J., Pepin, R.O., Merrill, R.B. (Eds.), Impact and Explosion Cratering: Planetary and Terrestrial Implications. Pergamon Press, New York, NY, pp. 815–841.

Hawke, B. R., & Bell, J. F. (1982). Remote sensing studies of lunar dark-halo impact craters-Preliminary results and implications for early volcanism. In *Lunar and Planetary Science Conference Proceedings, Vol. 12*, pp. 665-678.

Hazen, R. M., Mao, H. K., & Bell, P. M. (1977). Effects of compositional variation on absorption spectra of lunar olivines. *Lunar and Planetary Science Conference Proceedings*, *8,* 1081-1090.

Head, J. W., Adams, J. B., McCord, T. B., Pieters, C., & Zisk, S. (1978). Regional stratigraphy and geologic history of Mare Crisium. In *Mare Crisium: The view from Luna 24* (pp. 43-74).

Head, J. W. & Wilson, L. (1992). Lunar mare volcanism: Stratigraphy, eruption conditions, and the evolution of secondary crusts. *Geochimica et Cosmochimica Acta*, *56*(6), 2155-2175.

Head, J. W., & Wilson, L. (1993). Lunar graben formation due to near-surface deformation accompanying dike emplacement. *Planetary and Space Science*, *41*(10), 719-727.

Head, J. W., & Wilson, L. (2017). Generation, ascent and eruption of magma on the Moon: New insights into source depths, magma supply, intrusions and effusive/explosive eruptions (Part 2: Predicted emplacement processes and observations). *Icarus*, *283*, 176-223.

Hendrix, A. R., & Vilas, F. (2006). The effects of space weathering at UV wavelengths: S-class asteroids. *The Astronomical Journal*, *132*(3), 1396.

Hendrix, A. R., Retherford, K. D., Randall Gladstone, G., Hurley, D. M., Feldman, P. D., Egan, A. F., Kaufmann, D. E., Miles, P. F., Parker, J. W., Horvath, D., Rojas, P. M., Versteeg, M. H., Davis, M. W., Greathouse, T. K., Mukherjee, J., Steffl, A. J., Pryor, W. R., & Stern, S. A. (2012). The lunar far-UV albedo: Indicator of hydration and weathering. *Journal of Geophysical Research: Planets*, *117*(E12).

Herbert, F. (1980). Time-dependent lunar density models. *Lunar and Planetary Science Conference Proceedings*, *11,* 2015-2030.

Hess, P.C. , & Parmentier, E.M. (1995). A model for the thermal and chemical evolution of the Moon's interior: implications for the onset of mare volcanism. *Earth and Planetary Science Letters 134 (3),* 501–514.

Hiesinger, H., Head, J.W. III, Wolf, U., Jaumann, R., & Neukum, G. (2011) Ages and stratigraphy of lunar mare basalts: A synthesis. *Special Papers of the Geological Society of America, 477,* 1-51.

Hood, L. L., Zakharian, A., Halekas, J., Mitchell, D. L., Lin, R. P., Acuña, M. H., & Binder, A. B. (2001). Initial mapping and interpretation of lunar crustal magnetic anomalies using Lunar Prospector magnetometer data. *Journal of Geophysical Research: Planets*, *106*(E11), 27825-27839.

Hörz, F., & Schaal, R. B. (1981). Asteroidal agglutinate formation and implications for asteroidal surfaces. *Icarus, 46,* 337-353.

Hörz, F., Cintala, M. J., See, T. H., Cardenas, F., & Thompson, T. D. (1984). Grain size evolution and fractionation trends in an experimental regolith. *Journal of Geophysical Research: Solid Earth*, *89*(S01).

Hörz, F. & Cintala, M. (1997). The Barringer Award Address presented 1996 July 25, Berlin, Germany: Impact experiments related to the evolution of planetary regoliths. *Meteoritics & Planetary Science 32*, 179-209.

Housen, K. R., Schmidt, R. S., & Holsapple, K. A. (1983). Crater ejecta scaling laws: Fundamental forms based on dimensional analysis. *Journal of Geophysical Research, 88,* 2485-2499.

Housley, R. M., Grant, R. W., & Paton, N. E. (1973). Origin and characteristics of excess Fe metal in lunar glass welded aggregates. *Lunar and Planetary Science Conference Proceedings*, *4,* 2737.

Hurwitz, D. M., & Kring, D. A. (2014). Differentiation of the South Pole–Aitken basin impact melt sheet: Implications for lunar exploration. *Journal of Geophysical Research: Planets*, *119*(6), 1110-1133.

Isaacson, P. J., & Pieters, C. M. (2010). Deconvolution of lunar olivine reflectance spectra: Implications for remote compositional assessment. *Icarus*, *210*(1), 8-13.

Isaacson, P. J., Pieters, C. M., Besse, S., Clark, R. N., Head, J. W., Klima, R. L., Mustard, J. F., Petro, N. E., Staid, M. I., Sunshine, J. M., Taylor, L. A., Thaisen, K. G., & Tompkins, S. (2011). Remote compositional analysis of lunar olivine-rich lithologies with Moon Mineralogy Mapper (M^3) spectra. *Journal of Geophysical Research: Planets*, *116*(E6).

Isaacson, P. J., Klima, R. L., Sunshine, J. M., Cheek, L. C., Pieters, C. M., Hiroi, T., Dyar, D. M., Lane, M., & Bishop, J. (2014). Visible to near-infrared optical properties of pure synthetic olivine across the olivine solid solution. *American Mineralogist*, *99*(2-3), 467-478.

Ishii, H. A., Joswiak, D., Bradley, J. P., Teslich, N., Matzel, J., Hutcheon, I. D., Brownlee, D. E., Matrajt, G., MacPherson, G., & McKeegan, K. D. (2009). Enabling Al-Mg Isotopic Measurements on Comet Wild 2's Micro-CAIs. In *Lunar and Planetary Science Conference*, *40,* 2288.

Ishii, H. A., Stadermann, F. J., Floss, C., Joswiak, D., Bradley, J. P., Teslich, N., Brownlee, D. E., Matrajt, G., MacPherson, G., & McKeegan, K. D. (2010a). Lack of Evidence for In Situ Decay of Aluminum-26 in Comet 81P/Wild 2 CAI-like Refractory Particles' Inti'and'Coki'. In *Lunar and Planetary Science Conference*, *41,* 2317.

Ishii, H. A., Krot, A. N., Bradley, J. P., Keil, K., Nagashima, K., Teslich, N., Jacobsen, B., & Yin, Q. Z. (2010b). Discovery, mineral paragenesis, and origin of wadalite in a meteorite. *American Mineralogist*, *95*(4), 440-448.

Jette, E. R., & Foote, F. (1935). Precision determination of lattice constants. *The Journal of Chemical Physics*, *3*(10), 605-616.

Johnson, J. R., & Hörz, F. (2003). Visible/near-infrared spectra of experimentally shocked plagioclase feldspars. *Journal of Geophysical Research: Planets*, *108*(E11).

Jolliff, B. L., Gillis, J. J., Haskin, L. A., Korotev, R. L., & Wieczorek, M. A. (2000). Major lunar crustal terranes: Surface expressions and crust-mantle origins. *Journal of Geophysical Research: Planets (1991–2012)*, *105*(E2), 4197-4216.

Kaluna, H. M., & Gillis-Davis, J. J. (2017). Contexting Experimental Space Weathering with Lunar Soil Maturity. In *Lunar and Planetary Science Conference*, *48,* 2540.

Kaur, P., Chauhan, P., Rajawat, A. S., & Kumar, A. K. (2015). Study of olivine-rich dark halo crater–Beaumont L in Mare Nectaris using high resolution remote sensing data. *Planetary and Space Science*, *109*, 92-105.

Keller, L. P., & McKay, D. S. (1993). Discovery of vapor deposits in the lunar regolith. *Science*, *261*(5126), 1305-1308.

Keller, L. P., & McKay, D. S. (1997). The nature and origin of rims on lunar soil grains. *Geochimica et Cosmochimica Acta*, *61*(11), 2331-2341.

Keller, L. P., & Clemett, S. J. (2001). Formation of nanophase iron in the lunar regolith. In *Lunar and Planetary Science Conference*, *32,* 2097.

Kiefer, W. S. (2013). Gravity constraints on the subsurface structure of the Marius Hills: The magmatic plumbing of the largest lunar volcanic dome complex. *Journal of Geophysical Research: Planets*, *118*(4), 733-745.

Kissel, J., & Krueger, F. R. (1987). Ion formation by impact of fast dust particles and comparison with related techniques. *Applied Physics A: Materials Science & Processing*, *42*(1), 69-85.

Korotev, R. L., Jolliff, B. L., Zeigler, R. A., Gillis, J. J., Haskin, L. A. (2003). Feldspathic lunar meteorites and their implications for compositional remote sensing of the lunar surface and the composition of the lunar crust. *Geochimica et Cosmochimica Acta 67,* 4895-4923.

Kramer, G. Y., Kring, D. A., Nahm, A. L., & Pieters, C. M. (2013). Spectral and photogeologic mapping of Schrödinger Basin and implications for post-South Pole-Aitken impact deep subsurface stratigraphy. *Icarus*, *223*(1), 131-148.

Kring, D. A., McGovern, P. J., Potter, R. W. K., Collins, G. S. , Grange, M. L., & Nemchin, A. A. (2015) Was an epoch of lunar magmatism triggered by the South Pole-Aitken basin impact? *Workshop on Early Solar System Bombardment III,* Abstract #3009.

Lemelin, M., Lucey, P. G., Song, E., & Taylor, G. J. (2015). Lunar central peak mineralogy and iron content using the Kaguya Multiband Imager: Reassessment

of the compositional structure of the lunar crust. *Journal of Geophysical Research: Planets, 120.*

Li, S., Hsu, W., Guan, Y., Wang, L., & Wang, Y. (2016). Petrogenesis of the Northwest Africa 4898 high-Al mare basalt. *Meteoritics & Planetary Science, 51*(7), 1268-1288.

Li, S., Lucey, P. G., Milliken, R. E., Hayne, P. O., Fisher, E., Williams, J. P., Hurley, D. M., & Elphic, R. C. (2018). Direct evidence of surface exposed water ice in the lunar polar regions. *Proceedings of the National Academy of Sciences*, *115*(36), 8907-8912.

Loeffler, M. J., Baragiola, R. A., & Murayama, M. (2008). Laboratory simulations of redeposition of impact ejecta on mineral surfaces. *Icarus, 196(1),* 285-292.

Loeffler, M., Dukes, C., Christoffersen, R., Baragiola, R., 2016. Space weathering of silicates simulated by successive laser irradiation: In situ reflectance measurements of Fo_{90}, Fo_{99}+, and SiO_2. *Meteoritics & Planetary Science, 51***,** 261-275.

Loferski, P. J., & Arculus, R. J. (1993). Multiphase inclusions in plagioclase from anorthosites in the Stillwater Complex, Montana: implications for the origin of the anorthosites. *Contributions to Mineralogy and Petrology, 114(1),* 63-78.

Love, S. G., & Brownlee, D. E. (1993). A direct measurement of the terrestrial mass accretion rate of cosmic dust. *Science, 262(5133),* 550-553.

Lucey, P. G. (1998). Model near-infrared optical constants of olivine and pyroxene as a function of iron content. *Journal of Geophysical Research: Planets, 103*(E1), 1703-1713.

Lucey, P. G., Blewett, D. T., Taylor, G. J., & Hawke, B. (2000). Imaging of lunar surface maturity. *Journal of Geophysical Research: Planets*, *105*(E8), 20377-20386.

Lucey, P. G. (2002). Radiative transfer model constraints on the shock state of lunar anorthosites. *Geophysical Research Letters, 29(10),* 1486, doi:10.1029/2001GL014655.

Lucey, P. G. (2004). Mineral maps of the Moon. *Geophysical Research Letters*, *31*(8).

Lucey, P. G. (2006a). Radiative transfer modeling of the effect of mineralogy on some empirical methods for estimating iron concentration from multispectral imaging of the Moon. *Journal of Geophysical Research: Planets*, *111*(E8).

Lucey, P., Korotev, R. L., Gillis, J. J., Taylor, L. A., Lawrence, D., Campbell, B. A., Elphic, R., Feldman, B., Hood, L. L., Hunten, D., & Mendillo, M. (2006b). Understanding the lunar surface and space-moon interactions. *Reviews in Mineralogy and Geochemistry*, *60*(1), 83-219.

Lucey, P. G., & Riner, M. A. (2011). The optical effects of small iron particles that darken but do not redden: Evidence of intense space weathering on Mercury. *Icarus*, *212*(2), 451-462.

Lucey, P. G., Norman, J. A., Crites, S. T., Taylor, G. J., Hawke, B., Lemelin, M., & Melosh, H. J. (2014a). A large spectral survey of small lunar craters: Implications for the composition of the lunar mantle. *American Mineralogist*, *99*(11-12), 2251-2257.

Lucey, P. G., Neumann, G. A., Riner, M. A., Mazarico, E. M., Smith, D. E., Zuber, M. T., Paige, D. A., Bussey, D. B., Cahill, J. T., McGovern, A., Isaacson, P., Corley, L. M., Torrence, M. H., Melosh, H. J., Head, J. W. & Song, E. (2014b) The global albedo of the Moon at 1064 nm from LOLA. *Journal of Geophysical Research: Planets*, *119*(7), 1665-1679.

Lucey, P. G., Neumann, G.A., Paige, D. A, Riner, M. A., Mazarico, E. M., Smith, D.E., Zuber, M.T., Siegler, M., Hayne, P. O., Bussey, D.B. J., Cahill, J. T. S., McGovern, A., Isaacson, P., Corley, L. M., Torrence, M. H., Melosh, H. J., Head, J. W., Song, E. (2014c), Evidence for water ice and temperature dependent space weathering at the lunar poles from LOLA and Diviner. *Lunar and Planetary Science Conference, 45*, 2325.

Lucey, P.G., Greenhagen, B.T., Song, E., Arnold, J.A., Lemelin, M., Hanna, K.D., Bowles, N.E., Glotch, T.D., & Paige, D.A. (2017) Space weathering effects in Diviner Lunar Radiometer multispectral infrared measurements of the lunar Christiansen Feature: Characteristics and mitigation. *Icarus, 283,* 343–351.

Lundeen S. et al. (2012). M^3 AV-SIS, v. 3.17, JPL D-38529.

Matsuyama, I., Nimmo, F., Keane, J. T., Chan, N. H., Taylor, G. J., Wieczorek, M. A., Kiefer, W.S., & Williams, J. G. (2016). GRAIL, LLR, and LOLA constraints on the interior structure of the Moon. *Geophysical Research Letters*, *43*(16), 8365-8375.

Maxwell, T. A., & Phillips, R. J. (1978). Stratigraphic correlation of the radar-detected subsurface interface in Mare Crisium. *Geophysical Research Letters*, *5*(9), 811-814.

McGovern, P. J., W. S. Kiefer, G. Y. Kramer, M. T. Zuber, J. C. Andrews-Hanna, & Head III, J. W. (2014). Magma ascent at lunar impact basins: Effects of lithospheric tectonic stress gradients, brittle failure, and volatile generation. In *Lunar and Planetary Science Conference, 45,* 2771.

McGovern, P. J., Potter, R. W. K., Collins, G. S., Kring, D. A., Grange, M. L., & Nemchin, A. A. (2015) Pulses of magma movement triggered by the South Pole-Aitken basin impact. *Workshop on Early Solar System Bombardment III,* 3027.

McKay, D. S., & Basu, A. (1983). The production curve for agglutinates in planetary regoliths. *Journal of Geophysical Research: Solid Earth*, *88*(S01), B193-B199.

McKay, D., Swindle, T., & Greenberg, R. (1989) Asteroidal regoliths: What we do not know. *Asteroids II.* University of Arizona Press.

McKay, D. S., Heiken, G., Basu, A., Blanford, G., Simon, S., Reedy, R., French, B. M., & Papike, J. (1991), G. H. Heiken, D. T. Vaniman, B. M. French, (Eds.), The Lunar Regolith, *In: Lunar Sourcebook: A user's guide to the Moon.* Cambridge University Press, New York, pp. 285-365.

Melosh, H. J. (1989), *Impact Cratering: A Geologic Process*, Oxford monographs on Geology and Geophysics no. 11, Oxford Univ. Press, New York.

Melosh, H. J., Freed, A. M., Johnson, B. C., Blair, D. M., Andrews-Hanna, J. C., Neumann, G. A., Phillips, R. J., Smith, D. E., Solomon, S. C., Wieczorek, M. A., & Zuber, M. T. (2013). The origin of lunar mascon basins. *Science*, *340*(6140), 1552-1555.

Miljković, K., Wieczorek, M. A., Collins, G. S., Solomon, S. C., Smith, D. E., & Zuber, M. T. (2015). Excavation of the lunar mantle by basin-forming events on the Moon. *Earth and Planetary Science Letters, 409,* 243-251.

Mitrofanov, I. G., Sanin, A. B., Boynton, W. V., Chin, G., Garvin, J. B., Golovin, D., Evans, L. G., Harshman, K., Kozyrev, A. S., Litvak, M. L., Malakhov, A., Mazarico, E., McClanahan, T., Milikh, G., Mokrousov, M., Nandikotkur, G., Neumann, G. A., Nuzhdin, I., Sagdeev, R., Shevchenko, V., Shvestov, V., Smith, D. E., Starr, R., Tretyakov, V. I., Trombka, J., Usikov, D., Varenikov, A., Vostrukhin, A., & Zuber, M. T. (2010). Hydrogen mapping of the lunar south pole using the LRO neutron detector experiment LEND. *Science*, *330*(6003), 483-486.

Moroz, L. V., Starukhina, L. V., Rout, S. S., Sasaki, S., Helbert, J., Baither, D., Bischoff, A., & Hiesinger, H. (2014). Space weathering of silicate regoliths with various FeO contents: New insights from laser irradiation experiments and theoretical spectral simulations. *Icarus*, *235*, 187-206.

Morris, R. V. (1976). Surface exposure indices of lunar soils-A comparative FMR study. In *Lunar and Planetary Science Conference Proceedings*, *7,* 315-335.

Morris, R. V. (1978). The surface exposure/maturity/of lunar soils-Some concepts and Is/FeO compilation. In *Lunar and Planetary Science Conference Proceedings*, *9,* 2287-2297.

Muller, P. M., & Sjogren, W. L. (1968). Mascons: Lunar mass concentrations. *Science*, *161*(3842), 680-684.

Mustard, J. F., Pieters, C. M., Isaacson, P. J., Head, J. W., Besse, S., Clark, R. N., Klima, R. L., Petro, N. E., Staid, M. I., Sunshine, J. M., Runyon, C. J., and Tompkins, S. (2011). Compositional diversity and geologic insights of the Aristarchus crater from Moon Mineralogy Mapper data. *Journal of Geophysical Research: Planets*, *116*(E6).

Nagahara, H., Kushiro, I., & Mysen, B. O. (1993). Vaporization and condensation of chondritic materials-experimental studies. *Primitive Solar Nebula and Origin of Planets*, 427-446.

Noble, S. K., Pieters, C. M., Taylor, L. A., Morris, R. V., Allen, C. C., McKay, D. S., & Keller, L. P. (2001). The optical properties of the finest fraction of lunar soil: Implications for space weathering. *Meteoritics & Planetary Science*, *36*(1), 31-42.

Noble, S. K., Keller, L. P., & Pieters, C. M. (2005). Evidence of space weathering in regolith breccias I: Lunar regolith breccias. *Meteoritics & Planetary Science*, *40*(3), 397-408.

Noble, S. K., Pieters, C. M., & Keller, L. P. (2007). An experimental approach to understanding the optical effects of space weathering. *Icarus*, *192*(2), 629-642.

Noble, S.K., Hiroi, T., Keller, L.P., Rahman, Z., Sasaki, S., & Pieters, C.M. (2011). Experimental Space weathering of ordinary chondrites by nanopulse laser: TEM results. In *Lunar and Planetary Science Conference*, *42,* 1382.

Norman, M. D., & Nemchin, A. A. (2014). A 4.2 billion year old impact basin on the Moon: U–Pb dating of zirconolite and apatite in lunar melt rock 67955. *Earth and Planetary Science Letters*, *388*, 387-398.

Nozette, S., Lichtenberg, C. L., Spudis, P., Bonner, R., Ort, W., Malaret, E., Robinson, M., & Shoemaker, E. M. (1996). The Clementine bistatic radar experiment. *Science*, *274*(5292), 1495-1498.

Öhman, T., Kramer, G. Y., & McGovern, P. J. (2016). Geomorphologic Sketch Mapping of a Fresh Lunar Crater Eimmart A. In *Lunar and Planetary Science Conference, 47,* 1948.

Ohtake, M., Matsunaga, T., Haruyama, J., Yokota, Y., Morota, T., Honda, C., Ogawa, Y., Torii, M., Miyamoto, H., Arai, T., Hirata, N., Iwasaki, A., Nakamura, R., Hiroi, T., Sugihara, T., Takeda, H., Otake, H., Pieters, C. M., Saiki, K., Kitazato, K., Abe, M., Asada, N., Demura, H., Yamaguchi, Y, Sasaki, S., Kodama, S., Terazono, J., Shirao, M., Yamaji, A., Minami, S., Akiyama, H., & Josset, J. (2009). The global distribution of pure anorthosite on the Moon. *Nature*, *461*(7261), 236-240.

Osinski, G. R., Tornabene, L. L., & Grieve, R. A. (2011). Impact ejecta emplacement on terrestrial planets. *Earth and Planetary Science Letters*, *310*(3), 167-181.

Otake, H., Ohtake, M., & Hirata, N. (2012). Lunar iron and titanium abundance algorithms based on SELENE (Kaguya) Multiband Imager data. In *Lunar and Planetary Science Conference, 43,* 1905.

Paige, D. A., Siegler, M. A., Zhang, J. A., Hayne, P. O., Foote, E. J., Bennett, K. A., Vasavada, A. R., Greenhagen, B. T., Schofield, J. T., McCleese, D. J., Foote, M.

C., DeJong, E., Bills, B. G., Hartford, W., Murray, B. C., Allen, C. C., Snook, K., Soderblom, L. A., Calcutt, S., Taylor, F. W., Bowles, N. E., Bandfield, J. L., Elphic, R., Ghent, R., Glotch, T. D., Wyatt, M. B., Lucey, P. G. (2010). Diviner lunar radiometer observations of cold traps in the Moon's south polar region. *Science*, *330*(6003), 479-482.

Paige, D. A., Siegler, M. A., Harmon, J. K., Neumann, G. A., Mazarico, E. M., Smith, D. E., Zuber, M. T., Harju, E., Delitsky, M. L., & Solomon, S. C. (2013). Thermal stability of volatiles in the north polar region of Mercury. *Science*, *339*(6117), 300-303.

Papike, J. J., Hodges, F. N., Bence, A. E., Cameron, M., & Rhodes, J. M. (1976). Mare basalts: crystal chemistry, mineralogy, and petrology. *Reviews of Geophysics*, *14*(4), 475-540.

Paruso, D. M., Cassidy, W. A., & Hapke, B. W. (1978). An experimental investigation of fractionation by sputter deposition. In *Lunar and Planetary Science Conference Proceedings*, *9,* 1711-1724.

Peeples, W. J., Sill, W. R., May, T. W., Ward, S. H., Phillips, R. J., Jordan, R. L., Abbott, E. A., & Killpack, T. J. (1978). Orbital radar evidence for lunar subsurface layering in Maria Serenitatis and Crisium. *Journal of Geophysical Research: Solid Earth*, *83*(B7), 3459-3468.

Pelkey, S. M., Mustard, J. F., Murchie, S., Clancy, R. T., Wolff, M., Smith, M., Milliken, R., Bibring, J. P., Gendrin, A., Poulet, F., Langevin, Y., & Gondet, B. (2007). CRISM multispectral summary products: Parameterizing mineral diversity on Mars from reflectance. *Journal of Geophysical Research: Planets (1991–2012)*, *112*(E8).

Pierazzo, E., & Melosh, H. J. (2000). Hydrocode modeling of oblique impacts: The fate of the projectile. *Meteoritics & Planetary Science*, *35*(1), 117-130.

Pieters, C. M. (1982). Copernicus crater central peak: Lunar mountain of unique composition. *Science*, *215*(4528), 59-61.

Pieters, C. (1983) Strength of mineral absorption features in the transmitted component of near infrared reflected light - First results from RELAB. *Journal of Geophysical Research,* 88, 9534-9544.

Pieters, C. M. (1986). Composition of the lunar highland crust from near-infrared spectroscopy. *Reviews of Geophysics, 24(3),* 557–578, doi:10.1029/RG024i003p00557.

Pieters, C. M., Fischer, E. M., Rode, O., & Basu, A. (1993). Optical effects of space weathering: The role of the finest fraction. *Journal of Geophysical Research: Planets (1991–2012)*, *98*(E11), 20817-20824.

Pieters, C. M., & Tompkins, S. (1999). Tsiolkovsky crater: A window into crustal processes on the lunar farside. *Journal of Geophysical Research: Planets*, *104*(E9), 21935-21949.

Pieters, C. M., Taylor, L. A., Noble, S. K., Keller, L. P., Hapke, B., Morris, R. V., ... & Wentworth, S. (2000). Space weathering on airless bodies: Resolving a mystery with lunar samples. *Meteoritics & Planetary Science*, *35*(5), 1101-1107.

Pieters, C. M., Besse, S., Boardman, J., Buratti, B., Cheek, L., Clark, R. N., Combe, J. P., Dhingra, D., Goswami, J. N., Green, R. O., Head, J. W., Isaacson, P., Klima, R., Kramer, G., Lundeen, S., Malaret, E., McCord, T., Mustard, J., Nettles, J., Petro, N., Runyon, C., Staid, M., Sunshine, J., Taylor, L. A., Thaisen K., Tompkins, S., & Whitten, J. (2011). Mg-spinel lithology: A new rock type on the lunar farside. *Journal of Geophysical Research: Planets*, *116*(E6).

Pieters, C. M., & Noble, S. K. (2016). Space weathering on airless bodies. *Journal of Geophysical Research: Planets*, *121*(10), 1865-1884.

Pillinger, C. T. (1979). Solar-wind exposure effects in the lunar soil. *Reports on Progress in Physics*, *42*(5), 897.

Pirri, A. N. (1977). Theory for laser simulation of hypervelocity impact. *The Physics of Fluids*, *20*(2), 221-228.

Potter, R. W. K., Collins, G. S., Kiefer, W. S., McGovern, P. J., and Kring, D. A. (2012). Constraining the size of the South Pole-Aitken basin impact. *Icarus* 220, 730-743.

Potter, R. W. K., Kring, D. A., Collins, G. S., Kiefer, W. S., and McGovern, P. J. (2013a). Numerical modeling of the formation and structure of the Orientale impact basin. *Journal of Geophysical Research: Planets*, 118, 963-979.

Potter, R. W. K., D. A. Kring, & Collins, G. S. (2013b). Quantifying the attenuation of structural uplift beneath large lunar craters. *Geophysical Research Letters*, *40*, 5615-5620.

Potter, R. W., Kring, D. A., & Collins, G. S. (2015). Scaling of basin-sized impacts and the influence of target temperature. *In Osinski, G. R., and Kring, D. A., eds., Large Meteorite Impacts and Planetary Evolution V: Geological Society of America Special Paper,* 518, p. 99-113, doi10.1130/2015.2518(06).

Powell, K. E., McGovern, P. J., & Kramer, G. Y. (2012). Olivine detections at the rim of Crisium basin with Moon Mineralogy Mapper. *Lunar and Planetary Science XLIII, 43,* Abstract #1689.

Riner, M. A., & Lucey, P. G. (2012). Spectral effects of space weathering on Mercury: The role of composition and environment. *Geophysical Research Letters*, *39*(12).

Ringwood, A. E., & Kesson, S. E. (1976). A dynamic model for mare basalt petrogenesis. *Lunar and Planetary Science Conference Proceedings, 7,* 1697–1722.

Robinson, M. S., Brylow, S. M., Tschimmel, M., Humm, D., Lawrence, S. J., Thomas, P. C., Denevi, B. W., Bowman-Cisneros, E., Zerr, J., Ravine, M. A., Caplinger, M. A., Ghaemi, F. T., Schaffner, J. A., Malin, M. C., Mahanti, P., Bartels, A., Anderson, J., Tran, T. N., Eliason, E. M. McEwen, A. S., Turtle, E., Jolliff, B. L., & Hiesinger, H. (2010). Lunar reconnaissance orbiter camera (LROC) instrument overview. *Space Science Reviews, 150(1-4),* 81-124.

Ryder, G., & Wood, J. A. (1977). Serenitatis and Imbrium impact melts-Implications for large-scale layering in the lunar crust. In *Lunar and Planetary Science Conference Proceedings* (Vol. 8, pp. 655-668).

Ryder, G., & Marvin, U. B. (1978). On the origin of Luna 24 basalts and soils. In *Mare Crisium: The View from Luna 24*, *Vol. 1*, pp. 339-355).

Ryder, G. (1991). Lunar ferroan anorthosites and mare basalt sources: The mixed connection. *Geophysical Research Letters*, *18*(11), 2065-2068.

Ryder, G. (1992) Chemical variation and zoning of olivine in lunar dunite 72415: Near-surface accumulation. *Lunar and Planetary Science Conference Proceedings*, *22*, 373-380.

Sasaki, S., Nakamura, K., Hamabe, Y., Kurahashi, E., & Hiroi, T. (2001). Production of

iron nanoparticles by laser irradiation in a simulation of lunar-like space weathering. *Nature*, *410*(6828), 555-557.

Sasaki, S., Kurahashi, E., Yamanaka, C., & Nakamura, K. (2003). Laboratory simulation of space weathering: Changes of optical properties and TEM/ESR confirmation of nanophase metallic iron. *Advances in Space Research*, *31*(12), 2537-2542.

Schaible, M. J., & Baragiola, R. A. (2014). Hydrogen implantation in silicates: the role of solar wind in SiOH bond formation on the surfaces of airless bodies in space. *Journal of Geophysical Research: Planets*, *119*(9), 2017-2028.

Scherer, K., Fichtner, H., Borrmann, T., Beer, J., Desorgher, L., Flükiger, E., Fahr, H. J., Ferreira, S. E. S., Langner, U. W., Potgieter, M. S., Heber, B., Masarik, J., Shaviv, N. J., & Veizer, J. (2006). Interstellar-terrestrial relations: variable cosmic environments, the dynamic heliosphere, and their imprints on terrestrial archives and climate. *Space Science Reviews*, *127*(1-4), 327-465.

Schultz, P. H., & Spudis, P. D. (1979). Evidence for ancient mare volcanism. *Lunar and Planetary Science Conference Proceedings, 10*, 2899-2918.

Schultz, P. H., & Crawford, D. A. (2011). Origin of nearside structural and geochemical anomalies on the Moon. *Geological Society of America Special Papers*, *477*, 141-159.

Schultz, P. H., & Eberhardy, C. A. (2015). Spectral probing of impact-generated vapor in laboratory experiments. *Icarus*, *248*, 448-462.

See, T. H., Horz, F., Cintala, M. J., Smrekar, S. & Cardenas, F. (1988). Formation of agglutinate-like particles in an experimental regolith. In *Lunar and Planetary Science Conference Proceedings*, *18,* 900-901.

Serventi, G., Carli, C., Sgavetti, M., Ciarniello, M., Capaccioni, F., & Pedrazzi, G. (2013). Spectral variability of plagioclase–mafic mixtures (1): Effects of chemistry and modal abundance in reflectance spectra of rocks and mineral mixtures. *Icarus*, *226*(1), 282-298.

Shearer, C. K., & Papike, J. J. (1999). Magmatic evolution of the Moon. *American Mineralogist*, *84*, 1469-1494.

Shearer, C. K., Elardo, S. M., Petro, N. E., Borg, L. E. and McCubbin, F. M. (2015a). Origin of the lunar highlands Mg-suite: An integrated petrology, geochemistry,

chronology, and remote sensing perspective, *American. Mineralogist*, *100,* 294-325.

Shearer, C. K., Burger, P. V., Bell, A. S., Guan, Y., & Neal, C. R. (2015b). Exploring the Moon's surface for remnants of the lunar mantle 1. Dunite xenoliths in mare basalts. A crustal or mantle origin? *Meteoritics & Planetary Science*, *50*(8), 1449-1467.

Shu, A., Collette, A., Drake, K., Grün, E., Horányi, M., Kempf, S., Mocker, A., Munsat, T., Northway, P., Srama, R., 2012. 3 MV hypervelocity dust accelerator at the Colorado Center for Lunar Dust and Atmospheric Studies. *Review of Scientific Instruments 83,* 075108.

Singer, R. B. (1981). Near-infrared spectral reflectance of mineral mixtures: Systematic Combinations of pyroxenes, olivine, and iron oxides. *Journal of Geophysical Research: Solid Earth (1978–2012)*, *86*(B9), 7967-7982.

Sliz, M. U., & Spudis, P. D. (2016). New Geological Map of the Lunar Crisium Basin. *Lunar and Planetary Science XLVII, 47,* Abstract #1678.

Smith, D. E., Zuber, M. T., Jackson, G. B., Cavanaugh, J. F., Neumann, G. A., Riris, H., Sun, X., Zellar, R. S., Coltharp, C., Connelly, J., Katz, R. B., Kleyner, I., Liiva, P., Matuszeski, A., Mazarico, E. M., McGarry, J. F., Novo-Gradac, A. M., Ott, M. N., Peters, C., Ramos-Izquierdo, L. A., Ramsey, L., Rowlands, D. D., Schmidt, S., Scott, V. S. III, Shaw, G. B., Smith, J. C., Swinski, J.- P. Torrence, M. H., Unger, G., Yu, A. W., & Zagwodzki, T. W. (2010a). The Lunar Orbiter Laser Altimeter investigation on the Lunar Reconnaissance Orbiter mission, *Space Science Reviews, 150,* 209-241.

Smith, D. E., Zuber, M. T., Neumann, G. A., Lemoine, F. G., Mazarico, E., Torrence, M. H., McGarry, J. F., Rowlands, D. D., Head III, J. W., Duxbury, T. H., Aharonson, O., Lucey, P. G., Robinson, M. S., Barnouin, O. S., Cavanaugh, J. F., Sun, X., Liiva, P., Mao, D., Smith, J. C., & Bartels, A. E. (2010b). Initial observations from the lunar orbiter laser altimeter (LOLA). *Geophysical Research Letters*, *37*(18).

Smith, D. E., Zuber, M. T., Neumann, G. A., Mazarico, W., Lemoine, F. G., Head, J. W. III, Lucey, P. G., Aharonson, O., Robinson, M. S., Sun, X., Torrence, M. H.,

Barker, M. K., Oberst, J., Duxbury, T. C., Mao, D. -d., Barmouin, O. S., Jha, K., Rowlands, D. D., Goossens, S., Baker, D., Bauer, S., Gläser, P., Lemelin, M., Rosenburg, M., Sori, M. M., Whitten, J., & McClanahan. T. (2016). Summary of the results from the Lunar Orbiter Laser Altimeter after seven years in orbit, *Icarus, 283,*70-91*,* doi: 10.1016/j.icarus.2016.06.006.

Snyder, G. A., Taylor, L. A., & Neal, C. R. (1992). A chemical model for generating the sources of mare basalts: Combined equilibrium and fractional crystallization of the lunar magmasphere. *Geochimica et Cosmochimica Acta*, *56*(10), 3809-3823.

Snyder, G. A., Neal C. R., Taylor L. A., & Halliday, A. N. (1995). Processes involved in the formation of magnesian-suite plutonic rocks from the highlands of the Earth's Moon*, Journal of Geophysical Research*, *100,* 9365-9388.

Solomon, S. C., & Head, J. W. (1979). Vertical movement in mare basins: Relation to mare emplacement, basin tectonics, and lunar thermal history. *Journal of Geophysical Research: Solid Earth*, *84*(B4), 1667-1682.

Solomon, S. C., & Head, J. W. (1980). Lunar mascon basins: Lava filling, tectonics, and evolution of the lithosphere. *Reviews of Geophysics*, *18*(1), 107-141.

Song, E., Bandfield, J. L., Lucey, P. G., Greenhagen, B. T., & Paige, D. A. (2013). Bulk mineralogy of lunar crater central peaks via thermal infrared spectra from the Diviner Lunar Radiometer: A study of the Moon's crustal composition at depth. *Journal of Geophysical Research: Planets*, *118*(4), 689-707.

Spera, F. J. (1992). Lunar magma transport phenomena. *Geochimica et Cosmochimica Acta*, *56*(6), 2253-2265.

Spudis, P. D., & Sliz, M. U. (2017). Impact melt of the lunar Crisium multiring basin. *Geophysical Research Letters*, *44*(3), 1260-1265.

Srnka, L. J., Hoyt, J. L., Harvey, J. V. S., & McCoy, J. E. (1979). A study of the Rima Sirsalis lunar magnetic anomaly. *Physics of the Earth and Planetary Interiors*, *20*(2-4), 281-290.

Staid, M. I., & Pieters, C. M. (2001). Mineralogy of the last lunar basalts- Results from Clementine. *Journal of Geophysical Research. E. Planets*, *106*, 27.

Staid, M. I., Pieters, C. M., Besse, S., Boardman, J., Dhingra, D., Green, R., Head, J. W., Isaacson, P., Klima, R., Kramer, G., Mustard, J. M., Runyon, C., Sunshine, J., &

Taylor, L. A. (2011). The mineralogy of late stage lunar volcanism as observed by the Moon Mineralogy Mapper on Chandrayaan-1. *Journal of Geophysical Research: Planets*, *116*(E6).

Stöffler, D., Knöll, H. D., Marvin, U. B., Simonds, C. H., & Warren, P. H. (1980). Recommended classification and nomenclature of lunar highland rocks-a committee report. In *Lunar Highlands Crust*, *1,* 51-70.

Sunshine, J. M., & Pieters, C. M. (1998). Determining the composition of olivine from reflectance spectroscopy, *Journal of Geophysical Research*, *103*(E6), 13,675-13,688.

Sunshine, J. M., Connolly, H. C., McCoy, T. J., Bus, S. J., & La Croix, L. M. (2008). Ancient asteroids enriched in refractory inclusions. *Science*, *320*(5875), 514-517.

Syal, M. B., Schultz, P. H., & Riner, M. A. (2015). Darkening of Mercury's surface by cometary carbon. *Nature Geoscience*, *8*(5), 352.

Taylor, G. J., Warren, P., Ryder, G., Delano, J., Pieters, C., & Lofgren, G. (1991). Lunar rocks. *Lunar Sourcebook,* 183-284.

Taylor, L. A., Pieters, C. M., Keller, L. P., Morris, R. V., & McKay, D. S. (2001). Lunar mare soils: Space weathering and the major effects of surface-correlated nanophase Fe. *Journal of Geophysical Research: Planets*, *106*(E11), 27985-27999.

Taylor, G. J. (2009). Ancient lunar crust: Origin, composition, and implications. *Elements*, *5*(1), 17-22.

Taylor, L. A., Pieters, C., Patchen, A., Taylor, D. H. S., Morris, R. V., Keller, L. P., & McKay, D. S. (2010). Mineralogical and chemical characterization of lunar highland soils: Insights into the space weathering of soils on airless bodies. *Journal of Geophysical Research: Planets*, *115*(E2).

Tera, F., Papanastassiou, D. A., & Wasserburg, G. J. (1974), Isotopic evidence for a terminal lunar cataclysm. *Earth Planetary Science Letters, 22(1),* 1-21.

Tompkins, S., & Pieters, C. M. (1999). Mineralogy of the lunar crust: Results from Clementine. *Meteoritics & Planetary Science*, *34*(1), 25-41.

Trang, D., Lucey, P. G., Gillis-Davis, J. J., Cahill, J. T., Klima, R. L., & Isaacson, P. J. (2013). Near-infrared optical constants of naturally occurring olivine and

synthetic pyroxene as a function of mineral composition. *Journal of Geophysical Research: Planets*, *118*(4), 708-732.

Trang, D., Lucey, P. G., & Izenberg, N. R. (2017). Radiative transfer modeling of MESSENGER VIRS spectra: Detection and mapping of submicroscopic iron and carbon. *Icarus*, *293*, 206-217.

Trang, D., & Lucey, P. G. (2019). Improved space weathering maps of the lunar surface through radiative transfer modeling of Kaguya multiband imager data. *Icarus*, *321*, 307-323.

Tsuchiyama, A., Uesugi, M., Matsushima, T., Michikami, T., Kadono, T., Nakamura, T., Uesugi, K., Nakano, T., Sandford, S. A., Noguchi, R., Matsumoto, T., Matsuno, J., Nagano. T., Imai, Y., Takeuchi, A., Suzuki, Y., Ogami, T., Katagiri, J., Ebihara, M., Ireland, T. R., Kitajima, F., Nagao, K., Naraoka, H., Noguchi, T., Okazaki, R., Yurimoto, H., Zolensky, M. E., Mukai, T., Abe, M., Yada, T., Fujimura, A., Yoshikawa. M., & Kawaguchi, J. (2011). Three-dimensional structure of Hayabusa samples: origin and evolution of Itokawa regolith. *Science*, *333*(6046), 1125-1128.

Tsuchiyama, A. (2014). Asteroid Itokawa a source of ordinary chondrites and a laboratory for surface processes. *Elements, 10(1),* 45-50.

Urey, H. C. (1952), The Planets: Their Origin and Development, Yale Univ. Press, New Haven, Conn.

Vasavada, A. R., Paige, D. A., & Wood, S. E. (1999). Near-surface temperatures on Mercury and the Moon and the stability of polar ice deposits. *Icarus*, *141*(2), 179-193.

Vasavada, A. R., Bandfield, J. L., Greenhagen, B. T., Hayne, P. O., Siegler, M. A., Williams, J. P., & Paige, D. A. (2012). Lunar equatorial surface temperatures and regolith properties from the Diviner Lunar Radiometer Experiment. *Journal of Geophysical Research: Planets*, *117*(E12).

Vaughan, W. M., Head, J. W., Wilson, L., & Hess, P. C. (2013). Geology and petrology of enormous volumes of impact melt on the Moon: A case study of the Orientale basin impact melt sea. *Icarus*, *223*(2), 749-765.

Walker, R. M. (1980). Nature of the fossil evidence-Moon and meteorites. *The Ancient Sun: Fossil Record in the Earth, Moon and Meteorites*, *1,* 11-28.

Watson, K., Murray, B. C., & Brown, H. (1961). The behavior of volatiles on the lunar surface. *Journal of Geophysical Research, 66(9),* 3033–3045.

Whitten, J. L., & Head, J. W. (2015). Lunar cryptomaria: Physical characteristics, distribution, and implications for ancient volcanism. *Icarus*, *247*, 150-171.

Wieczorek, M. A., & Phillips, R. J. (1998). Potential anomalies on a sphere: Applications to the thickness of the lunar crust. *Journal of Geophysical Research*, *103*(E1), 1715-1724.

Wieczorek, M. A., Neumann, G. A., Nimmo, F., Kiefer, W. S., Taylor, G. J., Melosh, H. J., Phillips, R. J., Solomon, S. C., Andrews-Hanna, J. C., Asmar, S. W., Konopliv, A. S., Lemoine, F. G., Smith, D. E., Watkins, M. M., Williams, J. G., & Zuber, M. T. (2013). The crust of the Moon as seen by GRAIL. *Science*, *339*(6120), 671-675.

Wilhelms, D. E. & El-Baz, F. (1977). Geologic map of the east side of the Moon. U.S. Geological Survey, Map I-948.

Wilson, L., & Head, J. W. (2017). Generation, ascent and eruption of magma on the Moon: New insights into source depths, magma supply, intrusions and effusive/explosive eruptions (Part 1: Theory). *Icarus*, *283*, 146-175.

Wise, D. U., & Yates, M. T. (1970). Mascons as structural relief on a lunar 'Moho'. *Journal of Geophysical Research*, *75*(2), 261-268.

Wood, J. A., Dickey Jr, J. S., Marvin, U. B., & Powell, B. N. (1970). Lunar anorthosites and a geophysical model of the Moon. *Proceedings of the Apollo 11 Lunar Science Conference, 1,* 965-988.

Wood, I. G., Vočadlo, L., Dobson, D. P., Price, G. D., Fortes, A. D., Cooper, F. J., ... Neale, J. W., Walker, A. M., Marshall, W. G., Tucker, M. G., Francis, D. J., Stone, H. J., & McCammon, C. A., (2008). Thermoelastic properties of magnesiowüstite,(Mg1− xFex) O: determination of the Anderson–Grüneisen parameter by time-of-flight neutron powder diffraction at simultaneous high pressures and temperatures. *Journal of Applied Crystallography*, *41*(5), 886-896.

Yamada, M., Sasaki, S., Nagahara, H., Fujiwara, A., Hasegawa, S., Yano, H., Hiroi, T., Ohashi, H., & Otake, H. (1999). Simulation of space weathering of planet-forming materials: Nanosecond pulse laser irradiation and proton implantation on olivine and pyroxene samples. *Earth, Planets and Space*, *51*(11), 1255-1265.

Yamamoto, S., Nakamura, R., Matsunaga, T., Ogawa, Y., Ishihara, Y., Morota, T., Hirata, N., Ohtake, M., Hiroi, T., Yokota, Y., & Haruyama, J. (2010). Possible mantle origin of olivine around lunar impact basins detected by SELENE. *Nature Geoscience*, *3*(8), 533-536.

Yamamoto, S., Nakamura, R., Matsunaga, T., Ogawa, Y., Ishihara, Y., Morota, T., Hirata, N., Ohtake, M., Hiroi, T., Yokota, Y., & Haruyama, J. (2012). Olivine-rich exposures in the South Pole-Aitken basin. *Icarus*, *218*(1), 331-344.

Yin, L. I., Ghose, S., & Adler, I. (1972). Investigation of a possible solar-wind darkening of the lunar surface by photoelectron spectroscopy. *Journal of Geophysical Research*, *77*(8), 1360-1367.

Yokota, Y., Matsunaga, T., Ohtake, M., Haruyama, J., Nakamura, R., Yamamoto, S., Ogawa, Y., Morota, T., Honda, C., Saiki, K., Nagasawa, K., Kitazato, K., Sasaki, S., Iwasaki, A., Demura, H., Hirata, N., Hiroi, T., Honda, R., Iijima, Y., & Mizutani, H. (2011). Lunar photometric properties at wavelengths 0.5–1.6 μm acquired by SELENE Spectral Profiler and their dependency on local albedo and latitudinal zones. *Icarus*, *215*(2), 639-660.

Yue, Z., Johnson, B. C., Minton, D. A., Melosh, H. J., Di, K., Hu, W., & Liu, Y. (2013). Projectile remnants in central peaks of lunar impact craters. *Nature Geoscience*, *6*(6), 435-437.

Zhu, M. H., Chang, J., Ma, T., Ip, W. H., Fa, W., Wu, J., Cai, M., Gong, Y., Hu, Y., Xu, A., & Tang, Z. (2013). Potassium Map from Chang'E-2 Constraints the Impact of Crisium and Orientale Basin on the Moon. *Scientific reports*, *3*.

Zuber, M. T., Head, J. W., Smith, D. E., Neumann, G. A., Mazarico, E., Torrence, M. H., Aharonson, O., Tye, A. R., Fassett, C. I., Rosenburg, M. A., & Melosh, H. J. (2012). Constraints on the volatile distribution within Shackleton crater at the lunar south pole. *Nature*, *486*(7403), 378-381.

Zuber, M. T., Smith, D. E., Watkins, M. M., Asmar, S. W., Konopliv, A. S., Lemoine, F. G., Melosh, H. J., Neumann, G. A., Phillips, R. J., Solomon, S. C., Wieczorek, M. A., Williams, J. G., Goossens, S. J., Kruizinga, G., Mazarico, E., Park, R. S., & Yuan, D.- N. (2013). Gravity field of the Moon from the Gravity Recovery and Interior Laboratory (GRAIL) mission, *Science, 339(6120),* 668-671.

Zuber, M. T., Smith, D. E., Neumann, G. A., Goossens, S., Andrews-Hanna, J. C., Head, J. W., Kiefer, W. S., Asmar, S. W., Konopliv, A. S., Lemoine, F. G., Matsuyama, I., Melosh, H. J., McGovern, P. J., Nimmo, F., Phillips, R. J., Solomon, S. C., Taylor, G. J., Watkins, M. M., Wieczorek, M. A., Williams, J. G., Jansen, J. C., Johnson, B. C., Keane, J. T., Mazarico, E., Miljkovic, K., Park, R. S., Soderblom, J. M., and Yuan, D.-N. (2016) Gravity field of the Orientale basin from the Gravity Recovery and Interior Laboratory mission. *Science* 354, 438-441.